Volume 6 Issue 4 (2020) · ISSN 2424-7723

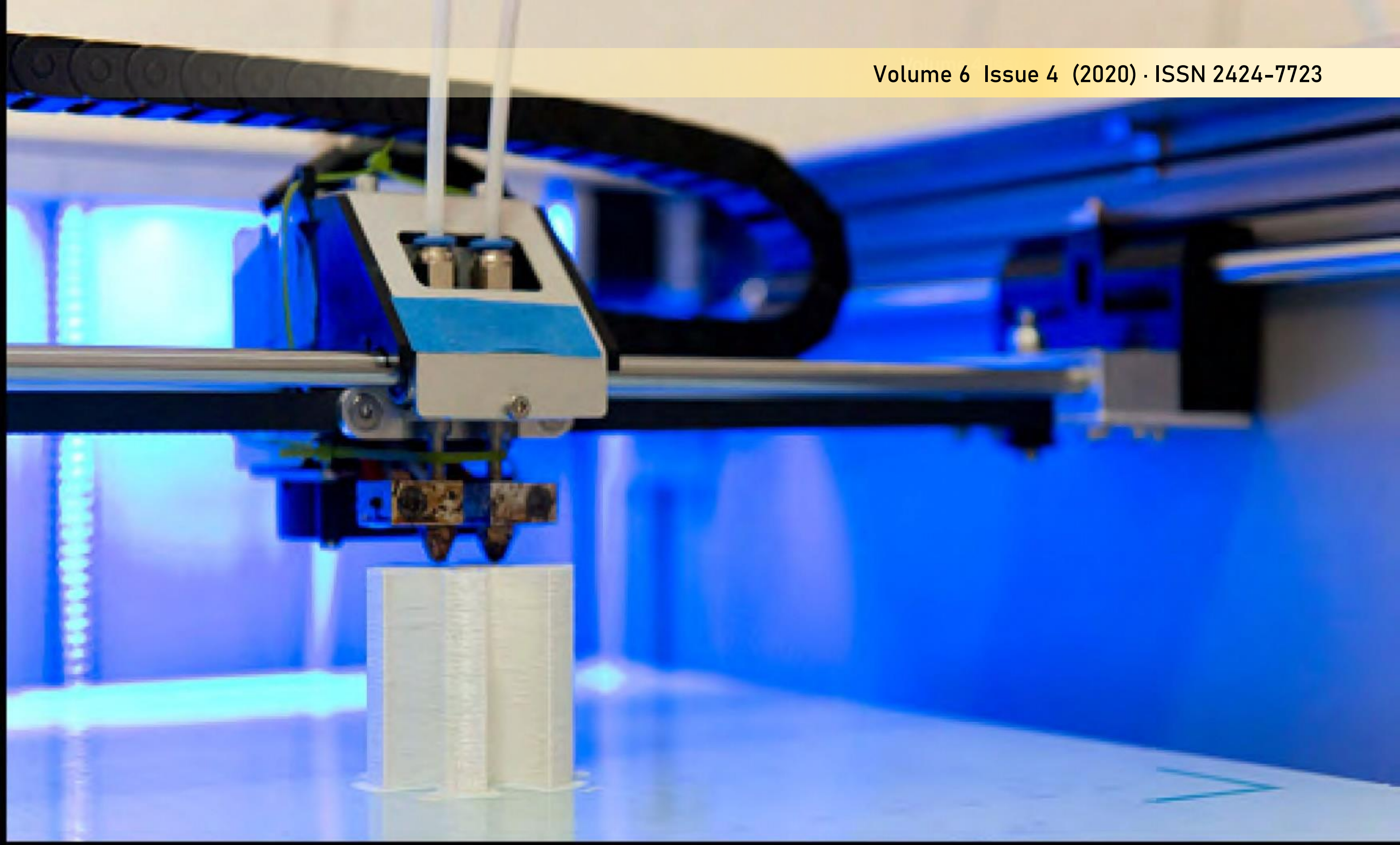

INTERNATIONAL JOURNAL OF BIOPRINTING

WHIOCE PUBLISHING PTE. LTD.
PROVIDING
FIRST-CLASS SCIENTIFIC INFORMATION
FOR TOP SCHOLARS

Volume 6 Issue 4 • 2020
ISSN 2424-7723 (print) ISSN 2424-8002 (online)

INTERNATIONAL JOURNAL OF BIOPRINTING

Editor-in-Chief

Chee Kai Chua

*Singapore University of Technology and Design,
Singapore*

WHIOCE
PUBLISHING PTE. LTD.

Volume 6 | Issue 4 | 2020 | Page 1 – 129 |

International Journal of Bioprinting

https://ijb.whioce.com/index.php/int-j-bioprinting

CONTENTS

Special Section: Research and Applications of 3D Printing and Bioprinting for Covid-19

Regular Section

SHORT COMMUNICATION

3D Printed and Electrospun, Transparent, Hierarchical Polylactic Acid Mask Nanoporous Filter

Haijun He[1], Min Gao[2], Balázs Illés[3], Kolos Molnar[1,4,*]

[1]Department of Polymer Engineering, Faculty of Mechanical Engineering, Budapest University of Technology and Economics, Műegyetem rkp. 3-9, H-1111, Budapest, Hungary

[2]Department of Mechatronics, Optics and Engineering Informatics, Faculty of Mechanical Engineering, Budapest University of Technology and Economics, Műegyetem rkp. 3-9, H-1111, Budapest, Hungary

[3]Department of Electronics Technology, Faculty of Electrical Engineering and Informatics, Budapest University of Technology and Economics, Műegyetem rkp. 3-9, H-1111, Budapest, Hungary

[4]MTA–BME Research Group for Composite Science and Technology, Műegyetem rkp. 3, H-1111, Budapest, Hungary

Abstract: Face masks are becoming one of the most useful personal protective equipment with the outbreak of the coronavirus (CoV) pandemic. The entire world is experiencing shortage of disposable masks and melt-blown non-woven fabrics, which is the raw material of the mask filter. Recyclability of the discarded mask is also becoming a big challenge for the environment. Here, we introduce a facile method based on electrospinning and three-dimensional printing to make changeable and biodegradable mask filters. We printed polylactic acid (PLA) polymer struts on a PLA nanofiber web to fabricate a nanoporous filter with a hierarchical structure and transparent look. The transparent look overcomes the threatening appearance of the masks that can be a feasible way of reducing the social trauma caused by the current CoV disease-19 pandemic. In this study, we investigated the effects of nozzle temperature on the optical, mechanical, and morphological and filtration properties of the nanoporous filter.

Keywords: Coronavirus disease-19, Electrospinning, Mask nanoporous filter, Nanofibers, Three-dimensional printing

***Corresponding Author:** Kolos Molnar, Department of Polymer Engineering, Faculty of Mechanical Engineering, Budapest University of Technology and Economics, Műegyetem rkp. 3-9, H-1111, Budapest, Hungary; molnar@pt.bme.hu

Received: April 19, 2020; ***Accepted***: May 18, 2020; ***Published Online***: July 1, 2020

(This article belongs to the *Special Section: Research and Applications of 3D Printing and Bioprinting for Covid-19*)

Citation: He H, Gao M, Illés B, *et al.*, 3D Printed and Electrospun, Transparent, Hierarchical Polylactic Acid Mask Nanoporous Filter, *Int J Bioprint*, 6(4): 278. DOI: 10.18063/ijb.v6i4.278.

1 Introduction

There are various biological aerosol particles in the outdoor air, including viruses, bacterial cells, bacterial and fungal spores, fragments, and pollen grains which may cause health issues, especially infectious diseases[1]. These particles of small sizes can easily penetrate the human respiratory system and cause flu, colds, pneumonia, and others. For example, the diameter of the 2019-novel coronavirus (nCoV) particles varies from about 60 to 140 nm[2], which poses a threat to global public health. One of the latest studies has indicated that surgical masks can prevent transmission of human CoVs from symptomatic individuals[3]. Therefore, it is essential and practical to wear personal protective equipment (e.g., face masks and respirators) during the outbreak period[4]. In general, good quality face masks are comprised of 3-4 textile layers. Melt-blown PP microfibers are widely used as the filter layer to capture the particles. However, to fulfill the requirement of mask with high filtration efficiency, the thickness of the filter has to be increased due to its microsized fiber diameter and large pore size[5]. The thickness of the mask can cause difficulty to breathe through, and as a result, the wearer will inhale unfiltered air through the edge of the mask. In comparison with melt-blown fibers, electrospun nanofiber web is an alternative candidate as a filtration media because of their small pore size, small diameter and large specific surface area. Liu *et al*.[6] prepared polyacrylonitrile (PAN)/polyacrylic acid composites nanofiber membranes as the filtration medium and it had a removal efficiency (99.994%) against the 300-500 nm NaCl aerosol particles at an airflow velocity of 5.3 cm/s. Zhang *et al*.[7] reported the use of PSU/PAN/PA-6 hybrid fibrous membranes to capture airborne particles and it can almost completely remove ~300 nm particles with an extremely small pore size of 270 nm. Most of the studies investigated the air filtration performance with 300 nm aerosol particles that are slightly bigger than the viruses. Although there is no direct measurement reported so far, we can still conclude that nanofibers are extremely good at capturing bigger airborne virions. Furthermore, severe acute respiratory syndrome-CoV-2 virus is usually transmitted by large respiratory droplets rather than by separate and individual virions. Therefore, based on the literature, the nanofiber filters can capture the vast majority of respiratory virions.

Although the electrospun nanofibers have such good advantages, including better filtration performance in the nanoscale compared with melt-blown fibers, optimizing their mechanical properties is still a big challenge. Therefore, the electrospun nanofibers must be combined with other supporting materials, for example, textile fabric, plastic mesh, and metallic mesh to make air filters[8]. Direct coating, where the electrospun nanofiber layer is deposited on the surface of the substrate, is the most common method to make such combined structure. However, there are a few issues with this process: (1) The conductive substrate can result in non-uniform deposition of nanofibers; (2) as the nanofibers are very sensitive, it is difficult to handle such flexible sheets without damaging the nanofibers; and (3) it is not possible to change such filter, so the mask can only be disposable.

Recently, three-dimensional (3D) printing technology is introduced to easily integrate nanofibers with 3D printed parts to support nanofibers. In the literature, fused deposition modeling (FDM) is the most common 3D printing technology to be combined with electrospinning[9-11]. In all these studies, the electrospun nanofibers were directly deposited onto the 3D printed objects. However, Kozior *et al*.[12] pointed out that the adhesion between the polylactic acid (PLA) printed objects and the PAN electrospun nanofibers was low. It could be better when soft TPU was used as the collecting substrate. To improve the adhesion between the nanofiber mat and the 3D printed object, the same research group[13] proposed another reverse method. They directly introduced 3D printed PLA on the electrospun PAN nanofiber mats, and it was found that the adhesion between the nanofibers and the printed polymer was stronger than the connection among the nanofibers within the nanofiber mat. However, as the nanofiber mat had glued onto the printing bed before printing, it is difficult to detach the composite, which is a big issue.

As the recyclability of disposable masks is going to become a big issue to the environment, it is necessary to make the disposable masks from biodegradable polymers urgently. It is also a good concept only if the filter within the mask is disposable, so the mask itself can be used multiple times after disinfection. PLA is the most popular material for FDM due to its easy processability and commercial availability[14,15]. It is an environmentally friendly polymer material and can be entirely biodegradable under certain conditions. Thus, the main goal of this study is to prepare PLA electrospun nanofibers combined with 3D printed PLA part for disposable filters of future masks. The layered filaments with a proper spacing support the nanofibers and simultaneously allow easy breath through. The transparent look can help to avoid the threatening appearance of the mask and can allow lipreading for people with mutism or hearing impairment.

In this study, we propose a simple transfer method to combine the nanofiber layer with a 3D printed substrate. As the printed filament and the nanofiber were made from identical material, the nozzle temperature is a crucial parameter to influence the morphology during the printing process. Therefore, we investigated the effects of nozzle temperature on the morphological, mechanical, optical, and filtration properties.

2 Materials and methods

2.1 Materials

PLA (M_w = 140,000 g/mol) (HP3100, NatureWorks LLC, USA) solution in a 10 wt% concentration was prepared by dissolving PLA pellets in a 9:1 wt. mixture of chloroform (Azure Chemicals, Hungary) and n,n-dimethylformamide (DMF, Merck). The solution was stirred at 50°C for 10 h at 250 rpm with a magnetic stirrer and then stored for 24 h. All the chemicals were used without further purification.

2.2 Sample preparation

2.2.1 Fabrication of nanofiber mat

The nanofibers were prepared with a vertical single needle electrospinning setup. The PLA solution was electrospun with the following parameters: 25 kV voltage, 0.51 mm nozzle diameter, and 20 cm distance between the needle and the grounded plate collector.

A syringe pump (Aitecs SEP-10S plus, Lithuania) supplied the PLA solution from a 20 ml syringe at a feeding rate of 0.3 ml/h. The high voltage was provided by a DC high-voltage generator (MA2000 NT 75/P, Hungary). Nanofibers were collected for 5 min (~1.0 μm thick) onto an aluminum foil.

2.2.2 Fabrication of the nanofiber filter

For the 3D printing and the electrospinning, we used the identical PLA grade to make a self-reinforced structure. Before the extrusion process, the PLA pellets were dried at 80°C for 12 h. We prepared custom filaments with a 1.75 mm diameter by extrusion. For the filament production, we used a Labtech LTE 26-44 type twin-screw extruder with a custom die. The first zone of the extruder and the die was set at 165°C and 185°C, respectively. The filaments were calibrated manually, cooled by air, and then wound up.

A CraftBot Plus (CraftUnique, Hungary) FDM printer with a nozzle diameter of 0.4 mm was used for processing the filters. The layer height and the printing speed were 0.2 mm and 50 mm/s, respectively. Even 100% infill setting results in a proper spacing between the laid filaments (struts). The porosity of the printed structure can be easily adjusted by this parameter. We set the infill density to 30% for filtration tests, as this setting made the filter even more comfortable to breathe through.

The fabrication process of the nanofiber filter is illustrated in **Figure 1**. The aluminum foil covered with the nanofiber mat was glued on the printing bed. Two layers (50 × 50 mm square) were printed directly on the nanofiber mat (30 × 30 mm) for optical transparency tests, while for the tensile tests, 30 × 10 mm samples were generated. Then, the nanofiber mat combined with the printed layers was easy to peel off from the foil without damaging the nanofiber structure. The technology allows us to make the filter in any shape (circle, oval, etc.) to fit any type of masks, and the filter is flexible.

2.3 Characterization

2.3.1 Microscopy

The morphology of the nanofibers was investigated with a scanning electron microscope (JEOL-JSM-6380 LA, Japan). The nanofiber sample was finely coated with gold-palladium (Au/Pd) alloy before the examination. We measured 100 random fibers and obtained the diameter frequency distributions using the ImageJ software. The pore size distribution was also evaluated with the same software.

We used a digital light microscope Olympus BX51M (Olympus, Hamburg, Germany) to observe the surface structure of the 3D printed nanofiber filter.

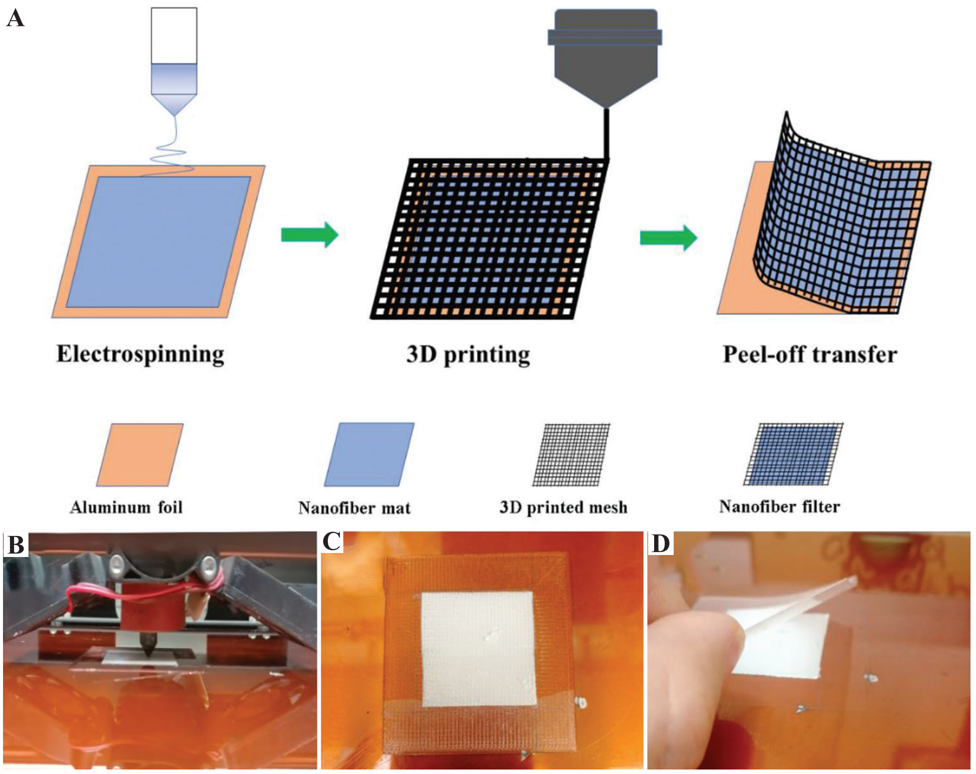

Figure 1. (A) The schematic of the fabrication of mask filter with the combination of three-dimensional (3D) printing and electrospinning, and the different components (aluminum foil, nanofiber mat, 3D printed mesh, and nanofiber filter); (B) printing in progress; (C) after printing; (D) peel-off (the sample is reflected on the base plate).

2.3.2 Optical properties

The prepared specimens were directly placed into the ultraviolet (UV) spectrophotometer (UV-1600, AOE, Shanghai, China) and analyzed at the wavelength of 200-1000 nm. Before each specimen measurement, the environment air was measured, respectively, as background.

2.3.3 Differential scanning calorimetry (DSC)

DSC was carried out with a DSC-Q2000 (TA Instruments, USA). All the samples were weighted with around 5 mg mass and sealed in an aluminum pan. They were subjected to heat/cool/heat cycles with a ramp rate of 5°C/min in the temperature range of 25°C and 200°C.

2.3.4 Mechanical properties

Tensile tests of the filters were performed with a Zwick Z005 (ZwickRoell, Germany) machine with a 5 kN load cell (0.01 N sensitivity). All the filter specimens were printed in a rectangular shape (30 mm × 10 mm × 0.4 mm). The crosshead speed and the gauge length were set at 10 mm/min and 10 mm, respectively. We measured three specimens for each group.

2.3.5 Particle filtration properties

Since the respiratory virus is airborne, we tested the filtration efficiency of the 3D printed nanofiber filters with ambient air. The particle filtering properties of the nanoporous filters were analyzed by an aerosol particle counter (Lasair III 310C, Artisan Technology Group, USA). It has six channels to detect the particle sizes of 0.3, 0.5, 1, 5, 10, and 25 µm, respectively. The PM particles in the air of our laboratory had a broad size distribution ranging from <300 nm to >25 µm. The median mass aerodynamic diameter (MMAD) of the particles in the air was between 500 and 600 nm, the size is similar to the criterion for filtering facepieces standard tests, which works with~600 nm NaCl aerosol particles. The filtration efficiency was calculated, respectively, from particle number difference (*n*%) and mass difference (wt%) before and after 1 min filtration. Filtration efficiency (*n*%) was used to describe the filtration performance with different particle sizes. Filtration efficiency (wt%) was mainly used to evaluate the particle removal ability of a mask for particles between 0.3 and 5 μm because they are the most harmful particulate matter pollutants to humans and can reach the lower respiratory tract. The nanoporous filters were printed into a 35 mm diameter circular shape and fixed into the filter holder connected to the particle counter. All the tests were conducted with an airflow of 30 l/min, which is approximately the average breathing flow of humans in a resting position. Five specimens were tested from each sample type. As good quality commercial masks contain several filtering layers, we also stacked the specimens in 2, 3, 4, and 5 layers after the single layer measurements.

4. Results and discussion

Figure 2A presents the morphology of electrospun PLA nanofibers. The average fiber diameter was 825.2 ± 80.0 nm. **Figure 2B** shows the DSC curve of the PLA nanofiber mat. We found that the glass transition and melting temperature of the PLA nanofibers were 60.5°C and 174.3°C, respectively. We also observed a broad peak related to cold crystallization at around 85°C. To keep the stable properties of the nanofibers, but achieve proper adhesion with the printed layer, we adjusted the bed temperature to 60°C.

The optical properties of all the filters printed with variable nozzle temperatures are shown in **Figure 3**. On the black background, the whitish nanofiber mat incorporated with the printed part was visible, as shown in **Figure 3A**. Compared with the reference samples without nanofibers, our university logo underneath the filter was a little bit blurry, but visible, as shown in **Figure 3B**. The UV–visible spectra were measured to examine the transmittance of the printed nanocomposite quantitatively. The results are shown in **Figure 3E**. It is worth noting that the reference sample (without nanofibers) presented better optical transmittance, and the reference sample printed at 210°C had the lowest transmittance amongst the references. In comparison with the reference samples, the fabricated filters had lower transmittance. The reason for the lower transmittance of the printed nanocomposite may be due to the nanofiber mat was suspended between the gaps between the printed struts, as shown in **Figure 3C and D**, leading to light loss caused by light reflection and scattering on the nanofiber mat. Besides, the filters printed at 220°C and 230°C became less transparent compared with the filter printed at 210°C. It can be explained that at a higher temperature, the printed strut with a lower modulus cannot support itself to suspend through the gap between the struts. Then, the strut sagged down and contacted the nanofiber mat, which increased

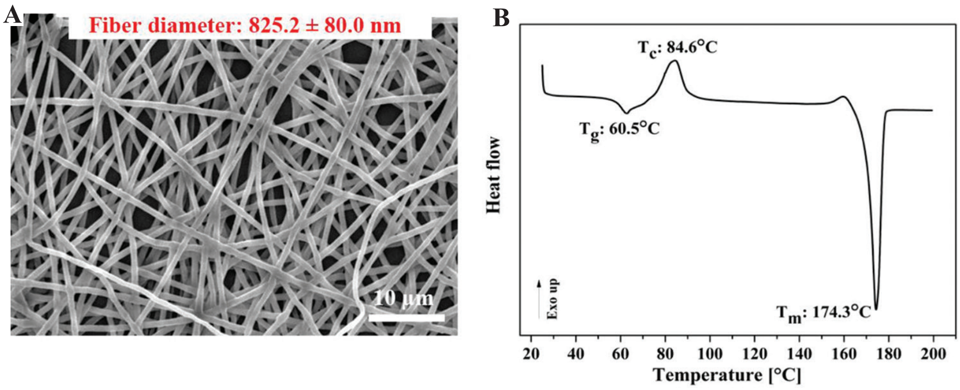

Figure 2. (A) Scanning electron microscope image of polylactic acid (PLA) electrospun nanofibers; (B) differential scanning calorimetry curve of PLA electrospun nanofibers.

the contact area between the printed strut and the nanofiber mat and reduced the porosity. Therefore, the light which went through the nanofiber mat was less. The change in the contact area is clearly seen in **Figure 3D** (230°C), in which a grid structure can be observed. This suggests that at higher temperatures, a larger interface was formed between the nanofiber mat and the printed layer. As the nanofibers were produced from the same polymer as the printing filament, we supposed that the hot printed filament might melt and destroy the nanofibers when it contacts with nanofibers. However, we observed in **Figure 3C and D** that nanofibers kept their original morphology in the printed filters, which proves that we had obtained the proper filter structure.

Figure 3F shows the typical stress-strain curves of the nanofiber filters printed with different nozzle temperatures. The results obtained from tensile testing are also listed in **Table 1**. The results presented that the tensile strength of the 3D printed nanoporous filters increases greatly as the nozzle temperature increase from 210°C to 220°C. The tensile strength slightly increased when the nozzle temperature was increased from 220°C to 230°C. Whereas the breaking strain decreased with an increase in the nozzle temperature.

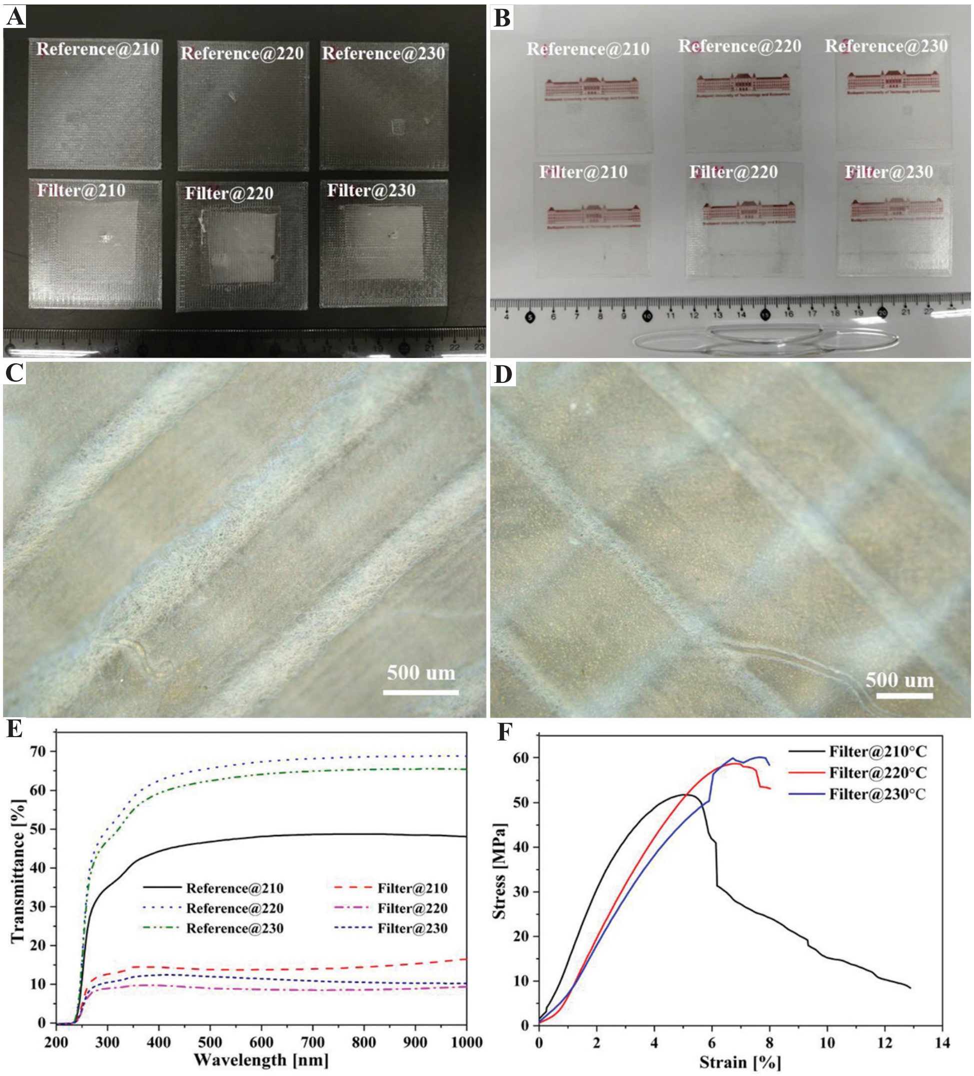

Figure 3. Optical images of the samples with different background (A) black background; (B) white background; (C) optical microscopic image of the filter with 210°C; (D) optical microscope image of the filter with 230°C (E) ultraviolet–visible spectra of the reference samples and filters; (F) the stress-strain curves of the filters with different nozzle temperatures.

Interestingly, it is noted that there was no significant change in the breaking strain when the nozzle temperature increased from 220°C to 230°C. It indicates that the nozzle temperature is a substantial factor in influencing the mechanical properties of printed nanofiber filters. It is because the higher nozzle temperature can enhance the interlayer adhesion which was also confirmed by the microscope image results. At higher temperatures, polymer chains have more mobility and take more time to form interdiffusion between the two layers. All the samples have provided proper mechanical characteristics to apply them as filters; therefore, we can conclude that the limiting factor is the change in morphology, i.e., fiber fusion.

Table 1. Main tensile properties of the 3D printed PLA filters

Nozzle temperature (°C)	Tensile strength (MPa)	Strain at break (%)
210	51.76±0.27	12.88±1.97
220	58.75±3.63	7.53±0.49
230	60.18±1.20	7.63±1.08

To evaluate the filtration efficiency of the nanoporous filters, we investigated their particle filtration properties. **Figure 4A** illustrates the filtration efficiency of the filters printed at different temperatures against the various filtered particle size (which are also summarized in **Supplementary File Table 1**). For the particle size with 5 µm and above, the filtration efficiency of the filters achieved more than 95 *n*%, except for the filter with 230°C (which had a filtration efficiency of 91.78 *n*%). For the air itself (500-600 nm MMAD), **Figure 4C** shows the single-layered specimens filtered 79 wt.%, 77 wt.%, and 66 wt.%, respectively, for 210, 220, and 230°C (the standard deviations can be found in **Supplementary File Table 2**). That means that the filters can overperform the standard surgical/sanitary masks (minimum 55% filtration efficiency at 700 nm MMAD according to the MSZ 4209 national standard).

We also found that the filters printed with higher temperatures had lower filtration efficiency when the particle size was smaller than 10 µm.

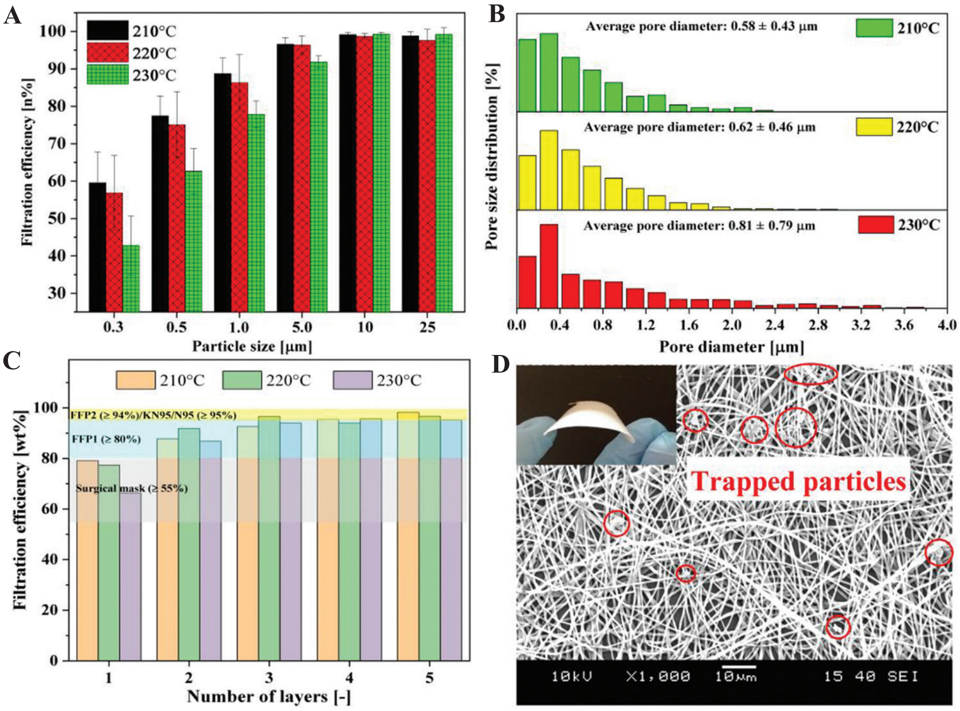

Figure 4. (A) Filtration efficiency of nanoporous filters with various particle size, (B) pore size distribution of nanoporous filter printed with different temperatures, (C) the filtration efficiency (wt%) of nanoporous filters with various stacking layers, (D) scanning electron microscope image of the nanoporous filter after filtration. Inset is the bent single-layered filter.

To understand the reason behind the observation, we evaluated the pore size distribution of all the filters (**Figure 4B**). The results of the pore size indicated that the average pore diameter of the filters with 210°C, 220°C, and 230°C was 0.58, 0.62, and 0.81 μm, respectively. The pore structure was observed at the area between the printed struts, and it was primarily determined by the electrospinning process instead of the printing temperature. Therefore, we conclude that the higher filtration efficiency was resulted from the smaller pore size and not directly related to the printing temperature. We further tested the filtration efficiency (in both [*n*%] and [wt.%]) by stacking multiple filter layers (**Supplementary file Tables 2-5**). The results we obtained are shown in **Figure 4C**. We found that a significant increase in filtration efficiency was obtained with an increase in the number of layers. Especially for the filter with 230°C, its filtration efficiency was increased from 66.32 wt.% to 95.24 wt.%. One layer performs better than a surgical mask, and two-layered filters had a filtration efficiency of more than 80 wt.%, which is the criterion for FFP1 respirators. Furthermore, when we stacked more than four layers of the filters, all of them achieved the filtration efficiency of FFP2 (≥94 wt%). Some of them even had a similar filtration performance as KN95/N95 (≥95 wt%). In **Figure 4D**, we can observe the trapped particles on the surface of the filter. The inset image shows that the printed filter was flexible and can be bent.

5 Conclusions

In this study, we introduced a simple and facile method to combine nanofiber mats to a 3D printed substrate successfully for making mask filters. Our main concept is that nanofibers give excellent filtration, while the 3D printed structure supports the fibers to avoid their damage. This technique allows printing slightly flexible mask filters in any shape achievable by 3D printing technology. The custom production also allows us to fit the mask to any face shape or to put such filters in existing masks.

As a result, we obtained a nanoporous PLA self-reinforced structure that is transparent. The transparent look overcomes the threatening appearance of the masks that can be effective in reducing the social trauma caused by the current CoV disease-19 pandemic. The transparency can also allow lipreading which can reduce communication barrier to people with mutism or hearing impairment when wearing mask. The all-PLA, self-reinforced structure renders the masks easy recyclability.

We explored the effects of nozzle temperature on the transmittance and mechanical properties of the filters developed. In comparison with the purely 3D printed mesh, the transmittance of the 3D printed filter was decreased, but they were still transparent with the transmittance around 20%. Among the filters printed with different nozzle temperatures, the filter printed at 210°C was the most transparent. The higher nozzle temperature can increase the tensile strength and decrease the breaking strain because of the better fusion between the adjacent layers. One layer can perform better than a classical surgical mask. Furthermore, the multiple layer filter can have a similar filtration performance as KN95/N95 and FFP2 filters. The results are particularly useful for future mask filter studies. Instead of stacking the layers, we can try to print the filters with multiple nanofiber layers, which can to be further investigated.

Acknowledgments

The research reported in this paper was supported by the BME-Nanotechnology FIKP grant (BME FIKP-NAT), the H2020-MSCA RISE No. 872152 - GREEN-MAP project of the European Union, the ÚNKP-17-4-I New National Excellence Program of the Ministry of Human Capacities, and the ÚNKP-19-4 New National Excellence Program of the Ministry for Innovation and Technology and BME-KKP. This paper was also supported by the János Bolyai Research Scholarship of the Hungarian Academy of Sciences and the Stipendium Hungaricum Scholarship of Tempus Public Foundation, and China Scholarship Council (201700500073).

References

1. Balazy A, Toivola M, Adhikari A, *et al.*, 2006, Do N95 Respirators Provide 95% Protection Level Against Airborne Viruses, and how Adequate are Surgical Masks? *Am J Infect Control*, 34:51–7. DOI: 10.1016/j.ajic.2005.08.018.
2. Zhu N, Zhang D, Wang W, *et al.*, 2020, A Novel Coronavirus from Patients with Pneumonia in China, 2019. *N Engl J Med*, 382:727–33. DOI: 10.1056/NEJMoa2001017.
3. Leung NH, Chu DK, Shiu EY, *et al.*, 2020, Respiratory Virus Shedding in Exhaled Breath and Efficacy of Face Masks. *Nat Med*, 26:676–80. DOI:10.1038/s41591-020-0843-2.
4. Ronkay FC, 2020, The Coronavirus and Plastics. *Express Polym Lett*, 14:510–1. DOI: 10.3144/expresspolymlett.2020.41.
5. Wang SX, Yap CC, He J, *et al.*, 2016, Electrospinning: A Facile Technique for Fabricating Functional Nanofibers for Environmental Applications. *Nanotechnol Rev*, 5: 51-73. DOI: 10.1515/ntrev-2015-0065.
6. Liu Y, Park M, Ding B, *et al.*, 2015, Facile Electrospun Polyacrylonitrile/poly(Acrylic Acid) Nanofibrous Membranes for High Efficiency Particulate Air Filtration. *Fiber Polym*, 16:629–33. DOI: 10.1007/s12221-015-0629-1.
7. Zhang S, Tang N, Cao L, *et al.*, 2016, Highly Integrated Polysulfone/Polyacrylonitrile/Polyamide-6 Air Filter for Multilevel Physical Sieving Airborne Particles. *ACS Appl Mater Interfaces*, 8:29062–72. DOI: 10.1021/acsami.6b10094.
8. Xu J, Liu C, Hsu PC, *et al.*, 2016, Roll-to-Roll Transfer of Electrospun Nanofiber Film for High-Efficiency Transparent Air Filter. *Nano Lett*, 16:1270–5. DOI: 10.1021/acs.nanolett.5b04596.s001.
9. Rajzer I, Kurowska A, Jabłoński A, *et al.*, 2018, Layered Gelatin/PLLA Scaffolds Fabricated by Electrospinning and 3D Printing- for Nasal Cartilages and Subchondral Bone Reconstruction. *Mater Des*, 155:297–306. DOI: 10.1016/j.matdes.2018.06.012.
10. Naghieh S, Foroozmehr E, Badrossamay M, *et al.*, 2017, Combinational Processing of 3D Printing and Electrospinning of Hierarchical Poly(Lactic Acid)/Gelatin-forsterite Scaffolds as a Biocomposite: Mechanical and Biological Assessment. *Mater Des*, 133:128–35. DOI: 10.31224/osf.io/yt6w7.
11. Mendoza-Buenrostro C, Rodriguez CL, 2015, Hybrid Fabrication of a 3D Printed Geometry Embedded with PCL Nanofibers for Tissue Engineering Applications. *Procedia Eng*, 110:128–34. DOI: 10.1016/j.proeng.2015.07.020.
12. Kozior T, Mamun A, Trabelsi M, *et al.*, 2019, Electrospinning on 3D Printed Polymers for Mechanically Stabilized Filter Composites. *Polymers* (*Basel*), 11:2034. DOI: 10.3390/polym11122034.
13. Kozior T, Trabelsi M, Mamun A, *et al.*, 2019, Stabilization of Electrospun Nanofiber Mats Used for Filters by 3D Printing. *Polymers* (*Basel*), 11:1618. DOI: 10.3390/polym11101618.
14. Naghieh S, Badrossamay M, Foroozmehr E, *et al.*, 2017, Combination of PLA Micro-fibers and PCL-Gelatin Nano-fibers for Development of Bone Tissue Engineering Scaffolds. *Int J Swarm Intell Evol Comput*, 6:1000150. DOI: 10.4172/2090-4908.1000150.
15. Sweeney CB, Lackey BA, Pospisil MJ, *et al.*, 2017, Welding of 3D-printed Carbon Nanotube-polymer Composites by Locally Induced Microwave Heating. *Sci Adv*, 3:e1700262. DOI: 10.1126/sciadv.1700262.

REVIEW ARTICLE

Engineering a Model to Study Viral Infections: Bioprinting, Microfluidics, and Organoids to Defeat Coronavirus Disease 2019 (COVID-19)

Anastasia Shpichka[1,2]*, Polina Bikmulina[1]†, Maria Peshkova[1]†, Nastasia Kosheleva[3,4], Irina Zurina[1,3], Ensieh Zahmatkesh[5,6], Niloofar Khoshdel-Rad[5,6], Marina Lipina[7], Elena Golubeva[2], Denis Butnaru[8], Andrei Svistunov[8], Massoud Vosough[5,6]*, Peter Timashev[1,2,9]*

[1] Department of Advanced Biomaterials, Institute for Regenerative Medicine, Sechenov University, Moscow, Russia

[2] Department of Chemistry, Lomonosov Moscow State University, Moscow, Russia

[3] Department of Molecular and Cell Pathophysiology, FSBSI Institute of General Pathology and Pathophysiology, Moscow, Russia

[4] Department of Embryology, Lomonosov Moscow State University, Faculty of Biology, Moscow, Russia

[5] Department of Regenerative Medicine, Cell Science Research Center, Royan Institute for Stem Cell Biology and Technology, ACECR, Tehran, Iran

[6] Department of Stem Cells and Developmental Biology, Cell Science Research Center, Royan Institute for Stem Cell Biology and Technology, ACECR, Tehran, Iran

[7] Department of Traumatology, Orthopedics and Disaster Surgery, Sechenov University, Moscow, Russia

[8] Rector's Office, Sechenov University, Moscow, Russia

[9] Department of Polymers and Composites, NN Semenov Institute of Chemical Physics, Moscow, Russia

†These authors contributed equally to this work.

Abstract: While the number of studies related to severe acute respiratory syndrome-related coronavirus 2 (SARS-CoV-2) is constantly growing, it is essential to provide a framework of modeling viral infections. Therefore, this review aims to describe the background presented by earlier used models for viral studies and an approach to design an "ideal" tissue model for SARS-CoV-2 infection. Due to the previous successful achievements in antiviral research and tissue engineering, combining the emerging techniques such as bioprinting, microfluidics, and organoid formation are considered to be one of the best approaches to form *in vitro* tissue models. The fabrication of an integrated multi-tissue bioprinted platform tailored for SARS-CoV-2 infection can be a great breakthrough that can help defeat coronavirus disease in 2019.

Keywords: Severe acute respiratory syndrome-related coronavirus 2, Coronavirus disease 2019, Coronavirus, Bioprinting, microfluidics, Organoids, Tissue models, Viral infection, Body-on-a-chip

***Corresponding Authors:** Anastasia Shpichka, Institute for Regenerative Medicine, Sechenov University, Moscow, Russia: ana-shpichka@yandex.ru; Massoud Vosough, Department of Regenerative Medicine, Cell Science Research Center, Royan Institute for Stem Cell Biology and Technology, ACECR, Tehran, Iran: masvos@royaninstitute.org; Peter Timashev, Institute for Regenerative Medicine, Sechenov University, Moscow, Russia: timashev.peter@gmail.com

Received: June 30, 2020; ***Accepted***: July 15, 2020; ***Published Online***: August 28, 2020

(This article belongs to the *Special Section: Research and Applications of 3D Printing and Bioprinting for Covid-19)*

Citation: Shpichka S, Bikmulina P, Peshkova M, *et al.*, 2020. Engineering a Model to Study ViralInfections: Bioprinting, Microfluidics, and Organoids to Defeat Coronavirus Disease 2019 (COVID-19) , *Int J Bioprint*, 6(4): 302. DOI: 10.18063/ijb.v6i4.302.

1 Introduction

Severe acute respiratory syndrome-related coronavirus 2 (SARS-CoV-2) that causes coronavirus disease 2019 (COVID-19) has become a great challenge for not only separate populations but also the whole mankind[1]. This new pathogen has almost conquered the world due to the lack of knowledge of COVID-19 pathogenesis and the absence of any vaccines or approved therapy[2].

The use of models enables the possibility to learn more about SARS-CoV-2 and infection-related conditions and to screen drugs and vaccines efficiently. Unfortunately, the number of approved models is limited, and researchers have to mainly rely on the past experience related to other viruses (SARS-CoV, Middle East respiratory syndrome coronavirus [MERS-CoV], influenza A virus [IAV], etc.) to develop new relevant models.

Models based on susceptible animals (ferrets[3,4], rhesus and cynomolgus macaques[5,6], transgenic mice[7], etc.) are highly demanded in investigations to study SARS-CoV-2 pathogenesis as well as clinical signs, and test drugs and vaccines as a part of the trials. However, high costs, virus species specificity, and ethical issues do not allow their use as a routine model. Hence, cell-based models can be a good option for screening and precise analysis of molecular pathways of COVID-19 pathogenesis. However, 2D cultures cannot provide biomimetic environment that can significantly influence virus spreading, infectivity, and drug efficiency. Therefore, 3D tissue models are of particular interest. To date, there is only one 3D model which is presented by organoids and used for studying SARS-CoV-2 infection[8]. Due to the past experience, its combination with 3D bioprinting and microfluidics, and fabrication of a multi-tissue integrated platform can help create a responsive and efficient immune-competent organism-like system tailored for SARS-CoV-2 infection (**Figure 1**).

Thus, this review aims to describe the background of previously used models for viral studies and an approach to design an "ideal" tissue model to study SARS-CoV-2 infection.

The main advantages of each technique and thus, their combination can allow the fabrication of a highly responsive immune-competent organism-like platform which is tailored for SARS-CoV-2 infection and enable real-time and high-throughput screening.

2 Modeling viral infections

2.1 Humans

Nowadays, humans are not a typical object to model viral infections that is mainly caused by ethical issues. However, there is a pool of studies describing controlled human infection (CHI) trials on influenza viruses, respiratory syncytial virus (RSV), etc. For instance, the CHI model was used to assess susceptibility and resistance to Norwalk virus infection[9]. DeVincenzo *et al*. experimentally infected adult volunteers with wild-type RSV (it usually infects children) and showed that viral load can significantly influence the disease manifestation and its variation permit achieving the manifestation similar to natural infection[10]. Such controllable adult RSV infection model was claimed to be useful for proof-of-concept trials of antivirals candidates. Human challenge model provided valuable data on immune response to influenza infection[11-14]. Particularly, Huang *et al*.[14] revealed that antibody-secreting cells are virus-specific and can be the earliest marker of new influenza infection. In the case of especially dangerous infections (Ebola virus, Zika virus, yellow fever virus, etc.), CHI trials are significantly limited and almost cannot be performed. The significant efforts have been carried out to develop a dengue human infection model which has minimum harm and represents wild-type infection[15]. Hence, if such infection occurs naturally, blood, mucosa, urine, stool, tissue biopsies, etc., can serve as appropriate materials for studying lifecycle, entry, and pathogenesis of virus, and drug efficacy.

Usually, humans are involved in clinical trials of actively developed vaccines and phage-based drugs. Particularly, a novel dengue vaccine was tested using the DEN2Δ30 model[16]. Moreover, CHI models have enabled the development of the first vaccines against the influenza virus[17] and the

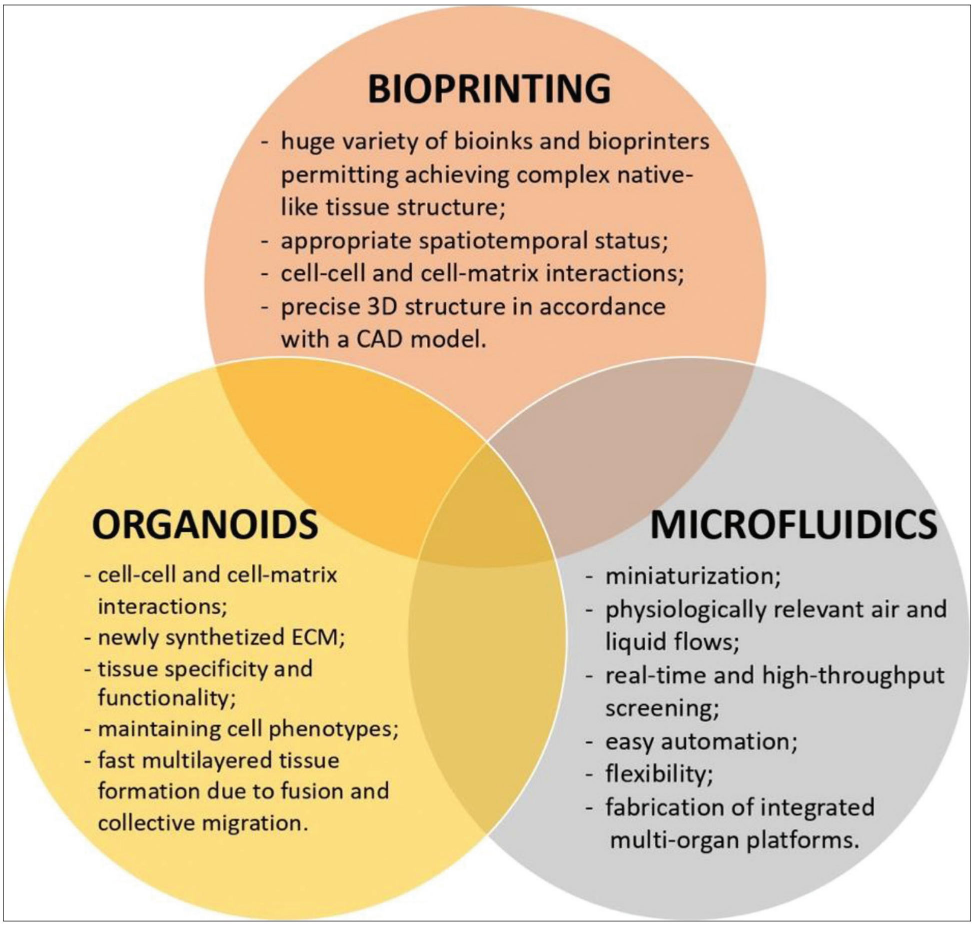

Figure 1. Bioprinting, microfluidics, and organoids as tools to defeat coronavirus disease 2019.

first anti-influenza drug, amantadine[18], and other antivirals[19-23]. Phage-based drugs are particularly interesting as a therapeutic agent to treat multidrug-resistant bacteria, such as *Staphylococcus aureus* or *Pseudomonas aeruginosa*[24,25], and to modify microbiota to decrease specific microbial populations[26].

2.2 Animals

Animals are widely applied to study viral infections and antivirals. Among them, rodent models are the most common, especially used in studies to reveal features of respiratory diseases caused by IAV and RSV[27,28]. Their advantages include the possibility to use standardized animals that allow comparison and analysis of data obtained from different experiments. They are well-characterized and can be easily modified to delete particular genes or transfer them from other species that enables the extrapolation of results and detection of virus targets and pathogenesis. For instance, type-I interferon receptor-deficient mice were engineered and used to study the Zika virus entry process[29]. Moreover, handling rodents are easy and low-cost; they reproduce rapidly, have small sizes, can accustom to standard diet, and do not require much space. However, their use is limited because of species-determined differences in anatomy, pathophysiology, immune response[27], and host-determined virus infectivity[28].

Another well-established animal model is ferrets, which are susceptible to most human respiratory viruses[3,4,28,30]. Their respiratory tract is very similar to human's, and they manifest a wide range of clinical signs[31]. Therefore, they have become a good model to test antiviral drugs. Particularly, using them, the efficacy of lopinavir-ritonavir, hydroxychloroquine sulfate, and emtricitabine-tenofovir was proven for

SARS-CoV-2 treatment[3]. Nevertheless, ferret models have many limitations which include the lack of standardized strains, detailed molecular profiling, and higher handling and housing costs.

Interestingly, there is a pool of studies describing domestic animals, such as cats and dogs, as a viral model. For instance, a recent study has shown that cats are susceptible to human SARS-CoV-2[4]. Such findings provide novel insights into virus targets and its lifecycle. However, cat and dog models have similar issues as ferret ones as well as ethical concerns.

Cattle, sheep, and pigs are also used to study human viruses. Particularly, sheep and cattle are susceptible to RSV and have human-like virus spreading due to similar sizes[27]. The application of such models is limited by high handling and housing costs and biosafety considerations (e.g., pigs can be a reservoir for the reassortment and transgenic shift of influenza viruses).

The animal model closest to humans is, undoubtedly, primates that have similar genetic, anatomical, and physiological features. For instance, RSV infection of chimpanzees has all symptoms and complications (inflammation, acute respiratory distress syndrome, lung edema, etc.) that are typical in humans[32,33]. Primates are perfect candidates for preclinical studies of vaccines[27]. Despite all of the mentioned advantages, they cannot be treated as a routine viral model due to extensive economic, ethical, and logistical burdens.

However, in general, virus strains are highly selective and host-specific; therefore, only a subset of data can be extrapolated to humans. Phylogenetically close viruses often have different hosts and targets, and these viruses also cause different pathophysiologic conditions. Some drugs, whose efficacy was confirmed using animal models, failed in clinical trials[34]. One of the approaches to overcome these issues is humanization. Humanized animals (usually mice) have specific human expression profiles and are immunodeficient due to the mutation caused by severe combined immunodeficiency. They are widely used to model human immunodeficiency viruses (HIV), herpesviruses, cytomegaloviruses, dengue virus, Epstein-Barr virus, and Ebola virus infections[35,36]. However, such models require expensive specific handling and housing and are not flexible to study different viral infections.

2.3 Tissue models

Compared to the above-mentioned models, tissue models can be considered as the most flexible and ethically humane tools to study viral infections. While designing such models, a researcher can use different cell types, biomaterials, and fabrication methods (including bioprinting) that can work with a wide range of host-specific viruses. Studying viruses *in vitro* under controllable conditions allow better understanding of host-pathogen interactions and high-throughput screening of drug candidates.

All tissue models can be divided into three types with ten subtypes: 2D models (monolayer culture of cell lines and primary cells), 2.5D models (suspension culture using microcarriers and simple air-liquid biointerfaces), and 3D models (explants, organoids/spheroids, embedded cells, cell-seeded scaffolds, bioprinted constructs, and combined systems [organ-on-a chip]).

Monolayer (2D) cultures are the oldest and the most widely used model. Cell lines are usually applied to isolate viruses, develop new serological assays, and produce diagnostic reagents or vaccines. The current “gold-standard” cell line is Vero, an interferon-deficient aneuploid line of kidney epithelial cells[37,38]. A549 and Madin–Darby canine kidney cell lines are mostly applied for influenza viruses[39].The most common cell line for the foot-and-mouth disease virus is the mammalian baby hamster kidney cells[40] which have been used since 1964[41]. Compared to cell lines, primary cell cultures have some advantages. For instance, cells isolated from ovine pulmonary adenocarcinoma are a unique platform to reveal mechanisms of epithelial transformation in a case of the lung cancer caused by the retrovirus infection[42]. Despite of the availability of cell variety and easy handling and scaling, 2D cultures are not capable of recapitulating fully cell-cell and cell-matrix interactions.

Suspension culture is also the oldest model for viral infections and very common for the industrial production of diagnostic reagents, vaccines, etc., due to a simple scaling procedure[40] V. However, it was significantly improved by adding microcarriers – small particles of a cell adhesive substrate (e.g., Cytodex 3). Such method modification was approved for the production of a RSV vaccine[43] and research on virus-host interactions[44].

Compared to 2D ones, 3D models are highly attractive because they are more relevant to the conditions *in vivo* (**Figure 2**). Such models can be fabricated through various approaches and were approved for different viruses (**Table 1**). The most common technique to form 3D tissue models is cell or spheroid/organoid encapsulation (embedding).

Organoids and spheroids can establish cell-cell and cell-matrix interactions and are genotypically and phenotypically stable[45]. They were shown to be an efficient model to study virus infectivity and host-pathogen interaction[46-48]. For instance, using intestinal organoids, Zhou *et al*. confirmed that MERS-CoV might infect the gastrointestinal tract[49].

Explant cultures can also be used in studying viral infections. Their main advantage is that they are native tissues with relevant morphology. However, their application is significantly limited because of low availability and shortage of donor materials, short viability, and rapid necrosis[50].

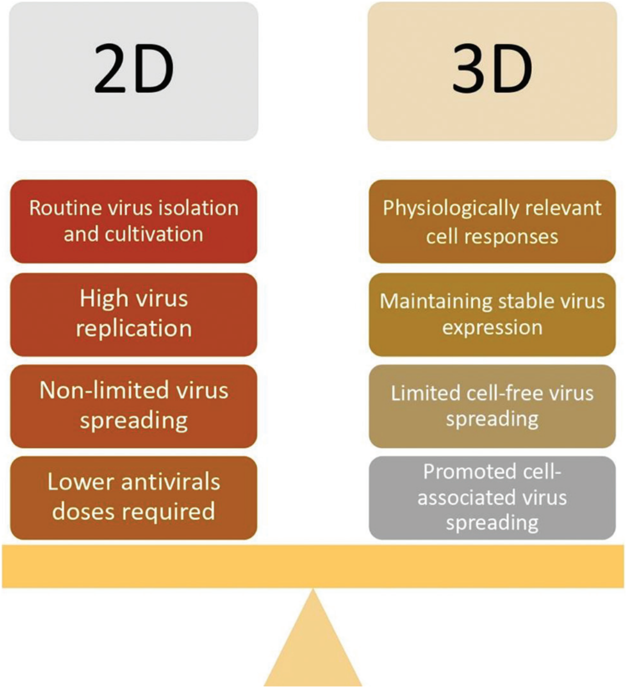

Figure 2. Viral infection: 2D versus 3D tissue models.

Scaffold- and hydrogel-based models can provide a 3D microenvironment that mimics conditions *in vivo* for cells. Biomaterials that ensure necessary cell-matrix interactions and appropriate spatiotemporal surrounding cells are used to form a structure of such models. It was shown that they could ensure physiologically relevant cell responses to virus infection and drugs[39,51]. For instance, Bhowmick *et al*.[39] revealed that compared to monolayer culture, the 3D chitosan-collagen-based cell model had the native airway epithelium-like morphology and high expression and release of pro-inflammatory cytokines and chemokines after IAV infection. The virus expression in such conditions has been shown to be higher. Particularly, Archer *et al*.[42] found out that compared to monolayer cultures, cultures of tumor-derived alveolar type II cells on a surface coated with fibronectin and collagen type I or Matrigel exhibited efficient maintenance of reverse transcriptase activity and stable expression of Jaagsiekte sheep retrovirus. Moreover, biomaterials have been shown to significantly influence virus spreading ability and even determine its mode. For instance, Imle *et al*.[52] revealed that cell-laden collagen gel significantly limited the transmission of cell-free HIV and shifted it to cell-associated transmission. To fabricate complex tissue-like constructs, bioprinting is a good option[53], and bioprinted models were shown not only to be susceptible to viruses but also to recapitulate virus-associated morphological patterns similar to *in vivo*[54,55].

Microfluidic-based tissue models additionally allow mimicking air and fluid flows typical to *in vivo* conditions. Organ-on-a-chip systems consisting of various cell types, perfusion chambers, air-liquid interfaces, etc., mimic and create physiological conditions relevant to viral infection of native tissues. Microfluidic-based tissue models have many advantages. Particularly, microfluidics enables liquid handling at a microscale through a system of microchannels; therefore, the total consumption of

Table 1. 3D tissue models used to study various viral infections.

Virus	Tissue model			Outcomes	Ref.
	Cells	Biomaterial	Fabrication method		
Respiratory viruses					
SARS-CoV-2	Organoids from iPSCs and hESCs	Matrigel, collagen	Cultivation in non-adhesive well plates	• Blood vessel and human kidney organoids were susceptible to SARS-CoV-2 • Viral infection can be blocked by hrsACE2	[8]
FCoV	BHK-21	–	Microfluidic chip	• Virus entry caused by binding to specific receptors, protease-induced priming, and low-pH • Kinetic rate parameters for the virus fusion were quantitatively measured	[62]
MERS-CoV	hPIECs and their organoids, small intestine explants	Matrigel	Encapsulation	• Tissue models were successfully infected by the virus	[49]
RSV	Organoids from basal cells, multi-ciliated cells, and secretory cells	Basement membrane extract	Encapsulation	• RSV induced organoid cell motility through NS2 protein	[45]
RSV	Organoids from hPSCs	Matrigel	Encapsulation	• Lung bud organoids were representable and susceptible to the viral infection	[46]
IAV (H1N1 and H3N2)	hPSAECs	Chitosan-collagen scaffold	Air-liquid interface	• 3D model's morphology was similar to in vivo condition • 3D model had high aquaporin-5 and cytokeratin-14 expression • After being infected, cells had significant changes in marker protein expression and released pro-inflammatory cytokines	[39]
IAV	A549	Alginate, gelatin, Matrigel	Extrusion bioprinting	• The model was highly susceptible to the infection and represented the pattern similar to in vivo condition • A high level of IL-29 (interferon λ1) was released	[71]
IAV (H1N1 PR8)	A549, HeLa	–	Inkjet bioprinting	• Geometric heterogeneity influenced on cell susceptibility to the virus	[55]
Hepatotrophic viruses					
HCV	Huh7	Cytodex-3 microcarrier beads	Cultivation in a rotating wall vessel bioreactor	• The phenotype of cells cultured in 3D were more hepatocyte-like • 3D model is susceptible to HCV infection	[72]
HCV	Huh7	Matrigel	Encapsulation	• Embedded cells were polarized and formed interconnected proto-bile canaliculi structures • They were easily infected by the virus and synthetized infective viral particles	[73]
HCV	Huh7	Mebiogel	Encapsulation	• Spheroids remained viable for 63 days and could be infected by the virus	[74]

(Contd...)

Table 1. *(Continued)*.

Virus	Tissue model			Outcomes	Ref.
	Cells	Biomaterial	Fabrication method		
Hepatotrophic viruses					
HBV	hPH	Collagen-coated polystyrene scaffolds	Microfluidic chip	• The 3D model was susceptible to infection and remained viable for up to 40 days • It reproduced all steps of the viral lifecycle observed in vivo	[75]
Herpesviruses					
HSV-1	Human abdominal skin explant	–	Microneedle pretreatment	• The virus infection model was developed • Infection-induced changes in histology and protein expression were revealed • Efficacy of pritelivir and acyclovir was similar	[67]
HSV-1	iPSC	Matrigel	Cultivation in Matrigel coated well plates	• IC50 of acyclovir in 2D cultures was lower than that in 3D cultures	[69]
HSV-2	hNVECs	–	Air-liquid interface	• HNVECs and their spheres had normal morphology and expressed epithelial markers • The hNVEC sphere-based model was permissive for the infection and representative for virus-induced pathological changes	[68]
HCMV	PSCs	Basement membrane extract	Cultivation in coated well plates	• The salivary epithelial model was developed and susceptible to the virus infection • The virus in lytic phase did not spread within the model and remained only in some cells.	[76]
HCMV	Organoids from iPSCs	Matrigel	Cultivation in non-adhesive well plates; encapsulation	• Infection disrupted the activity of purinergic receptors and voltage-gated calcium channels, causing a decrease in basal calcium levels • The virus disintegrated organoids, leading to insensitivity to response on stimulation	[70]
HCMV	HFF	Collagen	Encapsulation in mini-construct chambers	• The cumulative tissue contractile force was decreased due to actin microfilament disruption	[77]
VZV	NHNP	Cultispher microcarrier beads	Cultivation in a rotating wall vessel bioreactor	• The model remained viable for 180 days and expressed markers of human trigeminal ganglia • It was susceptible to the viral infection and could be maintained in long-term experiments	[78]

(Contd...)

Table 1. *(Continued).*

Virus	Tissue model			Outcomes	Ref.
	Cells	Biomaterial	Fabrication method		
Human immunodeficiency virus					
HIV-1	Primary human CD4+ T-lymphocytes	Collagen	Encapsulation	• The integrated spatial model was developed • Environment significantly influenced the transmission way • Cell motility and density determined the efficiency and way of the virus distribution	[52]

BHK-21: Baby hamster kidney-21, EBV: Epstein–Barr virus, FCoV: Feline coronavirus, HBV: Hepatitis B virus, HCMV: Human cytomegalovirus, HCV: Hepatitis C virus, hESCs: Human embryonic stem cells, HFF: Human foreskin fibroblasts, HIV-1: Human immunodeficiency virus-1, hNVECs: Human normal vaginal epithelial cells, hPH: Human primary hepatocytes, hPIECs: Human primary intestinal epithelial cells hPSAECs: Human primary small airway epithelial cells, hPSCs: Human pluripotent stem cells, hrsACE2: human recombinant soluble angiotensin converting enzyme 2, HSV-1: Herpes simplex virus-1, HSV-2: Herpes simplex virus-2, IAV: Influenza A virus, iPSCs: Induced pluripotent stem cells, MERS-CoV: Middle East respiratory syndrome-related coronavirus, NHNP: Normal human neural progenitor cells (NHNP), PSCs: Primary salivary cells, RSV: Respiratory syncytial virus, Ref: references, SARS-CoV-2: Severe acute respiratory syndrome-related coronavirus 2

reagents is relatively low that makes high-throughput screening easier and cheaper[56]. Such models are flexible to be automated[57,58], providing the possibility for real-time monitoring[59,60]. Moreover, they allow culturing cells in physiologically relevant dynamic conditions and controlling them[61]. Particularly, such system was tested to study the mechanism of the fusion of feline coronavirus with host cell membrane[62].

3 *In vitro* tissue models for modeling an infection caused by different viruses

3.1 Respiratory viruses

Tissue models that are used to study respiratory viral infections vary and include both monolayer cultures and functional airway organoids, enabling to obtain reliable data on virus infectivity, targets, and drug efficacy. Coronaviruses, a group of respiratory viruses, mostly infect epithelial cells that are used in designing relevant 3D models. The recent studies are based on organoids as a tissue model. For instance, Monteil *et al*.[8] revealed the efficacy of human recombinant soluble angiotensin-converting enzyme 2 against SARS-CoV-2 using infected blood vessel and kidney organoids. Moreover, intestinal organoids were used to prove that the intestine is a target organ for MERS-CoV[49]. Study of IAV using monolayer cultures fails to recapitulate the natural clustered pattern of disease transmission, but bioprinted 3D model was shown to be more relevant[54]. Using bioprinting, it was revealed that even geometrical position can significantly influence cell susceptibility to the virus[55]. Screening of drugs against RSV infection and detecting its pathogenesis was also successfully performed using airway and lung bud organoids[46,47].

3.2 Hepatotropic viruses

The hepatotropic viruses include different types and hepatitis A, B, C, D, and E viruses, which are the most common causes of viral hepatitis leading to liver failure worldwide[63]. Hepatitis B virus (HBV) and hepatitis C virus (HCV) induce chronic liver inflammation that results in cirrhosis and hepatocellular carcinoma[64]. Cell polarity and micro-environmental complexity and interactions are absent in 2D culture systems. Due to the drawbacks of 2D model systems, researchers are looking for alternative 3D models. The establishment of 3D models including spheroids, organoids with multi-cellular structures, and their specific extracellular matrix (ECM), was shown to exhibit higher tissue-specific environmental complexity, more mature cells, and better physiological functionality compared to simple 2D counterparts. For instance, several studies established liver spheroid models to study the hepatotrophic virus lifecycle in liver tissue. Chong *et al*. generated primary human hepatocyte spheroids from uninfected liver resections and inoculated the spheroids with HCV-positive serum[65]. Data showed that spheroids have differentiated phenotype and expressed putative HCV receptors; the HCV RNA was detected in the cells as well as supernatant of culture media[65]. Moreover, Nie *et al*. used a coculture system of human induced pluripotent stem cell (hiPSC)-derived endoderm, human umbilical vein endothelial cells, and mesenchymal stem cells in a 3D microwells to assess the potential of liver organoids for HBV infection and virus-host interactions[66]. The cells self-organized and differentiated into the functional liver organoids. Then, organoids were infected with the HBV genome. The liver organoids exhibited more functionality and higher susceptibility to HBV infection compared to human iPSC-derived 2D hepatic-like cells. These organoids could sustain HBV propagation and produce infectious virus up to 20 days. HBV infection decreased the expression of hepatic-specific genes and increased the expression of early biomarkers for acute liver failure, alanine aminotransferase, and lactate dehydrogenase in the supernatant of infected organoids. The advantage of hiPSC-derived 3D liver organoids was that they provided HBV infection models for precision medicine[66]. In addition, other cell culture models including, specific scaffold embedded cells and single-channel microfluidic devices are promising platforms *in vitro* models to study hepatotropic viruses[63].

3.3 Herpesviruses

Epithelial tissue is the initial site of infection for most herpesviruses. Although they cause latent infection mainly in neurons, they are still able to infect other cells. Therefore, there are numerous tissue models available, which include various cell types to study this virus group. For example, Tajpara *et al*. developed a model based on the microneedle-pretreated human abdominal skin explant to test antivirals and their combinations against human simplex virus (HSV-1) infection[67]. Zhu *et al*. fabricated 3D air-liquid interface culture consisting of human normal vaginal epithelial cells to describe viral transmission of HSV-2 and related pathological changes[68]. To study viral effects on neural tissue and acyclovir efficacy, D'Aiuto *et al*. proposed a scaffold-free 3D hiPSC-based neuronal model and showed that the IC50 of acyclovir in 2D cell cultures was lower than that in 3D culture[69]. Sison *et al*. also used iPSCs to fabricate cortical organoids to study human cytomegalovirus infection and revealed the organoid structure disruption and alterations in specific markers expression[70].

3.4 HIV

HIV infection is one the most difficult infections to study due to high selectivity and host specificity. HIV mainly infects immune cells, and the recent study has offered a novel efficient 3D model based on CD4+ T-lymphocytes[52]. By varying density of collagen gel embedding cells, Imle *et al*. evaluated the virus transmission and revealed that it can be significantly influenced by 3D environment.

4 Designing an "ideal" tissue model to study SARS-CoV-2 infection

4.1 Models and their limitations

To date, there is only a limited number of models available to study the SARS-CoV-2 infection. The most susceptible animals to this coronavirus are ferrets[3,4], cats[4], and rhesus and cynomolgus macaques[5,6]. The latter is considered to be a rapidly established SARS-CoV-2 model without any additional modifications[6]. Rhesus macaques were successfully applied to test siRNA to treat and prevent SARS-CoV infection[79]. Moreover, transgenic mice expressing human ACE2 can become a great option as ACE2 is one of the main SARS-CoV-2 targets[7]. Nevertheless, almost all animal models are expensive and do not allow researchers to fully overcome species specificity for such host-specific virus as well as their use is limited because of ethical issues.

Cell-based models are a good alternative to animal models. Particularly, Vero cell line cultured in 2D conditions was used for anti-SARS-CoV-2 drug screening[80]. However, the main limitation of such cell lines is the deficiency of interferon, which is an important regulator of binding proteins involved in SARS-CoV-2 infection[81]. This requires the use of other cell types and biofabrication methods that would better recapitulate *in vivo* conditions, including 3D environment, flows dynamics, and immune response. Moreover, blood vessel and human kidney organoids are still the only 3D models used to study SARS-CoV-2 infection[8].

4.2 Specific targets

Despite SARS-CoV-2 is a novel virus infecting humans, understanding of its possible entry mechanisms was already pre-defined because of earlier studies on other coronaviruses, for example, SARS-CoV[82-85]. Therefore, after its appearance, most research teams have been focusing on SARS-CoV receptor ACE2 and other related enzymes. Particularly, Hoffmann *et al*.[86] proved that the entry of SARS-CoV-2 into a cell occurs due to binding of the viral surface spike glycoprotein (S protein) to ACE2 and its priming by the transmembrane protease serine protease 2 (TMPRSS2). Zang *et al*. also revealed that the transmembrane protease serine protease 4 plays a crucial role in virus entry using human small intestinal enteroids as a model[87].

Actually, the entry mechanisms are considered the main targets for designing drugs treating and preventing COVID-19. Hence, their inhibition can block the infection that was proven to be true in several studies. For instance, Monteil *et al*. showed that human recombinant ACE2 prevented the virus entry into cells that form blood vessel and kidney organoids[8]. Hoffmann *et al*. revealed that Camostat mesylate, a serine protease inhibitor, blocked SARS-CoV-2 infection in lung cell line Calu-3[86].

These target enzymes, i.e., ACE2 and TMPR SS2, are widely expressed by tissues in human organisms. ACE2 is a monocarboxypeptidase that regulates the peptide cleavage in the renin-angiotensin system, and high levels of its expression could be found in alveolar epithelial type II cells, esophagus keratinocytes, small intestine, ileum and rectum enterocytes, stomach epithelial cells, colon colonocytes, liver cholangiocyte, arterial and venous endothelial cells, arterial smooth muscle cells, myocardial cells, sustentacular cells of the olfactory epithelium, spermatogonia and Leydig and Sertoli cells, prostate epithelial cells, bladder urothelial cells, and kidney proximal tubules cells[88-94]. TMPRSS2 regulating viral uptake by S protein priming is highly expressed by sustentacular cells of the olfactory epithelium, small intestine enterocytes, bronchial transient secretory cells, prostate epithelial cells, nasal goblet and ciliated cells, etc.[87,89,95-97].

4.3 Key points for the rational design

Our lack of knowledge in the COVID-19 pathogenesis and the absence of its adequate and licensed therapy[2] have led to the need to create novel *in vitro* platforms that mimic *in vivo* conditions and are specifically tailored for the SARS-CoV-2 infection. There is no doubt that 3D tissue models are more suitable than 2D models to study any viral infections because they share the similarity to the native tissue, organ structure, and physiological functionality, and this is also applicable to COVID-19.

3D tissue-like constructs can be fabricated by a huge variety of methods that can be divided into two main groups: Scaffold-based and scaffold-free. However, scaffold-free techniques such as bioprinting and cell self-organization (spheroidogenesis and organoidogenesis) and their combinations are considered to be the most promising ones as they allow precise reproduction of tissue morphological and functional properties.

Bioprinting is a complex technique that, particularly, enables tissue fabrication using spheroids or organoids (microtissues) as building blocks. Hence, the appropriate spatiotemporal status and cell-cell and cell-matrix contacts may be achieved[98]. In bioprinting, cells distributed in a hydrogel system ("bioink") are usually deposited by a bioprinter, which can be based on different technologies such as extrusion[99], ink jet[100], laser-induced forward transfer (LIFT)[101], stereolithography[102]. Extrusion-based bioprinting is the most widely used technique[103]; however, only LIFT bioprinter can enable precise deposition at high speed and resolution and is considered to be the best option to print minor cell populations within complex 3D tissue-like structures[101]. Regarding bioinks, the most promising cell components are spheroids or organoids establish intercellular junctions and newly synthetized ECM compared to a single cell suspension and maintain cell phenotype[22,104-106]; the biomaterial component – hydrogel system – is usually presented by natural and synthetic polymers, including their conjugates such as acellularized ECM, alginate, gelatin, fibrin, hyaluronic acid, cellulose, polyethylene glycol, and Pluronic-F127.[101,107-109].

As specific targets for SARS-CoV-2 are ACE2 and TMPRSS2, it is rational to include those tissues whose cells express these enzymes in the COVID-19 test tissue platform. Particularly, there should be 3D models of the nasal mucosa (including the olfactory neuroepithelium), lungs (particularly, the alveoli), blood vessels, heart, kidney, and intestine (**Figure 3**). To date, scientists have accumulated data on their fabrication through bioprinting, and this experience is shortly described further.

The nose is one of the main ports of SARS-CoV-2 infection, and the nasal mucosa is the first barrier tissue for the virus[81]. Among the existing models mimicking the nasal mucosa, none of them was fabricated through bioprinting. They are mainly presented by monolayers, air-fluid single or multilayered biointerfaces, and scaffold-based and explant-based cultures[110]. As the olfactory neuroepithelium located in the nasal mucosa is involved in virus entry and smell dysfunction[89,111], the rational model should contain sustentacular cells expressing high levels of ACE2 and TMPRSS2 and olfactory receptor neurons expressing these enzymes at lower levels. There are numerous efficient protocols to form olfactory neurospheres and to differentiate olfactory neuroepithelial cells[112-115]; therefore, these cells and their self-aggregates can be a perfect cell component for a bioink to print a "smell-sensitive" nasal mucosa construct.

The lungs, particularly the alveoli, are the main target for the SARS-CoV-2 infection and remain technically challenging. Only a limited number of studies achieved success in the 3D reconstruction of alveolar epithelial-endothelial barrier, and most scientists attempt to model only the air-cell and fluid-cell biointerfaces. For instance, Horvath *et al*.[116] bioprinted the epithelial/endothelial cell barrier system on a porous membrane and showed that it is possible to create reproducible thin homogenous cell layers. To date, the most complex lung-like structure was fabricated by Grigoryan *et al*. using a stereolithographic bioprinter[117]. To reproduce the alveoli scale and morphology, particularly their epithelial side, Lewis *et al*. created hollow epithelial cysts using the microsphere-based approach[118]. Such cysts as a cell component of a bioink can be easily hierarchically structured through bioprinting to achieve lung-like constructs.

Blood vessels containing ACE-expressing endothelial cells are a common object for bioprinting because they ensure the proper survivability and engraftment of tissue-engineered constructs. Different approaches varying in fabrication method and bioink blends were offered and can be classified as follows: Sacrificial and core/shell techniques. The choice depends on the required shape and sizes; vessels with bigger diameter can be fabricated using an extrusion-based bioprinter, vessels with smaller diameter using a laser-assisted bioprinter, and multibranched vessels using stereolithographic bioprinter[101,117,119,120].

Another target organ for COVID-19 that should be included in an integrated platform is

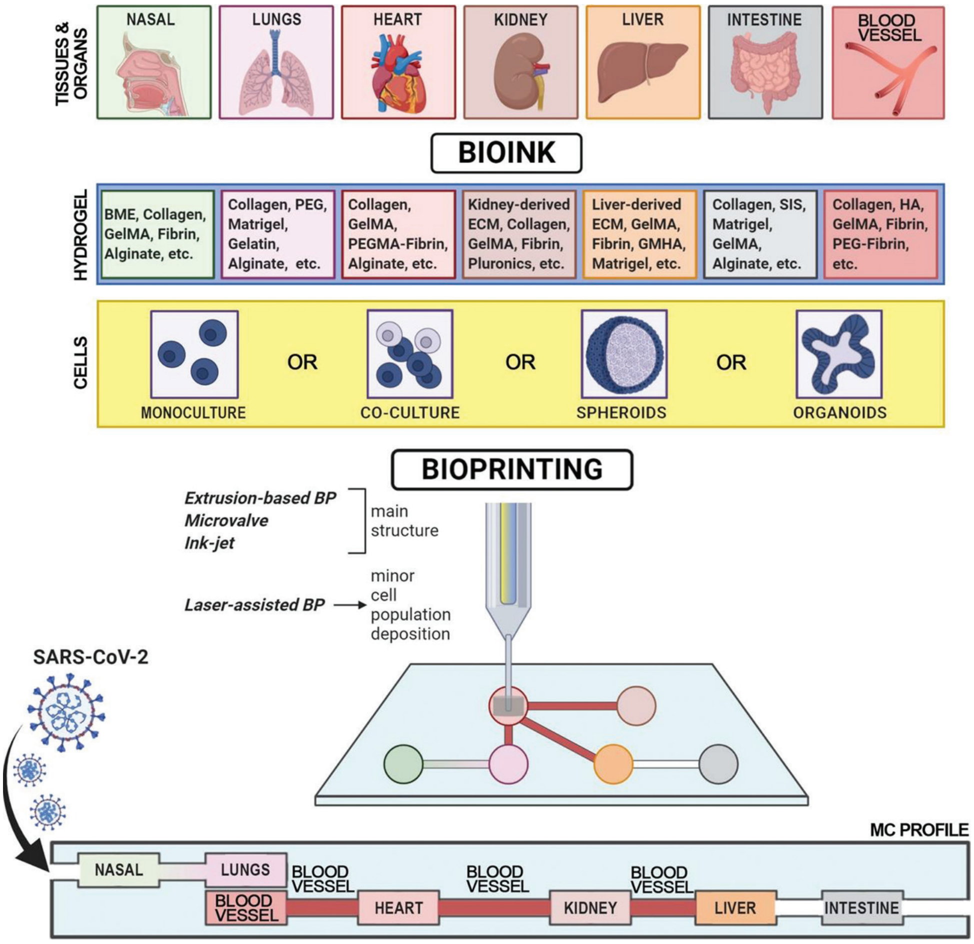

Figure 3. Designing an "ideal" tissue model to study severe acute respiratory syndrome-related coronavirus 2 infection. BME – basement memebrane extract; BP – bioprinting; BV – blood vessel; ECM – extracellular matrix; GelMA – gelatin methacrylated; GMHA – glycidyl methacrylated hyaluronic acid; MC – microfluidic chamber (chip); PEG – polyethylene glycol; PEGMA – polyethylene glycol monoacrylate; SARS-CoV-2 – severe acute respiratory syndrome-related coronavirus 2; SIS – small intestinal submucosa.

the heart. Engineering cardiac tissues requires the restoration of their functionality. To date, there is a number of successful studies that can be used as a base. Particularly, Maiullari *et al*. bioprinted a cardiac vascularized construct from hiPSC-derived cardiomyocytes and umbilical vein endothelial cells. This construct had native tissue-like morphology and successfully grafted with host tissues and vasculature[121]. Zhang *et al*. showed a complex approach to fabricate a vascularized-myocardium-on-a-chip, which was able to contract, using the combination of both bioprinting and microfluidics[122].

The kidneys play a crucial role in COVID-19[123,124], but its biofabrication remains an appealing goal. For sure, scientists have achieved particular success which is mostly related to engineering miniaturized kidney models[125-129]. Particularly, Homan *et al*. bioprinted renal proximal tubules placed into a microfluidic chip and showed that such model had the typical epithelial morphology and was sensitive to cyclosporine A[127]. King *et al*. fabricated an *in vitr*o multicellular model consisting of renal fibroblasts, endothelial cells, and proximal tubule epithelial cells and revealed its susceptibility to cisplatin in a dose-dependent manner and response to TGFβ[130].

The liver is also challenging for bioprinting mainly because of its complex structure that includes microvasculature and innervation[131]. However, there is a number of studies achieved good results in the restoration of the liver morphology and functionality. For instance, Yanagi *et al*. developed an approach to fabricate liver-like tissues based on the fusion of the bioprinted spheroids[132]. In addition, Bhise *et al*. designed a bioprinted liver-on-a-chip and showed its full functionality for 30 days and sensitivity to acetaminophen-induced toxicity[133].

The intestine is highly susceptible to the SARS-CoV-2 infection because its epithelial cells express ACE2[90] involved in amino acid homeostasis[134]. Therefore, it is essential to include it as a target organ in the designed tissue model platform. There are numerous approaches for fabrication of intestinal models, bioprinting is considered to be a promising approach[135]. Particularly, Madden *et al*. showed that it is possible to fabricate a two-layered construct consisting of epithelial cells and myofibroblasts through bioprinting[136]. Such construct had clear morphology, and cells expressed villin, E-cadherin, ZO-1, and enzymes and proteins participating in xenobiotics metabolism (cytochrome P450 2C9, multidrug resistance protein 1, breast cancer resistance protein, etc.)

To mimic air and liquid flow for recapitulating the *in vivo* conditions, microfluidics can be used as a tool. Such systems can be fabricated using bioprinting[137-139] and have been already approved as both single organ (organ-on-a-chip)[131,140-143] and integrated (body-on-a-chip) platforms[144-146]. Multi-organ model systems are more physiologically relevant and permits better detection of complex virus-host effects than the first ones. Particularly, Maschmeyer *et al*. fabricated a four-organ-chip representing the intestine, the liver, the skin, and the kidney[144]. Later, Vernetti *et al*. offered a more complex system reproducing the microphysiology of coupled intestine, liver, kidney proximal tubule, blood–brain barrier, and skeletal muscle models[145]. However, there are only several platforms which were fabricated using bioprinting because the combination of these emerging techniques is a relatively new approach. For instance, Skardal *et al*. developed a three-tissue system consisting of functional lung, cardiac, and liver modules and proved its applicability for drug testing[146]. Compared to such 2D models, bioprinted models ensure complex cell-cell and cell-matrix interactions that are crucial in studying COVID-19 pathogenesis.

The most challenging aspect of designing COVID-19 tissue platforms is modeling immune response relevant for this disease[2]. Hence, the "ideal" system should represent effects of dendritic cells and macrophages that secret inflammatory cytokines and chemokines (Interleukin [IL]-6, IL-8, IL-12, tumor necrosis factor-α, monocyte chemoattractant protein-1, Granulocyte-macrophage colony-stimulating factor, etc.) and cytotoxic T cells (CD4$^+$ and CD8$^+$ T cells). Hence, two approaches might be applied. The first one is designing immune-competent models[147,148] or integrated platforms by including lymph node models[149,150]. The second approach is based on the perfusion of immune cells suspension through a chip.

The integrated platform (**Figure 3**) includes six target tissues/organs (nasal tissue, lungs, heart, kidney, liver, and intestine), including blood vessels. They connect to each other using microfluidic channels ensuring virus transmission, cell supply with nutrients and oxygen, cell migration, etc. Each particular model is bioprinted to achieve native-like morphology and functionality. Bioink consists of cell (yellow) and hydrogel (blue) components and is tissue-specific. The best option for a bioink cell component is organoids/spheroids as they can perform cell-cell and cell-matrix interactions. To model immune response, two approaches might be applied: Designing immune-competent models/including lymph node models into such integrated platform and perfusing immune cells suspension through it.

5 Conclusion

To defeat COVID-19, the mankind should create new tools combining the emerging techniques such as bioprinting, microfluidics, and organoid formation. To date, our understanding of the fabrication of tissue models for different viruses and tissue engineering is growing, and they can be applied in designing an integrated multi-tissue bioprinted platform tailored for SARS-CoV-2 infection. Despite that none has yet tested such complex systems to study this virus and perform drug screening, this multidisciplinary approach can be a new chapter in antiviral research in view of the outstanding achievements described in this review.

Acknowledgments

This work was supported by the Russian Science Foundation (18-15-00407, Introduction and Section 4.1), Russian Foundation for Basic Research (18-29-06059, Section 2; 20-04-60063, Section 4.2 and 4.3), and Russian academic excellence project 5–100 (Section 3 and Conclusions).

Conflict of interest

The authors declare that they have no conflict of interest.

Author contributions

A.Sh., E.G., V.M., and P.S. outlined the manuscript. P.B. and M.P. contributed to Section 2.3 and 3 (except 3.2), D.B. – Section 2.1, N.K. – Section 2.2, M.V., E.Z., and N.K.R. – Section 3.2, and A.S. – Section 4 and 5, A.Sv. – Section 1 and 2.3. I.Z. drafted and prepared **Figure 3**, including its description; D.B., E.Z., and N.K.R. – **Figures 1 and 2**. A.S. drafted the manuscript with primary editing and revision support from A.Sv., P.S., and V.M. A.Sh., A.Sv., D.B., E.Z., E.G., and N.K.R. prepared the paper’s revision to address reviewers’ comments. A.Sv., P.S., and E.G. coordinated the manuscript preparation. All authors read and approved the final manuscript.

References

1. Choong YYC, Tan HW, Patel DC, *et al*., 2020, The Global Rise of 3D Printing During the COVID-19 Pandemic. *Nat Rev Mater*,1–3. DOI: 10.1038/s41578-020-00234-3.
2. Hossein-Khannazer N, Shokoohian B, Shpichka A, *et al*., 2020, Novel Therapeutic Approaches for Treatment of COVID-19. *J Mol Med*, 3:1–15. DOI: 10.1007/s00109-020-01927-6.
3. Park SJ, Yu KM, Kim YI, *et al*., 2020, Antiviral Efficacies of FDA-Approved Drugs against SARS-COV-2 Infection in Ferrets. *MBio*, 11(3):e01114–20. DOI: 10.1128/mbio.01114-20.
4. Shi J, Wen Z, Zhong G, *et al*., 2020, Susceptibility of Ferrets, Cats, Dogs, and other Domesticated Animals to SARS-coronavirus 2. *Science*, 368(6494):1016–20. DOI: 10.1126/science.abb7015.
5. Le Bras A, 2020, SARS-CoV-2 Causes COVID-19-Like Disease in Cynomolgus Macaques. *Lab Anim*, 49(6):174. DOI: 10.1038/s41684-020-0571-8.
6. Rockx B, Kuiken T, Herfst S, *et al*., 2020, Comparative Pathogenesis of COVID-19, MERS, and SARS in a Nonhuman Primate Model. *Science*, 368(6494):1012–5.
7. Lutz C, Maher L, Lee C, *et al*., 2020, COVID-19 Preclinical Models: Human Angiotensin-Converting Enzyme 2 Transgenic Mice. *Hum Genomics*, 14:20. DOI: 10.1186/s40246-020-00272-6.
8. Monteil V, Kwon H, Prado P, *et al*., 2020, Inhibition of SARS-CoV-2 Infections in Engineered Human Tissues Using Clinical-Grade Soluble Human ACE2. *Cell*, 181(4):905–13. DOI: 10.1016/j.cell.2020.04.004.
9. Lindesmith L, Moe C, Marionneau S, *et al*., 2003, Human Susceptibility and Resistance to Norwalk Virus Infection. *Nat Med*, 9(5):548–53. DOI: 10.1038/nm860.
10. DeVincenzo JP, Wilkinson T, Vaishnaw A, *et al*., 2010, Viral Load Drives Disease in Humans Experimentally Infected with Respiratory Syncytial Virus. *Am J Respir Crit Care Med*, 182(10):1305–14. DOI: 10.1164/rccm.201002-0221oc.
11. Memoli MJ, Shaw PA, Han A, *et al*., 2016, Evaluation of Antihemagglutinin and Antineuraminidase Antibodies as Correlates of Protection in an Influenza A/H1N1 Virus Healthy Human Challenge Model. *MBio*, 7(2):1–12. DOI: 10.1128/mbio.00417-16.
12. Wilkinson TM, Li CK, Chui CS, *et al*., 2012, Preexisting Influenza-Specific CD4 + T Cells Correlate with Disease Protection against Influenza Challenge in Humans. *Nat Med*, 18(2):274–80. DOI: 10.1038/nm.2612.
13. He XS, Holmes TH, Zhang C, *et al*., 2006, Cellular Immune Responses in Children and Adults Receiving Inactivated or Live Attenuated Influenza Vaccines. *J Virol*, 80(23):11756–66. DOI: 10.1128/jvi.01460-06.
14. Huang KY, Li CK, Clutterbuck E, *et al*., 2014, Virus-Specific Antibody Secreting Cell, Memory B-Cell, and Sero-antibody Responses in the Human Influenza Challenge Model. *J Infect Dis*, 209(9):1354–61. DOI: 10.1093/infdis/jit650.
15. Larsen CP, Whitehead SS, Durbin AP, 2015, Dengue Human Infection Models to Advance Dengue Vaccine Development. *Vaccine*, 33(50):7075–82. DOI: 10.1016/j.vaccine.2015.09.052.
16. Kirkpatrick BD, Whitehead SS, Pierce KK, *et al*., 2016, The Live Attenuated Dengue Vaccine TV003 Elicits Complete Protection Against Dengue in a Human Challenge Model. *Sci Transl Med*,

8(330): 330ra36. DOI: 10.1126/scitranslmed.aaf1517.

17. Henle W, Henle G, Stokes J Jr., 1943, Demonstration of the Efficacy of Vaccination Against Influenza Type A by Experimental Infection of Human Beings. *J Immunol*, 46(3):163–75.
18. Jackson GG, Muldon RL, Akers LW, 1963, Serological Evidence for Prevention of Influenzal Infection in Volunteers by an Anti-influenzal Drug Adamantanamine Hydrochloride. *Antimicrob Agents Chemother*, 161:703–7.
19. Calfee DP, Peng AW, Cass LM, *et al*., 1999, Safety and Efficacy of Intravenous Zanamivir in Preventing Experimental Human Influenza A Virus Infection. *Antimicrob Agents Chemother*, 43(7):1616–20. DOI: 10.1128/aac.43.7.1616.
20. Hayden FG, Zylidnikov DM, Iljenko VI, *et al*., 1982, Comparative Therapeutic Effect of Aerosolized and Oral Rimantadine HC1 in Experimental Human Influenza A Virus Infection. *Antiviral Res*, 2(3):147–53. DOI: 10.1016/0166-3542(82)90016-x.
21. Hayden FG, Treanor JJ, Fritz RS, *et al*., 1999, Use of the Oral Neuraminidase Inhibitor Oseltamivir in Experimental Human Influenza Randomized Controlled Trials for Prevention and Treatment. *JAMA*, 282(13):1240-6. DOI: 10.1001/jama.282.13.1240.
22. Mironov V, Visconti R, Kasyanov V, *et al*., 2009, Organ Printing: Tissue Spheroids as Building Blocks. *Biomaterials*, 30(12):2164–74. DOI: 10.1016/j.biomaterials.2008.12.084.
23. Gubareva LV, Kaiser L, Matrosovich MN, *et al*., 2001, Selection of Influenza Virus Mutants in Experimentally Infected Volunteers Treated with Oseltamivir. *J Infect Dis*, 183(4):523–31. DOI: 10.1086/318537.
24. McCallin S, Sarker SA, Sultana S, *et al*., 2018, Metagenome Analysis of Russian and Georgian Pyophage Cocktails and a Placebo-Controlled Safety Trial of Single Phage Versus Phage Cocktail in Healthy *Staphylococcus aureus* Carriers. *Environ Microbiol*, 20(9):3278–93. DOI: 10.1111/1462-2920.14310.
25. Jault P, Leclerc T, Jennes S, *et al*., 2019, Efficacy and Tolerability of a Cocktail of Bacteriophages to Treat Burn Wounds Infected by *Pseudomonas aeruginosa* (PhagoBurn): A Randomised, Controlled, Double-Blind Phase 1/2 Trial. *Lancet Infect Dis*, 19(1):35–45. DOI: 10.1016/s1473-3099(18)30482-1.
26. Febvre HP, Rao S, Gindin M, *et al*., 2019, PHAGE Study: Effects of Supplemental Bacteriophage Intake on Inflammation and Gut Microbiota in Healthy Adults. *Nutrients*, 11(3):666. DOI: 10.3390/nu11030666.
27. Bem RA, Domachowske JB, Rosenberg HF, 2011, Animal Models of Human Respiratory Syncytial Virus Disease. *Am J Physiol Lung Cell Mol Physiol*, 301:L148-56.
28. Radigan KA, Misharin AV, Chi M, *et al*., 2015, Modeling Human Influenza Infection in the Laboratory. *Infect Drug Resist*, 8:311–20. DOI: 10.2147/idr.s58551.
29. Dowall SD, Graham VA, Rayner E, *et al*. 2016, A Susceptible Mouse Model for Zika Virus Infection. *PLoS Negl Trop Dis*, 10(5):e0004658.
30. Ter Meulen J, Bakker AB, Van Den Brink EN, *et al*., 2004, Human Monoclonal Antibody as Prophylaxis for SARS Coronavirus Infection in Ferrets. *Lancet*, 363(9427):2139–41. DOI: 10.1016/s0140-6736(04)16506-9.
31. Ng PS, Böhm R, Hartley-Tassell LE, *et al*., 2014, Ferrets Exclusively Synthesize Neu5Ac and Express Naturally Humanized Influenza A Virus Receptors. *Nat Commun*, 5(1):1–9. DOI: 10.1038/ncomms6750.
32. Hancock GE, Smith JD, Heers KM, 2000, Serum Neutralizing Antibody Titers of Seropositive Chimpanzees Immunized with Vaccines Coformulated with Natural Fusion and Attachment Proteins of Respiratory Syncytial Virus. *J Infect Dis*, 181(5):1768–71. DOI: 10.1086/315475.
33. Clarke CJ, Watt NJ, Meredith A, *et al*., 1994, Respiratory Syncytial Virus-associated Bronchopneumonia in a Young Chimpanzee. *J Comp Pathol*, 110(2):207–12. DOI: 10.1016/s0021-9975(08)80191-0.
34. Perrin S, 2014, Make Mouse Studies Work. *Nature*, 517:423–5.
35. Ito R, Takahashi T, Ito M, 2018, Humanized Mouse Models: Application to Human Diseases. *J Cell Physiol*, 233:3723–8. DOI: 10.1002/jcp.26045.
36. Walsh NC, Kenney LL, Jangalwe S, *et al*., 2017, Humanized Mouse Models of Clinical Disease. *Annu Rev Pathol Mech Dis*, 12(1):187–215. DOI: 10.1146/annurev-pathol-052016-100332.
37. Kistner O, Barrett PN, Mundt W, *et al*., 1998, Development of a Mammalian Cell (Vero) Derived Candidate Influenza Virus Vaccine. *Vaccine*, 16(9-10):960–8. DOI: 10.1016/s0264-410x(97)00301-0.
38. de Lang A, Osterhaus AD, Haagmans BL, 2006, Interferon-γ and Interleukin-4 Downregulate Expression of the SARS Coronavirus Receptor ACE2 in Vero E6 Cells. *Virology*, 353(2):474–81. DOI: 10.1016/j.virol.2006.06.011.
39. Bhowmick R, Derakhshan T, Liang Y, *et al*., 2018, A Three-Dimensional Human Tissue-Engineered Lung Model to Study Influenza A Infection. *Tissue Eng Part A*, 24(19-20):1468–80. DOI: 10.1089/ten.tea.2017.0449.
40. Dill V, Hoffmann B, Zimmer A, *et al*., 2018, Influence of Cell Type and Cell Culture Media on the Propagation of Foot-and-Mouth Disease Virus with Regard to Vaccine Quality. *Virol J*, 15(1):1–11. DOI: 10.1186/s12985-018-0956-0.

41. Radlett PJ, Pay TW, Garland AJ, *et al*., 1985, The Use of BHK Suspension Cells for the Commercial Production of Foot and Mouth Disease Vaccines Over a Twenty Year Period. *Dev Biol Stand*, 60:163–70.
42. Archer F, Jacquier E, Lyon M, *et al*., 2007, Alveolar Type II Cells Isolated from Pulmonary Adenocarcinoma: A Model for JSRV Expression *In Vitro*. *Am J Respir Cell Mol Biol*, 36(5):534–40. DOI: 10.1165/rcmb.2006-0285oc.
43. Hayle AJ, 1986, Culture of Respiratory Syncytial Virus Infected Diploid Bovine Nasal Mucosa Cells on Cytodex 3 Microcarriers. *Arch Virol*, 89(1–4):81–8. DOI: 10.1007/bf01309881.
44. Gardner JK, Herbst-Kralovetz MM, 2016, Three-Dimensional Rotating Wall Vessel-Derived Cell Culture Models for Studying Virus-Host Interactions. *Viruses*, 8:304. DOI: 10.3390/v8110304.
45. Sachs N, Papaspyropoulos A, Zomer-van Ommen DD, *et al*., 2019, Long-term Expanding Human Airway Organoids for Disease Modeling. *EMBO J*, 38(4):e100300.
46. Chen YW, Huang SX, De Carvalho AL, *et al*., 2017, A Three-dimensional Model of Human Lung Development and Disease from Pluripotent Stem Cells. *Nat Cell Biol*, 19(5):542–9.
47. Zhou J, Li C, Sachs N, *et al*., 2018, Differentiated Human Airway Organoids to Assess Infectivity of Emerging Influenza Virus. *Proc Natl Acad Sci USA*, 115(26):6822–7. DOI: 10.1073/pnas.1806308115.
48. Ettayebi K, Crawford SE, Murakami K, *et al*., 2016, Replication of Human Noroviruses in Stem Cell-derived Human Enteroids. *Science*, 353(6306):1387–93.
49. Zhou J, Li C, Zhao G, *et al*., 2017, Human Intestinal Tract Serves as an Alternative Infection Route for Middle East Respiratory Syndrome Coronavirus. *Sci Adv*, 3(11):eaao4966.
50. Grivel JC, Margolis L, 2009, Use of Human Tissue Explants to Study Human Infectious Agents. *Nat Protoc*, 4(2):256–69.
51. Koban R, Neumann M, Daugs A, *et al*., 2018, A Novel Three-dimensional Cell Culture Method Enhances Antiviral Drug Screening in Primary Human Cells. *Antiviral Res*, 150:20–9. DOI: 10.1016/j.antiviral.2017.12.005.
52. Imle A, Kumberger P, Schnellbächer ND, *et al*., 2019, Experimental and Computational Analyses Reveal that Environmental Restrictions Shape HIV-1 Spread in 3D Cultures. *Nat Commun*, 10(1):2144. DOI: 10.1038/s41467-019-09879-3.
53. Shokoohian B, 2018, Bio-printing Damaged Tissues: A Novel Approach in Regenerative Medicine. *Mod Med Lab J*, 2(1):1–5. DOI: 10.30699/mmlj17.2.1.1.
54. Berg J, Hiller T, Kissner MS, *et al*., Optimization of Cell-laden Bioinks for 3D Bioprinting and Efficient Infection with Influenza A Virus. *Sci Rep*, 8(1):1–13. DOI: 10.1038/s41598-018-31880-x.
55. Park JA, Yoon S, Kwon J, *et al*., 2017, Freeform Micropatterning of Living Cells into Cell Culture Medium Using Direct Inkjet Printing. *Sci Rep*, 7(1):14610. DOI: 10.1038/s41598-017-14726-w.
56. Du G, Fang Q, den Toonder JM, 2016, Microfluidics for Cell-Based High Throughput Screening Platforms a Review. *Anal Chim Acta*, 903:36–50. DOI: 10.1016/j.aca.2015.11.023.
57. Montanez-Sauri SI, Sung KE, Puccinelli JP, *et al*., 2011, Automation of Three-Dimensional Cell Culture in Arrayed Microfluidic Devices. *J Lab Autom*, 16(3):171–85. DOI: 10.1016/j.jala.2011.02.003.
58. Kane KI, Moreno EL, Hachi S, *et al*., 2019, Automated Microfluidic Cell Culture of Stem Cell Derived Dopaminergic Neurons. *Sci Rep*, 9(1):1–12.
59. Super A, Jaccard N, Marques MP, *et al*., 2016, Real-Time Monitoring of Specific Oxygen Uptake Rates of Embryonic Stem Cells in a Microfluidic Cell Culture Device. *Biotechnol J*, 11(9):1179–89. DOI: 10.1002/biot.201500479.
60. Vergani M, Carminati M, Ferrari G, *et al*., 2012, Multichannel Bipotentiostat Integrated with a Microfluidic Platform for Electrochemical Real-time Monitoring Of Cell Cultures. *IEEE Trans Biomed Circuits Syst*, 6(5):498–507. DOI: 10.1109/tbcas.2012.2187783.
61. Yum K, Hong SG, Healy KE, *et al*., 2013, Physiologically Relevant Organs on Chips. *Biotechnol J*, 9(1):16–27. DOI: 10.1002/biot.201300187.
62. Costello DA, Millet JK, Hsia CY, *et al*., 2013, Single Particle Assay of Coronavirus Membrane Fusion with Proteinaceous Receptor-embedded Supported Bilayers. *Biomaterials*, 34(32):7895–904. DOI: 10.1016/j.biomaterials.2013.06.034.
63. Poortahmasebi V, Baghi HB, 2019, Living in the Shadows of Hepatitis. *Lancet Infect Dis*, 19(11):1171–2. DOI: 10.1016/s1473-3099(19)30534-1.
64. Ringehan M, McKeating JA, Protzer U, 2017, Viral Hepatitis and Liver Cancer. *Philos Trans R Soc Lond B Biol Sci*, 372:20160274. DOI: 10.1098/rstb.2016.0274.
65. Chong TW, Smith RL, Hughes MG, *et al*., 2006, Primary Human Hepatocytes in Spheroid Formation to Study Hepatitis C Infection. *J Surg Res*, 130(1):52–7.
66. Nie YZ, Zheng YW, Miyakawa K, *et al*., 2008, Recapitulation of Hepatitis B Virus Host Interactions in Liver Organoids from Human Induced Pluripotent Stem Cells. *EBioMedicine*, 35:114–23. DOI: 10.1016/j.ebiom.2018.08.014.

67. Tajpara P, Mildner M, Schmidt R, *et al*., 2019, A Preclinical Model for Studying Herpes Simplex Virus Infection. *J Invest Dermatol*, 139:673–82.
68. Zhu Y, Yang Y, Guo J, *et al*., 2017, *Ex vivo* 2D and 3D HSV-2 Infection Model Using Human Normal Vaginal Epithelial Cells. *Oncotarget*, 8(9):15267–82. DOI: 10.18632/oncotarget.14840.
69. D'Aiuto L, Naciri J, Radio N, *et al*., 2018, Generation of Three-dimensional Human Neuronal Cultures: Application to Modeling CNS Viral Infections. *Stem Cell Res Ther*, 9(1):134. DOI: 10.1186/s13287-018-0881-6.
70. Sison SL, O'Brien BS, Johnson AJ, *et al*., 2019, Human Cytomegalovirus Disruption of Calcium Signaling in Neural Progenitor Cells and Organoids. *J Virol*, 93(17):954. DOI: 10.1128/jvi.00954-19.
71. Berg J, Hiller T, Kissner MS, *et al*., 2018, Optimization of Cell-laden Bioinks for 3D Bioprinting and Efficient Infection with Influenza A Virus. *Sci Rep*, 8(1):13877. DOI: 10.1038/s41598-018-31880-x.
72. Sainz B, Tencate V, Uprichard SL, 2009, Three-Dimensional Huh7 Cell Culture System for the Study of Hepatitis C Virus Infection. *Virol J*, 6:103. DOI: 10.1186/1743-422x-6-103.
73. Molina-Jimenez F, Benedicto I, Thi VL, *et al*., 2012, Matrigel-Embedded 3D Culture of Huh-7 Cells as a Hepatocyte-Like Polarized System to Study Hepatitis C Virus Cycle. *Virology*, 425(1):31–9. DOI: 10.1016/j.virol.2011.12.021.
74. Rajalakshmy AR, Malathi J, Madhavan HN, *et al*., 2015, Mebiolgel, a Thermoreversible Polymer as a Scaffold for Three Dimensional Culture of Huh7 Cell Line with Improved Hepatocyte Differentiation Marker Expression and HCV Replication. *Indian J Med Microbiol*, 33(4):554–9. DOI: 10.4103/0255-0857.167330.
75. Ortega-Prieto AM, Skelton JK, Wai SN, *et al*., 2018, 3D Microfluidic Liver Cultures as a Physiological Preclinical Tool for Hepatitis B Virus Infection. *Nat Commun*, 9(1):682. DOI: 10.1038/s41467-018-02969-8.
76. Morrison KM, Beucler MJ, Campbell EO, *et al*., 2018, Development of a Primary Human Cell Model for the Study of Human Cytomegalovirus Replication and Spread within Salivary Epithelium. *J Virol*, 93(3):e01608–18. DOI: 10.1128/jvi.01608-18.
77. Lam V, Bigley T, Terhune SS, *et al*., 2012, A Method for Quantifying Mechanical Properties of Tissue Following Viral Infection. *PLoS One*, 7(8):e42197. DOI: 10.1371/journal.pone.0042197.
78. Goodwin TJ, McCarthy M, Osterrieder N, *et al*., 2013, Three-Dimensional Normal Human Neural Progenitor Tissue-Like Assemblies: A Model of Persistent Varicella-Zoster Virus Infection. *PLoS Pathog*, 9(8):e1003512. DOI: 10.1371/journal.ppat.1003512.
79. Li BJ, Tang Q, Cheng D, *et al*., 2005, Using siRNA in Prophylactic and Therapeutic Regimens against SARS Coronavirus in Rhesus Macaque. *Nat Med*, 11(9):944–51. DOI: 10.1038/nm1280.
80. Jeon S, Ko M, Lee J, *et al*., 2020, Identification of Antiviral Drug Candidates against SARS-CoV-2 from FDA-approved Drugs. *Antimicrob Agents Chemother*, 64(7):e00819-20. DOI: 10.1128/aac.00819-20.
81. Ziegler CG, Allon SJ, Nyquist SK, *et al*., 2020, SARS-CoV-2 Receptor ACE2 is an Interferon-Stimulated Gene in Human Airway Epithelial Cells and is Detected in Specific Cell Subsets across Tissues. *Cell*, 181(5):1016–35. DOI: 10.3410/f.737831436.793574366.
82. Li W, Moore MJ, Vasilieva N, *et al*., 2003, Angiotensin-Converting Enzyme 2 is a Functional Receptor for the SARS Coronavirus. *Nature*, 426(6965):450–4. DOI: 10.1038/nature02145.
83. Glowacka I, Bertram S, Muller MA, *et al*., 2011, Evidence that TMPRSS2 Activates the Severe Acute Respiratory Syndrome Coronavirus Spike Protein for Membrane Fusion and Reduces Viral Control by the Humoral Immune Response. *J Virol*, 85(9):4122–34. DOI: 10.1128/jvi.02232-10.
84. Li F, Li W, Farzan M, *et al*., 2005, Structural Biology: Structure of SARS Coronavirus Spike Receptor-binding Domain Complexed with Receptor. *Science*, 309(5742):1864–8. DOI: 10.1126/science.1116480.
85. Shirato K, Kawase M, Matsuyama S, 2013, Middle East Respiratory Syndrome Coronavirus Infection Mediated by the Transmembrane Serine Protease TMPRSS2. *J Virol*, 87(23):12552–61. DOI: 10.1128/jvi.01890-13.
86. Hoffmann M, Kleine-Weber H, Schroeder S, *et al*., 2020, SARS-CoV-2 Cell Entry Depends on ACE2 and TMPRSS2 and Is Blocked by a Clinically Proven Protease Inhibitor. *Cell*, 181(2):271–280. DOI: 10.1016/j.cell.2020.02.052.
87. Zang R, Castro MF, McCune BT, *et al*., 2020, TMPRSS2 and TMPRSS4 Promote SARS-CoV-2 Infection of Human Small Intestinal Enterocytes. *Sci Immunol*, 5(47):1–15. DOI: 10.1126/sciimmunol.abc3582.
88. Hamming I, Timens W, Bulthuis ML, *et al*., 2004, Tissue Distribution of ACE2 Protein, the Functional Receptor for SARS Coronavirus. A First Step in Understanding SARS Pathogenesis. *J Pathol*, 203(2):631–7. DOI: 10.1002/path.1570.
89. Bilinska K, Jakubowska P, Von Bartheld CS, *et al*., 2020, Expression of the SARS-CoV-2 Entry Proteins, ACE2 and TMPRSS2, in Cells of the Olfactory Epithelium: Identification

of Cell Types and Trends with Age. *ACS Chem Neurosci*, 11(11):1555–62. DOI: 10.1021/acschemneuro.0c00210.

90. Harmer D, Gilbert M, Borman R, *et al*., 2002, Quantitative mRNA Expression Profiling of ACE 2, a Novel Homologue of Angiotensin Converting Enzyme. *FEBS Lett*, 532(1–2):107–10. DOI: 10.1016/s0014-5793(02)03640-2.
91. Wang Z, Xu X, 2020, scRNA-seq Profiling of Human Testes Reveals the Presence of the ACE2 Receptor, A Target for SARS-CoV-2 Infection in Spermatogonia, Leydig and Sertoli Cells. *Cells*, 9:920. DOI: 10.3390/cells9040920.
92. Song H, Seddighzadeh B, Cooperberg MR, *et al*., 2020, Expression of ACE2, the SARS-CoV-2 Receptor, and TMPRSS2 in Prostate Epithelial Cells. *Eur Urol*, 78(2):296–8. DOI: 10.1101/2020.04.24.056259.
93. Qi F, Qian S, Zhang S, *et al*., 2020, Single Cell RNA Sequencing of 13 Human Tissues Identify Cell Types and Receptors of Human Coronaviruses. *Biochem Biophys Res Commun*, 526(1):135–40. DOI: 10.1101/2020.02.16.951913.
94. Zou X, Chen K, Zou J, *et al*., 2020, Single-Cell RNA-seq Data Analysis on the Receptor ACE2 Expression Reveals the Potential Risk of Different Human Organs Vulnerable to 2019-nCoV Infection. *Front Med*, 14(2):185–92. DOI: 10.1007/s11684-020-0754-0.
95. Lukassen S, Chua RL, Trefzer T, *et al*., 2020, SARS -CoV-2 Receptor ACE 2 and TMPRSS 2 are Primarily Expressed in Bronchial Transient Secretory Cells. *EMBO J*, 39(10):1–15. DOI: 10.15252/embj.20105114.
96. Chen YW, Lee MS, Lucht A, *et al*., 2010, TMPRSS2, a Serine Protease Expressed in the Prostate on the Apical Surface of Luminal Epithelial Cells and Released into Semen in Prostasomes, is Misregulated in Prostate Cancer Cells. *Am J Pathol*, 176(6):2986–96. DOI: 10.2353/ajpath.2010.090665.
97. Sungnak W, Huang N, Bécavin C, *et al*., 2020, SARS-CoV-2 Entry Factors are Highly Expressed in Nasal Epithelial Cells Together with Innate Immune Genes. *Nat Med*, 26(5):681–7. DOI: 10.1038/s41591-020-0868-6.
98. Ng WL, Chua CK, Shen YF, 2019, Print Me An Organ! Why We Are Not There Yet. *Prog Polym Sci*, 97:101145. DOI: 10.1016/j.progpolymsci.2019.101145.
99. Ozbolat IT, Hospodiuk M, 2016, Current Advances and Future Perspectives in Extrusion-Based Bioprinting. *Biomaterials*,;76:321–43. DOI: 10.1016/j.biomaterials.2015.10.076.
100. Saunders RE, Derby B, 2014, Inkjet Printing Biomaterials for Tissue Engineering: Bioprinting. *Int Mater Rev*, 59(8):430–48. DOI: 10.1179/1743280414y.0000000040.
101. Antoshin AA, Churbanov SN, Minaev NV, *et al*., 2019, LIFT-Bioprinting, is it Worth it? *Bioprinting*, 15:e00052. DOI: 10.1016/j.bprint.2019.e00052.
102. Ng WL, Lee JM, Zhou M, *et al*., 2020, Vat Polymerization-Based Bioprinting Process, Materials, Applications and Regulatory Challenges. *Biofabrication*, 12(2):22001. DOI: 10.1088/1758-5090/ab6034.
103. Matai I, Kaur G, Seyedsalehi A, *et al*., 2020, Progress in 3D Bioprinting Technology for Tissue/Organ Regenerative Engineering. *Biomaterials*, 226:119536. DOI: 10.1016/j.biomaterials.2019.119536.
104. Zurina I, Shpichka A, Saburina I, *et al*., 2018, 2D/3D Buccal Epithelial Cell Self-Assembling as a Tool for Cell Phenotype Maintenance and Fabrication of Multilayered Epithelial Linings *In Vitro*. *Biomed Mater*, 13(5):054104. DOI: 10.1088/1748-605x/aace1c.
105. Moldovan NI, Hibino N, Nakayama K, 2017, Principles of the Kenzan Method for Robotic Cell Spheroid-Based Three-Dimensional Bioprinting. *Tissue Eng Part B Rev*, 23(3):237–44. DOI: 10.1089/ten.teb.2016.0322.
106. Gorkun AA, Shpichka AI, Zurina IM, *et al*., 2018, Angiogenic Potential of Spheroids from Umbilical Cord and Adipose-Derived Multipotent Mesenchymal Stromal Cells within Fibrin Gel. *Biomed Mater*, 13(4):44108. DOI: 10.1088/1748-605x/aac22d.
107. Shpichka A, Osipova D, Efremov Y, *et al*., 2020, Fibrin-based Bioinks: New Tricks from an Old Dog. *Int J Bioprinting*, 6(3):1–14. DOI: 10.18063/ijb.v6i3.269.
108. Kornev VA, Grebenik EA, Solovieva AB, *et al*., 2018, Hydrogel-assisted Neuroregeneration Approaches Towards Brain Injury Therapy: A State-of-the-Art Review. *Comput Struct Biotechnol J*, 16:488–502. DOI: 10.1016/j.csbj.2018.10.011.
109. Shpichka AI, Konarev PV, Efremov YM, *et al*., 2020, Digging Deeper: Structural Background of PEGylated fi Brin Gels in Cell Migration and lumenogenesis. *RSC Adv*, 10:4190–200. DOI: 10.1039/c9ra08169k.
110. De Rudder C, Arroyo MC, Lebeer S, *et al*., 2018, Modelling Upper Respiratory Tract Diseases: Getting Grips on Host-microbe Interactions in Chronic Rhinosinusitis Using *In Vitro* Technologies. *Microbiome*, 6(1):75. DOI: 10.1186/s40168-018-0462-z.
111. Wang L, Shen Y, Li M, *et al*., 2020, Clinical Manifestations and Evidence of Neurological Involvement in 2019 Novel Coronavirus SARS-CoV-2: A Systematic Review and Meta-analysis. *J Neurol*, 2020;1–13. DOI: 10.1007/s00415-020-09974-2.
112. Li ST, Young TH, Huang TW, 2018, Poly (ethylene-co-

vinyl alcohol) is a Suitable Substrate for Human Olfactory Neuroepithelial Cell Differentiation *In Vitro* through a Defined Regulatory Pathway. *Acta Biomater*, 68:204–13. DOI: 10.1016/j.actbio.2017.12.029.

113. Li ST, Young TH, Wang CT, *et al*., 2018, Chitosan Films Promote Formation of Olfactory Neurospheres and Differentiation of Olfactory Receptor Neurons. *Rhinology*, 56(4):336–42. DOI: 10.4193/rhin17.155.
114. Du L, Zou L, Wang Q, *et al*., 2015, A Novel Biomimetic Olfactory Cell-based Biosensor with DNA-Directed Site-Specific Immobilization of Cells on a Microelectrode Array. *Sens Actuators B Chem*, 217:186–92. DOI: 10.1016/j.snb.2014.08.054.
115. Skaat H, Ziv-Polat O, Shahar A, *et al*., 2011, Enhancement of Migration, Growth and Differnatiation of Nasal Olfactory Mucosa Cells by Growth Factor-conjugated Fluorescent-maghemite Nanoparticles. *Bioconjugate Chem*, 22(12):2600–10. DOI: 10.1021/bc200454k.
116. Horvath L, Umehara Y, Jud C, *et al*., 2015, Engineering an *In Vitro* Air-blood Barrier by 3D Bioprinting. *Sci Rep*, 5:7974. DOI: 10.1038/srep07974.
117. Grigoryan B, Paulsen SJ, Corbett DC, *et al*., 2019, Multivascular Networks and Functional Intravascular Topologies within Biocompatible Hydrogels. *Science*, 364(6439):458–64. DOI: 10.1126/science.aav9750.
118. Lewis KJ, Tibbitt MW, Zhao Y, *et al*., 2015, *In Vitro* Model Alveoli from Photodegradable Microsphere Templates. *Biomater Sci*, 3(6):821–32. DOI: 10.1039/c5bm00034c.
119. Ozbolat IT, Moncal KK, Gudapati H, 2017, Evaluation of Bioprinter Technologies. *Addit Manuf*, 13:179–200. DOI: 10.1016/j.addma.2016.10.003.
120. Miri AK, Nieto D, Iglesias L, *et al*., 2018, Microfluidics-Enabled Multimaterial Maskless Stereolithographic Bioprinting. *Adv Mater*, 30(27):e1800242. DOI: 10.1002/adma.201870201.
121. Maiullari F, Costantini M, Milan M, *et al*., 2018, A Multi-cellular 3D Bioprinting Approach for Vascularized Heart Tissue Engineering Based on HUVECs and iPSC-Derived Cardiomyocytes. *Sci Rep*, 8(1):1–15. DOI: 10.1038/s41598-018-31848-x.
122. Zhang YS, Arneri A, Bersini S, *et al*., 2016, Bioprinting 3D Microfibrous Scaffolds for Engineering Endothelialized Myocardium and Heart-on-a-chip. *Biomaterials*, 110:45–59. DOI: 10.1016/j.biomaterials.2016.09.003.
123. Pan XW, Xu D, Zhang H, *et al*., 2020, Identification of a Potential Mechanism of Acute Kidney Injury During the COVID-19 Outbreak: A Study Based on Single-Cell Transcriptome Analysis. *Intensive Care Med*, 46:1114-1116. DOI: 10.1007/s00134-020-06026-1.
124. Ronco C, Reis T, 2020, Kidney Involvement in COVID-19 and Rationale for Extracorporeal Therapies. *Nat Rev Nephrol*, 16(6):308–10. DOI: 10.1038/s41581-020-0284-7.
125. Subramanian B, Rudym D, Cannizzaro C, *et al*., 2010, Tissue-Engineered Three-Dimensional *In Vitro* Models for Normal and Diseased Kidney. *Tissue Eng Part A*, 16(9):2821–31. DOI: 10.1089/ten.tea.2009.0595.
126. Sochol RD, Gupta NR, Bonventre JV, 2016, A Role for 3D Printing in Kidney-on-a-Chip Platforms. *Curr Transplant Rep*, 3(1):82–92. DOI: 10.1007/s40472-016-0085-x.
127. Homan KA, Kolesky DB, Skylar-Scott MA, *et al*., 2016, Bioprinting of 3D Convoluted Renal Proximal Tubules on Perfusable Chips. *Sci Rep*, 6:34845. DOI: 10.1038/srep34845.
128. Ali M, Kumar A, Yoo JJ, Zahran F, *et al*., 2019, A Photo-Crosslinkable Kidney ECM-Derived Bioink Accelerates Renal Tissue Formation. *Adv Healthc Mater*, 8(7):1800992. DOI: 10.1002/adhm.201800992.
129. Chuah JKC, Zink D, 2017, Stem Cell-Derived Kidney Cells and Organoids: Recent Breakthroughs and Emerging Applications. *Biotechnol Adv*, 35(2):150–67. DOI: 10.1016/j.biotechadv.2016.12.001.
130. King SM, Higgins JW, Nino CR, *et al*., 2017, 3D Proximal Tubule Tissues Recapitulate Key Aspects of Renal Physiology to Enable Nephrotoxicity Testing. *Front Physiol*, 8(1):1–18. DOI: 10.3389/fphys.2017.00123.
131. Heydari Z, Najimi M, Mirzaei H, *et al*., 2020, Tissue Engineering in Liver Regenerative Medicine: Insights into Novel Translational Technologies. *Cells*, 9(2):304.
132. Yanagi Y, Nakayama K, Taguchi T, *et al*., 2017, *In Vivo* and *Ex Vivo* Methods of Growing a Liver Bud Through Tissue Connection. *Sci Rep*, 7(1):1–15. DOI: 10.1038/s41598-017-14542-2.
133. Bhise NS, Manoharan V, Massa S, *et al*., 2016, A Liver-on-a-Chip Platform with Bioprinted Hepatic Spheroids. *Biofabrication*, 8(1):14101.
134. Hashimoto T, Perlot T, Rehman A, *et al*., 2012, ACE2 Links Amino Acid Malnutrition to Microbial Ecology and Intestinal Inflammation. *Nature*, 487(7408):477–81. DOI: 10.1038/nature11228.
135. Williams CF, Walton GE, Jiang L, *et al*., 2015, Comparative Analysis of Intestinal Tract Models. *Annu Rev Food Sci Technol*, 6(1):329–50. DOI: 10.1146/annurev-food-022814-015429.
136. Madden LR, Nguyen TV, Garcia-Mojica S, *et al*., 2018, Bioprinted 3D Primary Human Intestinal Tissues Model

Aspects of Native Physiology and ADME/Tox Functions. *iScience*, 2:156–67. DOI: 10.1016/j.isci.2018.03.015.

137. Ma J, Wang Y, Liu J, 2018, Bioprinting of 3D Tissues/Organs Combined with Microfluidics. *RSC Adv*, 8(39):21712–27. DOI: 10.1039/c8ra03022g.
138. Yu F, Choudhury D, 2019, Microfluidic Bioprinting for Organ-on-a-Chip Models. *Drug Discov Today*, 24(6):1248–57. DOI: 10.1016/j.drudis.2019.03.025.
139. Miri AK, Mostafavi E, Khorsandi D, *et al*., 2019, Bioprinters for Organs-on-Chips. *Biofabrication*, 11(4):42002. DOI: 10.1088/1758-5090/ab2798.
140. Koroleva A, Deiwick A, Nguyen A, *et al*., 2016, Hydrogel-Based Microfluidics for Vascular Tissue Engineering. *BioNanoMaterials*, 17(1–2):19–32. DOI: 10.1515/bnm-2015-0026.
141. Ashammakhi N, Wesseling-Perry K, Hasan A, *et al*., 2018, Kidney-on-a-Chip: Untapped Opportunities. *Kidney Int*, 94(6):1073–86. DOI: 10.1016/j.kint.2018.06.034.
142. Ribas J, Sadeghi H, Manbachi A, *et al*., 2016, Cardiovascular Organ-on-a-Chip Platforms for Drug Discovery and Development. *Appl Vitr Toxicol*, 2(2):82–96.
143. Jahromi MA, Abdoli A, Rahmanian M, *et al*., 2019, Microfluidic Brain-on-a-Chip: Perspectives for Mimicking Neural System Disorders. *Mol Neurobiol*, 56(12):8489–512. DOI: 10.1007/s12035-019-01653-2.
144. Maschmeyer I, Lorenz AK, Schimek K, *et al*., 2015, A Four-Organ-Chip for Interconnected Long-Term Co-culture of Human Intestine, Liver, Skin and Kidney Equivalents. *Lab Chip*, 15(12):2688–99. DOI: 10.1039/c5lc00392j.
145. Vernetti L, Gough A, Baetz N, *et al*., 2017, Functional Coupling of Human Microphysiology Systems: Intestine, Liver, Kidney Proximal Tubule, Blood-Brain Barrier and Skeletal Muscle. *Sci Rep*, 7(1):1–14. DOI: 10.1038/srep44517.
146. Skardal A, Murphy SV, Devarasetty M, *et al*., 2017, Multi-Tissue Interactions in an Integrated Three-Tissue Organ-on-a-Chip Platform. *Sci Rep*, 7(1):1–16.
147. Ramadan Q, Ting FC, 2016, *In Vitro* Micro-Physiological Immune-Competent Model of the Human Skin. *Lab Chip*, 16(10):1899–908. DOI: 10.1039/c6lc00229c.
148. Harrington H, Cato P, Salazar F, *et al*., 2014, Immunocompetent 3D Model of Human Upper Airway for Disease Modeling and *In Vitro* Drug Evaluation. *Mol Pharm*, 11(7):2082–91. DOI: 10.1021/mp5000295.
149. Gopalakrishnan N, Hannam R, Casoni GP, *et al*., 2015, Infection and Immunity on a Chip: A Compartmentalised Microfluidic Platform to Monitor Immune Cell Behaviour in Real Time. *Lab Chip*, 15(6):1481–7. DOI: 10.1039/c4lc01438c.
150. Rosa PM, Gopalakrishnan N, Ibrahim H, *et al*., 2016, The Intercell Dynamics of T Cells and Dendritic Cells in a Lymph Node-on-a-Chip Flow Device. *Lab Chip*, 16(19):3728–40. DOI: 10.1039/c6lc00702c.

ORIGINAL ARTICLE

Design and Additive Manufacturing of Medical Face Shield for Healthcare Workers Battling Coronavirus (COVID-19)

H. Kursat Celik[1]*, Ozkan Kose[2], Mihaela-Elena Ulmeanu[3], Allan E. W. Rennie[4], Thomas N. Abram[4], Ibrahim Akinci[1]

[1]Department of Agricultural Machinery and Technology Engineering, Faculty of Agriculture, Akdeniz University, Antalya, Turkey

[2]Department of Orthopaedics and Traumatology, Antalya Training and Research Hospital, University of Health Sciences, Antalya, Turkey

[3]Department of Manufacturing, University Politehnica of Bucharest, Bucharest, Romania

[4]Department of Engineering, Lancaster University, Lancaster, United Kingdom

Abstract: During the coronavirus disease-19 pandemic, the demand for specific medical equipment such as personal protective equipment has rapidly exceeded the available supply around the world. Specifically, simple medical equipment such as medical gloves, aprons, goggles, surgery masks, and medical face shields have become highly in demand in the health-care sector in the face of this rapidly developing pandemic. This difficult period strengthens the social solidarity to an extent parallel to the escalation of this pandemic. Education and government institutions, commercial and noncommercial organizations and individual homemakers have produced specific medical equipment by means of additive manufacturing (AM) technology, which is the fastest way to create a product, providing their support for urgent demands within the health-care services. Medical face shields have become a popular item to produce, and many design variations and prototypes have been forthcoming. Although AM technology can be used to produce several types of noncommercial equipment, this rapid manufacturing approach is limited by its longer production time as compared to conventional serial/mass production and the high demand. However, most of the individual designer/maker-based face shields are designed with little appreciation of clinical needs and nonergonomic. They also lack of professional product design and are not designed according to AM (Design for AM [DfAM]) principles. Consequently, the production time of up to 4 – 5 h for some products of these designs is needed. Therefore, a lighter, more ergonomic, single frame medical face shield without extra components to assemble would be useful, especially for individual designers/makers and noncommercial producers to increase productivity in a shorter timeframe. In this study, a medical face shield that is competitively lighter, relatively more ergonomic, easy to use, and can be assembled without extra components (such as elastic bands, softening materials, and clips) was designed. The face shield was produced by AM with a relatively shorter production time. Subsequently, finite element analysis-based structural design verification was performed, and a three-dimensional (3D) prototype was produced by an original equipment manufacturer 3D printer (Fused Deposition Modeling). This study demonstrated that an original face shield design with <10 g material usage per single frame was produced in under 45 min of fabrication time. This research also provides a useful product DfAM of simple medical equipment such as face shields through advanced engineering design, simulation, and AM applications as an essential approach to battling coronavirus-like viral pandemics.

Keywords: Medical face shield, Personal protective equipment, Product design, Additive manufacturing, Coronavirus disease-19

***Corresponding Author**: H. Kursat Celik, Department of Agricultural Machinery and Technology Engineering, Faculty of Agriculture, Akdeniz University, 07070, Antalya, Turkey; hkcelik@akdeniz.edu.tr

Received: May 29, 2020; ***Accepted:*** June 24, 2020; ***Published Online***: August 10, 2020

(This article belongs to the *Special Section: Research and Applications of 3D Printing and Bioprinting for Covid-19*)

Citation: Celik HK, Kose O, Ulmeanu ME, *et al.*, 2020, Design and Additive Manufacturing of Medical Face Shield for Healthcare Workers Battling Coronavirus (COVID-19), *Int J Bioprint*, 6(4): 286. DOI: 10.18063/ijb.v6i4.286.

1 Introduction

On December 31, 2019, the World Health Organization (WHO) Country Office in China was informed of cases of pneumonia which had unknown etiology from Wuhan City, Hubei Province of China. Following the identification and confirmation of a new type of coronavirus called 2019-nCoV by the Chinese authorities[1], the WHO officially named the disease caused by the coronavirus as coronavirus disease (COVID)-19, which stands for "COVID 2019" on February 11, 2020[2], and declare the pandemic on March 11, 2020[3]. Since the date of the first case of this virus spreading, the world has been struggling with this emergent state. During this period, international and national authorities have been announcing public advice and putting in place legal regulations regarding social behavioral habits and the use of personal protective equipment (PPE) for public and health-care services. During this pandemic, health-care institutions have become one of the most hazardous environments to work in, especially for healthcare workers (HW) who deliver care and services to the sick and ailing either directly as medical doctors and nurses or indirectly as aides, helpers, laboratory technicians, or even medical waste handlers, who are considered to be in the high-risk groups[4]. The outbreaks of serious airborne infectious diseases, such as severe acute respiratory syndrome (SARS), Avian Influenza and now the COVID-19, as well as severe infectious agents associated with body fluid exposures (e.g., Ebola virus) have called for increased attention to face/eye protection as the face is the most common body part exposed to the acutely-expelled aerosols of patient body fluids during HW-patient interaction[5].

Although it is understood that wearing a surgical face mask may provide protection during distanced interaction in the patient's room between the HW and patient who has suspected or confirmed COVID19, the use of additional PPE for closer operations potentially involving acutely-expelled aerosols of body fluids would be a necessity. Therefore, many international and national health service authorities/organizations advise the use of personal PPE for respiratory, eye/mouth/face, body, and hand protection while interacting with COVID-19 patients to avoid or minimize any likely contact, droplet, and airborne transmission[6-8]. The WHO also published a guide on the recommended types of PPE to be used in the context of SARS-CoV-2 (the virus causing COVID19), according to the setting, personnel, and type of activity[9].

For instance, the research carried out with cough aerosol and breathing simulators loaded with influenza virus (aerosol volume mean diameter of 8.5 µm) indicated 96% and 92% reductions in the risk of inhalational exposure immediately after a cough if a face shield at distances of 46 cm and 183 cm was used, respectively. In the case of a smaller aerosol diameter of 3.4 µm, the protection of the face shield is 68% at 46 cm immediately after the cough, and the protection rate decreases to 23% over 1 – 30 min post-cough (in the case of remaining airborne particles)[10].

It is understood that, in addition to face shield equipment, the use of surgical masks such as N95, filtering facepiece (FPP2), and FFP3 will give more effective and thorough protection during closer HW-patient interaction. Although there are risky cases for airborne transmitted viruses (which could have the ability to remain in the air for extended periods), in the case of larger aerosol droplet explosion, face shield (visor) products which have a simple design and manufacturable features would provide superior protection.

This face shield (visor) equipment could be designed and produced for single-use (disposable) or reusable following disinfection. In fact, before this pandemic, millions of HW, dental providers, veterinary care personnel, laboratory workers, pre-hospital emergency medical providers, police, firefighters, and custodial staff dealing with spills and contaminated waste have already been classified as the potential users of face shields. In addition to meeting the demand of this pre-existing group of face shield users, the need for this type of PPE in many countries, including Turkey and the United Kingdom, has increased drastically since the COVID-19 pandemic. On March 3, 2020, the WHO expressed the concern over the shortage of

PPE that could endanger HW worldwide; therefore, announced a call for increased manufacture of face shield by 40 % to meet the rising global demand for this type of PPE[11]. Based on WHO modeling, an estimated 89 million medical masks are required for tackling COVID-19 each month[11]. About 76 million of examination gloves are required, and the international demand for goggles (including face shield equipment) now stands at 1.6 million/month.

In the face of this high demand for PPE (specifically for face shield equipment), visors that are commercially produced by conventional manufacturing methods (mostly plastic injection molding) could be supplied on time, and the high demand for this PPE has raised the unit product costs and the shipping rate. Conversely, this situation strengthens our social solidarity to address the issues pertaining to this pandemic. Many educational and government institutions, commercial and noncommercial organizations, and home/individual makers produced face shield products (not mass/serial production) and shipped/donated them to personal-public users and health-care sectors. In many cases, additive manufacturing (AM) technology was utilized for their prototype designs as it is the fastest way to obtain a usable product/prototype. The use of this manufacturing technology with easily accessible relatively professional (trademarks) and original equipment manufacturer (OEM) 3D printers has become very popular and is productive enough to meet the high demand for PPE.

A face shield (visor) product has simple structural and functional design features, which consist of two main components: The frame (metal- or plastic material-based) and the transparent protective visor shield (mostly plastic material-based). However, additional components such as elastic bands (frame-head holder), face contact softening materials (sponge, foam, rubber, etc.), and clips for fastening the transparent shield to the frame can also be included.

Various concept designs for face shield products generated by AM for rapid prototyping/manufacturing have been introduced in addition to commercially existing ones (**Figure 1**). However, most of these products were not carefully designed with due consideration to professional and ergonomic product design principles, and design for AM (DfAM) approaches. A design can be functional and may correspond to the needs within pre-defined design specifications; however, this may not indicate that the design has structurally and functionally optimized features. For most of the designs generated, it was not known where or how they were approved. These designs also have relatively longer production and component assembly times per unit product (more than 4 – 5 production hours; about 2 h in average), and some of the products are heavier considering their custom designs. Besides, most of them, which are equipped with additional components such as elastic bands, softening materials, and fastening clips could cause user discomfort after using for long working hours and constant taking on/off operations. These facts appear as disadvantages for a product within the context of ergonomics and total AM-based production time. In addition, from a post-prototyping perspective, most of these products do not have convenient structural design features that are amenable for commercial mass/serial production using conventional manufacturing methods such as plastic injection molding. Therefore, a lighter, more ergonomic, and single frame medical face shield without extra components for assembly would be useful for homemakers, individual designers/makers, and noncommercial producers (primary target) to provide effective, functional rapid-prototyped products, which may have a commercial potential (secondary target) in a relatively shorter time. The disadvantages of the current PPE manufacturing method were the main sources of motivation for this design study as the product designs are dynamic, and can be seen changing stages on an existing product over time, in shape and function. These changing stages can be in different range and sudden, others move step by step. In any case, the major aim of the change is to improve the design, to make the product more effective or, put simply, just more appropriate for use in the current pandemic (i.e., low-cost, quick to produce, and disposable).

Considering the afore-mentioned specific product design issues, the aim of the current study

Figure 1. Examples of commercial and custom-made face shield products.

was to design a competitively lighter, relatively more ergonomic, and easy-to-use original medical face shield which can be produced within relatively shorter production times, assembled without extra components (such as elastic bands, softening materials, and clips), fully amenable to production using AM technology, and directed to more conventional manufacturing methods, by means of advanced computer-aided design, engineering, and AM applications.

2 Materials and methods

2.1 Background, design process, and original design details

Although international standards for industrial PPE (such as ANSI/ISEA Z87.1-2020, "American National Standard for Occupational and Educational Personal Eye and Face Protection" and British Standards of BS 7028:1999 BS EN 168:2002, BS EN 166:2002; BS EN 13921:2007, Statutory Instrument 2002 No. 1144 for eye protection regulations and specifications) are available, it is reported that there is currently no universal standard for eye/face protection from biological hazards during medical applications[10,12]. The common point related to the product descriptions and functionality. From the infection control standpoint, protector components serve to minimize or prevent eye and face exposure of the wearer to sprays, splashes, or droplets of blood, body fluids, excretions, secretions, and other potentially infectious materials in occupational and educational environments, where biological hazards are expected. Hence, in this perspective, various face shield design samples and patent registrations can be found from a simple internet search; however, the number of informative scientific publications for user guides, design details, and AM and conventional or non-conventional manufacturing applications of face shield are very limited. Within the limited literature, a useful scientific review regarding face shields used for infection control to assist in the selection and proper utilization of this type of PPE was published by Roberge (2016). In addition, the WHO, NHS England, and Texas Medical Association Turkey have been updating their advisory guidelines/publications for the use of medical PPE. These are the sources available to collect reference information related to design and structure, regulatory standards, and guidelines to proper use and selection of the PPE and describe the product as PPE that provides barrier protection to the facial area and related mucous membranes (eyes, nose, and lips). Consequently, these sources were carefully considered in describing the requirements for the design study detailed in this paper.

For the term "design," there is no single universal description in the product development applications; however, design is commonly considered as a total iterative process within the scopes of engineering design, product design, and industrial design applications; this begins with an idea or requirement and ends with a fully described product (or process or services). As shown schematically in **Figure 2** adapted from

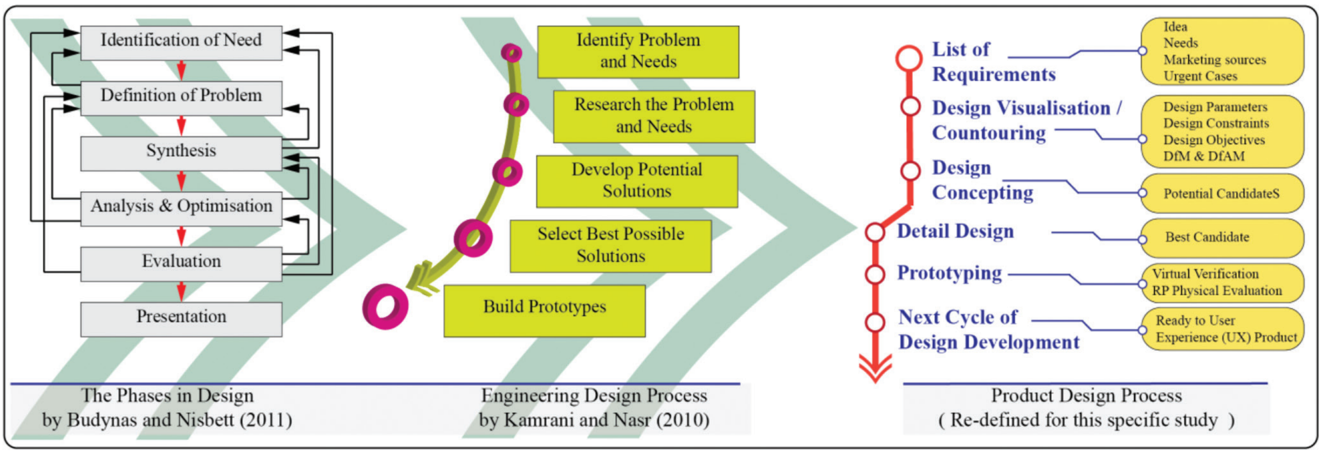

Figure 2. Product-specific redefined generic design process.

two of well-known references, Budynas and Nisbett (2011) outline the idealized, iterative, and top-down phases in design[13] and Kamrani and Nasr (2010) draws an engineering design process path which indicates a similar process for the product design[14]. In addition, the result of the design activity is often expected to be original, adding value to the existing designs by solving problems in new ways,[15] which is the emphasis in this research on the original design features of a PPE product through a product-specific, redefined generic design process.

For the first stage of the design process, essential design function objectives for an original face shield product compatible with an AM production approaches were defined as follows:

F1. Original ergonomic design, easy-to-use form with stable holding elasticity and equipped with as few components as possible
F2. Single frame design which is convenient for AM production (DfAM approach)
F3. Specific product originality feature: Comfortable, with non-classic goggle nose pad, and no ear hook structural features
F4. No additional components used in the assembly of the frame and the transparent shield (such as softening materials, and fastening clips)
F5. As little as possible additional processing time in preparation/assembly of the linkage points between the frame and the transparent visor
F6. Biodegradable thermoplastic polymer/polylactic acid (PLA) material-based production (for AM process)
F7. Less than 10 g product weight (no supports during AM production)
F8. Less than 60 min AM production time through OEM machine (at 60 m/s layering speed, in-fill rate of 100%) (production time may well be shorter with industrial AM equipment)
F9. Minimum 8 products per day from one OEM machine during AM production stage (8 working h)
F10. Through simple design changes/revisions, generated frame design should conveniently have the potential for conventional manufacturing methods (such as plastic injection molding) in addition to AM-based prototyping.

The innovation process, which can provide solutions for design needs, normally starts at the stage of conceptual design. A concept solution as the basis for the final design under pre-defined design needs and constraints can be generated from a “stand-off” between two sets of influences: The basic objective is to keep to the required size, shape, and “look” (esthetic) of the design, while improving on cost (such as material weight), lifetime, and integrity (**Figure 3**)[16]. In this regard, five design candidates, which have the potential to meet with these pre-defined objectives, were designed and proposed at the concept stage. These candidates were analyzed through technical functional analysis (TFA), and the best candidate design was selected for prototype testing. The core design contours and the concept design candidates are shown in **Figure 3**.

2.2 TFA

Redesigning/improving an existing product (different design for the same functionality) on the market can pose significant challenges even to the most experienced professional. Considering the importance of the product application as discussed within this work, the authors based their redesign/design improvement or new design decisions on the guidelines given from the value analysis (VA) methodology developed by Miles in 1948[17]. More specifically, TFA was deployed to develop the optimal technical solution that best meets the concrete expression of the customers” need, at minimum cost. The external and internal functional analysis takes into consideration the main functions that the face shield needs to perform to meet both customer expectations and manufacturer specifications[18]. TFA offers a variety of tools and instruments, but for the purpose of this study, the following main stages were deployed: Function identification and characterization; ranking and valuation of the functions; economic dimensioning; result and critical evaluation of the functions; and proposal of concepts. TFA can be

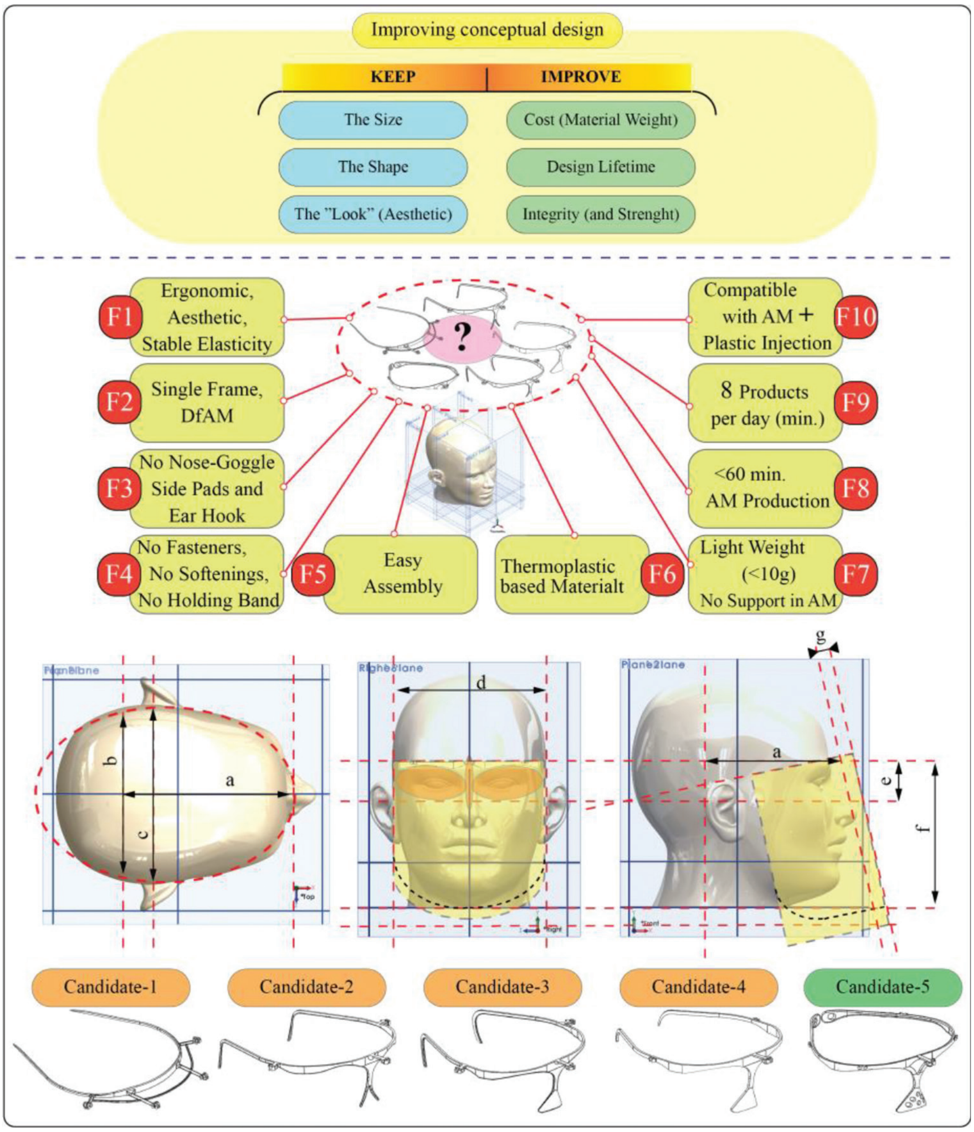

Figure 3. The concept design candidates.

conducted as an iterative method, which allows product performance improvement with each new step, thus obtaining at the end of the process an optimized concept. Function analysis system technique (FAST) diagrams[19] were used for all lifecycle stages of the face shield to accurately identify the main functions. Based on FAST and in relation to the main ten design objectives identified before for the face shield's functions were defined.

2.3 Functions importance levels

A TFA team comprised ten medical experts and industry specialists established the importance levels of the face shield by objectively grading and ranking each function in relation to the others. The valuation matrix is composed of weighting the answers of all ten team members, and their final rankings are displayed in **Table 1**.

The final valuation matrix shows that F10 and F4 are the most important functions in value, namely, that the redesigned face shield should allow an easy transition from AM processes to plastic injection molding and it should have a clean, simple one-part design and avoid fasteners, softening, and holding bands. This specific TFA stage highlights the functions of the redesign that should be focused on, from the value point of view. Function value weightings are noted

Table 1. Valuation matrix - value weighting of the functions for redesigning a face shield.

Functions	**F1**	**F2**	**F3**	**F4**	**F5**	**F6**	**F7**	**F8**	**F9**	**F10**	**Total**
F1	1	0.3	0.8	0.9	0.6	0.3	0.7	0.6	0.5	0.8	6.5
F2	0.7	1	0.7	0.9	0.8	0.5	0.5	0.9	0.9	0.8	7.7
F3	0.2	0.3	1	0.6	0.5	0.3	0.5	0.2	0.3	0.5	4.4
F4	0.1	0.1	0.4	1	0.3	0.4	0.6	0.4	0.3	0.5	4.1
F5	0.4	0.2	0.5	0.7	1	0.4	0.5	0.3	0.3	0.6	4.9
F6	0.7	0.5	0.7	0.6	0.6	1	0.6	0.8	0.8	0.8	7.1
F7	0.3	0.5	0.5	0.4	0.5	0.4	1	0.4	0.5	0.5	5
F8	0.4	0.1	0.8	0.6	0.7	0.2	0.6	1	0.5	0.9	5.8
F9	0.5	0.1	0.7	0.7	0.7	0.2	0.5	0.5	1	0.9	5.8
F10	0.2	0.2	0.5	0.5	0.4	0.2	0.5	0.1	0.1	1	3.7
Calculated weighted value $I=\left(\sum_{k=1}^{N} I_k\right)/N$	4.5	3.3	6.6	6.9	6.1	3.9	6	5.2	5.2	7.3	55
Global importance factor $\bar{C}=\left(\sum_{k=1}^{N} C_k\right)/N$	0.08181	0.06	0.12	0.12545	0.11091	0.07091	0.10909	0.09455	0.09455	0.13273	1
Global weight $W=\left(\sum_{k=1}^{N} W_k\right)/N$	8.18%	6.00%	12.00%	12.55%	11.09%	7.09%	10.91%	9.46%	9.46%	13.27%	100%

with x_{Fi}, where i = 1÷10. Based on the results obtained from the valuation matrix, the following percentage values were obtained: x_{F1} = 8.181%, x_{F2} = 6.0%, x_{F3} = 12.0%, x_{F4} = 12.545%, x_{F5} = 11.091%, x_{F6} = 7.091%, x_{F7} = 10.909%, x_{F8} = 9.455%, x_{F9} = 9.455%, x_{F10} = 13.273%.

2.4 Economic dimensioning of the functions

For the second step of TFA, economic dimensioning of the functions was conducted in accordance with thorough benchmarking in the medical device sector. Costs were estimated based on Ruffo *et al.* (2006) and Hopkinson and Dicken's (2003) models[20,21], in which they propose that the total cost (C) is the sum of the cost of the raw materials and the indirect costs, as shown in equation (1). The indirect cost of hourly activities is shown in **Table 2**.

$$C = P_{mat} \text{g} M + P_{ind} \text{g} T \quad (1)$$

where P_{mat} is the price of the raw material, measured in monetary units per kilogram;

M is the mass of the 3D printed product, measured in kilograms;

P_{ind} cost rate, measured in monetary units/hours;

T is the total production time of one part, measured in hours.

TFA is usually applied to existing products to increase their value or lower their costs, through redesign strategies. In the case of the face shield, economic dimensioning was based on the hypothesis of evaluating the average values of the main characteristics, which can include product weight, product performance, direct and indirect costs, and manufacturing time. After TFA is deployed, these average values are stated as final requirements and metrics with ideal values. Thus, market research considered different types of materials and their individual characteristics, costs, life span, recycling procedures, production volumes, and other particular features of the face shield and of the production process. The research team selected material extrusion (MEx, also referred to as Fused Deposition Modeling [FDM] or Fused Filament Fabrication) as the primary AM process to produce the redesigned face shield. PLA material was selected due to the ease of printing and an advantageous cost-performance ratio. Considering that singlepart weighs an average of 20 g (weight of reference products) and it can be manufactured in 60 min from medium grade PLA filament with a price of 170 monetary units per kilogram, the total cost of manufacturing one face shield structure is 32.48 monetary units. Based on the findings of the market analysis, the total calculated costs were assigned by a TFA specialist, as presented in **Table 3**. Each function participates in the total cost with a percentage value, noted with y_{Fi}, i = 1÷10. For the redesign of a face shield, the percentage values of the functions participation in the total costs are: y_{F1} = 9.852%, y_{F2} = 6.958%, y_{F3} = 13.793%, y_{F4} = 15.763%, y_{F5} = 10.160%, y_{F6} = 5.849%, y_{F7} = 7.758%, y_{F8} = 9.236%, y_{F9} = 8.312%, y_{F10} = 12.315%.

Table 2. The indirect cost of activities.

Activity	Cost/hour (monetary units)
Production work/time machine	7.99
Machine costs	14.78
Fixed and variable costs	5.9
Administrative costs	0.41

Economic dimensioning addresses the comparison between the functions value and cost weightings, aimed at the identification of three main function status: A function is too expensive in relation to other functions; a function is too expensive compared to its contribution in the products' value; a function is too expensive in relation to the existing manufacturing technical possibilities. To accurately analyze the relationship between function costs and value, four diagrams are plotted (**Figure 4**).

2.5 Diagrams

At this stage, the smallest squares method is used to plot the diagrams necessary for TFA. To properly deploy the smallest squares method, the following parameters need to be calculated:

- *The regression line*:

$$y = a \text{g} x \quad (2)$$

Table 3. Functions costs distribution matrix for redesigning a face shield.

No.	**Main constructing features**	**F1**	**F2**	**F3**	**F4**	**F5**	**F6**	**F7**	**F8**	**F9**	**F10**	**Feature cost***
1.	Main body frame	1	1	-	1.92	1.1	0.53	0.72	1	0.75	1.2	9.22
2.	Coronal plane positioning system	1	0.56	1.74	1	-	0.46	0.4	0.54	0.3	0.8	6.8
3.	Shield orientation and fixing system	0.2	-	-	0.6	1.6	-	0.2	-	0.2	0.5	3.3
4.	Lateral gripping features	0.5	0.2	1.74	-	0.3	0.41	0.4	0.46	0.7	0.5	-
5.	Forehead stabilizing rest	0.5	0.5	1	1.6	0.3	0.5	0.8	1	0.75	1	7.95
Total cost		3.2	2.26	4.48	5.12	3.3	1.9	2.52	3	2.7	4	32.48
Ratio		0.09852	0.06958	0.13793	0.15763	0.1016	0.05849	0.07758	0.09236	0.08312	0.12315	1
Cost of functions (%)		9.852	6.958	13.793	15.763	10.16	5.849	7.758	9.236	8.312	12.315	100

where x_i represents the functions value weighting;

y_i represents functions cost weighting;

$a = \frac{\sum x_i y_i}{\sum x_i^2}$ represents the regression parameter.

- *The estimator S* is determined with the smallest squares method:

$$S = \sum\left(y_i - agx_i\right)^2 \to min \tag{3}$$

- The *dispersion S'* must be as close as possible to zero value to validate the solution.

$$S' = \sum\left(2gagx_i^2 - 2gx_iy_i\right) \tag{4}$$

- The *angle* α of the regression line:

$$\alpha = arctg\left(a\right)\frac{180}{\pi} \tag{5}$$

All computational elements used in the smallest squares method are presented in **Table 4**.

After processing, the information in **Table 4**, the following values were obtained: a = 1.0021, α = 45.05998, S = 31.886, and S' = 0.

In **Figure 4**, Diagram A shows the functions t for the redesign process of a face shield. The diagram was constructed using the rankings of the functions by their value, as obtained in the valuation matrix. Diagram B represents the ranking of the functions by their functional cost, as defined in the cost distribution matrix. Both diagrams are used by the TFA team to compare the functions costs in relation to their contribution to the value of the product. It is important for the redesign process to identify the most expensive functions and those with the highest weighting in the total cost of the product. This way, secondary functions that are very expensive in relation to the objective functions, or even more expensive than these, can be identified for further improvement. The weighting of effort for a certain function must match its weighting in the total value of the product. Further, to validate these assumptions,

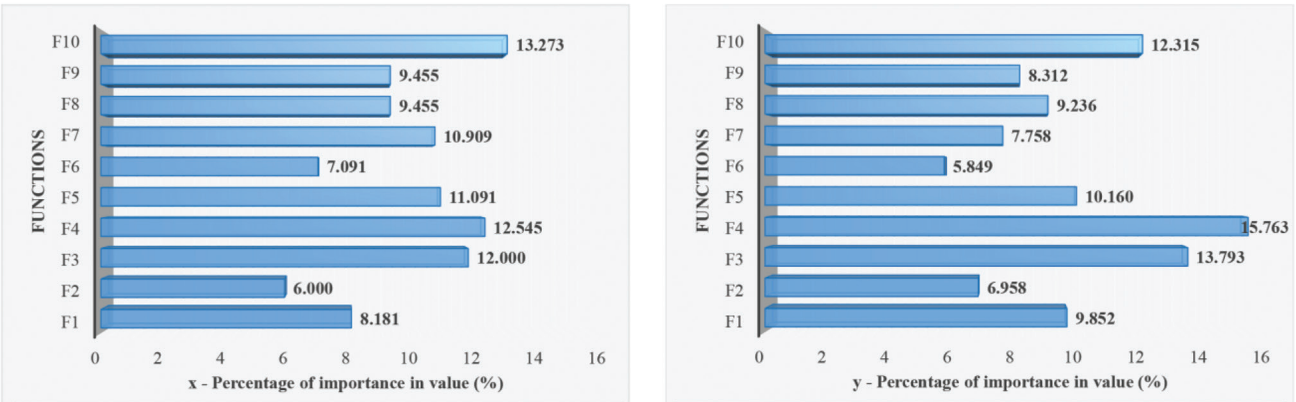

Diagram-A: Functions value weighting for a face shield redesign

Diagram-B: Functions costs weighting for a face shield redesign

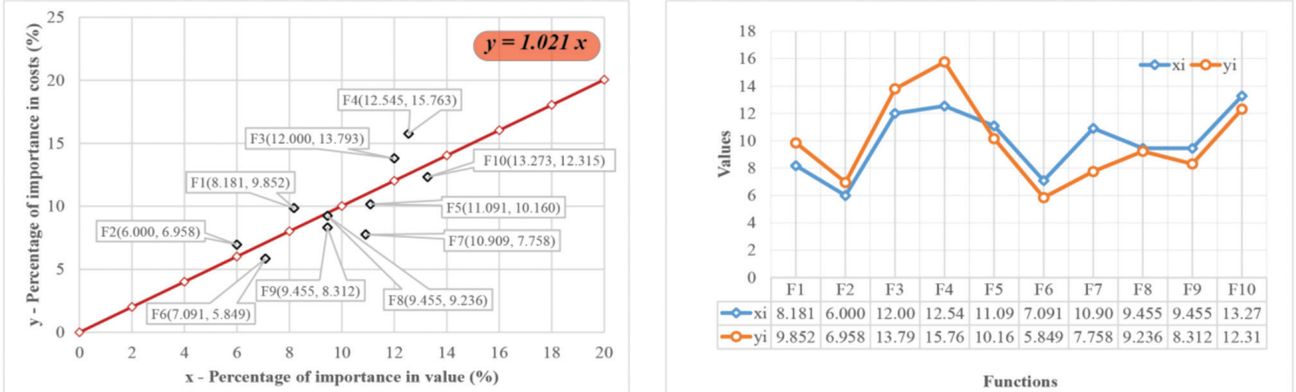

Diagram-C: Value and cost weightings of the functions

Diagram-D: Comparison of value weighting and functional costs

Figure 4. The relationship between functions cost and value.

regression analysis was used, and the regression line was plotted for further analysis.

The real situation is represented in Diagram C by plotting the regression line $y = 1.0021 * x$, with a slope angle of $\alpha = 45.05998$. The smallest squares method presumes that the estimator S should tend to a minimum value and the S' dispersion is zero. To diminish the *S* value, the points represented by the function weightings must be aligned as perfectly as possible along the regression line. The objective of TFA is to redesign and diminish costs or increase the value for the functions corresponding to the points above the regression line. By changing those specific points and re-plotting the diagram, the slope of the regression line modifies, and a new situation of TFA can be evaluated. As stated before, the process is iterative, and it is undertaken until the requirements of both customers and manufacturers are met.

The critical evaluation of the functions presented in Diagram D presents the most expensive functions in relation to their value. Functions F4, F1, and F2 have disproportionate costs in relation to their value contribution. Function F4 was also identified in the first TFA stage as being the second most important in value, and thus, the designers will focus on the face shield features that address this specific function.

Based on the above diagrams, the TFA team concluded that functions F1, F2, F3, and F4 need either a lower cost or an increase in value. This implies redesigning and providing new constructive solutions for ensuring the structure and the ergonomics of the frame. The redesign process will target ergonomics, single frame, and AM compatible face concepts. TFA was further used to define the final product requirements, which must be followed while designing the face shield.

Table 4. Computational elements for a face shield.

No.	Calculated elements	Functions										Total value
		F1	F2	F3	F4	F5	F6	F7	F8	F9	F10	
1.	xi	8.181	6	12	12.545	11.091	7.091	10.909	9.455	9.455	13.273	100
2.	yi	9.852	6.958	13.793	15.763	10.16	5.849	7.758	9.236	8.312	12.315	99.996
3.	xi^2	66.929	36	144	157.377	123.01	50.282	119.006	89.397	89.397	176.173	1051.571
4.	xi * yi	80.599	41.748	165.516	197.747	112.685	41.475	84.632	87.326	78.59	163.457	1053.775
6.	S	2.735	0.894	3.125	10.187	0.911	1.58	10.073	0.057	1.352	0.972	31.886
7.	S’	-27.06	-11.345	-42.428	-80.08	21.167	17.825	69.247	4.516	21.989	26.17	0

A specification is constructed from a metric and a value[18], which correspond to a specific function of the product. A function can have one or more metrics and values. The final list of specification objectives in relation to the TFA results is given in **Table 5**.

The analysis of alternative designs was undertaken using TFA instruments to select the best candidate for further investigation. The selection criteria and their weights were set by the TFA team. As shown in **Table 6**, Candidate 5 obtained the best total score, best ensuring the functional characteristics required.

2.6 Prototyping

Once the first functional prototype of a detail design is exhibited, prototype testing can be performed to validate the proposed design solution. If the design solution cannot meet the required design objectives, the product design process is repeated until a satisfactory desired solution is reached. At this stage, it is possible to undertake both virtual prototype and physical prototype-based design verifications.

2.7 Virtual prototyping: Finite element analysis (FEA) verification

After approval of the design details of Candidate 5, a 3D parametric solid model was constructed in the virtual environment, and then virtual prototype testing for the product’s elastic deformation ability was realized. The findings from the tests were evaluated in the virtual environment for potential design changes. In this study, the virtual prototype was tested to determine head holding force and deformation behavior. To evaluate the deformation behavior of the prototype, the finite element method (FEM)-based structural deformation analysis (FEA) was carried out. The structural module of the ANSYS Workbench FEM-based commercial code was employed for the FEA. In the FEA scenarios, head wearing and head holding positions were simulated. The FEA was set up using assumptions of a linear static loading and homogeneous, linear isotropic material model. At the meshing operation, a curvature meshing strategy was utilized and the

Table 5. Final product specifications for a face mask.

Functions	Requirements	Metric	Units	Limit values	Ideal values
F1	Elasticity	Tensile strength at yield	MPa	>35.9	34
	Ease of usage	Ergonomic design	Yes/ No	Yes	Yes
F2	Respect DfAM principles	AM technologies	-	MEX, SLA, SLS	MEX
F3	Comfortable	Wear period	hours	>6	8
	Maintains position	Ensures user protection	Yes/No	Yes	Yes
	Prevents condensation	Ensures ventilation features	Yes/No	Yes	Yes
F4	Single frame design	Number of components	No.	3	2
	Allow reuse	Sterilization procedure	-	Autoclave, UV, disinfectant liquids, ozone	Disinfectant liquids, ozone
F5	Ease of maintenance	Maintenance manual	Yes/No	Yes	Yes
	Ease of assembly	Assembly/disassembly time	minutes	0.5	0.5
F6	Biodegradable filaments	Thermoplastics	-	PLA	PLA
	Environmental friendly	Recyclable	Yes/No	Yes	Yes
F7	Light weight	Total weight	g	<20	10
F8	AM produced	Total production time (3D printing+post processing+assembly)	minutes	<60	45
F9	AM produced	Production rate	products/day/ machine	<10	8
F10	AM/plastic injection	Modular/parametric design	Yes/No	Yes/No	Yes

skewness metric, which is one of the primary mesh quality measures in a FEA, was checked. The shape and asymmetry of distribution can be measured by its skewness, which can be considered as the mesh quality verification of a FEM[22]. The skewness value of zero indicates an equilateral cell (best) and a value of one indicates a completely degenerate cell (worst)[23]. At the final meshing operation, FEM was created with minimum element size of 0.4 mm, and the average skewness value of 0.227 was obtained. This value indicated that the FE model used in the loading scenarios has an excellent mesh quality. Details related to the FEA set up, and simulation outputs are given in **Figure 5**.

The results of the FEA scenarios revealed that there was no plastic deformation (permanent deformation) during the maximum opening condition of wearing on the head and at the head holding positions. Maximum equivalent (Von-Mises) stress during the maximum opening condition and at the head holding position were 96.498 MPa and 58.929 MPa, respectively, which are lower than the material tensile stress at yield (which is 110 MPa). These numerical and visual results obtained from the simulation indicated that the stress distribution on the product is uniform and the elastic deformation ability of the product is satisfactorily within the design limits. For the second scenario, the head holding force after wearing was calculated as 2.744 N against each side displacements. This finding was also interpreted as the head holding capability of the product and was in a satisfactory comfort range.

2.8 Physical prototyping

As a dimensionally accurate physical part, the AM prototype is able to give the designer a sense of the appropriateness of form and fit before continuing with production[24]. The fastest technique to produce a physical prototype, most especially for a complex geometric structure, is utilizing AM technology. In short, models were created by adding successive layers of material together. To evaluate

Table 6. Analysis of the alternative designs for a face shield.

No.	Analysis criteria	Weight (%)	Candidate 1 Grade*	Candidate 1 Weighted grade	Candidate 2 Grade*	Candidate 2 Weighted grade	Candidate 3 Grade*	Candidate 3 Weighted grade	Candidate 4 Grade*	Candidate 4 Weighted grade	Candidate 5 Grade*	Candidate 5 Weighted grade
1	Cost	15	2	0.3	3	0.45	3	0.45	5	0.75	5	0.75
2	Functional characteristics	20	2	0.4	3	0.6	5	1	5	1	5	1
3	Life span	10	4	0.4	4	0.4	4	0.4	4	0.4	4	0.4
4	Re-usage	5	4	0.2	4	0.2	4	0.2	3	0.15	3	0.15
5	Complexity	10	2	0.2	3	0.3	4	0.4	4	0.4	4	0.4
6	DfAM characteristics	20	2	0.4	3	0.6	3	0.6	3	0.6	4	0.8
7	Ergonomics	5	3	0.15	4	0.2	4	0.2	4	0.2	4	0.2
8	Environmental effect	5	4	0.2	4	0.2	4	0.2	4	0.2	4	0.2
Total score				2.25		2.95		3.45		3.7		3.9
Rank				2		3		4		5		1
Selected model				-		-		-		-		√

*Grading scale: 1 – least important; 5 – most important

the physical prototype of the face shield, an AM approach was utilized in this study; however, the critical point here is that DfAM is a challenge for most designers as the convenient design methods that consider the unique capabilities of AM technologies are needed. Depending on the capabilities of the AM technology being utilized, DfAM can be described as a type of design method whereby functional performance and/or other key product lifecycle considerations such as manufacturability, reliability, and cost can be optimized[25]. In this regard, a useful worksheet/application guide designed for novices to AM was published by Booth *et al.* (2017)[26]. In using the DfAM method, some important approaches are in macroscale, mesoscale or microscale design studies: Structural optimization approach (i.e., size, shape, and topological) and manufacturability related to AM technology type, AM machine, material, build orientation, surface quality needs, production time, etc.

The production of the prototype was realized using an OEM - FDM machine with a production volume capacity of 200 mm × 220 mm × 220 mm, nozzle diameter of 0.4 mm at 210°C nozzle temperature. The production material was PLA thermoplastic with a filament diameter of 1.75 mm. Solid modeling and AM setup procedures for the face shield product handled in this study were conducted under consideration of these key approaches related to the DfAM methodology. To obtain time efficiency (short production), optimally designed (geometry and topology), and a functionally readytouse prototype with satisfying surface quality, production trials were made on STL conversion quality (geometrical parameters) and production layer heights during AM operations. The trials showed that despite the rearrangements, more precise (use of smaller triangles) STL conversion parameters and shorter production layer heights gave a smoother surface quality, the fine level of STL conversion (deviation tolerance: 0.099 mm, angle tolerance: 10°, and number of triangles: 16,736) and the layer height of 0.25 provided satisfactory results in the use of the physical prototype when considering the time efficiency approach (approximately 35 min

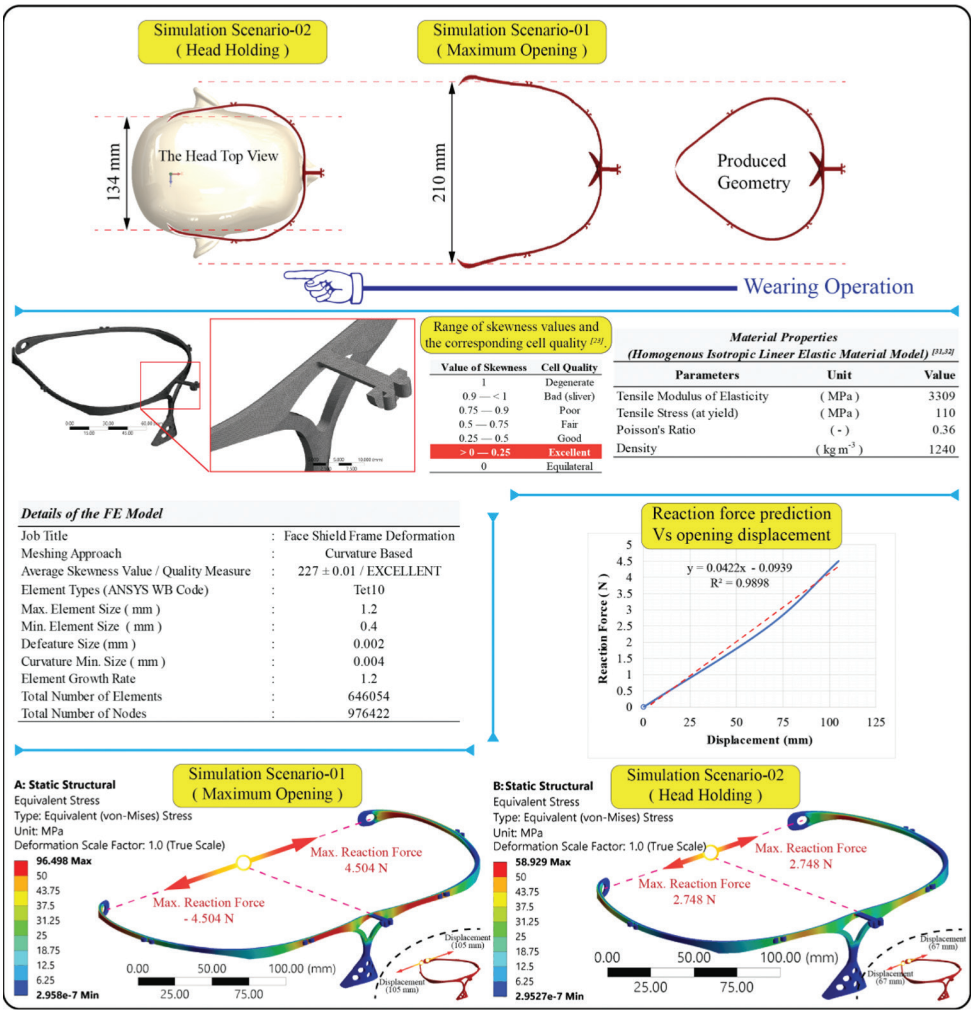

Range of skewness values and the corresponding cell quality [23].

Value of Skewness	Cell Quality
1	Degenerate
0.9 — < 1	Bad (sliver)
0.75 — 0.9	Poor
0.5 — 0.75	Fair
0.25 — 0.5	Good
> 0 — 0.25	Excellent
0	Equilateral

Material Properties
(Homogenous Isotropic Lineer Elastic Material Model) [31,32]

Parameters	Unit	Value
Tensile Modulus of Elasticity	(MPa)	3309
Tensile Stress (at yield)	(MPa)	110
Poisson's Ratio	(-)	0.36
Density	(kg m^{-3})	1240

Details of the FE Model

Job Title : Face Shield Frame Deformation
Meshing Approach : Curvature Based
Average Skewness Value / Quality Measure : 227 ± 0.01 / EXCELLENT
Element Types (ANSYS WB Code) : Tet10
Max. Element Size (mm) : 1.2
Min. Element Size (mm) : 0.4
Defeature Size (mm) : 0.002
Curvature Min. Size (mm) : 0.004
Element Growth Rate : 1.2
Total Number of Elements : 646054
Total Number of Nodes : 976422

Figure 5. Finite element analysis verification virtual prototype.

production time per unit). Details related to the AM procedures and prototypes produced are given in **Figure 6**.

2.9 Physical prototype trials

The model of Candidate 5 was highlighted through the TFA and the prototyping stage was successfully realized. In addition, to obtain first-hand user opinions about the prototype of Candidate 5, a survey was conducted. The survey was completed by health service workers (medical doctors, nurses, and the other health service workers) at Antalya Training and Research Hospital, Antalya, Turkey in April 2020. Ten questions related to the face shield product evaluation were answered by 15 HWs who used the product in routine daily hospital activities. The survey results were interpreted as having a high satisfaction level since the answers given to question no. 9 related to satisfaction of using this product were very positive overall, in addition to the positive responses to the other questions (40% of those completing the survey found the product to be "excellent," 40% found the product to be "good," 17% found the product "average," 7% found the product to be "poor," and no-one found the product "insufficient"). Thus, for the final evaluation, it was decided that Candidate 5 as the final product design should be approved and the design evaluation undertaken in this research was finalized. The participation details, survey questions, variation of the answers given to these questions, and the pictures obtained from the trials are provided in **Figure 7**.

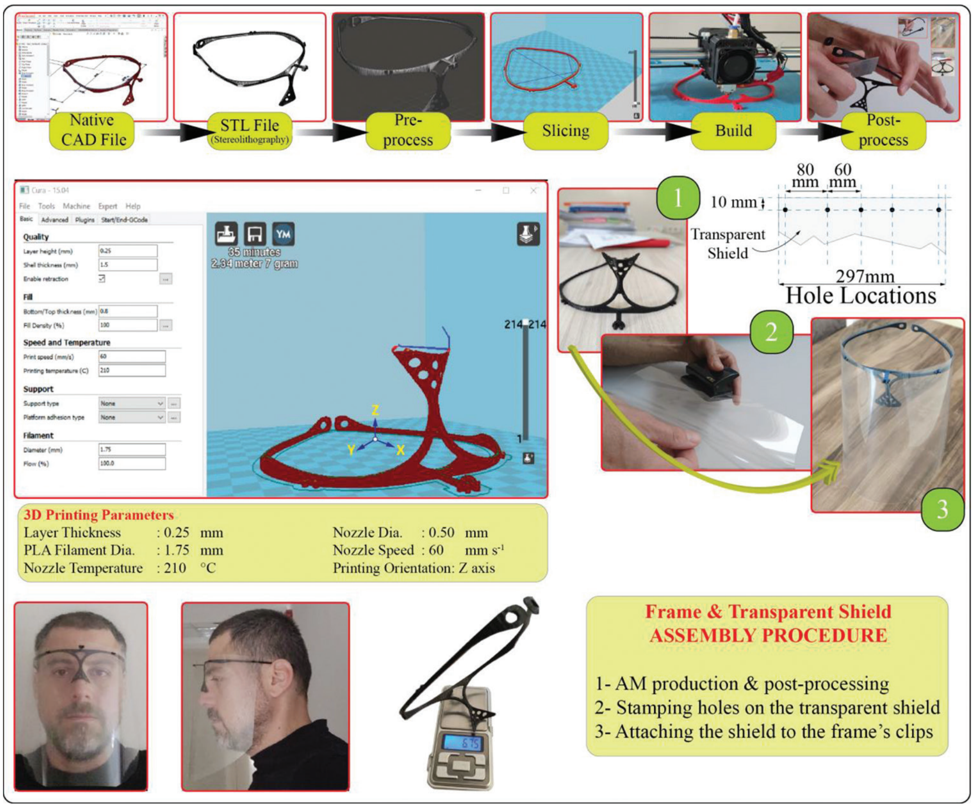

Quality
Layer height (mm): 0.25
Shell thickness (mm): 1.5
Enable retraction: ☑

Fill
Bottom/Top thickness (mm): 0.8
Fill Density (%): 100

Speed and Temperature
Print speed (mm/s): 60
Printing temperature (C): 210

Support
Support type: None
Platform adhesion type: None

Filament
Diameter (mm): 1.75
Flow (%): 100.0

3D Printing Parameters
Layer Thickness : 0.25 mm
PLA Filament Dia. : 1.75 mm
Nozzle Temperature : 210 °C
Nozzle Dia. : 0.50 mm
Nozzle Speed : 60 mm s^{-1}
Printing Orientation: Z axis

Frame & Transparent Shield ASSEMBLY PROCEDURE
1- AM production & post-processing
2- Stamping holes on the transparent shield
3- Attaching the shield to the frame's clips

Figure 6. Fabrication of prototype product for physical evaluation.

3 Results and discussion

After initial sketching and concept evaluation, TFA results suggested an optimum design: Candidate 5. Structural design verification was approved in the virtual environment and a physical prototype was tested by the experts and a product satisfaction survey was completed by HWs during real, *in situ* hospital activities. The product satisfaction survey revealed positive responses related to product design features and usability (**Figure 7**). The frame design was rated with 67% "excellent," 20% "good," and 13% "average" satisfaction. No user indicated an insufficiency rate for any of the survey questions. Under these considerations, the product design work detailed in this paper was completed, and the detailed design for Candidate 5 was approved (**Figure 8**). The single-frame design used <10 g FDM filament and took approximately 35 min to build. AM production time and only two-hole stamping operations are required to assemble the transparent shield to the frame. These product features can be interpreted as the originality and advantages achieved for this product against competitors as detailed in the myriad of social media.

During the product design process, advanced computer-aided design, engineering, and DfAM methods were successfully applied. The objectives given in the design process section were achieved. Critically, light weight and relatively shorter AM production times were accomplished. When considering the existing products being showcased in social media, the biggest disadvantages were perceived to be relatively longer AM production times per unit. Many approaches and concepts for face shield products produced using AM technologies have been proposed during the COVID-19 pandemic to support the health services. Although all of them provide some level of functionality, many of their design features lack adherence to professional design principles, optimum structural topology, ergonomics, and the application of DfAM approaches. A common goal in an industrial product is to improve product quality, shorten the product development cycle,

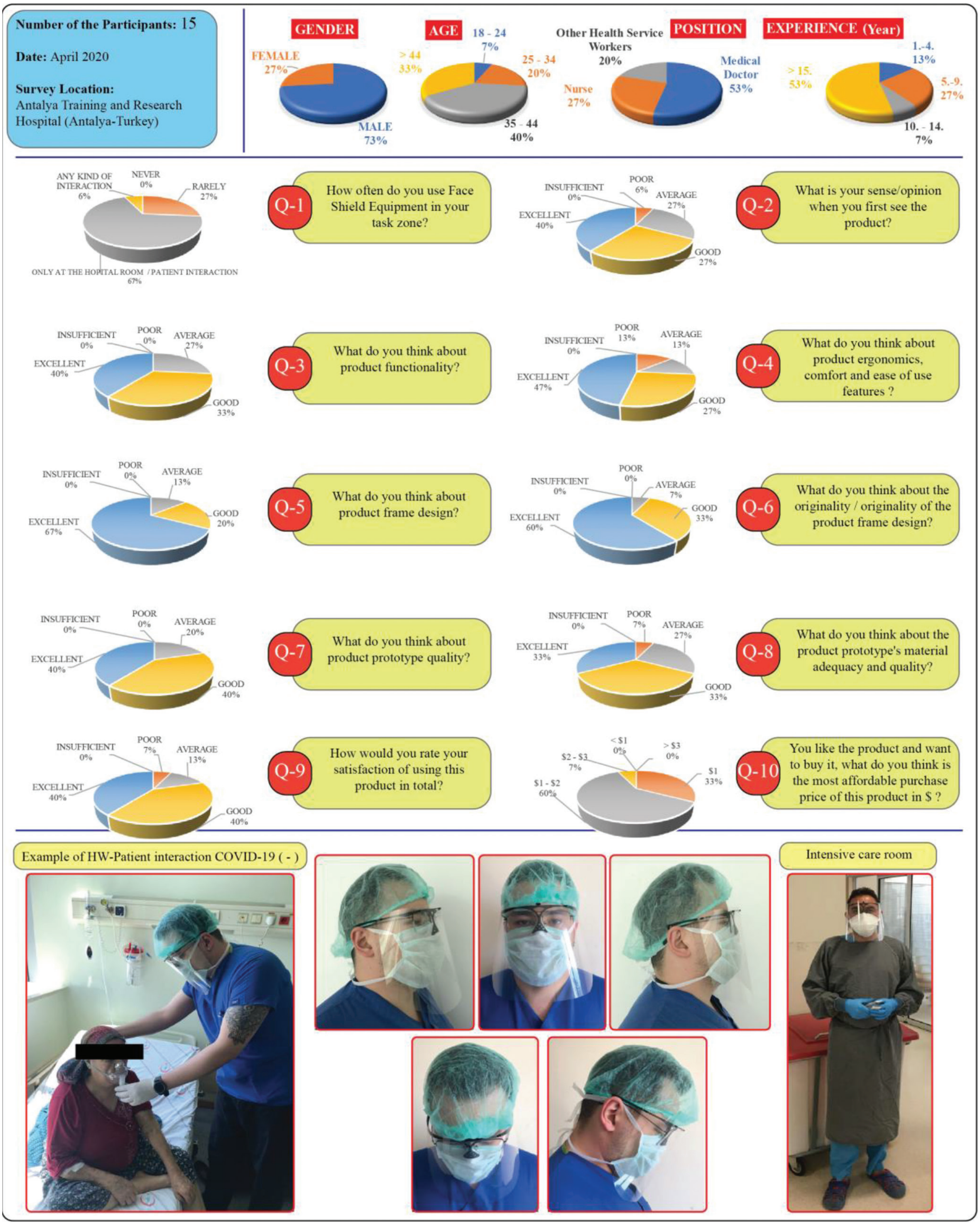

Figure 7. Product evaluation survey and user trials.

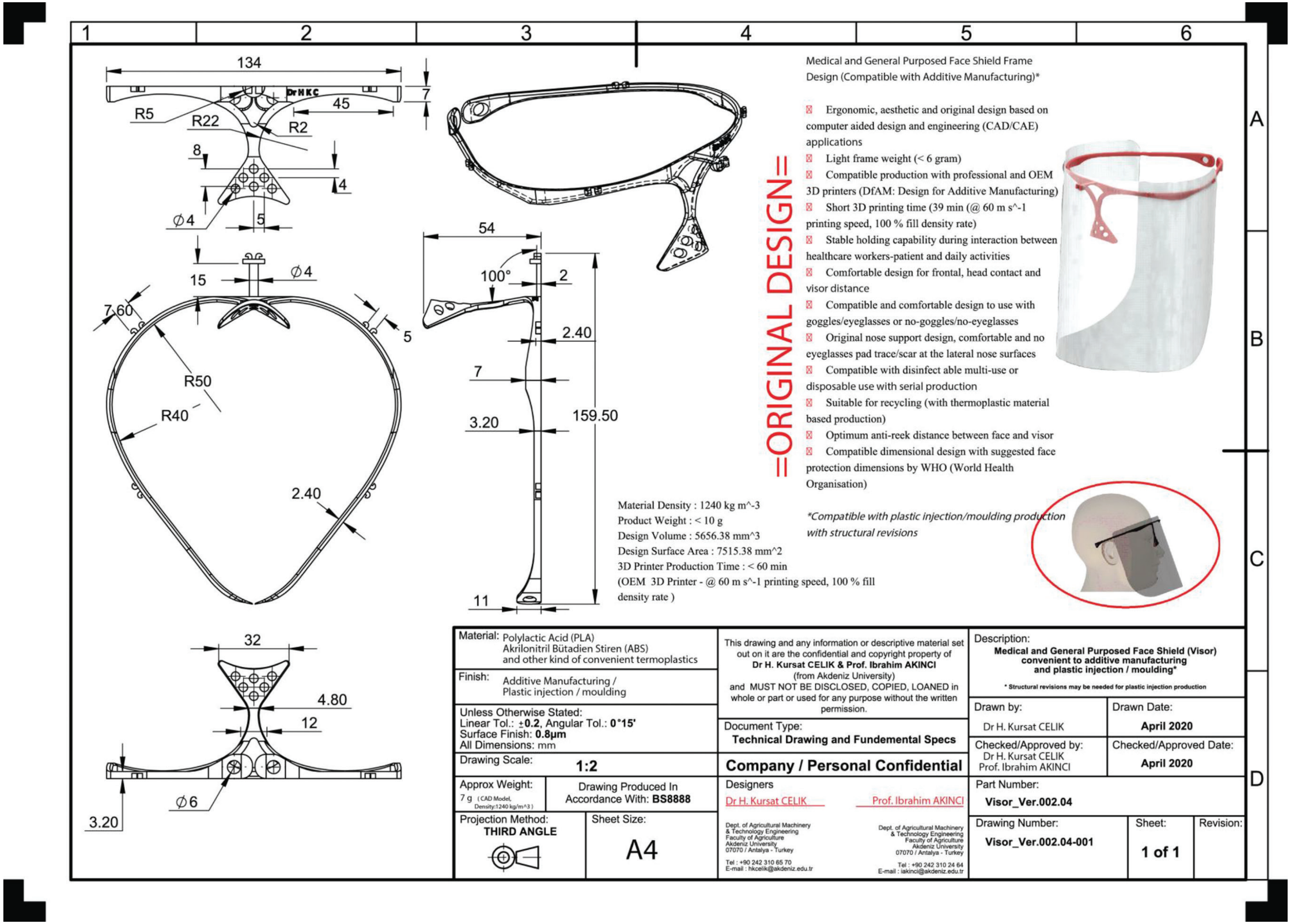

Medical and General Purposed Face Shield Frame Design (Compatible with Additive Manufacturing)*

- ☒ Ergonomic, aesthetic and original design based on computer aided design and engineering (CAD/CAE) applications
- ☒ Light frame weight (< 6 gram)
- ☒ Compatible production with professional and OEM 3D printers (DfAM: Design for Additive Manufacturing)
- ☒ Short 3D printing time (39 min (@ 60 m s^-1 printing speed, 100 % fill density rate)
- ☒ Stable holding capability during interaction between healthcare workers-patient and daily activities
- ☒ Comfortable design for frontal, head contact and visor distance
- ☒ Compatible and comfortable design to use with goggles/eyeglasses or no-goggles/no-eyeglasses
- ☒ Original nose support design, comfortable and no eyeglasses pad trace/scar at the lateral nose surfaces
- ☒ Compatible with disinfect able multi-use or disposable use with serial production
- ☒ Suitable for recycling (with thermoplastic material based production)
- ☒ Optimum anti-reek distance between face and visor
- ☒ Compatible dimensional design with suggested face protection dimensions by WHO (World Health Organisation)

**Compatible with plastic injection/moulding production with structural revisions*

Material Density : 1240 kg m^-3
Product Weight : < 10 g
Design Volume : 5656.38 mm^3
Design Surface Area : 7515.38 mm^2
3D Printer Production Time : < 60 min
(OEM 3D Printer - @ 60 m s^-1 printing speed, 100 % fill density rate)

Material: Polylactic Acid (PLA)
Akrilonitril Bütadien Stiren (ABS)
and other kind of convenient termoplastics

Finish: Additive Manufacturing /
Plastic injection / moulding

Unless Otherwise Stated:
Linear Tol.: ±**0.2**, Angular Tol.: **0°15'**
Surface Finish: **0.8μm**
All Dimensions: mm

Drawing Scale: **1:2**

Approx Weight: 7 g (CAD Model, Density:1240 kg/m^3)

Drawing Produced In Accordance With: **BS8888**

Projection Method: **THIRD ANGLE**

Sheet Size: A4

This drawing and any information or descriptive material set out on it are the confidential and copyright property of **Dr H. Kursat CELIK & Prof. Ibrahim AKINCI** (from Akdeniz University) and MUST NOT BE DISCLOSED, COPIED, LOANED in whole or part or used for any purpose without the written permission.

Document Type: **Technical Drawing and Fundemental Specs**

Company / Personal Confidential

Designers

Dr H. Kursat CELIK
Dept. of Agricultural Machinery
& Technology Engineering
Faculty of Agriculture
Akdeniz University
07070 / Antalya - Turkey
Tel : +90 242 310 65 70
E-mail : hkcelik@akdeniz.edu.tr

Prof. Ibrahim AKINCI
Dept. of Agricultural Machinery
& Technology Engineering
Faculty of Agriculture
Akdeniz University
07070 / Antalya - Turkey
Tel : +90 242 310 24 64
E-mail : iakinci@akdeniz.edu.tr

Description: **Medical and General Purposed Face Shield (Visor) convenient to additive manufacturing and plastic injection / moulding***

* Structural revisions may be needed for plastic injection production

Drawn by: Dr H. Kursat CELIK

Drawn Date: **April 2020**

Checked/Approved by: Dr H. Kursat CELIK, Prof. Ibrahim AKINCI

Checked/Approved Date: **April 2020**

Part Number: **Visor_Ver.002.04**

Drawing Number: **Visor_Ver.002.04-001**

Sheet: **1 of 1**

Revision:

Figure 8. Technical drawing of Candidate 5.

and reduce product cost/time. As such, the product detailed in this study has satisfactorily met these conditions. Realistically, industry nowadays will not survive in a globally competitive marketplace unless they introduce new products of better quality, at a lower cost, and with shorter lead times[27].

AM brings unique considerations for engineers in the design process for medical PPE. An important issue in the use of PPE for medical purposes is biological consideration (including cleaning, sterilization, and biocompatibility). In consideration of unregulated PPE production during this COVID-19 pandemic, recently, a discussion was reported by MIT news on the limitations and dangers of using AM/3D printing for PPE fabrication[28]. The text reports that one of the biggest risks with AM-fabricated products for COVID-19 is the false sense of hope as quickly produced PPE inevitably fails to meet any of the needs previously discussed. This is crucial when considering critical PPE products such as filtration masks, which may need expert design consideration and medical/health service authority approvals, may do more harm than good. The additional risk from unregulated PPE also exists as many FDM filaments retain ambient moisture, which could pose a paradoxically increased risk for virus transmission during use or reuse[29]. Similar risks and concerns were also reviewed and reported by Clifton *et al*. (2020)[30]. The authors reported that during this pandemic, the open distribution and propagation of PPE prototypes happened before validation and hypothesis formulation (in the context of both engineering and biological considerations) that emphasized on the fundamentally important factors for prototype testing, such as number needed to treat and reduce harm for patients, and the approval of health service authorities had not been considered. Hence, it was possible to highlight the need for universal standardization for PPE, such as medical face shield products. True innovation can prevail over brief notoriety and avoid unintentional harm from good intentions led by poor science[30]. This study provided an original design which was developed based on scientific principles of advanced engineering design and AM methods, with the product being convenient for single-use (means of economic base) and sterilization (with limited cycles) in case of reuse in a risk-based environment such as COVID-19 (+) with close HW-patient interaction.

4 Conclusion

In this study, a competitively lighter, relatively more ergonomic, and easy-to-use medical face shield design which can be assembled without extra components (such as elastic bands, softening materials, and clips) and has a relatively shorter AM based production time were successfully realized. The motivation for this study was to provide an original AM compatible PPE product (primary target), which was designed in accordance with professional product design principles to support social solidarity against COVID-19 pandemic and potential future needs. The product design feature is also compatible with plastic injection molding-based serial production (secondary target). The survey carried out in a health service environment revealed that the product can be used for medical purposes with a good level of user/HW satisfaction. Taken together, this design study satisfactorily responded to the design requirements for a face shield PPE. Although the product provides safety features (dimensional features) described by the WHO, health safety risks should be carefully considered while using this product in health service facilities and public areas. This research provides a useful product design case study for informing further research on design, prototyping, and manufacture of simple medical equipment such as face shields for battling coronavirus-like viral pandemics by employing advanced engineering design, simulation, and AM applications.

Acknowledgments

This research study was supported financially by The Scientific Research Projects Coordination Unit of Akdeniz University, Antalya, Turkey. In addition, the authors wish to acknowledge the Department of Agricultural Machinery and Technology Engineering at Akdeniz University, Antalya, Turkey, for the contribution to the product design and prototyping stages, Department of Manufacturing at University Politehnica of Bucharest, Bucharest, Romania, for setting up the product function analysis algorithm, Antalya Training and Research Hospital, Antalya, Turkey, for medical product evaluations and Lancaster Product Development Unit (LPDU) at Lancaster University, Lancaster, United Kingdom, for technical evaluation processes employed in this research paper. The frame features and transparent shield assembly process of the face shield product detailed in this study was originally designed by Dr. H. Kursat CELIK (70%) and Prof. İbrahim AKINCI (30%). The product was submitted for consideration to the Turkish Patent and Trademark Office for Design Registration/Copyright Protection (Application No: 2020/03321; Application Date: May 15, 2020). Authors declare that they have no known competing financial interests or personal relationships that could have appeared to influence the work reported in this paper.

Conflict of interest

The authors declare no conflict of interest.

References

1. World Health Organisation, 2020, Novel Coronavirus (2019-nCoV): Situation Report-1 (21 January 2020). Available from: https://www.who.int/docs/default-source/coronaviruse/situation-reports/20200121-sitrep-1-2019-ncov.pdf?sfvrsn=20a99c10_4. [Last accessed on 2020 Apr 14].
2. World Health Organisation, 2020, Novel Coronavirus (2019-nCoV): Situation Report-22 (11 February 2020). Available from: https://www.who.int/docs/default-source/coronaviruse/situation-reports/20200211-sitrep-22-ncov.pdf?sfvrsn=fb6d49b1_2. [Last accessed on 2020 Apr 14].
3. World Health Organisation, 2020, Novel Coronavirus (Covid-19): Situation Report-51 (11 March 2020). Available from: https://www.who.int/docs/default-source/coronaviruse/situation-reports/20200311-sitrep-51-covid-19.pdf?sfvrsn=1ba62e57_10. [Last accessed on 2020 Apr 14].
4. Joseph B, Joseph M, 2016, The Health of the Healthcare Workers. *Indian J Occup Environ Med*, 20:71–2.
5. Talikwa L, 2002, Facing up to Wearing Facial Protection Equipment. *Manag Inf Control*, 2:38.
6. European Centre for Disease Prevention and Control, 2020, Guidance for Wearing and Removing Personal Protective Equipment in Healthcare Settings for the Care of Patients with Suspected or Confirmed COVID-19. Available from: https://www.ecdc.europa.eu/sites/default/files/documents/COVID-19-guidance-wearing-and-removing-personal-protective-equipment-healthcare-settings-updated.pdf. [Last accessed on 2020 Apr 15]. DOI: 10.12996/gmj.2020.74.
7. National Health Service-England, 2020, COVID-19: Visual Guide to Safe PPE. https://www.assets.publishing.service.gov.uk/government/uploads/system/uploads/attachment_data/file/878056/PHE_COVID-19_visual_guide_poster_PPE.pdf. [Last accessed on 2020 Apr 15].
8. TMA, 2020, Turkish Medical Association: Use of Personal Protective Equipment (PPE) with Suspected or Confirmed COVID-19. https://www.ttb.org.tr/kollar/COVID19/index.php. [Last accessed on 2020 Apr 15].
9. World Health Organisation, 2020, Rational Use of Personal Protective Equipment for Coronavirus Disease 2019 (COVID-19). (WHO Reference Number: WHO/2019-nCov/IPC PPE_use/2020.1). https://www.apps.who.int/iris/bitstream/handle/10665/331215/WHO-2019-nCov-IPCPPE_use-2020.1-eng.pdf. [Last accessed on 2020 Apr 15]. DOI: 10.5222/bmj.2020.22931
10. Roberge RJ, 2016, Face Shields for Infection Control: A Review. *J Occup Environ Hyg*, 13(4):23542.
11. World Health Organisation, 2020, Shortage of Personal Protective Equipment Endangering Health Workers Worldwide. Available from: https://www.who.int/news-room/detail/03-03-2020-shortage-of-personal-protective-equipment-endangering-health-workers-worldwide. [Last accessed on 2020 Apr 14]. DOI: 10.26616/nioshpub2009106
12. Health Protection Scotland, 2020, Standard Infection Control Precautions Literature Review: Personal Protective Equipment (PPE) Eye/Face Protection. Available from: https://www.hpspubsrepo.blob.core.windows.net/hpswebsite/nss/2605/documents/1_sicp-lr-eyewearv2.1.pdf. [Last accessed on 2020 Apr 22].
13. Budynas RG, Nisbett JK, 2011, Shigley's Mechanical Engineering Design. 9th ed. McGraw-Hill, New York, USA.
14. Kamrani AK, Nasr EA, 2010, Engineering Design and Rapid Prototyping. Springer Science and Business Media, Berlin, Germany. pp. 442–6.
15. Yilmaz S, Seifert CM, 2011, Creativity through Design Heuristics: A Case Study of Expert Product Design. *Des Stud*, 32:384–415. DOI: 10.1016/j.destud.2011.01.003
16. Matthews C, 1998, Case Studies in Engineering Design. Elsevier, Arnold, London, UK, pp. 272–4.

17. Miles LD, 1989. Techniques of Value Analysis and Engineering. 3rd ed. Lawrence D. Miles Value Foundation, USA.
18. Eppinger S, Ulrich K, 2012, Product Design and Development. 5th ed. McGraw Hill Publishing Company Ltd., New York.
19. Lupeanu ME, Rennie AE, Neagu C, 2011, Additive Manufacturing Technologies and Functional Analysis Used in Product Development Optimization. 12th Rapid Design, Prototyping and Manufacturing Conference, Lancaster, UK. CRDM Ltd., High Wycombe, pp. 105–12.
20. Ruffo M, Tuck C, Hague R, 2006, Cost Estimation for Rapid Manufacturing Laser Sintering Production for Low to Medium Volumes. *Proc Inst Mech Eng B J Eng Manuf*, 220(9):141727. DOI: 10.1243/09544054jem517
21. Hopkinson N, Dickens P, 2003, Analysis of Rapid Manufacturing Using Layer Manufacturing Processes for Production. *Proc Inst Mech Eng C J Mech Eng Sci*, 217(1):31–9.
22. Brys G, Hubert M, Struyf A, 2004, A Robust Measure of Skewness. *J Comput Graph Stat*, 13(4):996–1017.
23. ANSYS Documentation, 2020, Meshing User's Guide: Skewness. Release 2020 R1, Ansys Inc., USA.
24. Chua CK, Teh SH, Gay RK, 1999. Rapid Prototyping Versus Virtual Prototyping in Product Design and Manufacturing. *Int J Adv Manuf Technol*, 15(8):597–603. DOI: 10.1007/s001700050107.
25. Tang Y, Zhao YF, 2016, A Survey of the Design Methods for Additive Manufacturing to Improve Functional Performance. *Rapid Prototyp J*, 22(3):569–90.
26. Booth JW, Alperovich J, Chawla P, *et al*., 2017, The Design for Additive Manufacturing Worksheet. *J Mech Des*, 139(10):100904.
27. Cang KH, 2014, Product Design Modeling using CAD/CAE the Computer Aided Engineering Design Series. Academic Press, Elsevier Inc., USA. pp. 438–9.
28. Gallagher MB, 2020, 3 Questions: The Risks of Using 3D Printing to Make Personal Protective Equipment. MIT News. Available from: http://www.news.mit.edu/2020/3q-risks-using-3d-printing-make-personal-protective-equipment-0326. [Last accessed on 2020 Apr 29]. DOI: 10.17504/protocols.io.bd77i9rn
29. Jurischka C, Dinter F, Efimova A, *et al.*, 2020, An Explorative Study of Polymers for 3D Printing of Bioanalytical Test Systems. *Clin Hemorheol Microcirc*, 74:1–28.
30. Clifton W, Damon A, Martin AK, 2020, Considerations and Cautions for Three-Dimensional-Printed Personal Protective Equipment in the COVID-19 Crisis. *3D Print Addit Manuf*, 1:1–3. DOI: 10.1089/3dp.2020.0101.
31. Oo-Kuma, 2020, 3D Printing Filaments Technical Data Sheet (ISO) PLA (Polyactic Acid). http://www.oo-kuma.com/uploads/1/4/0/8/14080379/elitepla.pdf. [Last accessed on 2020 Apr 23].
32. Żur P, Kołodziej A, Baier A, 2019, Finite Elements Analysis of PLA 3D-Printed Elements and Shape Optimization. *Eur J Eng Sci Technol*, 2(1):5964.

ORIGINAL ARTICLE

Using Large-Scale Additive Manufacturing as a Bridge Manufacturing Process in Response to Shortages in Personal Protective Equipment during the COVID-19 Outbreak

Elizabeth G. Bishop*, Simon J. Leigh

School of Engineering, University of Warwick, Coventry, CV4 7AL, United Kingdom

Abstract: The global coronavirus disease (COVID)-19 pandemic has led to an international shortage of personal protective equipment (PPE), with traditional supply chains unable to cope with the significant demand leading to critical shortfalls. A number of open and crowdsourcing initiatives have sought to address this shortfall by producing equipment such as protective face shields using additive manufacturing techniques such as fused filament fabrication (FFF). This paper reports the process of designing and manufacturing protective face shields using large-scale additive manufacturing (LSAM) to produce the major thermoplastic components of the face shield. LSAM offers significant advantages over other additive manufacturing technologies in bridge manufacturing scenarios as a true transition between prototypes and mass production techniques such as injection molding. In the context of production of COVID-19 face shields, the ability to produce the optimized components in under 5 min compared to what would typically take 1 – 2 h using another additive manufacturing technologies meant that significant production volume could be achieved rapidly with minimal staffing.

Keywords: Additive manufacturing, Three-dimensional printing, Coronavirus disease-19, Coronavirus, Face shield, Personal protective equipment

***Corresponding Author:** Elizabeth G. Bishop, School of Engineering, University of Warwick, Coventry, CV4 7AL, United Kingdom; E.G.Bishop@warwick.ac.uk

Received: May 14, 2020; ***Accepted:*** June 15, 2020; ***Published Online:*** September 04, 2020

(This article belongs to the *Special Section: Research and Applications of 3D Printing and Bioprinting for COVID-19)*

Citation: Bishop EG, Leigh SJ, 2020, Using Large-Scale Additive Manufacturing as a Bridge Manufacturing Process in Response to Shortages in Personal Protective Equipment during the COVID-19 Outbreak, *Int J Bioprint*, 6(4):281. DOI: org/10.18063/ijb.v6i4.281

1 Introduction

In December of 2019, an outbreak of infections from a novel coronavirus (now named severe acute respiratory syndrome coronavirus 2 [SARS-Cov-2]) was reported in China[1]. The class of viruses known as coronaviruses are responsible for most of the common colds and have often arisen due to transmission from animals to humans[2]. Initially focused on Wuhan in the Hubei province[3], the infection has since spread globally, with the spread of coronavirus disease 2019 (also more commonly known as COVID-19) reaching the necessary level of spreading to be classified as a global pandemic according to the World Health Organisation (WHO)[4]. At the time of writing, it is believed that over 4 million people have been infected globally, leading to over 278,000 deaths[5]. It has been established that the contagiousness of the disease is higher than previous outbreaks such as SARS in 2002 – 2004[6] and can be transmitted through an airborne droplet and contact transmission[7]. It has also been established that people are able to transmit the infection despite not obviously displaying symptoms (asymptomatic)[8].

For these reasons, the wearing of personal protective equipment (PPE) has become a vital requirement for frontline medical staff, those with critical caring responsibilities and key workers facing increased potential exposure to SARS-Cov-2. The WHO has recommended that PPE also includes eye protection to safeguard against droplet and airborne transmission[9]. Droplet transmission (as happens with influenza) occurs when droplets from an infected individual that is generated during coughing, sneezing, or even talking pass through the air and land on the eyes, nose, and mouth of another individual leading to infection[10].

With this increased global demand for PPE, governments and organizations have struggled to source enough for millions of regular PPE users, let alone for non-typical users such as pharmacies and general practitioners who are now at increased risk of infection during their daily activities. These supply chain issues have arisen due to a global shortage of PPE items such as eye protection/face shields and the inability to manufacture enough items quick enough[11]. In response to this unprecedented demand, many companies, academic institutions, and individuals have sought to use democratized manufacturing facilities and equipment such as three-dimensional (3D) printers (generally fused filament fabrication [FFF] systems) to produce components for much needed PPE items such as face shields[12,13]. This manufacturing effort has seen members of the international 3D printing community come together in vast, rapidly formed collaborative networks to address the PPE shortfall in a way reminiscent of the often-proposed concept of localized microfactories[14,15]. In the context of a traditional product development cycle, this type of activity can be likened to bridge manufacturing, where the use of additive manufacturing techniques is used to bridge the gap between small volume, time-intensive manufacturing processes, and other mass manufacturing techniques such as injection molding when increased demand makes the production of tooling and moulds a cost-effective option.

Due to the prevalence of desktop FFF 3D printers, most of the designs being manufactured by these global communities are optimized for common 3D printer formats, such as build plates of approximately 200 × 200 mm and 0.4 mm (sub-mm) extrusion nozzles[16]. These limitations generally mean that the main components of face shields can take 1 – 2 h to produce, which presents a significant issue for producing larger volumes of components. Typical thermoplastic deposition rates on desktop 3D printers are usually on the order of 10 mm^3/s[17]. Large-scale additive manufacturing (LSAM) systems have built volumes with dimensions of 1 m or greater and typically use nozzles with diameters of 1 mm or greater, allowing for significantly higher deposition rates on the order of 100 mm^3/s. LSAM has been used previously to manufacture tooling for various applications[18-20], as well as being used for direct manufacture of large single objects[21] such as furniture[22] and bike frames[23].

The ability to deposit thermoplastic materials at rates of up to 100 mm^3/s with LSAM means that bridge manufacturing rates for PPE components can be significantly increased addressing immediate requirements in advance of an eventual increase in production capacity using techniques such as injection molding. In this paper, we report the design and development of face shield components optimized for production using LSAM technology such that a component that would normally take 1 – 2 h to produce can be made in under 5 min. The development of process parameters to ensure continued part quality with larger part volumes per production run is also presented.

2 Materials and methods

The headbands were printed on a 3D Platform 300 Series Workbench Pro (3D Platform, USA) with High Flow Extruder 300 3D Printer Extruder, fitted with a 1.8 mm nozzle. The material used for the thermoplastic component was 3DFilaPrint Premium polylactic acid (PLA) 2.85 mm (3DFilaPrint, UK). All print parameters were previously determined empirically through an iterative process. The key print parameters used were: 1.8 mm extrusion width; 1 mm layer height; 0% infill; 230°C extrusion temperature; and 50 mm/s default printing speed.

3 Results and discussion

A typical face shield for use during the COVID-19 pandemic comprises several key components (**Figure 1**): A headband (1), clear lens/visor (2), a strap (3), top protection (4), and a bottom support piece (5). Other crowdsourcing projects have sought to produce the headband and bottom support pieces using desktop 3D printers. Within this study, LSAM was applied in the same way but with the goal of speeding up the production of these parts by approximately ×20.

The design requirements dictated by the functionality of the 3D printed parts were as follows (key function analysis, **Figure 2**). The headband is needed to easily conform to the user's head and hold a lens/visor with sufficient splash protection to meet the required regulations. The headband also needed to have a way to be held onto the head of the user using some form of strap and be lightweight as it would need to be worn for extended periods of time. The parts of the face shield should also be entirely free from sharp regions or defects that are likely to cause injury or discomfort to a user. To aid clarity for this paper, the production of the largest component, the headband will be the focus. As the target production time for the headband was sub-10 min, the design needed to be fully optimized for production with LSAM, leveraging the key advantages of the process. The material used for the thermoplastic component was 3DFilaPrint Premium PLA 2.85 mm (3DFilaPrint, UK).

To optimize the design, the obvious strategy to adopt first in designing a part for LSAM is reducing the amount of material required (dematerialization) which dictates that all material must contribute to the critical function of the device, with no excess, unrequired material present.

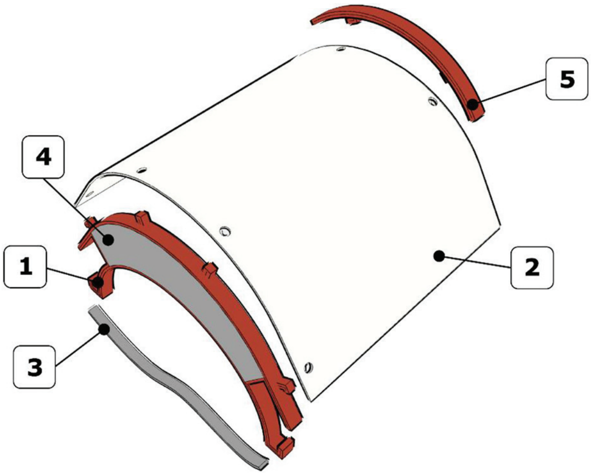

Figure 1. Typical components that make up an emergency face shield.

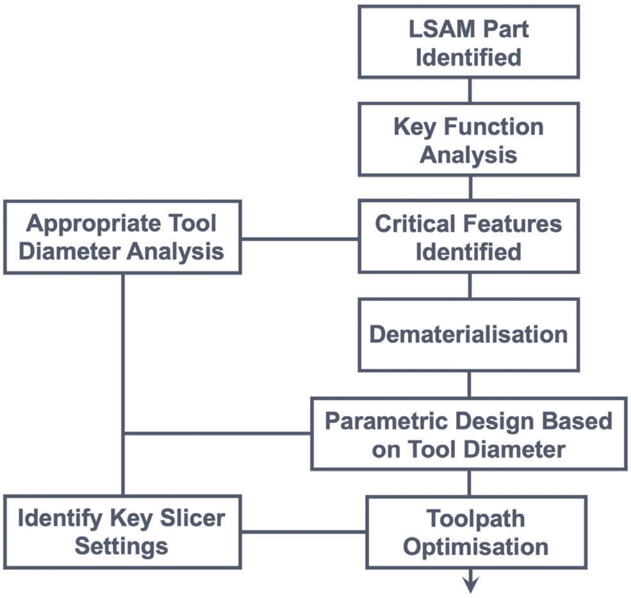

Figure 2. InVision Freehand schematic showing the design methodology employed in optimizing a design for large-scale additive manufacturing.

To print effectively, the minimum feature size of the printed design needs to be specifically selected as it is determined by the nozzle diameter of the LSAM system (tool diameter analysis). For example, the minimum horizontal width of any section which protrudes from the main headband must be at least ×2 nozzle diameter, but no larger than ×2.5 nozzle diameter, or else, the printed extrusions will not bond together (parametric design based on tool diameter). To reduce overall travel moves made by the printer, the largest possible nozzle should be chosen, but to ensure that the parts stay lightweight with sensible feature sizes, a balance must be struck. In this case, a 1.8 mm nozzle was selected to achieve this required balance. The 1.8 mm nozzle allowed for deposition rates of 92 mm^3/s, (printing a headband with <20 g of PLA) while allowing for the features to be small enough for functions such as the attachment of the lens/visor. The headbands were designed with no overhanging sections to ensure that no material or time wasted in printing support material. The final strategy to adopt is to ensure that every move of the print nozzle in the print job is a useful move, that is, all moves made are contributing to the deposition of material, and there are minimal non-print travel moves (toolpath optimization). To ensure this toolpath optimization, the design was first optimized for production with only single walls (Version 1) and then optimized for production using "vase mode" (Version 2). In vase mode (also known as "Spiralize Outer Contour") throughout the print, the nozzle does not (i) travel without printing, (ii) retract, or (iii) stop extruding.

3.1 Initial design (version 1)

The initial design took inspiration from various community-driven face shield designs available (e.g., *N3DPS*[24], *Prusa*[25], and *Verkstan*[26]) and the digital design work was carried out in Autodesk Fusion 360. A key focus for the design was to ensure the final shield would pass any relevant regulatory testing, which determined aspects such as the height of the headband being no <10 mm tall. The second key design aspect was the attachment points for the clear lens/visor. The visor holes would be made using a standard 6 mm diameter hole punch, and therefore, the attachment points were designed with a 5.5 mm width, distributed around the front loop of the headband. Ensuring that the printed parts were not sharp and likely to injure the user might normally require filleting of edges in the design, but fillets were not required in the computer-aided design model (**Figure 3A**) as when printing with LSAM, the machine will essentially "self-fillet" at sharp turns which can be seen in comparing the corners of the strap attachment points in **Figure 3A** and **C**. The final design focus was on ensuring the individual sections of the headband met the requirements based on a tool diameter of 1.8 mm (parametric design based on tool diameter). Therefore, the front and rear sections were set to 1.8 mm thick, and the thicker sections of the design set to double the extrusion width (3.6 mm), crucially with a 0.1 mm gap between the deposited tracks to allow for single wall extrusion printing to happen rather than the slicer infilling the region, which can be

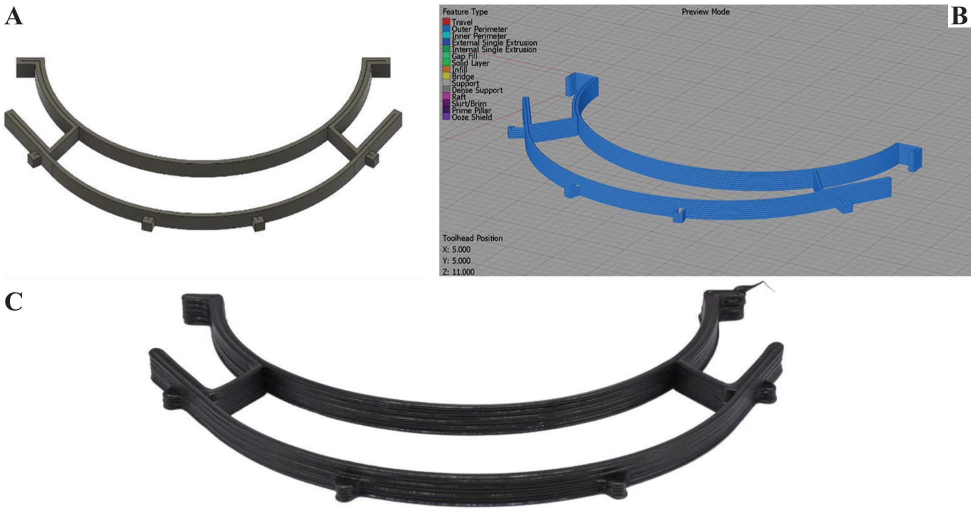

Figure 3. Initial design for face shield components produced using large-scale additive manufacturing, (A) showing the computer-aided design model, (B) the Simplify3D sliced print preview, and (C) the final printed part.

seen in the sliced file in **Figure 3B**. An example of the final print can be seen in **Figure 3C**. The preparation of the designs for printing was carried out in Simplify 3D and printing was carried out using a 3D Platform Workbench system. This version of the design took just 5 min to print. The nature of the printing method meant that the seam line (from the start and stop point of the layers) led to defects in the final print (as can be seen on the strap attachment point), meaning some hand finishing was required.

3.2 Design iteration (version 2)

While the initial design worked, the clear lens/visor which is held on at 4 points, did not hold on very well, as the lip which can be found in many of the small scale designs needed to be removed for LSAM to be possible. The headband was therefore redesigned to change the two outer two attachment pins into hooks which could be printed with the 1.8 mm nozzle which vastly improved the design. At this point, it was also decided to change the design to allow for "vase mode" to be employed (toolpath optimization) vase mode is where the printhead moves continuously in Z throughout the print, varying the Z parameter slightly, in contrast to printing a single layer, at constant Z value, stopping in XY and then moving to the next layer. The toolpath for a "vase mode" print is generated through the additive slicer used for LSAM, by taking a solid and extracting the outermost perimeters. Thus, the headband design was modified to create a fully solid design (**Figure 4A**), with the slicer software generating the required toolpath (**Figure 4B**). The resulting headband was printed in 4 min. The most notable impact of using this strategy is that the visible seam line and defects are completely removed, thereby removing the requirement for any hand finishing (**Figure 4C**).

3.3 Speeding up the manufacturing process/sequential deposition for quality

To speed up the manufacturing process and ensure continued part quality (crucial for scaling up production), the use of a sequential manufacturing strategy was employed. In a conventional additive manufacturing process, when producing multiple parts on a single print bed, all the parts will be produced in parallel such that the layers of each are incremented at the same time. Producing parts in this way leads to lots of non-print travel moves (red lines), as can be seen in the toolpath preview in **Figure 5A**. Printing multiple parts on a single print bed using traditional parallel printing with FFF systems can result in defects on the parts, such as stringing that can occur when material exits the nozzle during non-print moves between parts[27,28].

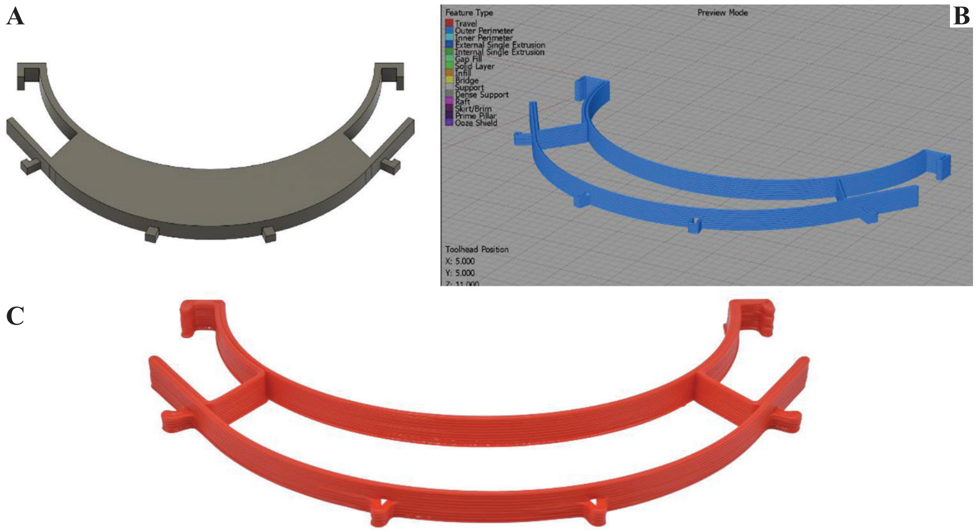

Figure 4. Improved face shield design using large-scale additive manufacturing, (A) showing the computer-aided design model, (B) the Simplify3D sliced print preview, and (C) the final printed part.

Stringing is often difficult to minimize, especially when using large print nozzles. When producing multiple copies of the face shield parts on a single print bed, it was found that stringing often occurred (**Figure 5B**), leading to significant, sharp defects, and random deposits of material on certain regions of the headband piece (**Figure 5C**). This parallel print strategy also meant that "vase mode" could not be used, leading to the reintroduction of the seam line defects caused by the layer change. The total print time for 27 headbands was 2 h 9 min giving a time of 4 min 47 s per headband.

Instead, a sequential production process was employed, where each part was first completed, in "vase mode," before a new part was commenced (**Figure 5D**), significantly reducing the number of travel moves (red lines) during the total print. The small overall Z height of the individual parts ensured that the sequential deposition was achievable by limiting potential print head collisions with parts already produced. Switching to sequential deposition had no significant impact on part production time and improved the quality of the final parts, with no visible defects or sharp areas requiring hand finishing (**Figure 5B and C**). Interestingly, switching to sequential deposition (while less could be printed on the bed at the same time due to print head geometry constraints), actually reduced the print time per headband (compared to parallel printing) as time is saved in removing the travel moves within a single layer. Other benefits of using sequential printing include minimizing both the risk of a single print failure causing a whole print bed of parts to be damaged and the risk of the print material running out and leaving a whole print bed of incomplete parts. The resultant print time for a headband was 3 min 20 s per headband (1 h 30 min for 27 headbands).

Overall, the production time achieved was significantly less compared to other community and open-source face shield designs. To quantify the reduction in time, multiple other designs were produced on either a standard desktop 3D printer (Ultimaker 3) or the 3D Platform with the results shown in Table 1.

3.4 Mechanical testing

To further compare the different designs and ascertain their robustness, the Version 2 printed on the large-scale system (3D Platform [3DP]) and the Version 2 printed on a desktop system

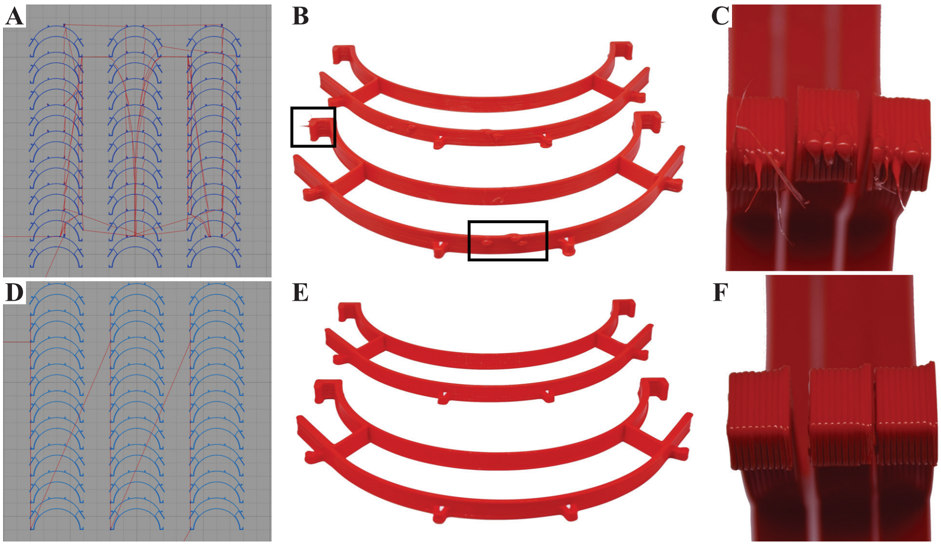

Figure 5. (A) Toolpath preview of parallel print process with travel moves shown in red, and photos showing a comparison of the quality of (B) multiple parts on a single build plate using parallel production strategy with defect areas highlighted and (C) multiple defects versus (D) toolpath preview of a sequential print process and photos of (E) multiple parts on a single build plate using sequential production strategy showing (F) minimal defects.

Table 1. Results showing different print times for open source and the headbands described in this paper

Design	N3DPS[24]	Prusa-reduced[25]	Verkstan[26]	Version 2 (desktop printer)	Version 1	Version 2	Version 2 parallel	Version 2 sequential
Printer	Ultimaker 3	Ultimaker 3	Ultimaker 3	Ultimaker 3	3DP	3DP	3DP	3DP
Nozzle size (mm)	0.4	0.4	0.4	0.4	1.8	1.8	1.8	1.8
Layer height (mm)	0.2	0.2	0.2	0.2	1	1	1	1
Total print time (min)	115	75	69	92	5	4	129	90
Print time per headband (min)	115	75	69	92	5	4	4 min 47 s	3 min 20 s

3DP: 3D platform

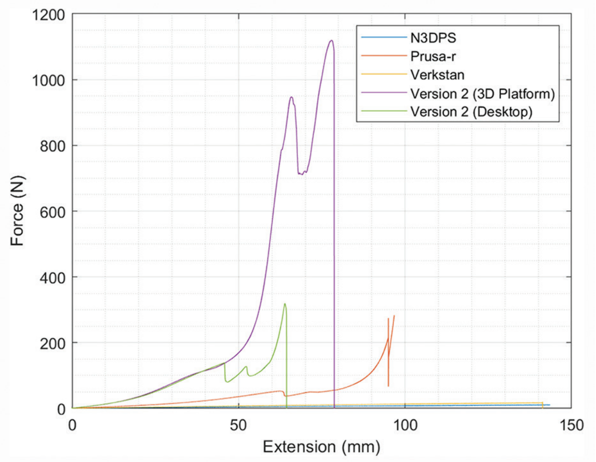

Figure 6. Mechanical testing results of the three-dimensional printed headbands.

(Ultimaker 3) were mechanically tested (tensile parallel to layers) alongside other open-source designs, with the results shown in **Figure 6**. Version 2 (Desktop) had a similar breaking force to the Prusa-r design, the Verstan and N3DPS show a different characteristic plot which reflects the very different design approach to these two designs. Version 2 (Large-Scale) can be seen to be much stronger with a breaking force of 1120 N compared to Version 2 (Desktop) of 320 N.

4 Conclusions

LSAM has been shown to be a technology capable of producing components of PPE devices in significantly less time than the traditional 3D printing systems such as desktop FFF devices. Through the thorough understanding of the interplay between design and process parameters, it is feasible to parametrically optimizing a design for a simple thermoplastic component for production using LSAM, with areas of the design that would typically take a number of nozzles passes with a traditional sub-mm nozzle able to be deposited with just a single pass from a nozzle on a LSAM system. By leveraging the key advantages of LSAM, it is possible to achieve production rates up to ×20 faster than traditional desktop 3D printing, achieving a production rate that more closely bridges to manufacturing processes such as injection molding.

Acknowledgments

The authors would like to acknowledge 3DFilaPrint Ltd. for support with the sourcing and provision of material for the project and the EPSRC for the Ph.D. studentship for EGB.

Conflicts of interest

No conflicts of interest were reported by all authors.

References

[1] Riou J, Althaus CL, 2020, Pattern of Early Human-to-Human Transmission of Wuhan 2019 Novel Coronavirus (2019-nCoV), December 2019 to January 2020. *Euro Surveill*, 25:2000058. DOI: 10.2807/1560-7917.es.2020.25.4.2000058.

[2] Paules CI, Marston HD, Fauci AS, 2020, Coronavirus Infections-more than Just the Common Cold. *JAMA*, 2020:0757. DOI: 10.1001/jama.2020.0757.

[3] Li Q, Guan X, Wu P, *et al*., 2020, Early Transmission

Dynamics in Wuhan, China, of Novel Coronavirus-Infected Pneumonia. *N Engl J Med*, 382:1199–207.

[4] World Health Organization, 2020, WHO Virtual Press Conference on COVID-19. World Health Organization, Genevs. Available from: https://www.who.int/docs/default-source/coronaviruse/transcripts/who-audio-emergencies-coronavirus-press-conference-22apr2020.pdf?sfvrsn=4f8821b6_2 [Last accessed on 2020 Jun 01].

[5] World Health Organisation, 2020, Coronavirus Disease 2019 (COVID-19): Situation Report. Vol. 112. World Health Organisation, Geneva.

[6] Liu Y, Gayle AA, Wilder-Smith A, *et al*., The Reproductive Number of COVID-19 is Higher Compared to SARS Coronavirus. *J Travel Med*, 27:taaa021. DOI: 10.1093/jtm/taaa021.

[7] Ather A, Patel B, Ruparel NB, *et al*., 2020, Coronavirus Disease 19 (COVID-19): Implications for Clinical Dental Care. *J Endod*, 46:584–95. DOI: 10.1016/j.joen.2020.03.008.

[8] Bai Y, Yao L, Wei T, *et al*., 2020, Presumed Asymptomatic Carrier Transmission of COVID-19. *JAMA*, 323:1406–7. DOI: 10.1001/jama.2020.2565.

[9] World Health Organization, 2020, Rational Use of Personal Protective Equipment for Coronavirus Disease 2019 (COVID-19). World Health Organization, Geneva.

[10] World Health Organization, 2020, Modes of Transmission of Virus Causing COVID-19: Implications for IPC Precaution Recommendations. *Intensive Care Med*, 46:854–87.

[11] Livingston E, Desai A, Berkwits M, 2020, Sourcing Personal Protective Equipment during the COVID-19 Pandemic. *JAMA*, 2020:5317. DOI: 10.1001/jama.2020.5317.

[12] Larrañeta E, Dominguez-Robles J, Lamprou DA, 2020, Additive Manufacturing Can Assist in the Fight Against COVID-19 and Other Pandemics and Impact on the Global Supply Chain. *3D Printing and Additive Manufacturing*, 2020:106. DOI: 10.1089/3dp.2020.0106.

[13] Flanagan ST, Ballard DH, 2020, 3D Printed Face Shields: A Community Response to the COVID-19 Global Pandemic. *Acad Radiol*, 27:905–6. DOI: 10.1016/j.acra.2020.04.020.

[14] Phillips W, Dalgarno K, Medcalf N, *et al*., 2017, Redistributed Manufacturing in Healthcare: Creating New Value through Disruptive Innovation. 2017:14567.

[15] Tardieu H, Daly D, Esteban-Lauzán J, *et al*. Case study 6: The digital transformation of manufacturing. In: *Deliberately Digital*. Springer, 2020, pp. 269–80.

[16] Redwood B, Schöffer F, Garret B, 2017, The 3D Printing Handbook. Technologies, Design and Applications. 3D Hubs B.V, Amsterdam, Netherlands.

[17] E3D Blog, E3D. Available from: https://www.e3d-online.com/blog/2019/02/28/supervolcano. [Last accessed on 2020 May 13].

[18] Post BK, Chesser PC, Lind RF, *et al*., 2018, Using big area additive manufacturing to directly manufacture a boat hull mould. *Virtual and Physical Prototyping*, 14:123–9. DOI: 10.1080/17452759.2018.1532798.

[19] Kunc V, Hassen AA, Lindahl J, *et al*., 2017, Large Scale Additively Manufactured Tooling for Composites. Conference: 15th Japan International Sampe Symposium And Exhibition, At Tokyo, Japan.

[20] Post BK, Richardson B, Lind R, *et al*., 2017, Big Area Additive Manufacturing Application In Wind Turbine Molds. In: Solid Freeform Fabrication 2017: Proceedings of the 28th Annual International Solid Free Form Fabrication Symposium. DOI: 10.32656/sff.

[21] Nieto DM, López VC, Molina SI, 2018, Large-format Polymeric Pellet-based Additive Manufacturing for the Naval Industry. *Additive Manufacturing*, 23:79–85. DOI: 10.1016/j.addma.2018.07.012.

[22] Murat A, 2015, Additive Manufacturing: Is it a New Era for Furniture Production? *Journal of Mechanics Engineering and Automation*, 5:338–47.

[23] Reinforced Plastics, 2019, Continuous CF bike frame. Reinforced Plastics, 63:163-220. https://doi.org/10.1016/j.repl. 2019.06.043.

[24] National 3D Printing Society. Medical AM (COVID-19). Available from: https://www.national3dprintingsociety.co.uk/medical-am-covid-19. [Last accessd on 2020 Jun 01].

[25] Prusa Research. “Prusa Face Shield”. Available from: https://www.prusaprinters.org/prints/25857-prusa-face-shield. [Last accessed on 2020 Jun 01].

[26] 3DVerkstan. “3D-Printed Protective Visor”. Available from: https://www.3dverkstan.se/protective-visor. [Last accessed on 2020 Jun 01].

[27] Devicharan R, Garg R, 2019, Optimization of the Print Quality by Controlling the Process Parameters on 3D Printing Machine. In: 3D Printing and Additive Manufacturing Technologies. Springer, Singapore, pp. 187–94. DOI: 10.1007/978-981-13-0305-0_16.

[28] Galatia M, Minetola P, Marchiandi G, *et al*., 2019, A Methodology for Evaluating the Aesthetic Quality of 3D Printed Part. *Procedia CIRP*, 79:95–100. DOI: 10.1016/j.procir.2019.02.018.

REVIEW ARTICLE

Applications of 3D Bioprinted-Induced Pluripotent Stem Cells in Healthcare

Soja Saghar Soman[1], **Sanjairaj Vijayavenkataraman**[1,2]

[1]Division of Engineering, New York University Abu Dhabi, Abu Dhabi, UAE

[2]Department of Mechanical and Aerospace Engineering, Tandon School of Engineering, New York University, NY, USA

Abstract: Induced pluripotent stem cell (iPSC) technology and advancements in three-dimensional (3D) bioprinting technology enable scientists to reprogram somatic cells to iPSCs and 3D print iPSC-derived organ constructs with native tissue architecture and function. iPSCs and iPSC-derived cells suspended in hydrogels (bioinks) allow to print tissues and organs for downstream medical applications. The bioprinted human tissues and organs are extremely valuable in regenerative medicine as bioprinting of autologous iPSC-derived organs eliminates the risk of immune rejection with organ transplants. Disease modeling and drug screening in bioprinted human tissues will give more precise information on disease mechanisms, drug efficacy, and drug toxicity than experimenting on animal models. Bioprinted iPSC-derived cancer tissues will aid in the study of early cancer development and precision oncology to discover patient-specific drugs. In this review, we present a brief summary of the combined use of two powerful technologies, iPSC technology, and 3D bioprinting in health-care applications.

Keywords: Induced pluripotent stem cells, Three-dimensional bioprinting, Regenerative medicine, Disease modeling, Cancer iPSCs, Drug screening.

***Corresponding Author:** Sanjairaj Vijayavenkataraman, Division of Engineering, New York University Abu Dhabi, Abu Dhabi, UAE; vs89@nyu.edu

Received: March 05, 2020; ***Accepted***: June 24, 2020; ***Published Online***: July 30, 2020

Citation: Soman SS, Vijayavenkataraman S, 2020, Applications of 3D Bioprinted Induced Pluripotent Stem Cells in Healthcare, *Int J Bioprint*, 6(4): 280. DOI: 10.18063/ijb.v6i4.280.

1 Introduction

The advent of induced pluripotent stem cell (iPSC) technology in 2006 paved the way for paradigm shifting changes in regenerative medicine, disease modeling, and drug discovery applications. The technology facilitates to de-differentiate an adult cell to its pluripotent stem cell state and then differentiate into defined cell lineages. iPSCs are phenotypically indistinguishable from embryonic stem cells and they can differentiate into specialized cells of the body in cell culture and in animal models. Initially, human iPSCs were derived using transduction of genes coding for four embryonic transcriptional regulators; Oct4, Sox2, Klf4, and c-Myc (OSKM), popularly known as the Yamanaka factors[1] or Oct4, Sox2, Lin28, and Nanog (OSLN)[2]. Each of the Yamanaka factor serve specific purposes, *Sox2* interacts with *Oct3/4* to control gene expression. This interaction is important in maintaining pluripotency[3]. *C-Myc* plays an important role in controlling growth and differentiation of cells[4], whereas *klf4* is crucial for cell division and maintenance of pluripotency[5]. Later, different combinations of at least 24 embryonic transcription factors were identified to induce stemness in adult cells[6]. The Yamanaka factors are highly conserved and sufficient to induce pluripotency across species.

Reprogramming of somatic cells is orchestrated by cooperative binding of pioneer factors (Oct4, Sox2, and Klf4)[7], followed by epigenetic remodeling of entire genome and two waves of transcriptional events[8,9]. Each cell type in the body require different combinations of transcriptional factors to induce the stemness where Oct4 is considered as an indispensable core pluripotency gene in the reprogramming process[10]. Exogenous supply of Oct4 alone could convert adult neural stem cells into iPSCs. Recent work by An *et al.* showed that Sox2 and Klf4 were enough to prepare iPSCs from various types of somatic cells[7]. Small molecules that inhibit DNA or histone modifications were also used for generating iPSCs more efficiently along with the use of reprogramming transcription factors. The hematopoietic stem cells can be de-differentiated into iPSCs much more efficiently compared to the highly specialized cells such as B and T lymphocytes[11,12].

Fibroblasts are the most popular cell type used to generate iPSCs. However, well-differentiated adult cells such as keratinocytes, neural cells, fat cells, melanocytes, amniotic fluid cells, pancreatic beta cells, and peripheral blood derived cells had also been successfully reprogrammed to pluripotent stem cells. The capacity to induce pluripotency to somatic cells helps to generate pluripotent patient-specific cell lines that can help model human diseases and can aid in the reconstruction of damaged tissues and organs. The “disease in a dish” models derived from IPSCs provide insights into disease pathogenesis and can serve as a novel tool for drug evaluation in precision medicine field[13-15]. Human iPSCs reinforced with biocompatible scaffold materials are valuable in three-dimensional (3D) bioprinting applications[16]. Current bioprinting techniques allow to print undifferentiated iPSCs and iPSC-derived cells mixed with a suitable bioink[17,18]. Popular bioprinting techniques used to print iPSCs are extrusion, stereolithography (SLA), laser-assisted, and drop-on-demand bioprinting[19-22]. A single biomaterial or a mixture of several biomaterials in the bioink are used to suspend the desired cells for bioprinting[23,24]. The bioinks should be non-toxic, biocompatible and should provide structural support for the printed cells. The commonly used bioinks for printing iPSC derived cells are hydrogels derived from alginate, carboxymethyl chitosan, agarose, nano-fibrillated cellulose, hydroxypropyl chitin, gelatin methacryloyl (GelMA), and Matrigel. Most of these hydrogels need a crosslinker to give the final structure of the intended tissue constructs. Calcium chloride, ultraviolet (UV) radiation, photo crosslinking, and altered temperatures are used for crosslinking the bioink molecules[25-27].

Here, we review the applications of the 3D bioprinted iPSCs or iPSC-derived cellular products in healthcare, especially in regenerative medicine, disease modeling, and drug testing (**Figure 1**). The methods of reprograming of iPSCs were described. Glimpses of the technological advancement in organ bioprinting were discussed. The advantages, limitations, and future directions of using iPSCs in clinics were outlined.

2 Human iPSC reprogramming methods

For clinical application and disease modeling, the reprogramming method of choice should have adequate efficiency to produce iPSCs from less abundant samples[28]. Production of iPSCs using a combination of reprogramming methods can augment the efficiency of iPSCs generation even from the most difficult type of adult cells[29]. More than 10 years of extensive research on iPSC technology lead to the establishment of novel strategies for the production of iPSCs including the use of right cell type for reprogramming, use of non-integrative gene introduction methods, overexpression of gene enhancers of transcription factors, and the use of small molecules[30,31] (**Figure 2**).

2.1 Integrating viral vectors

Initial iPSC experiments used lentivirus and retrovirus vectors to deliver Yamanaka factors in adult fibroblasts[2,32]. These retroviral-vectors possess the risk of creating mutagenesis by integrating to the host cell genetic material[33]. Moreover, the reprogramming procedure is tedious, also, it can cause chromosomal instability and potential threat of tumorigenesis from the

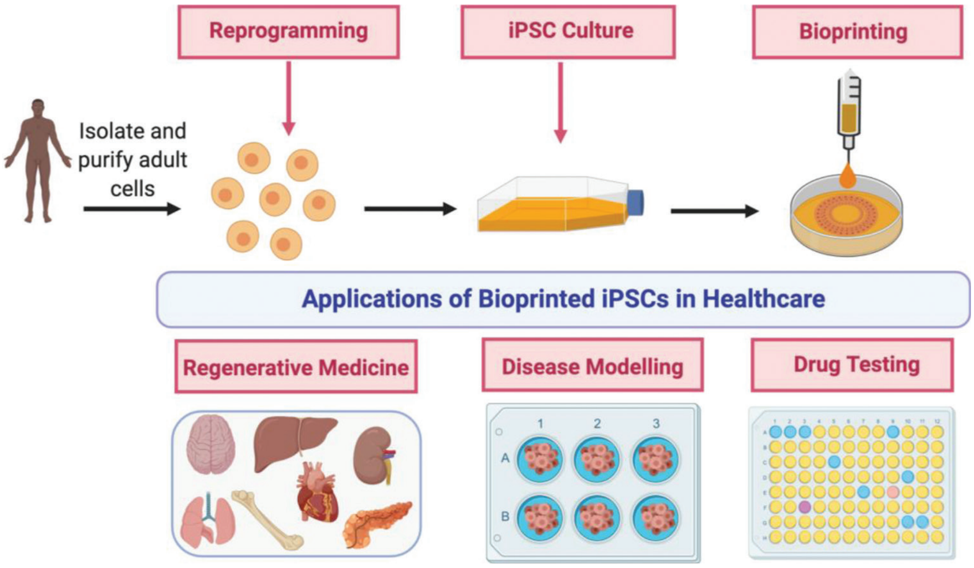

Figure 1. Bioprinting of induced pluripotent stem cell (Ipsc)-derived tissues for regenerative medicine, disease modeling, and drug testing. Adult somatic cells are collected from a donor or a patient; the cells are reprogrammed to iPSCs and differentiated to specialized cells.

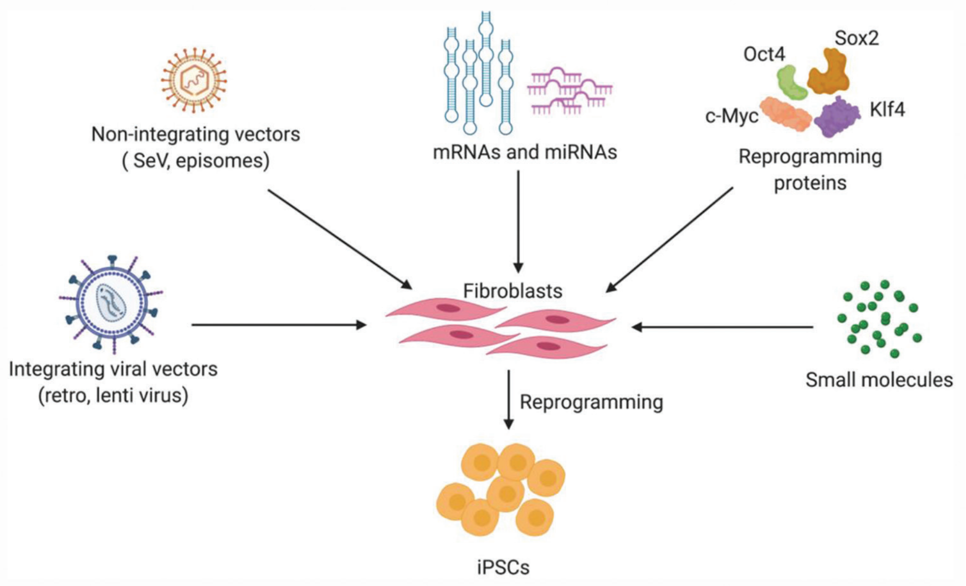

Figure 2. Reprogramming methods used to generate induced pluripotent stem cell.

viral vectors[1,2,31-34]. It is essential to do the quality control of the iPSC lines created using viral vectors using whole-genome single nucleotide polymorphism array and karyotyping to verify the genomic integrity.

2.2 Non-integrating vectors

To reduce the risk of unwanted genetic perturbations, there was introduction of non-integrating methods for transcription factor delivery. Recent methods of reprogramming use Sendai Virus (SeV) particles and episomes. SeV particles are used to transduce the reprogramming genes: Oct4, Sox2, Klf4, and c-Myc[8]. SeV reprogramming offers the absence of viral sequences in the host cell lines and is an efficient method to induce pluripotency[35]. In 2009, Yu *et al*. reported the episomal reprogramming in human cells where Epstein-Barr virus–derived sequences were used for the non-integrated expression of the transcription genes that enable episomal plasmid DNA replication in dividing cells[36]. Polycistronic expression plasmids generates transgene-free and vector-free iPSCs with limited genomic integration, but this method requires multiple transfections[37,38].

2.3 mRNAs and miRNAs

Human primary fibroblasts were reprogramed by introducing synthetic modified mRNAs coding for reprogramming proteins. MicroRNAs like miRNA-367/302s are used to reprogram human primary fibroblasts into iPSCs[39]. The mRNA transfection is foot print free reprogramming. The capped mRNAs coding for a 6-factor modified-mRNA referred to as 5fM$_3$O mod-mRNAs was used in fibroblasts to make iPSCs[40]. Yamanaka factors and the miRNA-367/302s act synergistically to increase the efficiency of transfection[41]. It has been reported that microRNAs such as miR-294, miR-291-3, and miR-295 can replace *c*-myc transcription factor and help to generate homogeneous populations of iPSC colonies[42]. Downregulation of let-7 miRNA upregulates the expression of target genes of *c-myc* and *Lin-28* to promote cell reprogramming[43,44].

2.4 Reprogramming proteins

This method allows the direct introduction of the recombinantly expressed reprogramming factors to cells[49]. This method mitigates the risks associated with the introduction of viral and external DNA and harmful chemicals into the cells[46]. The reprogramming proteins Oct4, Sox2, Klf4, and c-Myc were successfully delivered into adult somatic cells with the help of cell penetrating peptides (CPP). The cationic amino acid rich CPPs are capable of penetrating the cell membrane barrier and deliver the exogene-free reprogramming proteins directly inside the cells[47]. This method enables the production of foot print-free iPSCs.

2.5 Small molecules

Reprogramming can be achieved using small molecules by epigenetic modifications[48]. Small molecules used for reprogramming fall under the category of epigenetic events regulators, mesenchymal-epithelial transition inhibitors, metabolic pathway modulators, wingless and integration site growth factor (WNT) signal pathway modulators, regulators of cell death, and senescence pathways[48]. These small molecules alone or in combination can substitute exogenous transcription factors. Using valproic acid, a Histone deacetylase inhibitor improved the reprogramming efficiency to 100-fold compared to the transcription factor mediated reprogramming method[49]. Another histone methyltransferase inhibitor compound, BIX-01294 activated calcium channels in the cell membrane, and improve reprogramming efficiency by increasing the expression of October 4 and Klf4[50,51]. In 2013, Hou *et al*. replaced all transcription factors and made chemical induced iPSCs of mouse embryo fibroblasts using the small molecules VC6TFZ and 2i but the reprogramming was incomplete[52]. Optimizing the use of small molecules to enhance reprogramming will definitely help to generate safer and higher quality iPSCs for clinical use without the risk of genomic integration and tumor induction.

The advantages and limitations of these reprogramming methods are summarized in **Table 1**.

3 Sources of iPSCs for bioprinting and cell differentiation strategies of iPSCs to different cell lineages

The iPSC technology allows the use of autologous cells derived from the patients to be used in regenerative medicine. The iPSC cell lines have been derived from a variety of cells namely neuronal progenitor cells, keratinocytes, hepatocytes, B cells, fibroblasts, hepatocytes, gastric epithelial cells, muscles, adipocytes, and adrenal glandular cells. The reprograming efficiency varies among the type of cells used depending on the developmental origins and the epigenetic status. Multiple studies showed that the efficiency of reprogramming of keratinocytes is better than fibroblasts[53-55]. The difference in the efficiency is

Table 1. Advantages and limitations of the reprogramming methods.

Delivery method	Advantages	Limitations	References
Integrated viral vectors	High efficiency, validated in many cell types	Create insertional mutations, tumor induction	[1,2,31-34]
Integration free viral vectors. For example, Sendai virus, Episomes	Completely free of vector and transgene sequences and can use in clinical applications, GMP compatible	Low efficiency of reprogramming, reprogramming efficiency varies with cell types	[8,35-38]
mRNAs and miRNAs	Faster, high efficiency, absence of integration, need low input of starting cells	Multiple transfection required, may elicit immune response, not evaluated in many cell types	[40-44]
Reprogramming Proteins	Foot print-free, cGMP compliant	Not evaluated in many cell types, expensive	[45-47]
Small molecules	Foot print-free, cGMP compliant, economical	Incomplete reprogramming, reprogramming efficiency varies from cell to cell	[48-52]

attributed to the high-level endogenous expression of c-Myc and Klf4 in keratinocytes compared to other cell types. For therapeutic scenarios such as internal organ reconstruction (e.g., liver, and peripheral nerve), an ideal starting material to create iPSCs should be peripheral tissue. Peripheral tissue samples such as keratinocytes collected from patients can be reprogrammed to produce iPSCs and these iPSCs can serve as a valuable source for the cellular component in the tissue bioprinting[56]. Peripheral blood cells may represent a good source to derive iPSCs because taking blood samples from patients are a less invasive clinical procedure. Several research groups standardized the protocols for making iPSC lines from blood cells[57,58]. The iPSC-derived cells such as neurons, hepatocytes, osteoblasts, myocytes, skin cells, and pancreatic beta cells are in great demand in clinics for regenerative medicine applications[59-61]. Small molecules and growth factors such as recombinant proteins are used in the iPSC cultures to differentiate specific lineage cells from iPSCs[62,63].

4 Application of bioprinted iPSCs in healthcare

3D bioprinting using iPSCs hold high potential for several applications in the health-care sector. Current bioprinting techniques allow to print undifferentiated iPSCs and differentiated iPSC-derived cells embedded in a suitable bioink. Development of novel bioinks, iPSC-derived cells, and the technological advancement in devising new generation 3D bioprinters has created a whole new field of medical bioprinting that hold great promise for artificial tissue/organ printing for regenerative medicine, disease modeling, and drug testing[64]. Here, in section 4, we describe about the commonly used bioprinting techniques to print iPSCs and the application of bioprinting in health-care field.

4.1 Commonly used iPSC 3D bioprinting technologies

Bioprinting iPSCs could avoid the ethical and immunological bottle necks of organ printing. iPSCs and iPSC derived cells for developing into cartilage, bone, skin, heart, liver, and neural tissues have been successfully printed using 3D bioprinting technology. iPSC-derived chondrocytes along with irradiated chondrocytes were bioprinted to cartilage tissues using mixture of alginate and nanocellulose bioink. RegenHu 3D discovery bioprinter was used to print the chondrocytes. Extrusion bioprinting is the most commonly used method to print iPSCs and organs, followed by SLA, laser-assisted, drop-on demand, inkject, and microvalve based methods. The extrusion method applies a pneumatic (air) or mechanical (screw or piston) force to extrude iPSCs or its derivatives embedded in hydrogel bioinks through a nozzle orifice using seamless direct printing[65]. The printing is carried out in a spatially controlled layer-by-layer fashion precisely to biofabricate 3D tissue constructs. Extrusion printing permits printing of cell-dense high viscous hydrogels, but cells may experience high shear force stress during the printing process. All three germ layers[66], neural tissues[67], cortical neural constructs[68], chondrocytes[69], cardiac tissue,[70] and peripheral blood mononuclear cells have been bioprinted from iPSC or iPSC derived cells using extrusion method.

SLA and digital light projection (DLP) are popular nozzle-free bioprinting techniques work through photopolymerization. The liquid resin is solidified by UV laser beam in SLA. The DLP uses visible light for polymerization of the resin[71,72]. There are two types of SLA and DLP, i.e., bottom-up and top-down approach. The layer of resin on a support platform is cured by a light from above in bottom-up biofabrication, while the light source is located under a transparent platform in the top-down fabrication. iPSC-derived 3D liver models which mimic the native liver module architecture were printed using this technique[73]. The flipside of SLA is that, it can be detrimental to the living cells by damaging the genetic materials due to the use of UV. Moreover, the use of photo-initiator resins may be cytotoxic to the cells[74]. Vat polymerization (VP) based bioprinting is a novel and accurate bioprinting method tissue engineering applications[75]. Various types of photo-initiators are used for the cross-linking of the printed tissues in the VP based bioprinting. VP use light sensitive hydrogels such as polyethylene glycol–diacrylate (PEGDA) and gelatin-methylacryloyl (GelMA). Label-free diamagnetophoretic printing is another method for microtissue printing uses intrinsic diamagnetic forces to control positioning of cells in a paramagnetic medium. Magnetic bioprinting is a contactless technique which does not use nozzles and therefore promise less contamination of cell suspension. Whole blood cells were printed using this technique[76], this technique may be efficient to adopt to print iPSCs as there is fewer chemical manipulations that are involved.

Droplet-based bioprinting is simple, fast, and precisely controlled bioprinting method to deposit composites of cells, growth factors, biomolecules, drugs, and scaffolds. Droplet-based bioprinting is derived from inkjet printing technology. It has been noted as a prominent technique widely used in regenerative medicine to print cells due to its flexibility. The droplet-based bioprinting can be subdivided into inkjet, acoustic, and micro-valve bioprinting modalities. The drawback of using this technology is that the rage of biomaterials compatible for this method of bioprinting is limited[77]. A valve-based bioprinting method is used to print iPSCs differentiated post-printing into hepatocyte-like cells (HLC cells). A 40-layer thick alginate bioink containing HLC cells showed typical liver tissue structure and the construct secreted hepatic albumin throughout the differentiation protocol. The work proved that the valve-based printing process is safe to print human iPSCs by maintaining pluripotency and differentiation[19].

The laser-assisted bioprinting uses pulsed laser beam with a focusing device. It consists of an energy-absorbing layer coated with further layers of cell-encapsulated hydrogel. It is a nozzle-free bioprinting method that excludes clogging during printing[78]. Human iPSCs combined with bioinks were bioprinted with laser-assisted bioprinting method and the cells were evaluated for their efficacy, pluripotency, and differentiation capacity. The hyaluronic acid-based bioinks are ideal for laser-assisted bioprinting[16,79]. While designing a tissue structure for bioprinting, factors such as shape, size, resolution, scaffold materials, iPSCs, or iPSC derived cellular components, and post-processing tissue dynamics are to be considered. Bioprinting can be carried out as direct printing, crosslinking during the bioprinting, post-printing crosslinking, and hybrid methods, where more than one technique is used for printing the final tissue construct. The factors appear to affect cell survival after bioprinting are shear stress, laser exposure, duration, temperature, humidity, mechanical pressure, and vibration of the printing process. The selection of the printing techniques depends on the end use of the printed tissues, such as organ/tissue transplantation, disease modeling, or drug evaluation. Among, all the methods mentioned, extrusion bioprinting is the most commonly used technique in iPSC bioprinting[80,81] (**Table 2**). Extrusion method causes less damage to the cellular components while printing, as it uses adjustable mechanical forces with no harsh treatments for the deposition of the bioink to the platform.

4.2 Regenerative medicine

Autologous iPSCs derived from individuals provide unlimited source of cells for tissue regeneration. The unspecialized iPSCs can differentiate and develop to organoids/spheroids with specific characteristics of organs *in vivo*[74,82-84]. These mini-organoids can serve as building blocks for bioprinting of whole organs. Bioengineers and surgeons are looking for novel methods to synthesize artificial skin substitutes that is readily available and easily implantable in burn injury patients[85,86]. Scaffold-free cellular spheroids obtained from a coculture of human iPSC-derived cardiomyocytes, fibroblasts, and endothelial cells were 3D printed and these cardiac cellular patches were tested successfully in rat models of myocardial infarction[87]. Bioprinted organ substitutes such as pancreas, ovary, liver, kidney, and nervous tissues also will be in high demand in the near future. **Figure 3** shows the workflow of 3D bioprinting of peripheral nerve tissue[88,89] for the treatment of peripheral nerve injury.

Human iPSCs are capable of differentiation into many types of specialized cells and have high value in clinical use. These cells require specific cell culture media to keep their pluripotent characteristics intact. The isolation, expansion, and maintenance of human iPSCs intended for clinical use should be cultured in xeno-free conditions in compliance with the good manufacturing practice to avoid hypersensitivity reactions after transplantation in patients[90,91]. However, many conventional protocols of iPSC culture require to culture in feeder cells. The feeder cells are usually derived from mouse embryonic fibroblasts (MEFs). The cells are cultured on feeder cells to reduce the genetic instability of the cultured cells[89]. Culturing in MEF feeder cells or the usage of matrix coating substance (e.g., gelatin or Matrigel) made of animal components make the iPSCs xeno-positive. Recent introduction of synthetic polymers enables to maintain the iPSC cultures in xeno-free environment[92].

Yamanaka factor introduction techniques use different type of retroviral or plasmid vectors to integrate to the genome of the cell to make it pluripotent. For making clinical grade iPSCs and

Table 2. Summary of iPSC-based Bioprinting works

Printing technique	Cell source	Cells/tissues printed	Bioink used	Reference
Extrusion	iPSCs, BJFF iPSCs	Cardiac	Collagen I, Matrigel, Gelatin	[70]
	Human iPSCs	Chondrocytes	Nano-fibrillated cellulose in alginate	[69]
	Fibroblasts derived human iPSCs	Germ layers	Geltrex	[66]
	Human iPSCs ((WT I line)	Neural construct	Matrigel/alginate mixture	[68]
	Human iPSCs	Neural tissues	Alginate, carboxymethyl-chitosan, agarose	[67]
	Human peripheral blood mononuclear cells derived iPSCs	Pluripotent cells	Hydroxypropyl chitin, Matrigel	[79]
Stereolithography	Human iPSCs	Hepatic progenitor cells	Gelatin methacrylate (GelMA), Glycidal methacrylate-hyaluronic acid (GMHA)	[73]
Laser-assisted	Human iPSCs from cord blood	Germ layers	Matrigel, Collagen type I, Alginate, Hyaluronic acid	[16]
Microvalve-based	Human iPSCs	Hepatocyte-like cells (HLCs)	Geltrex	[19]

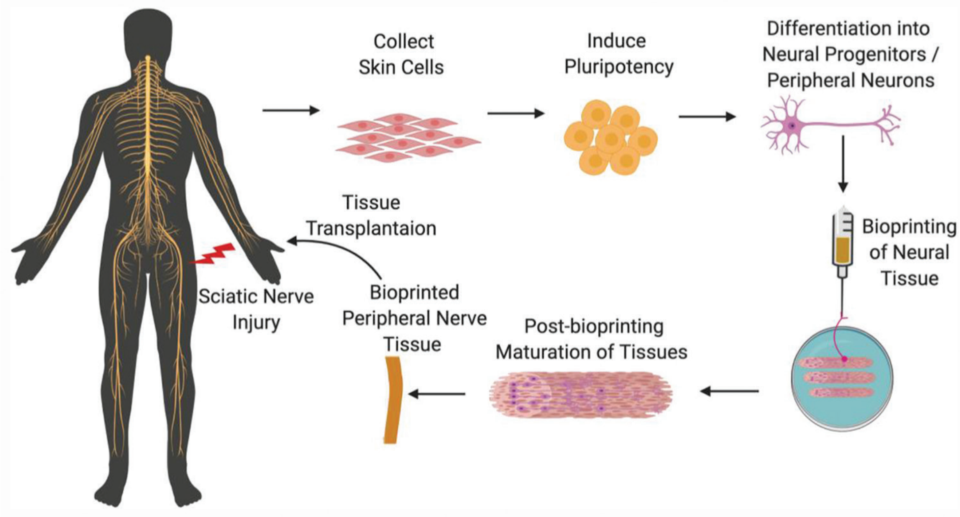

Figure 3. Workflow of three-dimensional bioprinting of peripheral nerve tissue for treatment of peripheral nerve injury. Sciatica is the pain due to the injury to the largest nerve in the body. Extreme case of sciatica needs surgical intervention and if possible, regenerative therapy. The autologous peripheral tissues can be collected from the patient, reprogram to induced pluripotent stem cells and differentiate to peripheral nerve tissue progenitors or peripheral neurons, then bioprint using a suitable scaffold material, allow the maturation of the bioprinted tissue in a bioreactor and transplant to the patient to repair and regenerate the injured nervous tissue.

its products, the cells should be free from any genetic integration of foreign DNA materials in the iPSC genome. mRNA-based, episomal, and recombinant protein-based introduction of transcription factors eliminate the risk of genomic integrations or aberrations in the iPSCs, which is an important step toward using the iPSCs for cell-based therapies in patients[93-95].

4.2.1 Type 1 diabetes mellitus (T1DM) treatment by the replacement of pancreatic beta cells

T1DM is known to be associated with the immune-mediated destruction of insulin producing pancreatic β-cells[96,97]. Effective treatment of T1DM is a long pending requirement in diabetes care. Islet cell transplantation is a traditional method of managing T1DM, but the transplanted islets are rejected by the host immune system. Bioprinted islets encapsulated in a suitable biocompatible material have been emerged as a treatment method to tackle this immune rejection. Biofabrication of 3D constructs of patient-derived iPSCs differentiated to insulin-producing pancreatic islet cells can potentially be an allogeneic source of cells for T1DM treatment. In 2019, Kim *et al.* successfully developed a pancreatic tissue-derived (pdECM)-bioink to provide the pancreatic tissue-specific microenvironment to bioprint the human iPSC-derived pancreatic islet cells. The study used decellularized porcine pancreas to provide the extra cellular matrix support for the growth of the cells[98]. Biotechnology companies such as Cellheal and Celprogen are working toward to bioprint the functional pancreatic tissues for diabetic treatment[99].

4.2.2 Reproductive system disorders

Ovarian failure is a major cause of infertility worldwide[100,101]. Functional 3D printed ovarian tissues would be a boon for infertility treatment. In 2017, Laronda *et al.* reported that the 3D bioprinted ovary using porous gelatin scaffold material could support the growth and maturation of printed ovarian follicles in laboratory conditions. The lab-grown ovary is tested in a sterilized mouse model and found to be functional. The bioprosthetic ovary used scaffold materials such as gelatin and gelatin methacrylate for bioprinting[102]. The structural features of the scaffold material such as pore size, pore geometry, and the surface contact area are the deciding factors for successful growth of functional ovarian tissue. Stem cells isolated from the patient's own ovarian tissue can serve as the starting material to bioprint the functional ovary.

4.2.3 Thyroid gland replacement in thyrectomized patients

Bioprinting of a functional vascularized mouse thyroid gland construct from embryonic tissue spheroids was reported by Bulenova *et al.* in 2017[103]. Self-assembling thyroid spheres, thyrocytes, and endothelial cells suspended in collagen gel were used for bioprinting the thyroid gland. The bioprinted construct was implanted in a hypothyroid mouse and it could normalize the blood thyroxine levels and body temperature in the tested mice. Bioprinting of functional mouse thyroid gland tissue represents a major advance in bioprinting technology and organ regeneration research. In March 2019, NASA announced a plan for bioprinting thyroid gland in international space station to study the effect of microgravity on organs[104].

4.3 Bioprinted iPSCs in disease modeling

The most advantageous aspect of using induced pluripotent cells in clinics is the ability of reprogramming of autologous cells taken directly from patients**.** At present, the majority of disease modeling studies makes use of the traditional 2D cultures. Any monogenic or polygenic disease conditions can be re-created in a cell culture system[83]. While 2D cultures are good to understand the molecular level interactions, they possess several limitations including lack of heterogenic cell environment and the cell to cell communication cues[105]. The disease progression hugely depends on the extracellular matrix (ECM) mechanics and the cell to cell interactions[106]. Cellular phenotypes and the non-cell autonomous disease pathogenesis require mimicking the disease conditions in a more realistic 3D environment. 3D disease models would help in understanding the disease mechanism in detail in the early stages of the disease[107,108]. A few examples of disease modeling in cardiac, neurodegenerative and neurodevelopmental diseases and oncology are briefly discussed in the following sections.

4.3.1 Cardiac diseases

Cardiovascular diseases remain the leading cause of death in the developed world, accounting for more than 30% of all deaths. Collection of cardiac tissue from patients with disease causing mutations for genetic studies and functional analyses is a highly invasive procedure. iPSCs derived from the peripheral tissues of patients with disease specific mutations are a valuable tool to study the cardiac pathophysiology and drug development. Cardiac tissues were biofabricated using hydrogels and supporting cells such as cardiomyocytes, endothelial cells, smooth muscle cells, and fibroblasts[109,110]. The cells were cocultured and engineered to resemble their natural physiological microenvironment and recapitulate coordinated contractile and electrophysiological interactions with the ECM and heterogeneous cell types that make up the myocardial tissue environment[111]. The iPSC-derived cardiac cells were successfully used to model cardiac diseases such as dilated cardiomyopathy and myocardial infarction[112]. These disease models help identifying the cellular phenotypes critical to cardiac pathology[113,114]. The microfluidic organ-on-chip methods were also developed to evaluate the vascular perfusion in cardiac tissue. The tissue composition and architecture of the *in vitro* 3D microdevice can be precisely defined using microfabrication methods[115-117]. The iPSC and embryonic stem cell derived organ-on-chip systems are being used for modeling a wide range of diseases, including dilated cardiomyopathy, kidney glomerular injury, and wound healing[118,119].

4.3.2 Neurodegenerative and neurodevelopmental diseases

4.3.2.1 Alzheimer's disease (AD)

AD is a progressive neurodegenerative disorder characterized by loss of cognition and disruption of basic functions, such as swallowing, walking, attention, and memory[120]. All major nerve cell types can be differentiated from iPSCs and can be cultured in complex conditions, which mimic the AD conditions. Precise Genome editing techniques can be used to introduce or correct AD-linked mutations to examine phenotypes in isogenic backgrounds cells[14]. It has become increasingly clear in recent years that multiple different brain cell types can contribute to AD progression[121]. Thus, examining their interactions and impacts on each other are of critical importance. The iPSCs can be differentiated into neural crest or neural progenitor cells, which can subsequently be patterned to different neuron subtypes including glutamatergic, GABAergic, cholinergic, and dopaminergic neurons[122-124]. 3D bioprinted AD models will facilitate the development of effective therapeutics to combat AD-induced dementia. Moreover, bioprinted AD tissue models can serve as a more humanized model system for AD drug testing, as many drugs tried in experimental animals failed in clinical trials due to species variability[125,126].

4.3.2.2 Parkinson’s disease (PD)

PD is the second most common neurodegenerative disorder[127]. Studies using iPSC-derived dopaminergic neurons from patients with monogenic and sporadic PD have successfully illustrated key features of PD pathophysiology, including impaired mitochondrial function, increased oxidative stress, and accumulation of α-synuclein protein, namely, Lewy bodies[128]. Using iPSC-derived dopaminergic neurons from PD patients with mutations in the disease causing genes, many investigators have drawn mechanistic insights on how mutations of these genes are linked to PD. Coculturing glial cells and neurons both derived from iPSCs of PD patients should therefore be another platform to advance insights into the multifactorial pathogenesis of PD. Bioprinted dopaminergic neurons can be treated with neurotoxins such as 6-hydroxydopamine, 1-methyl-4-phenyl-1,2,3,6-tetrahydropyridine, paraquat, and rotenone to induce PD like syndrome to study PD pathogenesis[129-131].

4.3.2.3 Amyloid lateral sclerosis (ALS)

ALS is the most prevalent motor neuron (MN) disease characterized by the progressive loss of the upper and lower MNs, leading to muscular atrophy, paralysis, and death within 5 years after the first diagnosis[130]. The iPSC-derived disease models of ALS showed increased oxidative stress and DNA damage in neurons. ALS specific mutations and altered transcriptome profile were also noticed in the iPSC models. Osborne *et al.* reported the effectiveness of the small molecule vardenafil, in regaining the resilience of MNs by regulating the insulin-like growth factor-II signaling in an iPSC-derived ALS model[132]. Researchers created 3D bioprinted ALS disease model using iPSC-derived MNs from a patient with *TDP-43* gene mutation. *TDP-43* gene mutation causes sporadic ALS. Bioprinted iPSC derived autologous tissue models of ALS disease serve as a valuable tool for studying the disease pathology as well as aid in the screening of personalized drugs against the disease[133].

4.3.3 Bioprinted iPSCs in oncology

The iPSCs derived from cancer tissues present a range of new opportunities for the study of human cancer. If human cancer cells were converted to pluripotency and then allowed to differentiate back into specific cancer tissue, they might shed light on the early stages of cancer[134].

Although 3D printing was developed decades ago, recent times witnessing a huge jump in adapting this versatile technology to the field of cancer modeling by fabricating sophisticated biological structures typical to cancer tissues. The cancer cells could be isolated from surgically removed cancer tissues. The isolated tumor cells are reprogrammed to pluripotent state by introducing the four transcription factors Oct4, Sox2, Klf4, and c-myc using a suitable method. The colonies are grown for a period of 2 – 4 weeks and cells with pluripotent stem cell morphology and molecular characters are expanded to create specific cancer iPSC lines[135]. These lines are differentiated into the tumor cell type of origin. The iPSC-derived differentiated cells could be then bioprinted into tumor tissues which mimic the tumor microenvironment (TME). The commonly used cancer bioprinting methods are: Inkject printing, extrusion-based printing, lase-assisted printing, and SLA. The tissues can be 3D bioprinted in the format of spheroids, organoids, coculture with other tumor TME cells, and organ-on chip. Improvements in the 3D bioprinting technology enable to distribute the cancer derived iPSCs in a 3D space with high precision and reproducibility. The 3D bioprinted tissues can be used as cancer tissue-on-chip models or transplanted into animal models to study different stages of cancer pathogenesis.

The most important hurdle in establishing iPSC-derived cancer models are the variation of intrinsic transcription factors in the cancer cells. This variation can affect the reprogramming efficiency of tumor cells. Many published studies showed that cancer cells are generally difficult to reprogram than normal cells[136]. The differentiation of cancer iPSCs to its initial tumor cell of origin also appears tedious and inconsistent. The success rate of establishing a cancer iPSC depends on the type cancer. So far, the successful reprogramming of myeloid tumors is established[137-139]. Establishing protocols for generating cancer iPSCs can help to model cancer progression, to understand the complex cancer genetics, and contribution of TME in cancer progression, anti-cancer drug development, and precision oncology (**Figure 4**).

4.4 Bioprinted iPSCs for drug and cosmetic testing

4.4.1 Bioprinted iPSCs for drug testing

More than 90% of drug molecules under different phase of clinical trials fail to reach market because of unanticipated toxicity to vital organs or lack of efficacy. This failure rate is partly attributed to the use of overly simplistic 2D cell culture-based assays[140]. The spectrum of activity of most of the drug molecules varied across the species, so animal testing has limited predictive value[107]. 3D bioprinting and iPSC technology enable printing of

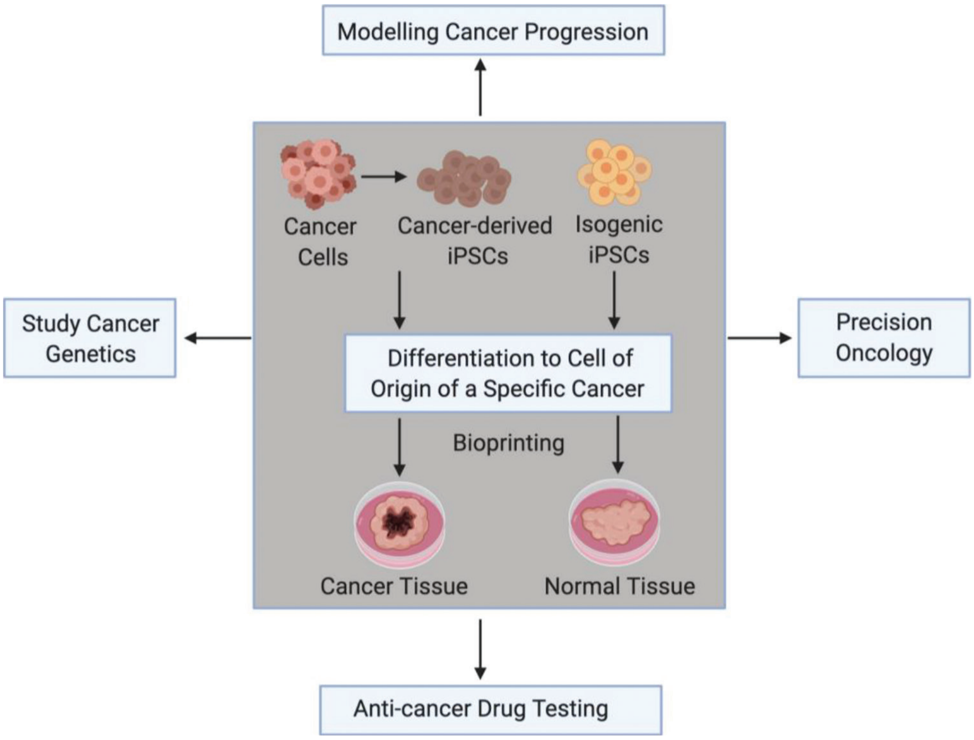

Figure 4. Bioprinted cancer tissue with induced pluripotent stem cell (iPSC)-derived cells: Establishing protocols for generating cancer iPSCs can help to model cancer progression, to understand the complex cancer genetics, and contribution of tumor microenvironment in cancer progression, anti-cancer drug development, and precision oncology.

any tissue in its native architecture by preserving the complexity of cellular pathways, cell-cell interactions, and cellular-microenvironment interactions. The tissue microenvironment is critical for the understanding of drug acting mechanisms in humans[141]. The use of 3D bioprinted tissue is predicted to be an integral part of future drug discovery research for improved *in vitro* assays with better predictive value.

4.4.2 Cosmetics testing

The European Union Cosmetics Directive was introduced in 1976 to enforce high safety standards for cosmetics across the EU member states. In 2009, the EU commission has introduced new directives to phasing out animal testing for cosmetic products. The directive bans the testing of the cosmetic products and cosmetic ingredients on animals. The law even prohibits the marketing of finished cosmetic products and ingredients tested on animals in the European Union[142]. Hence, the cosmetic industry is looking for methods to replace the animal testing. Bioprinted artificial skin tissue can substitute the use of animals for cosmetics testing (**Figure 5**). At present, the human skin models required for cosmetic testing are manufactured by layering fibroblasts in a collagen hydrogel, then adding keratinocytes on top. The cells are allowed to differentiate and mature into the different epidermal layers. This type of artificial skin models is simple and would not exactly reflect the complexity of the native skin. Advanced bioprinting technology and iPSCs as cell source allow fabrication of more realistic artificial skin models for drug testing as well as for regenerative medicine[143]. This would help develop skin models with different skin types with respect to race (Asian, Caucasian, etc.), character (dry, oily, etc.), or other specific skin types depending on the intended use of the cosmetic as these models incorporate iPSC-derived cells. Collagen-based skin construct reinforced with biocompatible materials such as polycaprolactone (PCL) mesh prevented the contraction of collagen during tissue maturation and enable manufacturing of biomimetic human skin models[144,145]. Other biomaterials such as polylactic acid, Pluronic, alginate, chitosan, hyaluronic acid, fibrin, and

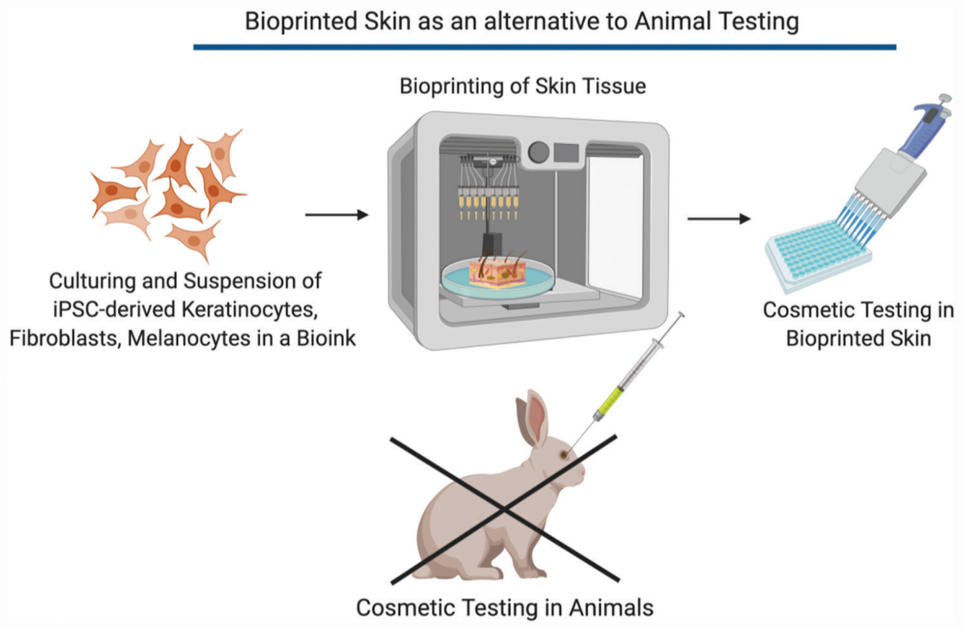

Figure 5. Bioprinting of human skin tissue models for cosmetic testing to replace the animal testing procedures. Use of induced pluripotent stem cell-derived skin cells would help develop skin models with different skin types (Asian, Caucasian, etc.), character (dry, oily, etc.), or other specific skin types depending on the intended use of the cosmetic.

gelatin, or a combination of PEGDA and GelMA were used as the scaffold material for printing skin models[145-147].

5 Bioinks used in iPSC bioprinting

Native tissue has complex architecture consisting of different cell types, ECM materials, growth factors, and many signaling molecules. ECM is organized in a highly delicate manner in a tissue to serve the tissue specific functions such as shape, consistency, mechanical strength, and molecular miscibility. Bioinks are cell laden hydrogels containing ECM components of the tissue to be printed. The materials used in the bioinks should be biocompatible without eliciting any undesirable response inside the body, should allow seamless printing, and should have tissue compatible rheological properties[56]. The bioink components can be natural, synthetic, different types of cells, and soluble growth factors specific for the cell types used. Natural polymers such as collagen, gelatin, fibronectin, laminin, and silk fibroin have been widely used in bioinks to augment cell attachment and migration in the matrix material[148] Polysaccharides such as alginate, agarose, and chitosan are also widely using in bioinks. Alginate is obtained from a type of brown algae and is widely used in 3D bioprinting applications due to its biocompatibility, promotion of cell proliferation, low price, and the ability of crosslinking in calcium ion solutions. However, alginate lacks sufficient mechanical stiffness for 3D bioprinting. Agarose is another biocompatible polysaccharide but it liquifies above physiological temperatures. Chitin and chitosan obtained from crustaceous animal are widely used polysaccharide component of bioinks, but it is slow in solidification. The methacrylated form of gelatin (GelMA) is a popular bioink component to print iPSCs which possess easily tunable physiochemical properties to use in bioprinters[149].

Still, many of these polysaccharides are too fragile and lack sufficient mechanical strength to retain in the transplant tissue site and often suffer from low mechanical properties, and thus, other materials have been combined as additive elements in the bioinks[150]. PCL and Poly (propylene fumarate) are polymers utilized in bioprinting due to its superior viscoelastic and rheological properties, biodegradability, and biocompatibility compared to the natural compounds. Synthetic hydrogels such as PEGDA are used as resins in 3D bioprinting, where cells can be entrapped[147]. The major limitation of these kind of hydrogels is that the bioprinted structure tends to collapse because of low viscosity and low mechanical strength[151]. New generation bioprinters have enabled us to print combinatorial bioinks with spatial and nanoscale resolution in seamless swift ways, aiming to reproduce the complex architecture of the native tissues. There are different types of bioinks available depends up on the tissue structure. One example is that researchers bioprinted hepatic tissue constructs using iPSC derived hepatocytes, endothelial cells, and mesenchymal cells resuspended in two different bioinks; GelMA with stiffness similar to healthy liver tissues, and a mix of glycidyl methacrylate-hyaluronic acid/GelMA which supported vascularization[73,152]. New generation polymers responsive to light, thermal, magnetic, humidity, and pH stimuli would allow the 3D bioprinting to leap to the next level.

6 Challenges associated with the use of reprogrammed iPSCs and bioprinting:

The combinatorial application of 3D bioprinting and iPSC technologies would have a major impact on regenerative medicine research. However, how much have we achieved to take this technique to clinics and how far we have to go? Many obstacles still remain regarding the production of safer iPSCs that are to be resolved to take full advantage of this technology for therapeutic purpose[67]. One of the most important problems is the use of retroviral and lentiviral vectors to introduce the transcription factor genes into somatic cells for cell reprogramming, which can cause mutagenesis and tumor induction in the host cell. The iPSCs derived using viral vectors may be still suitable for the study of disease mechanisms or for drug testing but they lack the suitability for clinical bioprinting. The use of non-integrative methods and small molecules to activate the pluripotency program in somatic cells represents the safest approach to produce clinical grade iPSCs cells. High throughput screening to identify small molecules for cell reprogramming is ongoing in many laboratories, with a goal to establish iPSCs free of any exogenously introduced DNA fragments. Incompletely differentiated cells evoked immune response in transplanted animals[153]. Therefore, obtaining completely differentiated cells for therapeutic purpose are of prime importance. Futuristic technology should be focused on establishing safe strategies for genetic modification of iPSCs, devise efficient methods for differentiation and purification of iPSCs into required cell types *in vitro* for transplantation.

After production of iPSCs, there are limitations in the bioprinting process itself and associated challenges in the preparation of optimized bioinks suitable for each cell type. 3D bioprinting has the advantage of reconstructing complex structures from computed tomography or magnetic resonance imaging images and producing accurate structures from predetermined digital designs such as computer-aided design models. The support scaffold materials with suitable mechanical and biological properties can be designed and printed using advanced 3D printers. Directed differentiation of printed iPSCs to different cell lineages is required for organ printing. When we use undifferentiated iPSCs for bioprinting, the printing parameters should be adjusted to avoid any mechanical damage to the cells, as iPSCs are highly sensitive cells. Depending on the type of the bioprinting method used, the cells are exposed to high shear forces, radiation-induced damage, and electric or thermal stresses during the printing process[154,155].

Vascularization and innervation of the bioprinted tissue are a challenge to achieve. Bioprinted iPSC constructs are unable to form long-term viable and vascularized tissue. To resolve this problem, researchers at Wyss institute recently developed a method called sacrificial writing into functional tissue (SWIFT), which is a multistep biomanufacturing process that involves creating organ building blocks composed of hundreds of thousands of iPSCs and then rapidly 3D bioprinting vasculature into those building blocks[70]. The SWIFT method could create a perfusable cardiac tissue that fuses and beats synchronously for more than a week, taking the field of bioprinting vascularized functional tissues using iPSCs to the next level.

7 Future perspectives for iPSCs in bioprinting

Despite the challenges associated with the use of reprogrammed iPSCs and limitations of bioprinting, the potential of bioprinting iPSC-derived tissue is tremendous in the health-care field. Resolution of these challenges will have significant implications in the understanding of human diseases and will have major effects on the treatment of these diseases. Future perspectives of bioprinting iPSCs should focus on:

- Establishing xeno-free and footprint-free clinical-grade iPSC reprogramming protocols: The use of non-integrative methods and small molecules should be further explored. High throughput screening to identify small molecules for cell reprogramming to establish iPSCs free of any exogenously introduced DNA fragments would be potential area to focus on.
- Development of tissue-specific bioinks for bioprinting: New bioinks with tunable mechanical and rheological properties that mimic the native tissue ECM is to be developed and a deeper understanding of cell-bioink interactions must be sought as the mechanobiology and the molecular pathways would have a major effect on the differentiation of the bioprinted iPSCs.
- Improved bioprinting strategies to mitigate harmful effects on cells: Since iPSCs are sensitive cells (not as sturdy as cancer cell lines), the mechanical, thermal, or chemical stressors induced by the bioprinting process might result in cell-phenotype changes and functionality. Strategies to mitigate the exposure of cells to these process-induced stressors must be developed.
- Integrated bioreactor systems for tissue maturation: Bioprinting of functional tissues with iPSC-derived cells would be successful only if they can be matured and maintained over a long-term in physiologically-relevant

environments. Hence, development of suitable post-processing strategies such as integrated perfusion bioreactor systems becomes necessary.
- Pathway for clinical translation: A coordinated effort between the clinicians, scientists, and bioengineers in solving the technological limitations and support from the government and policy-makers would go a long way in establishing a pathway for clinical translation of bioprinted iPSC-derived tissues for regenerative medicine, disease modeling and drug testing.

Conflicts of interest

The authors declare no conflict of interest.

References

1. Takahashi K, Yamanaka S, 2006, Induction of Pluripotent Stem Cells from Mouse Embryonic and Adult Fibroblast Cultures by Defined Factors. *Cell*, 126:663–76. DOI: 10.1016/j.cell.2006.07.024.
2. Yu J, Vodyanik MA, Smuga-Otto K, *et al*., 2007, Thomson, Induced Pluripotent Stem Cell Lines Derived from Human Somatic Cells. *Science*, 318:1917–20. DOI: 10.1126/science.1151526.
3. Zhang Y, Chen K, Sloan SA, *et al*., 2004, An RNA-sequencing Transcriptome and Splicing Database of Glia, Neurons, and Vascular Cells of the Cerebral Cortex. *J Neurosci*, 34:11929–47. DOI: 10.1523/jneurosci.1860-14.2014.
4. Chappell J, Dalton S, 2013, Roles for MYC in the Establishment and Maintenance of Pluripotency. *Cold Spring Harb. Perspect Med*, 3:a014381. DOI: 10.1101/cshperspect.a014381.
5. Zhang P, Zhang X, Brown J, *et al*., 2010, Global Healthcare Expenditure on Diabetes for 2010 and 2030. *Diabetes Res Clin Pract*, 87:293–301. DOI: 10.1016/j.diabres.2010.12.025.
6. Han JW, Yoon YS, 2011, Induced Pluripotent Stem Cells: Emerging Techniques for Nuclear Reprogramming. *Antioxidants Redox Signal*, 15:1799–820. DOI: 10.1089/ars.2010.3814.
7. An Z, Liu P, Zheng J, *et al*., 2019, Sox2 and Klf4 as the Functional Core in Pluripotency Induction without Exogenous Oct4. *Cell Rep*, 29:1986–2000. DOI: 10.1016/j.celrep.2019.10.026.
8. Chen IP, Fukuda K, Fusaki N, *et al*., 2013, Induced Pluripotent Stem Cell Reprogramming by Integration-free Sendai Virus Vectors from Peripheral Blood of Patients with Craniometaphyseal Dysplasia. *Cell Reprogram*, 15:503–13. DOI: 10.1089/cell.2013.0037.
9. Sridharan R, Tchieu J, Mason MJ, *et al*., 2009, Role of the Murine Reprogramming Factors in the Induction of Pluripotency. *Cell*, 136:364–77. DOI: 10.1016/j.cell.2009.01.001.
10. Kim JB, Greber B, Arazo-Bravo MJ, *et al*., 2009, Direct Reprogramming of Human Neural Stem Cells by OCT4. *Nature*, 461:649–53. DOI: 10.1038/nature08436.
11. Stadtfeld M, Hochedlinger K, 2010, Induced Pluripotency: History, Mechanisms, and Applications. *Genes Dev*, 24:2239–63. DOI: 10.1101/gad.1963910.
12. Yee JK, 2010, Turning Somatic Cells into Pluripotent Stem Cells. *Nat Educ*, 3:25.
13. Mertens J, Reid D, Lau S, *et al*., 2018, Aging in a Dish: iPSC-Derived and Directly Induced Neurons for Studying Brain Aging and Age-Related Neurodegenerative Diseases. *Annu Rev Genet*, 52:271–93. DOI: 10.1146/annurev-genet-120417-031534.
14. Penney J, Ralvenius WT, Tsai LH, 2019, Modeling Alzheimer's Disease with iPSC-Derived Brain Cells. *Mol Psychiatry*, 25:148–67. DOI: 10.1038/s41380-019-0468-3.
15. Chen IY, Matsa E, Wu JC, 2016, Induced Pluripotent Stem Cells: At the Heart of Cardiovascular Precision Medicine. *Nat Rev Cardiol*, 13:333–49. DOI: 10.1038/nrcardio.2016.36.
16. Koch L, Deiwick A, Franke A, *et al*., 2018, Laser Bioprinting of Human Induced Pluripotent Stem Cells the Effect of Printing and Biomaterials on Cell Survival, Pluripotency, and Differentiation. *Biofabrication*, 10:035005. DOI: 10.1088/1758-5090/aab981.
17. Maiullari F, Costantini M, Milan M, *et al*., 2018, A Multi-cellular 3D Bioprinting Approach for Vascularized Heart Tissue Engineering Based on HUVECs and iPSC-Derived Cardiomyocytes. *Sci Rep*, 8:13532. DOI: 10.1038/s41598-018-31848-x.
18. Yeung E, Fukunishi T, Bai Y, *et al*., 2019, Cardiac Regeneration Using Human-induced Pluripotent Stem Cell-derived Biomaterial-free 3D-bioprinted Cardiac Patch *In Vivo*. *J Tissue Eng Regen Med*, 13:2031-9. DOI: 10.1002/term.2954.
19. Faulkner-Jones A, Fyfe C, Cornelissen DJ, *et al*., 2015, Bioprinting of Human Pluripotent Stem Cells and their Directed Differentiation into Hepatocyte-like Cells for the Generation of Mini-livers in 3D. *Biofabrication*, 7:044102. doi.org/10.1088/1758-5090/7/4/044102.
20. Nguyen HX, Hooshmand MJ, Saiwai H, *et al*., 2017, Systemic Neutrophil Depletion Modulates the Migration and Fate of Transplanted Human Neural Stem Cells to Rescue Functional Repair. *J Neurosci*, 37:9269–87. DOI: 10.1523/jneurosci.2785-16.2017.

21. Li Y, Lu B, Sheng L, *et al*., 2018, Hexokinase 2-dependent Hyperglycolysis Driving Microglial Activation Contributes to Ischemic Brain Injury. *J Neurochem*, 144:186–200. DOI: 10.1111/jnc.14267.
22. Koch SC, Acton D, Goulding M, 2018, Spinal Circuits for Touch, Pain, and Itch. *Annu Rev Physiol*, 80:189–217. DOI: 10.1146/annurev-physiol-022516-034303.
23. Gungor-Ozkerim PS, Inci I, Zhang YS, *et al*., 2018, Bioinks for 3D Bioprinting: An Overview. *Biomater Sci*, 6:915–46. DOI: 10.1039/c7bm00765e.
24. Montero FE, Rezende RA, da Silva JV, *et al*., 2019, Development of a Smart Bioink for Bioprinting Applications. *Front Mech Eng*, 5:56. DOI: 10.3389/fmech.2019.00056.
25. Noor N, Shapira A, Edri R, *et al*., 2019, 3D Printing of Personalized Thick and Perfusable Cardiac Patches and Hearts. *Adv Sci*, 6:3–10. DOI: 10.1002/advs.201970066.
26. Gopinathan J, Noh I, 2018, Recent Trends in Bioinks for 3D Printing. *Biomater Res*, 22:11. DOI: 110.1186/s40824-018-0122-1.
27. Gu J, Bradbury J, Xiong C, *et al*., 2018, Non-autoregressive Neural Machine Translation. 6th International Conference Learning Representations 2018 Conference Track Proceeding.
28. Rao ZMS, Malik N, 2012, Assessing iPSC Reprogramming Methods for their Suitability in Translational Medicine. *J Cell Biochem*, 113:3061–8. DOI: 10.1002/jcb.24183.
29. Kamath A, Ternes A, McGowan S, *et al*., 2017, Efficient Method to Create Integration-free, Virus-free, Myc and Lin28-free Human Induced Pluripotent Stem Cells from Adherent Cells. *Future Sci OA*, 3:FSO211. DOI: 10.4155/fsoa-2017-0028.
30. Malik N, Rao MS, 2013, A Review of the Methods for Human iPSC Derivation. *Methods Mol Biol*, 997:23–33.
31. Omole AE, Fakoya AO, 2018, Ten Years of Progress and Promise of Induced Pluripotent Stem Cells: Historical Origins, Characteristics, Mechanisms, Limitations, and Potential Applications. *PeerJ*, 6:e4370. DOI: 10.7717/peerj.4370.
32. Shi Y, Inoue H, Wu JC, *et al*., 2017, Induced Pluripotent Stem Cell Technology: A Decade of Progress. *Nat Rev Drug Discov*, 16:115–30. DOI: 10.1038/nrd.2016.245.
33. Yamanaka S, 2012, Induced Pluripotent Stem Cells: Past, Present, and Future. *Cell Stem Cell*, 10:678–84. DOI: 10.1016/j.stem.2012.05.005.
34. Takahashi K, Tanabe K, Ohnuki M, *et al*., 2007, Yamanaka, Induction of Pluripotent Stem Cells from Adult Human Fibroblasts by Defined Factors. *Cell*, 131:861–72. DOI: 10.1016/j.cell.2007.11.019.
35. Schlaeger TM, Daheron L, Brickler TR, *et al*., 2015, A Comparison of Non-integrating Reprogramming Methods. *Nat Biotechnol*, 33:58–63. DOI: 10.1038/nbt.3070.
36. Junying Y, Kejin H, Kim SO, *et al*., 2009, Human Induced Pluripotent Stem Cells Free of Vector and Transgene Sequences. *Science*, 324:797–801. DOI: 10.1126/science.1172482.
37. Shao L, Fujii H, Colmegna I, *et al*., 2009, Deficiency of the DNA Repair Enzyme ATM in Rheumatoid Arthritis. *J Exp Med*, 206:1435–49. DOI: 10.1084/jem.20082251.
38. Carey BW, Markoulaki A, Hanna J, *et al*., 2009, Reprogramming of Murine and Human Somatic Cells Using a Single Polycistronic Vector. *Proc Natl Acad Sci USA*, 106:157–62. DOI: 10.1073/pnas.0811426106.
39. McGrath PS, Diette N, Kogut I, *et al*., 2018, RNA-based Reprogramming of Human Primary Fibroblasts into Induced Pluripotent Stem Cells. *J Vis Exp*, 141:58687. DOI: 10.3791/58687.
40. Kogut I, McCarthy SM, Pavlova M, *et al*., 2018, High-efficiency RNA-based Reprogramming of Human Primary Fibroblasts. Nat Commun, 9:745. DOI: 10.1038/s41467-018-03190-3.
41. Qiao S, Deng Y, Li S, *et al*., 2019, Partially Reprogrammed Induced Pluripotent Stem Cells Using MicroRNA Cluster miR-302s in Guangxi Bama Minipig Fibroblasts. *Cell Reprogram*, 21:229–37. DOI: 10.1089/cell.2019.0035.
42. Baker M, 2009, MicroRNAs Boost Reprogramming, Boot Out cMyc. *Nat Reports Stem Cells*, 1:46. DOI: 10.1038/stemcells.2009.62 .
43. Hirschi KK, Li S, Roy K, 2014, Induced Pluripotent Stem Cells for Regenerative Medicine. *Annu Rev Biomed Eng*, 16:277–94. DOI: 10.1146/annurev-bioeng-071813-105108.
44. Worringer KA, Rand TA, Hayashi Y, *et al*., 2014, The Let-7/LIN-41 Pathway Regulates Reprogramming to Human Induced Pluripotent Stem Cells by Controlling Expression of Prodifferentiation Genes. *Cell Stem Cell*, 14:40–52. DOI: 10.1016/j.stem.2013.11.001.
45. Kim D, Kim CH, J. Il Moon, *et al*., 2009, Generation of Human Induced Pluripotent Stem Cells by Direct Delivery of Reprogramming Proteins. *Cell Stem Cell*, 4:472–6. DOI: 10.1016/j.stem.2009.05.005.
46. Zhou H, Wu S, Joo JY, *et al*., 2009, Generation of Induced Pluripotent Stem Cells Using Recombinant Proteins. *Cell Stem Cell*, 4:381–4. DOI: 10.1016/j.stem.2009.04.005.
47. Seo BJ, Hong YJ, Do JT, 2017, Cellular Reprogramming Using Protein and Cell-Penetrating Peptides. *Int J Mol Sci*, 18:552. DOI: 10.3390/ijms18030552.
48. Lin T, Wu S, 2015, Reprogramming with Small Molecules Instead of Exogenous Transcription Factors. *Stem Cells Int*,

2015:794632. DOI: 10.1155/2015/794632.

49. Huangfu D, Maehr R, Guo W, *et al*., 2008, Induction of Pluripotent Stem Cells by Defined Factors is Greatly Improved by Small-molecule Compounds. *Nat Biotechnol*, 26:795–7. DOI: 10.1038/nbt1418.
50. Shi Y, Desponts C, Do JT, *et al*., 2008, Induction of Pluripotent Stem Cells from Mouse Embryonic Fibroblasts by Oct4 and Klf4 with Small-Molecule Compounds. *Cell Stem Cell*, 3:568–74. DOI: 10.1016/j.stem.2008.10.004.
51. Vijayavenkataraman S, Kannan S, Cao T, *et al*., 2019, 3D-Printed PCL/PPy Conductive Scaffolds as Three-Dimensional Porous Nerve Guide Conduits (NGCs) for Peripheral Nerve Injury Repair. *Front Bioeng Biotechnol*, 7:266. DOI: 10.3389/fbioe.2019.00266.
52. Hou P, Li Y, Zhang X, *et al*., 2013, Pluripotent Stem Cells Induced from Mouse Somatic Cells by Small-molecule Compounds. *Science*, 341:651–4. DOI: 10.1126/science.1239278.
53. Zhang Y, Hu W, Ma K, *et al*., 2019, Reprogramming of Keratinocytes as Donor or Target Cells Holds Great Promise for Cell Therapy and Regenerative Medicine. *Stem Cell Rev Reports*, 15:680–9. DOI: 10.1007/s12015-019-09900-8.
54. Aasen T, Raya A, Barrero MJ, *et al*., 2008, Efficient and Rapid Generation of Induced Pluripotent Stem Cells from Human Keratinocytes. *Nat Biotechnol*, 26:1276–84. DOI: 10.1038/nbt.1503.
55. Sun N, Panetta NJ, Gupta DM, *et al*., 2009, Feeder-free Derivation of Induced Pluripotent Stem Cells from Adult Human Adipose Stem Cells. *Proc Natl Acad Sci USA*, 106:15720–5. DOI: 10.1073/pnas.0908450106.
56. Medvedev SP, Shevchenko AI, Zakian SM, 2010, Induced Pluripotent Stem Cells: Problems and Advantages when Applying them in Regenerative Medicine. *Acta Nat*, 2:18–27. DOI: 10.32607/20758251-2010-2-2-18-27.
57. Kim Y, Rim YA, Yi H, *et al*., 2016, The Generation of Human Induced Pluripotent Stem Cells from Blood Cells: An Efficient Protocol Using Serial Plating of Reprogrammed Cells by Centrifugation. *Stem Cells Int*, 2016:1329459. DOI: 410.1155/2016/1329459.
58. Okumura T, Horie Y, Lai CY, *et al*., 2019, Robust and Highly Efficient hiPSC Generation from Patient Non-mobilized Peripheral Blood-derived CD34+ Cells Using the Auto-erasable Sendai Virus Vector. *Stem Cell Res Ther*, 10:185. DOI: 10.1186/s13287-019-1273-2.
59. Corbett JL, Duncan SA, 2019, iPSC-Derived Hepatocytes as a Platform for Disease Modeling and Drug Discovery. *Front Med*, 6:265. DOI: 10.3389/fmed.2019.00265.
60. Kwong G, Marquez HA, Yang C, *et al*., 2019, Generation of a Purified iPSC-Derived Smooth Muscle-like Population for Cell Sheet Engineering. *Stem Cell Reports*, 13:499–514. DOI: 10.1016/j.stemcr.2019.07.014.
61. Abdul Manaph NP, Sivanathan KN, Nitschke J, *et al*., 2019, An Overview on Small Molecule-induced Differentiation of Mesenchymal Stem Cells Into Beta Cells for Diabetic Therapy. *Stem Cell Res Ther*, 10:2194. DOI: 10.1186/s13287-019-1396-5.
62. Tabar V, Studer L, 2014, Pluripotent Stem Cells in Regenerative Medicine: Challenges and Recent Progress. *Nat Rev Genet*, 15:82–92. DOI: 10.1038/nrg3563.
63. Kang H, Shih YR, Nakasaki M, *et al*., Small Molecule Driven Direct Conversion of Human Pluripotent Stem Cells into Functional Osteoblasts. *Sci Adv*, 2:e1600691. DOI: 10.1126/sciadv.1600691.
64. Ong CS, Yesantharao P, Huang CY, *et al*., 2018, 3D Bioprinting Using Stem Cells. *Pediatr Res*, 83:223–31.
65. Ozbolat IT, Hospodiuk M, 2016, Current Advances and Future Perspectives in Extrusion-based Bioprinting. *Biomaterials*, 76:321–43. DOI: 10.1016/j.biomaterials.2015.10.076.
66. Reid JA, Mollica PA, Johnson GD, *et al*., 2016, Accessible Bioprinting: Adaptation of a Low-cost 3D-Printer for Precise Cell Placement and Stem Cell Differentiation. *Biofabrication*, 8:025017. DOI: 10.1088/1758-5090/8/2/025017.
67. Gu Q, Tomaskovic-Crook E, Wallace GG, *et al*., 2017, 3D Bioprinting Human Induced Pluripotent Stem Cell Constructs for *In Situ* Cell Proliferation and Successive Multilineage Differentiation. *Adv Healthc Mater*, 6:1700175. DOI: 10.1002/adhm.201700175.
68. Colosi S, Soloperto B, Benedetti T, *et al*., 2019, 3D Bioprinted Human Cortical Neural Constructs Derived from Induced Pluripotent Stem Cells. *J Clin Med*, 8:1595. DOI: 10.3390/jcm8101595.
69. Nguyen D, Hägg DA, Forsman A, *et al*., 2017, Cartilage Tissue Engineering by the 3D Bioprinting of iPS Cells in a Nanocellulose/Alginate Bioink. *Sci Rep*, 7:6684. DOI: 10.1038/s41598-017-00690-y.
70. Skylar-Scott MA, Uzel SG, Nam LL, *et al*., 2019, Biomanufacturing of Organ-Specific Tissues with High Cellular Density and Embedded Vascular Channels. *Sci Adv*, 5:eaaw2459. DOI: 10.1126/sciadv.aaw2459.
71. Zhang C, Yang F, Cornelia R, *et al*., 2011, Hypoxia-inducible Factor-1 is a Positive Regulator of Sox9 Activity in Femoral Head Osteonecrosis. *Bone*, 48:507–13. DOI: 10.1016/j.bone.2010.10.006.
72. Sun AX, Lin H, Beck AM, *et al*., 2015, Projection

Stereolithographic Fabrication of Human Adipose Stem Cell-Incorporated Biodegradable Scaffolds for Cartilage Tissue Engineering. *Front Bioeng Biotechnol*, 3:115. DOI: 10.3389/fbioe.2015.00115.

73. Ma X, Qu X, Zhu W, *et al*., 2016, Deterministically Patterned Biomimetic Human iPSC-Derived Hepatic Model Via Rapid 3D Bioprinting. *Proc Natl Acad Sci*, 113:2206–11. DOI: 10.1073/pnas.1524510113.
74. Fairbanks BD, Schwartz MP, Bowman CN, *et al*., 2009, Photoinitiated Polymerization of PEG-diacrylate with Lithium Phenyl-2,4,6-Trimethylbenzoylphosphinate: Polymerization Rate and Cytocompatibility. *Biomaterials*, 30:6702–7. DOI: 10.1016/j.biomaterials.2009.08.055.
75. Ng WL, Lee JM, Zhou M, *et al*., 2020, Vat Polymerization-Based Bioprinting Process, Materials, Applications and Regulatory Challenges. *Biofabrication*, 12:022001. DOI: 410.1088/1758-5090/ab6034.
76. Fattah AR, Meleca E, Mishriki S, *et al*., 2016, *In Situ* 3D Label-Free Contactless Bioprinting of Cells through Diamagnetophoresis. ACS *Biomater Sci Eng*, 2:2133–8. DOI: 10.1021/acsbiomaterials.6b00614.
77. Gudapati H, Dey M, Ozbolat I, 2016, A Comprehensive Review on Droplet-based Bioprinting: Past, Present and Future. *Biomaterials*, 102:20–42. DOI: 10.1016/j.biomaterials.2016.06.012.
78. Guillotin B, Souquet A, Catros S, *et al*., 2010, Laser Assisted Bioprinting of Engineered Tissue with High Cell Density and Microscale Organization. *Biomaterials*, 31:7250–6. DOI: 10.1016/j.biomaterials.2010.05.055.
79. Li Y, Jiang X, Li L, *et al*., 2018, 3D Printing Human Induced Pluripotent Stem Cells with Novel Hydroxypropyl Chitin Bioink: Scalable Expansion and Uniform Aggregation. *Biofabrication*, 10:044101. DOI: 10.1088/1758-5090/aacfc3.
80. Ng WL, Chua CK, Shen YF, 2019, Print Me An Organ! Why We Are Not There Yet. *Prog Polym Sci*, 97:101145. DOI: 10.1016/j.progpolymsci.2019.101145.
81. Romanazzo S, Nemec S, Roohani I, 2019, iPSC Bioprinting: Where are we at? *Materials* (*Basel*), 12:2453. DOI: 10.3390/ma12152453.
82. McCauley HA, Wells JM, 2017, Pluripotent Stem Cell-derived Organoids: Using Principles of Developmental Biology to Grow Human Tissues in a Dish. *Development*, 144:958–62. DOI: 10.1242/dev.140731.
83. Liu C, Oikonomopoulos A, Sayed N, *et al*., 2018, Modeling Human Diseases with Induced Pluripotent Stem Cells: From 2D to 3D and Beyond. *Development*, 145:dev156166. DOI: 10.1242/dev.156166.
84. Zhang B, Gao L, Ma L, *et al*., 2017, 3D Bioprinting: A Novel Avenue for Manufacturing Tissues and Organs. *Engineering*, 5:777–94.
85. Varkey M, Visscher DO, van Zuijlen PP, *et al*., 2019, Skin Bioprinting: The Future of Burn Wound Reconstruction? *Burn Trauma*, 7:8171. DOI: 10.1186/s41038-019-0142-7.
86. Kamel RA, Ong JF, Eriksson E, *et al*., 2013, Tissue Engineering of Skin. *J Am Coll Surg*, 217:533–55.
87. Yang B, Lui C, Yeung E, *et al*., 2019, A Net Mold-Based Method of Biomaterial-Free Three-Dimensional Cardiac Tissue Creation. *Tissue Eng Part C Methods*, 25:243–52. DOI: 10.1089/ten.tec.2019.0003.
88. Vijayavenkataraman S, Kannan S, Cao T, *et al*., 2019, 3D-Printed PCL/PPy Conductive Scaffolds as Three-Dimensional Porous Nerve Guide Conduits (NGCs) for Peripheral Nerve Injury Repair. *Front Bioeng Biotechnol*, 7:266. DOI: 10.3389/fbioe.2019.00266.
89. Chen YM, Chen LH, Li MP, *et al*., 2017, Xeno-free Culture of Human Pluripotent Stem Cells on Oligopeptide-Grafted Hydrogels with Various Molecular Designs. *Sci Rep*, 7:45146. DOI: 10.1038/srep45146.
90. Wiley LA, Anfinson KR, Cranston CM, *et al*., 2017, Generation of Xeno-Free, cGMP-Compliant Patient-Specific iPSCs from Skin Biopsy. *Curr Protoc Stem Cell Biol*, 42:4A.12.1–4A.12.4. Doi: 10.1002/cpsc.30.
91. Pruksananonda K, Rungsiwiwut R, 2016, Moving toward xeno-free culture of human pluripotent stem cells. In: Pluripotent Stem Cells: From the Bench to the Clinic. BoD-Books on Demand, Norderstedt, Germany. DOI: 10.5772/62770.
92. Boreström C, Simonsson S, Enochson L, *et al*., 2014, Footprint-Free Human Induced Pluripotent Stem Cells From Articular Cartilage With Redifferentiation Capacity: A First Step Toward a Clinical-Grade Cell Source. *Stem Cells Transl Med*, 3:433–47. DOI: 10.5966/sctm.2013-0138.
93. Attwood S, Edel M, 2019, iPS-Cell Technology and the Problem of Genetic Instability can it ever be Safe for Clinical Use? *J Clin Med*, 8:288. DOI: 10.3390/jcm8030288.
94. Matz P, Wruck W, Fauler B, *et al*., 2017, Footprint-free Human Fetal Foreskin Derived iPSCs: A Tool for Modeling Hepatogenesis Associated Gene Regulatory Networks. *Sci Rep*, 7:310. DOI: 10.1038/s41598-017-06546-9.
95. Atkinson MA, Eisenbarth GS, Michels AW, 2014, Type 1 Diabetes. *Lancet*, 383:69–82.
96. Katsarou A, Gudbjörnsdottir S, Rawshani A, *et al*., 2017, Type 1 Diabetes Mellitus. *Nat Rev Dis Prim*, 3:17016.
97. Kim J, Shim IK, Hwang DG, *et al*., 2019, 3D Cell Printing

of Islet-laden Pancreatic Tissue-derived Extracellular Matrix Bioink Constructs for Enhancing Pancreatic Functions. *J Mater Chem B*, 7:1773–81. DOI: 10.1039/c8tb02787k.

98. Taalesen H, Ketner MA, 2018, Milestone in Development of 3D Bioprinting of Biomimetic Pancreas to Treat Diabetes. University of Oslo, Hybrid Technology Hub, Oslo. Available from: https://www.med.uio.no/hth/english/news-and-events/news/3dbioprinting.html. [Last accessed on 2020 Jun 20].
99. Davies S, 2016, Successfully 3D Print Functioning Pancreas Model. Mag Des Innovations. Celprogen Inc., Torrance.
100. Ebrahimi M, Asbagh FA, 2011, Pathogenesis and Causes of Premature Ovarian Failure: An Update. *Int J Fertil Steril*, 5:54–65.
101. Laronda MM, Rutz AL, Xiao S, *et al*., 2017, A Bioprosthetic Ovary Created Using 3D Printed Microporous Scaffolds Restores Ovarian Function in Sterilized Mice. *Nat Commun*, 8:15261. DOI: 10.1038/ncomms15261.
102. Irvine SA, Agrawal A, Lee BH, *et al*., 2015, Printing cell-laden gelatin constructs by free-form fabrication and enzymatic protein crosslinking. *Biomed Microdevices*, 17:16. DOI: 10.1007/s10544-014-9915-8.
103. Bulanova EA, Koudan EV, Degosserie J, *et al*., 2017, Bioprinting of a Functional Vascularized Mouse Thyroid Gland Construct. *Biofabrication*, 9:034105. DOI: 10.1088/1758-5090/aa7fdd.
104. International Space Station Program Science Forum, 2018, International Space Station Benefits for Humanity. 3rd ed. NASA. Available from: https://www.nasa.gov/sites/default/files/atoms/files/benefits-for-humanity_third.pdf. [Last accessed on 2020 Jun 20].
105. Hamazaki T, El Rouby N, Fredette NC, *et al*., 2017, Concise Review: Induced Pluripotent Stem Cell Research in the Era of Precision Medicine. *Stem Cells*, 35:545–50. DOI: 10.1002/stem.2570.
106. Walker C, Mojares E, Del Río Hernández A, 2018, Role of Extracellular Matrix in Development and Cancer Progression. *Int J Mol Sci*, 19:3028. DOI: 10.3390/ijms19103028.
107. Ma X, Liu J, Zhu W, *et al*., 2018, 3D Bioprinting of Functional Tissue Models for Personalized Drug Screening and *In Vitro* Disease Modeling. *Adv Drug Deliv Rev*, 132:235–51. DOI: 10.1016/j.addr.2018.06.011.
108. Antill-O'Brien N, Bourke J, O'Connell CD, 2019, Layer-by-layer: The case for 3D bioprinting neurons to create patient-specific epilepsy models. *Materials* (*Basel*), 12:3218. DOI: 10.3390/ma12193218.
109. Alonzo M, AnilKumar S, Roman B, et al., 2019, 3D Bioprinting of Cardiac Tissue and Cardiac Stem Cell Therapy. Transl Res, 211:64–83. DOI: 10.1016/j.trsl.2019.04.004.
110. Zimmermann WH, Cesnjevar R, 2009, Cardiac Tissue Engineering: Implications for Pediatric Heart Surgery. *Pediatr Cardiol*, 30:716–23. DOI: 10.1007/s00246-009-9405-6.
111. Tzatzalos E, Abilez OJ, Shukla P, *et al*., 2016, Engineered Heart Tissues and Induced Pluripotent Stem Cells: Macro and Microstructures for Disease Modeling, Drug Screening, and Translational Studies. *Adv Drug Deliv Rev*, 96:234–44. DOI: 10.1016/j.addr.2015.09.010.
112. Yoshida Y, Yamanaka S, 2017, Induced Pluripotent Stem Cells 10 Years Later. *Circ Res*, 120:1958–68. DOI: 10.1161/circresaha.117.311080.
113. Hinson JT, Chopra A, Nafissi N, *et al*., 2015, Titin Mutations in iPS Cells Define Sarcomere Insufficiency as a Cause of Dilated Cardiomyopathy. *Science*, 349:982–6. DOI: 10.1126/science.aaa5458.
114. Tiburcy M, Hudson JE, Balfanz P, *et al*., 2017, Defined Engineered Human Myocardium with Advanced Maturation for Applications in Heart Failure Modeling and Repair. *Circulation*, 135:1832–47.
115. Takebe T, Zhang B, Radisic M, 2017, Synergistic Engineering: Organoids Meet Organs-on-a-Chip. *Cell Stem Cell*, 21:297–300. DOI: 10.1016/j.stem.2017.08.016.
116. Bhatia SN, Ingber DE, 2014, Microfluidic Organs-on-chips. *Nat Biotechnol*, 32:760–72. DOI: 10.1038/nbt.2989.
117. Huh D, Matthews BD, Mammoto A, *et al*., 2010, Ingber, Reconstituting Organ-level Lung Functions on a Chip. *Science*, 328:1662–8. DOI: 10.1126/science.1188302.
118. Low LA, Tagle DA, 2017, Tissue Chips-innovative Tools for Drug Development and Disease Modeling. *Lab Chip*, 17:3026–36. DOI: 10.1039/c7lc00462a.
119. Eiraku M, Watanabe K, Matsuo-Takasaki M, *et al*., 2008, Self-Organized Formation of Polarized Cortical Tissues from ESCs and its Active Manipulation by Extrinsic Signals. *Cell Stem Cell*, 3:519–32. DOI: 10.1016/j.stem.2008.09.002.
120. Montine TJ, Phelps CH, Beach TG, *et al*., 2012, National Institute on Aging-Alzheimer's Association Guidelines for the Neuropathologic Assessment of Alzheimer's Disease: A Practical Approach. *Acta Neuropathol*, 123:1–11. DOI: 10.1007/s00401-011-0910-3.
121. van Giau V, Lee H, Shim KH, *et al*., 2018, Genome-editing Applications of CRISPR Cas9 to Promote *In Vitro* Studies of Alzheimer's Disease. *Clin Interv Aging*, 13:221–33.
122. De Strooper B, Karran E, 2016, The Cellular Phase of Alzheimer's Disease. *Cell*, 164:603–15. DOI: 10.1016/j.cell.2015.12.056.
123. Vijayavenkataraman S, Thaharah S, Zhang S, *et al*., 2019,

3D-Printed PCL/rGO Conductive Scaffolds for Peripheral Nerve Injury Repair. *Artif Organs*, 43:515–23. DOI: 10.1111/aor.13360.

124. Chambers SM, Fasano CA, Papapetrou EP, *et al*., 2009, Highly Efficient Neural Conversion of Human ES and iPS Cells by Dual Inhibition of SMAD Signaling. *Nat Biotechnol*, 27:275–80. DOI: 10.1038/nbt.1529.
125. Ortiz-Virumbrales M, Moreno CL, Kruglikov I, *et al*., 2017, CRISPR/Cas9-Correctable Mutation-related Molecular and Physiological Phenotypes in iPSC-Derived Alzheimer's PSEN2N141I Neurons. *Acta Neuropathol Commun*, 5:77. DOI: 10.1186/s40478-017-0475-z.
126. Drummond E, Wisniewski T, 2017, Alzheimer's Disease: Experimental Models and Reality. *Acta Neuropathol*, 133:155–75. DOI: 10.1007/s00401-016-1662-x.
127. Li H, Jiang H, Zhang B, *et al*., 2018, Modeling Parkinson's Disease Using Patient-specific Induced Pluripotent Stem Cells. *J Parkinsons Dis*, 8:479–93.
128. Torrent R, De Angelis Rigotti F, Dell'Era P, *et al*., 2015, Using iPS Cells Toward the Understanding of Parkinson's Disease. *J Clin Med*, 4:548–66. DOI: 10.3390/jcm4040548.
129. Zeng XS, Geng WS, Jia JJ, 2018, Neurotoxin-Induced Animal Models of Parkinson Disease: Pathogenic Mechanism and Assessment. *ASN Neuro*, 10:1759091418777438. DOI: 10.1177/1759091418777438.
130. Bordoni M, Rey F, Fantini V, *et al*., 2018, From Neuronal Differentiation of iPSCs to 3D Neuro-organoids: Modelling and Therapy of Neurodegenerative Diseases. *Int J Mol Sci*, 19:3972. DOI: 10.3390/ijms19123972.
131. Thomas M, Willerth SM, 2017, 3-D Bioprinting of Neural Tissue for Applications in Cell Therapy and Drug Screening. *Front Bioeng Biotechnol*, 5:69. DOI: 10.3389/fbioe.2017.00069.
132. Osborn TM, Beagan J, Isacson O, 2018, Increased Motor Neuron Resilience by Small Molecule Compounds that Regulate IGF-II Expression. *Neurobiol Dis*, 110:218–30. DOI: 10.1016/j.nbd.2017.11.002.
133. Osaki T, Uzel SG, Kamm RD, 2018, Microphysiological 3D Model of Amyotrophic Lateral Sclerosis (ALS) from Human iPS-derived Muscle Cells and Optogenetic Motor Neurons. *Sci Adv*, 4:eaat5847. DOI: 10.1126/sciadv.aat5847.
134. Câmara DA, Mambelli LI, Porcacchia AS, *et al*., 2016, Advances and Challenges on Cancer Cells Reprogramming Using Induced Pluripotent Stem Cells Technologies. *J Cancer*, 7:2296–303. DOI: 10.7150/jca.16629.
135. Papapetrou EP, 2016, Patient-derived Induced Pluripotent Stem Cells in Cancer Research and Precision Oncology. *Nat Med*, 22:1392–401. DOI: 10.1038/nm.4238.
136. Kotini AG, Chang CJ, Chow A, *et al*., 2017, Stage-Specific Human Induced Pluripotent Stem Cells Map the Progression of Myeloid Transformation to Transplantable Leukemia. *Cell Stem Cell*, 20:315–28. DOI: 10.1016/j.stem.2017.01.009.
137. Hu K, Yu J, Suknuntha K, *et al*., 2011, Efficient Generation of Transgene-free induced Pluripotent Stem Cells from Normal and Neoplastic Bone Marrow and Cord Blood Mononuclear Cells. *Blood*, 117:e109–19. DOI: 10.1182/blood-2010-07-298331.
138. Gandre-Babbe S, Paluru P, Aribeana C, *et al*., 2013, Patient-derived Induced Pluripotent Stem Cells Recapitulate Hematopoietic Abnormalities of Juvenile Myelomonocytic Leukemia. *Blood*, 121:4925–9. DOI: 10.1182/blood-2013-01-478412.
139. Kotini AG, Chang CJ, Boussaad I, *et al*., 2015, Functional Analysis of a Chromosomal Deletion Associated with Myelodysplastic Syndromes using Isogenic Human Induced Pluripotent Stem Cells. *Nat Biotechnol*, 33:646–55. DOI: 10.1038/nbt.3178.
140. Fang Y, Eglen RM, 2017, Three-Dimensional Cell Cultures in Drug Discovery and Development. *SLAS Discov*, 22:456–72. DOI: 10.1177/1087057117696795.
141. Senthebane DA, Rowe A, Thomford NE, *et al*., 2017, The Role of Tumor Microenvironment in Chemoresistance: To Survive, Keep your Enemies Closer. *Int J Mol Sci*, 18:1586. DOI: 10.3390/ijms18071586.
142. Abbott A, 2019, The Lowdown on Animal Testing for Cosmetics. *Nature*, 2:496.
143. Skardal A, Mack D, Kapetanovic E, *et al*., 2012, Bioprinted Amniotic Fluid-Derived Stem Cells Accelerate Healing of Large Skin Wounds. *Stem Cells Transl Med*, 1:792–802. DOI: 10.5966/sctm.2012-0088./
144. Teoh JH, Thamizhchelvan AM, Davoodi P, *et al*., 2019, Investigation of the Application of a Taylor-Couette Bioreactor in the Post-processing of Bioprinted Human Dermal Tissue. *Biochem Eng J*, 151:107317. DOI: 10.1016/j.bej.2019.107317.
145. Kim BS, Lee JS, Gao G, *et al*., 2017, Direct 3D Cell-printing of Human Skin with Functional Transwell System. *Biofabrication*, 9:025034. DOI: 10.1088/1758-5090/aa71c8.
146. Gentile P, McColgan-Bannon K, Gianone NC, *et al*., 2017, Biosynthetic PCL-Graft-collagen Bulk Material for Tissue Engineering Applications. *Materials* (*Basel*), 10:693. DOI: 10.3390/ma10070693.
147. Ashammakhi N, Ahadian S, Xu C, *et al*., 2019, Bioinks and Bioprinting Technologies to Make Heterogeneous and Biomimetic tissue Constructs. *Mater Today Bio*, 1:100008.

DOI: 10.1016/j.mtbio.2019.100008.

148. Mosadegh B, Xiong G, Dunham S, *et al*., 2015, Current Progress in 3D Printing for Cardiovascular Tissue Engineering. *Biomed Mater* (*Bristol*), 10:034002. DOI: 10.1088/1748-6041/10/3/034002.

149. Mandrycky C, Wang Z, Kim K, et al., 2016, 3D Bioprinting for Engineering Complex Tissues. Biotechnol Adv, 34:422–34. DOI: 10.1016/j.biotechadv.2015.12.011.

150. Zhang XF, Huang Y, Gao G, *et al*., 2017, Current Progress in Bioprinting. In: Tripathi A, Melo JS, editor. Advances in Biomaterials for Biomedical Applications. Springer, Singapore, pp. 227–59. DOI: 10.1016/j.mtbio.2019.100008.

151. Skardal A, Atala A, 2015, Biomaterials for Integration with 3-D Bioprinting. *Annals of Biomedical Engineering*, 43:730–46. DOI: 10.1007/s10439-014-1207-1.

152. Billiet T, Vandenhaute M, Schelfhout J, *et al*., 2012, A Review of Trends and Limitations in Hydrogel-rapid Prototyping for Tissue Engineering. *Biomaterials*, 33:6020-41. DOI: 10.1016/j.biomaterials.2012.04.050.

153. Zhao T, Zhang ZN, Rong Z, *et al*., 2011, Immunogenicity of Induced Pluripotent Stem Cells. *Nature*, 474:212–6. DOI: 10.1038/nature10135.

154. Vijayavenkataraman S, Yan WC, Lu WF, *et al*., 2018, 3D Bioprinting of Tissues and Organs for Regenerative Medicine. *Adv Drug Deliv Rev*, 132:296–332. DOI: 10.1016/j.addr.2018.07.004.

155. Zhang S, Vijayavenkataraman S, Lu WF, *et al*., 2019, A Review on the Use of Computational Methods to Characterize, Design, and Optimize Tissue Engineering Scaffolds, with a Potential in 3D Printing Fabrication. *J Biomed Mater Res Part B Appl Biomater*, 107:1329–51. DOI: 10.1002/jbm.b.34226.

REVIEW ARTICLE

3D-printed Bioreactors for *In Vitro* Modeling and Analysis

Balasankar Meera Priyadarshini[1], Vishwesh Dikshit[1], Yi Zhang[1,2]*

[1]HP-NTU Digital Manufacturing Corporate Lab, Nanyang Technological University, 50 Nanyang Ave, 639798, Singapore
[2]School of Mechanical and Aerospace Engineering, Nanyang Technological University, 50 Nanyang Ave, 639798, Singapore

Abstract: In recent years, three-dimensional (3D) printing has markedly enhanced the functionality of bioreactors by offering the capability of manufacturing intricate architectures, which changes the way of conducting *in vitro* biomodeling and bioanalysis. As 3D-printing technologies become increasingly mature, the architecture of 3D-printed bioreactors can be tailored to specific applications using different printing approaches to create an optimal environment for bioreactions. Multiple functional components have been combined into a single bioreactor fabricated by 3D-printing, and this fully functional integrated bioreactor outperforms traditional methods. Notably, several 3D-printed bioreactors systems have demonstrated improved performance in tissue engineering and drug screening due to their 3D cell culture microenvironment with precise spatial control and biological compatibility. Moreover, many microbial bioreactors have also been proposed to address the problems concerning pathogen detection, biofouling, and diagnosis of infectious diseases. This review offers a reasonably comprehensive review of 3D-printed bioreactors for *in vitro* biological applications. We compare the functions of bioreactors fabricated by various 3D-printing modalities and highlight the benefit of 3D-printed bioreactors compared to traditional methods.

Keywords: Cell culture, Bacteria, Three-dimensional-printed chip, Three-dimensional-printed devices, Three-dimensional-printed bioreactors

***Corresponding Author**: Yi Zhang, HP-NTU Digital Manufacturing Corporate Lab, Nanyang Technological University, 50 Nanyang Ave, 639798, Singapore; yi_zhang@ntu.edu.sg

Received: March 12, 2020; ***Accepted***: June 03, 2020; ***Published Online:*** August 18, 2020

Citation: Priyadarshini BM, Dikshit V, Zhang Y, 2020, Three-dimensional-printed Bioreactors for *In Vitro* Modeling and Analysis, *Int J Bioprint*, 6(4): 267. DOI: org/10.18063/ijb.v6i4.267.

1 Introduction

1.1 Bioreactor

Bioreactors are essential tools that not only guide and support the development of *in vitro* live tissues but also act as culture vessels to study the biological response of the tissues to physiologically relevant conditions[1]. In the context of this review, bioreactors refer to devices for cellular and biochemical assays. The design and configuration of a bioreactor should complement the requirements of biological systems. For example, bioreactors for the study of vascularization and cardiac regeneration are coupled with the pulsatile flow to augment cell differentiation and maturation[2]. Similarly, bioreactors for lung tissue models are often linked to airflow setup to imitate native lung functions[3]. In addition, various operational parameters related to the flexibility, design, and other characteristics of bioreactors greatly influence the biological performance of bioreactors[4]. In the past few years, modeling and applications of bioreactors have evolved in various fields of research. Due to their enormous versatility, bioreactors have been employed in many industries, including biological, biomedical, pharmaceutical, food, wastewater treatment, chemical, and fermentation[5]. This review focuses on biological applications in detail.

1.2 Three-dimensional (3D)-printed bioreactor

Conventional bioreactors grant operators the convenience of controlling the environment and experimental manipulation of two-dimensional tissue models[6]. However, their incompatibility with *in vivo* systems and their inability to reflect true cell traits and tissue morphology has necessitated 3D systems which exhibit better spatial distribution and structurally complex tissue architecture. Nevertheless, it is challenging to produce 3D bioreactors with complex geometry using conventional manufacturing methods[7].

Additive manufacturing (AM), also known as 3D-printing technology, has shown enormous potential in the fabrication of complex, low-cost, and custom-designed structures constructed by depositing a layer on top of earlier printed layers[5]. Over the past three decades, several 3D-printing strategies have been established with a focus on the fabrication of bioreactors of various shapes and sizes[8,9]. Through 3D-printing, specialized bioreactors can be engineered with high performance in terms of experimental throughput, liquid controllability, and stability[10]. 3D-printing not only grants freedom to optimize new bioreactor designs but also enhances cellular functionality and suitability of bioreactor for specific applications such as *in vitro* culturing and testing[11].

In view of this article, any 3D-printed culture apparatus, including chip, culture chamber, or filters that directly contact the cells, are considered as 3D-printed bioreactors. Moreover, various customized components and accessories of bioreactors such as culture tube holders, test parts, chamber inserts, and sensors fabricated with various 3D-printing modalities have been discussed. Several bioreactor models were designed to encourage the flow of culture medium for even distribution of nutrients throughout the culture vessel. The fluid flow in bioreactors could be manipulated at the micro-level by coupling bioreactors with microfluidic networks. The compartmentalized microfluidic devices with interconnected microchannels created cellular environments confined in a culture vessel that directed fluid flow through the cell culture[12,13]. In addition, these devices were shown to emulate physiological relevance by creating *in vitro* microenvironments on the same scale of cells. However, devices with challenging functionalities and dimensional specifications, such as channel height and aspect ratio, are difficult to achieve by conventional microfluidic techniques. Recent advancements have led to the development of 3D-microfluidics with intricate detailing, greater accuracy, and better resolution[14] using 3D-printing techniques.

1.3 Methods for fabricating 3D-printed bioreactors

Features of 3D-printed devices rely primarily on the chosen printing method. Some applications only 3D-printed the substrate in cell culture for *in vitro* analysis, whereas other applications embedded living cells into biocompatible printable materials (bio-inks)[15]. In this review, we primarily focus on the 3D-printed bioreactors for *in vitro* studies, not including the direct printing of cells. Various 3D-printing methods have been used to fabricate 3D structures and devices based on various printing techniques including selective laser melting (SLM), direct metal laser sintering (DMLS), fused deposition modeling (FDM), fused filament fabrication (FFF), inkjet, PolyJet, material jetting, stereolithography (SLA), digital light processing (DLP), micro-SLA (μSLA), and multiphoton lithography, each with their own advantages and disadvantages[16]. These 3D-printing processes are also used to fabricate bioreactors. However, none of these 3D-printing processes are ideal due to their specific limitations such as biocompatibility issues, difficulty in removing support materials, low printing resolution, poor dimensional accuracy, and rough surface texture[17-19]. Considerations for the choice of 3D-printing methods are shown in **Tables 1 and 2**. 3D-printing process can be selected based on the manufacturing capability of the printer and the type of material used by printer[20,21]. However, 3D-printing process can be also selected according to the given main design requirements of bioreactor, including functionality and visual appearances[9,18].

Different laser sintering approaches such as SLM and DMLS are highly reproducible AM techniques used to fabricate porous and 3D

Table 1. 3D-printed bioreactors used in mammalian cell culture applications for assessing of cell viability, cell encapsulation, cell/tissue models, cell imaging, cell therapy, and organ-on-chip applications.

Printing technique	**Printer model**	**Possible reason for choice of printer**	**Material**	**3D construct developed**	**Application**	**Cells used**	**Ref.**
Cell viability							
SLA	ILIOS 3D-printer	High precision, transparency	PEG-DA-250 resin	Transparent disks	Bioreactor for studying resin compatibility on cells	Chinese hamster ovary cells (CHO-K1), Primary hippocampal neurons	[18]
SLA	Form 1+3D-printer	High accuracy, high resolution	Photocurable liquid resin	Cylindrical test parts	Bioreactor accessory for studying resin compatibility on cells	Zebrafish	[17]
FDM	Dimension Elite 3D-printer	Affordable, easily available	ABS				
Material jetting	Objet350 Connex 3D-printer	Dimensional accuracy	Objet Vero Clear	Microfluidic chip	Bioreactor for resin compatibility on cells	Bovine pulmonary artery endothelial cells	[31]
Cell encapsulation							
SLA	Commercial 3D-printer (Proto Labs)	High accuracy	3D Systems Accura® 60	Pump-free perfusion cell culture device	Bioreactor for cell encapsulation	Oral squamous cell carcinoma tumor, Liver cells	[32]
Material jetting	Objet260 Connex3 3D-printer	Dimensional accuracy	VeroClear-RGD810				
Cell/tissue models							
SLA	Commercial 3D-printer (EnvisionTEC)	Structural robustness	Eshell 300	Chamber and insert	Bioreactor accessory for tissue interactions	Human bone marrow stem cell	[33]
Testing of therapeutics							
Material jetting	Objet Connex 350 3D-printer	Droplet precision	Objet Vero White Plus	Device	Bioreactor for cell toxicity+drug transport	Endothelial cells	[34]
Material jetting	Objet Connex 350 3D-printer	Geometrical precision	Objet VeroClear	Microfluidic chip	Bioreactor for drug metabolism	Red blood cells	[13]
Material extrusion	MakerBot Replicator 2X 3D-printer	Good mechanical properties	ABS	Cartridges	Accessory item for cell toxicity	Human embryonic kidney cells	[35]

(Contd...)

Table 1. *(Continued)*.

Printing technique	Printer model	Possible reason for choice of printer	Material	3D construct developed	Application	Cells used	Ref.
Organ-on-a-chip							
Material jetting	Objet30 Pro 3D-printer	Rigidity, transparency	Objet VeroClear	Modular chamber	Bioreactor for blood-brain-barrier environment	Endothelial cells, rat primary astrocytes	[36]
SLA	Cellbricks 3D-bioprinter	High resolution	Gelatin and polyethylene glycol	Liver lobule	Bioreactor for characterization of liver organoid under static conditions	Human hepatoma cell line, human stellate cells	[37]
SLA	Perfactory 3 Mini-Multi Lens 3D-printer	High resolution	PIC100 resin	3D vessel	Bioreactor that mimics healthy and stenotic blood vessels	Human umbilical vein endothelial cells	[38]
Material extrusion	MakerBot Replicator 2 3D-printer	Affordable, geometrical precision	Polylactic acid	Input/output multiplexer	Bioreactor for endocrine tissue function	Endocrine cells	[39]
Material extrusion	ROSTOCK MAX V2 Desktop 3D-printer	Affordable, geometrical precision	Polymer	Molds	Bioreactor for bone metastasis	MC3T3-E1 cells	[40]
Material extrusion	Printrbot Simple Metal 3D-printer	Affordable, geometrical precision	Thermoplastic	Conformal device	Bioreactor for whole organ biomarker profiling	Microfluidic devices that interface with surface of whole organs	[41]
Material extrusion	Custom microextrusion-based 3D-printer	Micro-extrusion	Silicone, sodium polyacrylate hydrogel				
Cell observation							
DLP	Micro Plus Hi-Re 3D-printer	High resolution	HTM140	Microscopy chamber	Bioreactor accessory for multidimensional imaging	Human cell lines infected by membrane-GFP lentivirus, nuclear-tdTomato	[42]
DLP	EnvisionTEC Perfactory 3D-printer	High resolution	Eshell® 300	Fluidic culture chamber	Bioreactor for cell imaging	hMSCs	[43]
SLA	3D Systems Viper SLA system	Affordable, high accuracy, high resolution	WaterShed XC 11122 resin	Cell perfusion system (valves and pumps)	Bioreactor for cellular calcium imaging	CHO-K1 cells	[44]
SLA	PicoPlus 27 3D-printer	High accuracy, high resolution	Polypropylene/acrylnitril-butadien-styrol	Semiconductor-based biosensors	Bioreactor for cell growth and metabolism imaging, resin compatibility on cells	CHO-K1 cells	[45]

3D: Three-dimensional, FDM: Fused deposition modeling, SLA: Stereolithography, DLP: Digital light processing, ABS: Acrylonitrile butadiene styrene uniform metal structures with distinct cavities, and precisely control geometric parameters down to several hundred microns using laser power as low as 90 W[22,23]. Extrusion printing and its common variants such as FDM and FFF extrude molten polymer in a layer-by-layer manner to construct 3D objects[17,24]. This 3D-printing technique is cost-effective and could be easily adopted as a viable manufacturing option to create 3D constructs with high resolution, structural integrity, and transparency. Jetting-based methods, including inkjet, PolyJet, and material jetting deposit fluidic materials in a controlled fashion through a nozzle onto a 3D platform and are used to create highly complex constructs[25]. These direct cell printing techniques will not be discussed in this review. Another widely used 3D-printed method is the vat photopolymerization, including SLA and DLP, which prints by curing photosensitive resins with ultraviolet light[17,26]. SLA uses a laser beam that scans line-by-line to cure the photosensitive resin, whereas DLP uses a digital light projector to cure each layer of photoreactive resin in one go. Compared to DLP, SLA-based printers offer a higher spatial resolution, resulting in structures with dimensions <10 μm. μSLA-based systems that utilize two-photon optics further improve the resolution to submicrons[17]. The resulting ultrafine features may influence the mechanistic properties of cells in tissues. Nevertheless, resins used for SLA printers often contain methacrylate and/or acrylate monomers that have a reputation to be cytotoxic[17].

2 3D-printed bioreactor for biological applications

3D-printing is a rapidly evolving technology that provides an opportunity to fabricate complex 3D structures for biological applications[5,27]. It is an important tool for translational research that focuses on the *in vitro* biology and disease models in bioreactors. The increasing accessibility to 3D-printing has spurred substantial efforts toward many creative developments of 3D-printed bioreactors for the cultivation of mammalian as well as microbial cells. Various bioreactors have been fabricated with 3D-printing to study the response of these cells to the smallest details of their local environments such as substrate geometric arrangement, chemistry, and mechanics[28,29].

Much of our understanding of fundamental cellular mechanisms is garnered from the aberrant interactions of cells on 2D substrates. As we move toward more-compliant microenvironment, it is vital to demystify exactly what factors are operative in 3D systems rather than simply considering a dimensionality factor at play[30]. The increased capabilities of 3D-printers have resulted in well-architecture constructs with fine features and application-specific geometries. The key challenge here lies in achieving the geometry that provides the correct degree of biomimicry, mechanical and chemical cues needed for sufficient cell-cell signaling, cell development, and gene expression. Indeed, surface parameters such as porosity, roughness, and curvature are tunable according to experimental needs, and their effect on the collective cell behavior including adhesion, growth, alignment, proliferation, and differentiation has been demonstrated as well. Ideally, the role of 3D-printing is to provide cells a suitable environment supporting their transition into functional tissue *in vitro*. With 3D-printing, we are able to fabricate bioreactors of different sizes and shapes and introduce cells into the bioreactors post-printing for *in vitro* testing. Overall, this article aims to cover 3D-printed bioreactors for the *in vitro* study of both mammalian and bacterial cell culture.

2.1 3D-printed bioreactor for *mammalian cell culture*

3D-printed bioreactors used in mammalian cell culture applications for assessment of cell viability, cell encapsulation, cell/tissue models, cell imaging, testing of therapeutics, and organ-on-chip applications are discussed below and summarized in **Table 1**.

2.1.1 Cell viability in 3D-printed bioreactors

Bioreactors are an indispensable tool for maintaining cellular microenvironment to promote cell viability, growth, and proliferation.

The biocompatibility of cells with the materials used for 3D-printing also affects cell viability and survivability. Biocompatibility could be achieved with post-printing modification and has already been reviewed earlier[46]. The compatibility of zebrafish larvae on parts 3D-printed by FDM (using acrylonitrile butadiene styrene, [ABS]) and SLA (using photocurable liquid resin) (**Figure 1A**) indicated that materials used for FDM were less toxic compared to SLA evidenced by significantly lower rates of malformations. Following the UV treatment of SLA parts, the toxicity was significantly reduced but not completely eliminated[17]. In contrast, a concurrent study indicated the potential of transparent PEG-DA-250 resin disks (printed by SLA) for supporting the long-term culture of adherent CHO-K1 cells and primary hippocampal neurons[18]. Elsewhere, bovine endothelial cells were immobilized on a 3D transparent microfluidic chip made from photocurable resins by material jetting. Owing to unknown resin properties, the internal channels of the chip were coated with polydimethylsiloxane (PDMS) and polystyrene, respectively. Cell adherence and survival were favorable to PDMS, in comparison to polystyrene-coated, polished, and untreated samples[31].

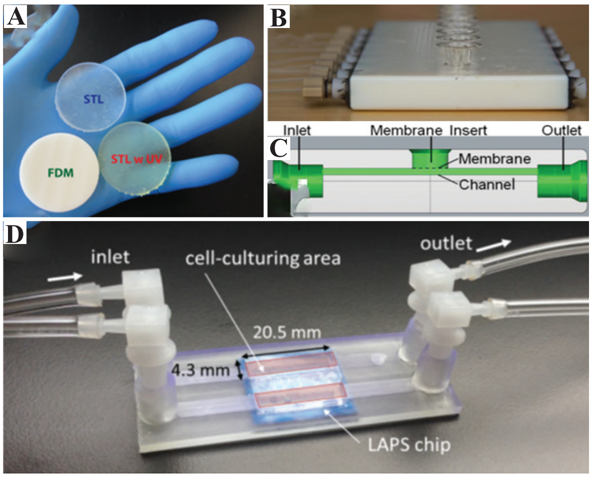

Figure 1. (A) Resin disks three-dimensional (3D)-printed by fused deposition modeling, stereolithography (SLA), and SLA w UV used for testing resin toxicity on zebrafish (40 mm diameter and 4 mm height)[17]. (B) 3D-printed device design showing adapters for syringe-based pumps, channels, membrane insertion port, and outlets. (C) The side view schematic of the 3D-printed device to understand the channel and fluid to flow under the membrane. The membrane is manually inserted into the port on top of the device. Finally, there is an outlet to allow fluid to leave the device[34]. (D) Potentiometric sensor-based biosensor chip showing inlet, outlet, and sensing area (20.5 mm × 4.3 mm) with attached microfluidic channels[45].

2.1.2 3D-printed bioreactor for cell encapsulation

A pump-free perfusion device was fabricated by SLA (3D Systems Accura 60) and material jetting (VeroClear-RGD810) for immobilizing multicellular spheroids and maintaining their viability. Even though SLA resulted in cell-immobilizing microstructures with smoother surfaces, good spheroid functionality, and prolonged viability compared to PolyJet printing, the inferior optical properties restricted sample visualization by microscopy[32]. Despite a conducive capsule housing for cell culture, it remains a challenging task to entrap certain cell models with biocompatible substrates and mandates optical transparency of capsules due to their suitability for cell imaging.

2.1.3 3D-printed bioreactor for cell/tissue models

In addition to providing a complex yet controlled ambient for cell viability and cell encapsulation through spatial and temporal control of cell growth, the increasing versatility of 3D-printing also enables the development of tissue culture constructs that mimic specific biological functions and capture cell-tissue interactions inside the culture system. For example, the pathogenesis associated with a tissue can be studied. A 3D-printed multichambered bioreactor fabricated with non-cytotoxic Eshell 300 resin using SLA was fitted into a microfluidic base, creating tissue-specific environments for the study of interactions between chondral and osseous tissues during osteochondral differentiation[33]. This system provided opportunities to investigate the tissue physiology and the role of each tissue in the pathogenesis of osteoarthritis.

2.1.4 3D-printed bioreactor for testing of therapeutics

3D-printed bioreactors are also useful in the clinical translation and commercialization of standardized cell-based products for cell-based therapies and drug-testing. A reusable material jetted (Objet Connex 350) fluidic device incorporated a porous polycarbonate membrane not only enabled molecular transport and drug migration through the membrane (**Figure 1B and C**) but also indicated drug susceptibility of mammalian cells[34]. Moreover, collecting analytes while simultaneously measuring the release stimulus was also possible with this 3D-printed bioreactor[13]. Electrodes and other additional functionalities such as membrane inserts and fluidic interconnects were integrated to ensure signal detection and flow control. A compact ready-to-use material extruded (MakerBot Replicator 2X) cartridge containing assay reagents was integrated with genetically engineered sentinel cells and interfaced with a custom-developed smartphone Tox-App for rapid quantification of cellular toxicity[35].

2.1.5 3D-printed bioreactor for organ-on-chip applications

An organ-on-a-chip device fabricated by 3D-printing aims to assemble organ models in 3D specific architecture on a microfluidic chip. By virtue of precise geometrical features attained by 3D-printing coupled with controlled flow dynamics and imaging compatibility of microfluidics, a continuous perfusion model had been developed to imitate the blood-brain barrier environment[36]. This setup consisted of a porous membrane that allowed coculture of different cell types across the membrane and a 3D-printed cell insert module that accommodated cell monolayers which formed a fully functional closed-loop perfusion model. This 3D-printed bioreactor was able to overcome the limitations faced by static culture models and demonstrated the synergy between microfluidics and 3D-printing[47]. Similarly, a 3D bone-on-a-chip device used coculture strategies to study disease mechanisms of the metastasis of breast cancer cells to bone marrow[40]. In the study, transparent PDMS chambers for cell growth casted from a 3D-printed mold (Rostock MAX V2 Desktop printer) were separated from the media reservoir by a membrane. 3D-printing of this geometrical design enabled frequent monitoring of interactions between cancer cells and the bone matrix *in vitro* and eliminated the need to take bone metastasis samples from patients.

Another study demonstrated the use of a perfusion-type liver organoid model using a sinusoidal liver lobule on a chip 3D-printed by SLA (Cellbricks bioprinter) with polyethylene glycol and gelatin containing bio-inks[37]. Cells cultured within the liver organoid model revealed high-yield protein expression compared to monolayer cultures. This *in vitro* model in 3D-printed bioreactor ensured hepatocyte functionality and could be modified to accommodate nutritional supply for larger tissue models to explore the mechanistic properties. The organ-on-a-chip systems could also be personalized by integrating additional systems to emulate the complexities of an organ. To design a 3D arterial thrombosis model, anatomical models were obtained from imaging scans and converted into a printable 3D model. The molds for chips with miniaturized healthy and stenotic vasculatures were then developed using a Perfactory 3 SLA 3D-printer with PIC100 resin. The vascular structures incorporated on-chip successfully mimicked vessel environments, showing human blood flow at physiologically relevant conditions and with artificially induced thrombosis[38]. Another system non-invasively interfaced a 3D-printed microfluidic device with a porcine kidney model to isolate and profile biomarkers from whole organs in real-time. From the cortex of the kidney, relevant metabolic and pathophysiological biomarkers were transported to the microfluidic device by virtue of the fluid flow in the microchannel. Hence, the 3D organ-on-a-chip could perhaps overcome the drawbacks of whole organ structures[41]. For a complex organ model, a multi-channel perfusion-type chamber was developed to assess endocrine secretions, due to their multiple inlet and outlet needs[39]. The device warranted precise control of nutrient inputs, hormone outputs, and permitted observation by fluorescence imaging.

2.1.6 3D-printed bioreactor to facilitate cell observation

The visualization of real-time cellular response to a 3D culture environment through imaging facilitates the monitoring of specific cellular processes. Another research group proposed a multidimensional observation chamber (the UniveSlide) with an SLA 3D-printed frame for medium/high throughput long-term imaging in controlled culture environments, which was also compatible with different microscopy techniques[42]. Moreover, this all-in-one device may be suitable for automatized multi-position imaging of thick samples. The use of agarose gel with imprinted microwells as a base support frame was a convenient addition for trapping cells and subsequent 3D viewing. A 3D-printed fluidic culture chamber was used to dynamically culture hMSCs, study the mechanical behavior of the cells in a controlled microenvironment, and visualize cells within 3D-printed constructs without sectioning using imaging techniques such as confocal or fluorescence laminar optical tomography[43]. Bioreactor accessories such as 3D-printed valves and pumps used for cell culture were also fabricated with SLA (3D Systems Viper system) using WaterShed XC 11122 resin. This study demonstrated controlled adenosine triphosphate (ATP) stimulation of live cells in an incubation chamber for observation of Ca2+ response[44]. Recently, a semiconductor-based biosensor chip was fabricated using Asiga Pico Plus 27 by DLP (**Figure 1D**) to facilitate the observation of cell metabolism on the microfluidics-based light-addressable potentiometric sensor chip[45].

2.2 3D-printed bioreactor for microbial cell culture applications

In the recent past, several studies have attempted to unravel the gaps of our understanding of bacteria survival mechanisms in complex microenvironments. AM offers an opportunity to reproduce the geometry of actual environments. The focal point of this section revolves around the use of 3D-printed bioreactors for various microbial applications such as long-term microbial culture, pathogen detection, pathogen phenotypic study, and antibacterial assays, which are summarized in **Table 2**.

2.2.1 3D-printed bioreactor for long-term microbial culture

Tracking the bacterial cell growth for a prolonged period provides crucial information on cell survival and proliferation conditions in addition to their nutrition and energetic physiology[64]. A number of bioreactors were built by 3D-printing to assist in monitoring the growth of bacteria in liquid cultures. A customized FDM-printed culture tube holder (**Figure 2A**) was interfaced with a mini-spectrophotometer connected to a light source through optical fibers to monitor bacteria growth in liquid culture through turbidimetric measurement[20]. Elsewhere, 3D-printed

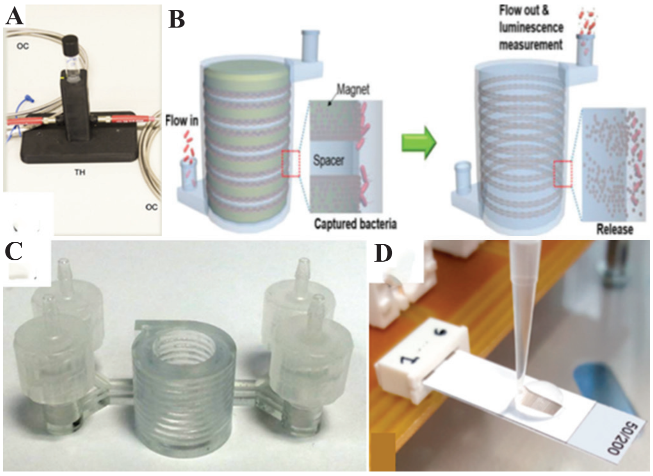

Figure 2. (A) Three-dimensional (3D)-printed culture tube holder for monitoring the bacterial growth of liquid microbial cultures (OC: Optical cable; TH: Tube holder)[49]. (B) 3D-printed magnet-spacer assembly showing bacterial separation by 3D immunomagnetic flow assay[58]. (C) 3D-printed vertically designed cylindrical chamber was developed for bioluminescent bacterial detection[7]. (D) Inkjet-printed interdigitated electrode sensor for phage detection[26].

Table 2. 3D-printed devices for various microbial applications such as long-term microbial culture, pathogen detection, pathogen phenotype study, antibacterial assays, and 3D-printing of bacteria and biofilms.

Printing technique	Printer model	Possible reason for choice of printer	Material	3D construct developed	Application	Bacteria used	Ref.
Long-term microbial culture							
FDM	Fortus 250 mc 3D-printer	Good mechanical properties	ABS plus	Culture tube holder	Accessory item for bacterial growth monitoring	*E. coli,* *S. aureus*	[20]
SLA	Form 2 3D-printer	High resolution, high accuracy	STL 3D-printed resins	Culture millifluidic disks	Bioreactor for biotoxicity of 3D-printing resin on bacteria	*P. putida*	[48]
SLA	Form 1+ 3D-printer	Affordable, high resolution, high accuracy	Formlabs: ClearV2 and flexible, Shapeways: Elastoplastic, extreme detail, frosted acrylic, white strong, and flexible	Culture tubes	Accessory item for microbial liquid culture	*E. coli*	[49]
Material jetting	Connex350 3D-printer	High precision	Stratasys: MED610, VeroClear, TangoBlack, Tango Plus				
Pathogen detection							
Material extrusion	Profi3Dmaker 3D-printer	Affordable, optimal printing quality	ABS	Chip	Bioreactor for colorimetric detection	*S. aureus,* *E. coli, S. typhimurium,* *L. rhamnosus,* *Methicillin-resistant S. aureus*	[50]
Material extrusion	Easy 3D Maker 3D-printer	Affordable, geometrical precision	Polylactide	Bead-based microfluidic chip	Bioreactor for electrochemical detection	Influenza virus	[51]
Material extrusion	UPBOX+ 3D-printer	Affordable, optimum resolution	ABS	Smartphone platform	Accessory item for detection of viable algae in fresh and marine water	*C. reinhardtii,* *M. aeruginosa,* *Amphiprora sp., and C. closterium*	[52]
Material jetting	3D Systems ProJet 3000UHD 3D-printer	Ultra-high resolution	VisiJet EX200 polymer	Finger actuated microfluidic device	Bioreactor for colorimetric detection	*E. coli*	[53]

(Contd....)

Table 2. *(Continued)*.

Printing technique	Printer model	Possible reason for choice of printer	Material	3D construct developed	Application	Bacteria used	Ref.
Material jetting	Stratasys Objet24 3D-printer	High precision	Vero White Plus	Microfluidic chip	Bioreactor for colorimetric detection	*E coli*	[54]
Material jetting	Objet30 Pro 3D-printer	Accuracy, versatility	Vero™ Black material	Micro-millifluidic bioreactor	Bioreactor for microalgal culture	*D. tertiolecta*	[55]
SLA	3D Systems Viper SLA system	High resolution, high accuracy	DSM Somos WaterShed XC 11122	Cylindrical microchannel device	Bioreactor for detection by ATP bioluminescence assay	*Salmonella*	[56]
SLA	3D Systems Viper SLA system	High resolution, high accuracy	DSM Somos WaterShed XC 11122 resin	Helical microchannel device	Bioreactor for detection and separation by ATP bioluminescence assay	*E. coli*	[7]
DLP	Carima DP 110 3D-printer	Dimensional precision, good reproducibility	Acrylic resin	Trapezoidal-shaped concentration chamber	Bioreactor for detection by ATP luminescence assay	*E. coli*	[57]
DLP	Carima IM-96 3D-printer	Dimensional precision	Photocurable resin	Millifluidic device	Bioreactor for detection in blood by PCR and qPCR	*E. coli* and *S. aureus*	[8]
Ink jetting	Fuji Dimatix printer	Controllability, efficiency	Polyethylene terephthalate	Microfluidic device	Bioreactor for electrochemical detection	*Salmonella*	[58]
Ink jetting	Epson ET-2550 EcoTank® printer	Low-cost	Conductive inks based on silver nanoparticles and transparent and flexible polyethylene terephthalate sheets	Interdigitated electrode sensor	Accessory item for electrochemical detection of bacteriophages contamination	*L. lactis* subsp. *Lactis* and its phage	[25]
FDM	Prusa MovtecH model open-source 3D-printer	Rapid fabrication	ABS	T-junction device	Bioreactor for bacterial detection	*E. coli*	[59]
Pathogen phenotype analysis							
Material jetting	ProJet™ MJP 2500 Plus 3D-printer	High resolution	VisiJet M2 RCL, 3D Systems	Microfluidic chip	Bioreactor for live/dead bacterial cell differentiation with propidium monoazide pretreatment	*E. coli*	[60]
SLA	Form 2 3D-printer	Affordable, high resolution	Resin	Incubation/diffusion chamber	Bioreactor for pathogen phenotype analysis in soil matrices	*B. cereus*, *E. coli*	[61]
Wastewater treatment							
SLA	028 J Plus 3D-printer	High resolution	Urethane-acrylate based resin with 20% silica-alumina powder	Magnetic cylindrical (planar and spiral) microrobots	Bioreactor for antibacterial activity, biocompatibility	*S. aureus*	[26]

(Contd....)

Table 2. *(Continued)*.

Printing technique	Printer model	Possible reason for choice of printer	Material	3D construct developed	Application	Bacteria used	Ref.
SLA	Form 1 3D-printer	Affordable, high resolution, high accuracy	Formlabs Clear FLGPCL02	40-mL anaerobic digester	Bioreactor for wastewater treatment	Microbial inoculum	[62]
SLS	FARSOON 251 3D-printer	Good mechanical properties	Nylon FS3200PA	Bio-carrier sphere	Biofilm reactor for wastewater treatment	Biofilm	[21]
Material jetting	Objet30 3D-printer	High resolution	Acrylate-based monomer resin	Gyroid media carrier	Biofilm reactor for wastewater treatment	Biofilm of nitrifying bacteria	[63]

3D: Three-dimensional, FDM: Fused deposition modeling, *E. coli*: *Escherichia coli*, *S. aureus*: *Staphylococcus aureus*, *S. typhimurium*: *Salmonella typhimurium*, *P. putida*: *Pseudomonas putida*, *L. rhamnosus*: *Lactobacillus rhamnosus*, *Methicillin-resistant S. aureus*: *Methicillin-resistant Staphylococcus aureus*, *C. reinhardtii*: *Chlamydomonas reinhardtii*, *M. aeruginosa*: *Microcystis aeruginosa*, *D. tertiolecta*: *Dunaliella tertiolecta*, *C. closterium*: *Cylindrotheca closterium*, *L. lactis*: *Lactococcus lactis*, *B. cereus*: *Bacillus cereus*, ABS: Acrylonitrile butadiene styrene

bioreactors built by SLA and material jetting were used for long-term culture that mimicked the shape and dimensions of a standard commercial polystyrene tube[49]. Ten different 3D-printable resin materials were tested, of which only MED610 (ISO-certified biocompatible), VeroClear, and Frosted Acrylic exhibited no significant bacteria growth inhibition. Other materials were unsuitable because of rapid media evaporation (elastoplastic), sticky residue formation (Extreme Detail), deposition of particles inside the bioreactor after storage (White Strong and Flexible), physical instability (TangoBlack), and drastically reduced growth rates of bacteria cells (ClearV2, Flexible and Tango Plus). In a later study, an SLA-printed bioreactor in the form of a disk (Formlabs) was tested for biotoxicity effects of resins on bacteria and suggested a dose-response relationship to resin[48].

2.2.2 3D-printed bioreactor for pathogen detection

Undesired pathogen contamination in water, food, and blood poses a great public health threat. Rapid detection and separation of bacterial pathogens are therefore necessary in the field of food industry, clinical diagnostics, and environment quality control to ensure safety[65]. To monitor and quantify the presence of microbes, the design and fabrication of new 3D-printed diagnostic devices have been the focus of these areas. Considering the importance of an appropriate pathogen detection system, several studies had combined the 3D-printed bioreactors with detection methods such as calorimetry, bioluminescence, polymerase chain reaction (PCR), electrochemical, and contactless conductivity for bacteria sensing. Colorimetric detection is a rapid, easy-to-operate technique capable of simple visual detection. A material extrusion-based 3D-printed chip using ABS was made from Profi3Dmaker for bacteria culture, DNA isolation, and colorimetric detection of mecA genes, specific to the presence of methicillin-resistant *Staphylococcus aureus*. The entire chip was placed in a thermostatic box for maintaining a homogenous magnetic field and facilitating non-crosslinking aggregation of nanoparticle probes with bacterial DNA for *in vitro* diagnostic applications[50]. Another study used a manually actuated miniature 3D-printed device fabricated using VisiJet EX200 polymer by material jetting for rapid on-site multiplexed bacterial detection using calorimetric measurement[53]. The finger-actuated pumping membrane seated on the pumping chamber was connected to individual enrichment/detection chambers through serpentine channels for bacteria detection in drinking water. Upon depressing and releasing the membrane, a vacuum pressure filled in each chamber and sucked in the sample. The lowest detection limit of 1e^6 colony forming units (CFU)/mL was observed in approximately 6 hours. Furthermore, these pathogen detection devices were also connected to accessories for colorimetric readout, which would improve the limit of detection[54].

Some groups have resorted to combined ATP bioluminescence and magnetic particle-based immunomagnetic separation for bacteria sensing. This is a more rapid and efficient approach for increasing the sensitivity and specificity of pathogen identification. A 3D-printed bioreactor with cylindrical hollow microchannel and high-capacity efficient magnetic O-shaped separator (HEMOS) was designed for Salmonella detection in large-volume samples (**Figure 2B**). The magnet-spacer feature in the central area of HEMOS maximized the magnetic field, thereby allowing ultra-rapid capture of 10 CFU/mL of nanocluster-immobilized bacteria within 3 min[56]. Similarly, a 3D-printed bioreactor with helical chambers (**Figure 2C**) was developed for bioluminescent *Escherichia coli (E. coli)* detection in milk[7]. The device enabled sheath inlet flow for improved size-dependent separation of bacteria-nanocluster complexes in the helical microchannel. A number of studies employed 3D-printed millifluidic platforms to process samples larger than 1 mL. At sub-millimeter scale, recyclable, 3D-printed trapezoidal preconcentration chamber built by DLP (acrylic resin) was used to isolate *E. coli* in blood samples[57]. Another 3D-printed millifluidic device preconcentrated bacterial DNA by sequential isolation using magnetic silica beads was also developed for improved pathogen detection in blood. This method extracted bacterial DNA in 10 mL of buffer and 10% blood within 30 min and detected as low as 1 CFU bacterial using either PCR or quantitative PCR[8].

Electrochemical detection has also been accepted as a powerful tool for bacterial and viral detection in 3D-printed biomarkers by identifying disease-related biomarkers and environmental hazards. A pump-free bioreactor used for electrochemical detection of Salmonella consisted of two flexible polyethylene terephthalate layers with sintered inkjet-printed electrodes directly bonded to the channel-containing layer, forming a sealed microfluidic device[58]. This high throughput device accommodated immunomagnetic bacterial separation. Similarly, a material-extruded bead-based microfluidic chip with a three-electrode setup was used for the detection of influenza hemagglutinin[51]. Elsewhere, a prototype system with real-time impedance measurements was used to detect phage infection of cultured *Lactococcus lactis*[25]. The two standard microbiological testing methods used for comparison were based on plaque assay and turbidity measurements. Only the inkjet-based biosensor system showed a greater sensitivity to phage infection with a response within the first 3 h of phage inoculation. Another study described a T-junction microfluidic device with integrated sensing electrodes developed by FDM (using ABS) for label-free counting of *E. coli* cells incorporated in spherical oil droplets. Cells were counted using a single-step contactless conductivity system and quantified by plate counting method. This approach offered noticeable advantages as a single-step method with minimal incubation time before detection[59]. Studies have also explored the use of 3D-printed bioreactors for the culture of microbes other than bacteria, such as algae. A material jetted milli-microfluidic device (Vero™ Black material) with growth chambers, microchannels, and semi-integrated optical detection system was used for algal culture[55]. Even though the growth was unsuccessful due to poor microalgal retention resulting from photopolymer incompatibility with cells, other metrics observed during the culture offered a mechanical perspective that indicated the 3D-printed architecture posed promising advantages in comparison to other complex microfabrication processes. Another group developed a 3D-printed smartphone platform integrated with an optoelectrowetting-operated microfluidic device for on-site detection of viable algae cells[52]. The collected data were wirelessly transmitted to a central host for real-time monitoring of water quality with reduced analysis time. Given its sensitivity, this chip allowed sample preparation methods such as droplet immobilization and mixing, target cell counting, and fluorescent detection.

2.2.3 3D-printed bioreactor for pathogen phenotypic analysis

Profiling pathogen phenotypes is important in decoding the virulence and interaction of pathogen with its surroundings. A propidium monoazide (PMA) pretreatment was carried out in a 3D-printed bioreactor to efficiently discriminate live waterborne bacterial pathogens in natural pond water samples[60]. The material jetted bioreactor was designed with an inlet, splitter, and mixers for proper sample-PMA mixing followed by incubation in serpentine channels containing herringbone structures for alternating dark and light incubation. The results obtained from this 3D-printed bioreactor suggested the need for species-specific optimization of pretreatment performance. Elsewhere, an SLA-printed incubation/diffusion chamber was designed for culturing bacteria from soil samples to study their interaction dynamics. The chamber facilitated diffusion of soil components with target cells and also allowed single-cell and ensemble bacterial phenotypic analyses[61].

2.2.4 3D-printed bioreactor for wastewater treatment

Several 3D-printed bioreactors have demonstrated great potential in water treatment applications that were difficult to be achieved by conventional wastewater treatment systems. Cylindrical microrobots printed by SLA conveyed excellent water purification capability and great biocompatibility with mammalian cells[26]. Other intricate 3D-printed bioreactor designs, including fullerene-shaped bio-carriers[21] and gyroid-shaped carrier[63], have been shown to stimulate microbial assemblages for improved organic matter removal and better performance of biofilm reactors. Other studies employed SLA-printed miniature anaerobic digester reactors as a process screening tool for sustainable treatment of wastewater and biowaste[62].

3 Conclusions and future directions

In recent years, significant advances have been made in 3D-printed bioreactor technologies. Bioreactors have been tailored to easy online monitoring and automated bioprocesses, thereby closing the gap between conventional bioreactors and their miniature 3D-printed counterparts. However, in addition to their basic functions, other design aspects, such as flexible operation and process optimization, should be taken into account, especially for devices used to study complex physiological phenomena. It is noteworthy to mention that there has been limited clinical translation of 3D-printed bioreactors. This could be attributed to the lack of optimized protocols that are fine-tuned to respective 3D-printing methods and materials. The reproducibility of certain 3D-printing processes is suboptimal.

At present, 3D-printing research for *in vitro* biological applications focuses mostly on relatively simple systems that only incorporate a limited number of cells and cell types. Future studies should aim to attend to relatively complex tissues and organs. Moreover, several concerns such as 3D-printing compatible design, removal of support structures, the choice of appropriate cell lines, better cocultivation concepts, establishment of optimal conditions, and protocol standardization remain to be resolved and should be the focus of future research. With advances in various aspects of 3D-printing, one would be able to design and manufacture customized bioreactors with tailored functionalities using 3D-printing in laboratory settings, which would significantly drive future biomedical research by offering on-demand *in vitro* testing.

Conflicts of interest

The authors declare no conflicts of interest.

Funding

The authors are thankful for the support by HP-NTU Digital Manufacturing Corporate Lab, Nanyang Technological University, Singapore. The content is solely the responsibility of the authors. This research was conducted in collaboration with HP Inc. and supported/partially supported by the Singapore Government through the Industry Alignment Fund-Industry Collaboration Projects Grant.

References

1. Wang D, Liu W, Han B, *et al.*, 2005, The Bioreactor: A Powerful Tool for Large-scale Culture of Animal Cells. *Curr Pharm Biotechnol*, 6:397–403.
2. Govoni M, Lotti F, Biagiotti L, *et al.*, 2014, An Innovative Stand-alone Bioreactor for the Highly Reproducible Transfer of Cyclic Mechanical Stretch to Stem Cells Cultured in a 3D Scaffold. *J Tissue Eng Regen Med*, 8:787–93.
3. Shimizu T, Sekine H, Yamato M, *et al.*, 2009, Cell Sheet-based Myocardial Tissue Engineering: New Hope for Damaged Heart Rescue. *Curr Pharm Des*, 15:2807–14.
4. Ozturk SS, 1996, Engineering Challenges in High Density Cell Culture Systems. *Cytotechnology*, 22:3–16.
5. Capel AJ, Rimington RP, Lewis MP, *et al.*, 2018, 3D Printing for Chemical, Pharmaceutical and Biological Applications. *Nat Rev Chem*, 2:422–36.
6. Hjertager BH, Morud K, 1995, Computational Fluid Dynamics Simulation of Bioreactors. *J Mod Identif Control*, 16:177–91.
7. Lee W, Kwon D, Choi W, *et al.*, 2015, 3D-printed Microfluidic Device for the Detection of Pathogenic Bacteria Using Size-based Separation in Helical Channel with Trapezoid Cross-section. *Sci Rep*, 5:7717.
8. Kim Y, Lee J, Park S, 2018, A 3D-printed Millifluidic Platform Enabling Bacterial Preconcentration and DNA Purification for Molecular Detection of Pathogens in Blood. *Micromachines*, 9:472.
9. Alessandri K, Feyeux M, Gurchenkov B, *et al.*, 2016, A 3D Printed Microfluidic Device for Production of Functionalized Hydrogel Microcapsules for Culture and Differentiation of Human Neuronal Stem Cells (hNSC). *Lab on a Chip*, 16:1593–604.
10. Bancroft GN, Sikavitsas VI, Mikos AG, 2003, Design of a Flow Perfusion Bioreactor System for Bone Tissue-engineering Applications. *Tissue Eng*, 9:549–54.
11. Richards DJ, Tan Y, Jia J, *et al.*, 2013, 3D Printing for Tissue Engineering. *Israel J Chem*, 53:805–14.
12. Pasirayi G, Auger V, M Scott S, *et al.*, 2011, Microfluidic Bioreactors for Cell Culturing: A Review. *Micro Nanosyst*, 3:137–60.
13. Erkal JL, Selimovic A, Gross BC, *et al.*, 2014, 3D Printed Microfluidic Devices with Integrated Versatile and Reusable Electrodes. *Lab Chip*, 14:2023–32.
14. Rupal BS, Garcia EA, Ayranci C, *et al.*, 2018, 3D Printed 3D-Microfluidics: Recent Developments and Design Challenges. *J Integr Des Proc Sci*, 22:5–20.
15. Ball O, Nguyen BN, Placone JK, *et al.*, 2016, 3D Printed Vascular Networks Enhance Viability in High-volume Perfusion Bioreactor. *Ann Biomed Eng*, 44:3435–45.
16. Ngo TD, Kashani A, Imbalzano G, *et al.*, 2018, Additive Manufacturing (3D Printing): A Review of Materials, Methods, Applications and Challenges. *Compos B Eng*, 143:172–96.
17. Oskui SM, Diamante G, Liao C, *et al.*, 2015, Assessing and Reducing the Toxicity of 3D-Printed Parts. *Environ Sci Technol Lett*, 3:1–6.
18. Urrios A, Parra-Cabrera C, Bhattacharjee N, *et al.*, 2016, 3D-printing of Transparent Bio-microfluidic Devices in PEG-DA. *Lab Chip*, 16:2287–94.
19. Jiménez M, Romero L, Domínguez IA, *et al.*, 2019, Additive Manufacturing Technologies: An Overview about 3D Printing Methods and Future Prospects. *Complexity*, 2019;2019:9656938.
20. Maia MR, Marques S, Cabrita AR, *et al.*, 2016, Simple and Versatile Turbidimetric Monitoring of Bacterial Growth in Liquid Cultures Using a Customized 3D Printed Culture Tube Holder and a Miniaturized Spectrophotometer: Application to Facultative and Strictly Anaerobic Bacteria. *Front Microbiol*, 7:1381.
21. Dong Y, Fan SQ, Shen Y, *et al.*, 2015, A Novel bio-carrier Fabricated Using 3D Printing Technique for Wastewater Treatment. *Sci Rep*, 5:12400.
22. Qing Y, Li K, Li D, *et al.*, 2019, Antibacterial Effects of Silver Incorporated Zeolite Coatings on 3D Printed Porous Stainless Steels. *Mater Sci Eng C*, 108:110430.
23. Bassous NJ, Jones CL, Webster TJ, 2019, 3-D Printed Ti-6Al-4V Scaffolds for Supporting Osteoblast and Restricting Bacterial Functions without Using Drugs: Predictive Equations and Experiments. *Acta Biomater*, 96:662–73.
24. Morgan AJ, San Jose LH, Jamieson WD, *et al.*, 2016, Simple and Versatile 3D Printed Microfluidics Using Fused Filament

Fabrication. *PLoS One*, 11:e0152023.

25. Rosati G, Cunego A, Fracchetti F, *et al.*, 2019, Inkjet Printed Interdigitated Biosensor for Easy and Rapid Detection of Bacteriophage Contamination: A Preliminary Study for Milk Processing Control Applications. *Chemosensors*, 7:8.
26. Bernasconi R, Carrara E, Hoop M, *et al.*, 2019, Magnetically Navigable 3D Printed Multifunctional Microdevices for Environmental Applications. *Addi Manufact*, 28:127–35.
27. Lerman MJ, Lembong J, Gillen G, *et al.*, 2018, 3D Printing in Cell Culture Systems and Medical Applications. *Appl Phys Rev*, 5:041109.
28. Chen CS, Mrksich M, Huang S, *et al.*, 1997, Geometric Control of Cell Life and Death. *Science*, 276:1425–8.
29. Discher DE, Janmey P, Wang Y, 2005, Tissue Cells Feel and Respond to the Stiffness of their Substrate. *Science*, 310:1139–43.
30. Baker BM, Chen CS, 2012, Deconstructing the Third Dimension how 3D Culture Microenvironments Alter Cellular Cues. *J Cell Sci*, 125:3015–24.
31. Gross BC, Anderson KB, Meisel JE, *et al.*, 2015, Polymer Coatings in 3D-printed Fluidic Device Channels for Improved Cellular Adherence Prior to Electrical Lysis. *Anal Chem*, 87:6335–41.
32. Ong LJ, Islam A, DasGupta R, *et al.*, 2017, A 3D Printed Microfluidic Perfusion Device for Multicellular Spheroid Cultures. *Biofabrication*, 9:045005.
33. Lin H, Lozito TP, Alexander PG, *et al.*, 2014, Stem Cell-based Microphysiological Osteochondral System to Model Tissue Response to Interleukin-1β. *Mol Pharm*, 11:2203–12.
34. Anderson KB, Lockwood SY, Martin RS, *et al.*, 2013, A 3D Printed Fluidic Device that Enables Integrated Features. *Anal Chem*, 85:5622–6.
35. Cevenini L, Calabretta MM, Tarantino G, *et al.*, 2016, Smartphone-interfaced 3D Printed Toxicity Biosensor Integrating Bioluminescent “Sentinel Cells”. *Sens Actuators B Chem*, 225:249–57.
36. Wang YI, Abaci HE, Shuler ML, 2017, Microfluidic Blood Brain Barrier Model Provides *In Vivo*-Like Barrier Properties for Drug Permeability Screening. *Biotechnol Bioeng*, 114:184–94.
37. Grix T, Ruppelt A, Thomas A, *et al.*, 2018, Bioprinting Perfusion-enabled Liver Equivalents for Advanced Organ-on-a-chip Applications. *Genes*, 9:176.
38. Costa PF, Albers HJ, Linssen JE, *et al.*, 2017, Mimicking Arterial Thrombosis in a 3D-Printed Microfluidic *In Vitro* Vascular Model Based on Computed Tomography Angiography Data. *Lab Chip*, 17:2785–92.
39. Li X, Brooks JC, Hu J, *et al.*, 2017, 3D-templated, Fully Automated Microfluidic Input/Output Multiplexer for Endocrine Tissue Culture and Secretion Sampling. *Lab Chip*, 17:341-9.
40. Hao S, Ha L, Cheng G, *et al.*, 2018, A Spontaneous 3D Bone-on-a-chip for Bone Metastasis Study of Breast Cancer Cells. *Small*, 14:1702787.
41. Singh M, Tong Y, Webster K, *et al.*, 2017, 3D Printed Conformal Microfluidics for Isolation and Profiling of Biomarkers from Whole Organs. *Lab Chip*, 17:2561–71.
42. Alessandri K, Andrique L, Feyeux M, *et al.*, 2017, All-in-one 3D Printed Microscopy Chamber for Multidimensional Imaging, the UniverSlide. *Sci Rep*, 7:42378.
43. Lembong J, Lerman MJ, Kingsbury TJ, *et al.*, 2018, A Fluidic Culture Platform for Spatially Patterned Cell Growth, Differentiation, and Cocultures. *Tissue Eng A*, 24:1715–32.
44. Au AK, Bhattacharjee N, Horowitz LF, *et al.*, 2015, 3D-printed Microfluidic Automation. *Lab Chip*, 15:1934–41.
45. Takenaga S, Schneider B, Erbay E, *et al.*, 2015, Fabrication of Biocompatible Lab-on-chip Devices for Biomedical Applications by Means of a 3D-Printing Process. *Phys Status Solidi*, 212:1347–52.
46. Zhang Y, 2017, Post-printing Surface Modification and Functionalization of 3D-Printed Biomedical Device. *Int. J. Bioprint*, 3:93–9.
47. Zhang Y, 2019, Three-dimensional-printing for Microfluidics or the Other Way Around? *Int J Bioprint*, 5:61-73.
48. Kadiak A, 2017, Advanced Manufacturing and Microenvironment Control for Bioengineering Complex Microbial Communities. Available from: https://opencommons.uconn.edu/dissertations/1340.
49. Walsh ME, Ostrinskaya A, Sorensen MT, *et al.*, 2016, 3D-Printable Materials for Microbial Liquid Culture. *3D Print Addit Manufact*, 3:113–8.
50. Chudobova D, Cihalova K, Skalickova S, *et al.*, 2015, 3D-printed Chip for Detection of Methicillin-resistant *Staphylococcus aureus* Labeled with Gold Nanoparticles. *Electrophoresis*, 36:457–66.
51. Krejcova L, Nejdl L, Rodrigo MAM, *et al.*, 2014, 3D Printed Chip for Electrochemical Detection of Influenza Virus Labeled with CdS Quantum Dots. *Biosens Bioelectron*, 54:421–7.
52. Sweet EC, Liu N, Chen J, *et al.*, Entirely-3D Printed Microfluidic Platform For On-site Detection of Drinking Waterborne Pathogens. In: IEEE 32nd International Conference on Micro Electro Mechanical Systems, 2019. IEEE, pp. 79–82.

53. Zheng L, Cai G, Wang S, *et al.*, 2019, A Microfluidic Colorimetric Biosensor for Rapid Detection of *Escherichia coli* O157: H7 Using Gold Nanoparticle Aggregation and Smart Phone Imaging. *Biosens Bioelectron*, 124:143–9.
54. Lee W, Kwon D, Chung B, *et al.*, 2014, Ultrarapid Detection of Pathogenic Bacteria Using a 3D Immunomagnetic Flow Assay. *Anal Chem*, 86:6683–8.
55. Park C, Lee J, Kim Y, *et al.*, 2017, 3D-printed Microfluidic Magnetic Preconcentrator for the Detection of Bacterial Pathogen Using an ATP Luminometer and Antibody-conjugated Magnetic Nanoparticles. *J Microbiol Methods*, 132:128–33.
56. Chen J, Zhou Y, Wang D, *et al.*, 2015, UV-nanoimprint Lithography as a Tool to Develop Flexible Microfluidic Devices for Electrochemical Detection. *Lab Chip*, 15:3086–94.
57. Cox CA, 2016, A Multi-Channel 3D-Printed Bioreactor for Evaluation of Growth and Production in the microalga *Dunaliella* sp. Available from: https://digitalcommons.library.umaine.edu/etd/2560.
58. Lee S, Thio SK, Park SY, *et al.*, 2019, An Automated 3D-printed Smartphone Platform Integrated with Optoelectrowetting (OEW) Microfluidic Chip for on-site Monitoring of Viable Algae in Water. *Harmful Algae*, 88:101638.
59. Duarte LC, Figueredo F, Ribeiro LE, *et al.*, 2019, Label-free Counting of *Escherichia coli* Cells in Nanoliter Droplets Using 3D Printed Microfluidic Devices with Integrated Contactless Conductivity Detection. *Anal Chim Acta*, 1071:36–43.
60. Zhu Y, Huang X, Xie X, *et al.*, 2018, Propidium Monoazide Pretreatment on a 3D-Printed Microfluidic Device for Efficient PCR Determination of "Live Versus Dead' microbial Cells. *Environ Sci*, 4:956–63.
61. Wilson L, Iqbal K M, Simmons-Ehrhardt T, *et al.*, 2019, Customizable 3D Printed Diffusion Chambers for Studies of Bacterial Pathogen Phenotypes in Complex Environments. *J Microbiol Methods*, 162:8–15.
62. Achinas S, Euverink GJ, 2019, Development of an Anaerobic Digestion Screening System Using 3D-Printed Mini-Bioreactors. In: New Advances on Fermentation Processes. IntechOpen, London.
63. Elliott O, Gray S, McClay M, *et al.*, 2017, Design and Manufacturing of High Surface Area 3D-Printed Media for Moving Bed Bioreactors for Wastewater Treatment. *J Contemp Water Res Educ*, 160:144–56.
64. Koch AL, 2009, Microbial Growth Measurement, Methods. Encyclopedia of Industrial Biotechnology: Bioprocess, Bioseparation, and Cell Technology. Willy, Hoboken, New Jersey, pp. 1–11.
65. Okoh AI, Odjadjare EE, Igbinosa EO, *et al.*, 2007, Wastewater Treatment Plants as a Source of Microbial Pathogens in Receiving Watersheds. *Afr J Biotechnol*, 6:2932–44.

ORIGINAL ARTICLE

Rational Design of a Triple-Layered Coaxial Extruder System: *in silico* and *in vitro* Evaluations Directed Toward Optimizing Cell Viability

Christian Silva[1]*, Carlos J. Cortés-Rodriguez[1], Jonas Hazur[2], Supachai Reakasame[2], Aldo R. Boccaccini[2]

[1]Department of Mechanical Engineering and Mechatronics, School of Engineering, Universidad Nacional de Colombia, Bogotá 111321, Colombia

[2]Department of Materials Science and Engineering, Institute of Biomaterials, University of Erlangen-Nuremberg, Erlangen 91058, Germany

Abstract: Biofabrication is a rapidly evolving field whose main goal is the manufacturing of three-dimensional (3D) cell-laden constructs that closely mimic tissues and organs. Despite recent advances on materials and techniques directed toward the achievement of this goal, several aspects such as tissue vascularization and prolonged cell functionality are limiting bench-to-bedside translation. Extrusion-based 3D bioprinting has been devised as a promising biofabrication technology to overcome these limitations, due to its versatility and wide availability. Here, we report the development of a triple-layered coaxial nozzle for use in the biomanufacturing of vascular networks and vessels. The design of the coaxial nozzle was first optimized toward guaranteeing high cell viability upon extrusion. This was done with the aid of *in silico* evaluations and their subsequent experimental validation by investigating the bioprinting of an alginate-based bioink. Results confirmed that the values for pressure distribution predicted by *in silico* experiments resulted in cell viabilities above 70% and further demonstrated the effect of layer thickness and extrusion pressure on cell viability. Our work paves the way for the rational design of multi-layered coaxial extrusion systems to be used in biofabrication approaches to replicate the very complex structures found in native organs and tissues.

Keywords: Three-dimensional bioprinting, Coaxial nozzle, Vascularized tissues, Tissue-engineered vessels, Biomaterials

***Corresponding Author:** Christian Silva, Department of Mechanical Engineering and Mechatronics, School of Engineering, Universidad Nacional de Colombia, Bogotá 111321, Colombia; casilvaca@unal.edu.co

Received: May 12, 2020; ***Accepted:*** June 22, 2020; ***Published Online***: July 24, 2020

Citation: Silva C, Cortés-Rodriguez C, Hazur J, *et al*., 2020, Rational Design of a Triple-Layered Coaxial Extruder System: *in silico* and *in vitro* Evaluations Directed Toward Optimizing Cell Viability, Int J Bioprint, 6(4): 282. DOI: 10.18063/ijb.v6i4.282.

1 Introduction

Three-dimensional (3D) bioprinting is an additive manufacturing technology that permits the spatiotemporal patterning of hydrogels embedded with cells, namely bioinks, into 3D structures[1,2]. Its goal is to fabricate cell-laden constructs that mimic tissues and organs, where cell viability is preserved and overall physiological functionality is replicated[1,3]. Among its several techniques, extrusion-based bioprinting (EBB) has emerged as the most promising additive manufacturing technique for achieving 3D structures of sufficient complexity, since it can work with a broad range of cell densities and printable materials[4,5]. Moreover, the versatility and affordability provided by EBB systems have contributed to its positioning as the most popular biofabrication technology among researchers worldwide for applications that range from cancer research and drug testing to tissue engineering[6].

Replicating complex internal tissue structures is, however, still a challenge for the available biomanufacturing technologies[3,6]. In the case of EBB, the time lag between hydrogel extrusion and its subsequent crosslinking is one of the limiting factors in the formation of complex geometries[7,8]. This is mainly because the viscoelastic properties of extruded bioinks are often not sufficient to support these geometries before extensive crosslinking is applied[7,9,10]. Therefore, the shape fidelity of the printed constructs is greatly compromised, especially in the fabrication of hollow or highly detailed structures. Emerging techniques such as freeform reversible embedding of suspended hydrogels (FRESH)[11] and volumetric printing[12] have contributed to alleviating some of these limitations by allowing the formation of complex structures. In the FRESH technique, hydrogels are printed in a support bath of sacrificial microparticles, which provides structural support while the hydrogel is crosslinked and therefore guarantees a high degree of shape fidelity[13]. Despite the superior printing resolution achieved in constructs manufactured with this technique, results have not yet been reported when depositing cell-embedded hydrogels[3,14]. Similarly, volumetric bioprinting allows the fabrication of convoluted free-form geometries with the spatially selective exposition of cell-laden photocrosslinkable hydrogels to ultraviolet (UV) or blue light. In particular, this technique has demonstrated the rapid fabrication of anatomically relevant hollow structures with high cell viability[15]. However, the current technique cannot include multiple materials within the same bioprinting process and can lead to unwanted heterogeneous stiffness of the constructs, which greatly limits its exploitability.

Despite recent advances on the development of techniques that allow an increased structural complexity of constructs and novel hydrogel formulations that support bioprinting and maturation of tissues, functionality is a challenge that has not been fully addressed yet[3,16,17]. To engineer functionally relevant tissues *in vitro*, the current inability to recreate the 3D microenvironments seen *in vivo* is a key restriction that must be overcome. Among the attributes that bioprinted constructs must have to permit appropriate tissue maturation, vascular networks appear to be one of the most important[1-3,18]. The scalability of bioprinted constructs toward clinically relevant sizes is often limited by the accessibility of nutrients throughout the construct, as nutrient access and waste removal depend solely on diffusion-mediated transport. As a result, perfusable networks within bioprinted constructs are imperative to create tissues of clinically relevant size, as they will allow adequate nutrient availability and prevent waste accumulation in the innermost regions of the construct[19,20]. This, in turn, will facilitate the maturation of multilayered constructs and shorten the gap between native and *in vitro* functionality. In addition, the biomanufacturing of hollow tubular structures might also be beneficial for generating multilayered large and medium-diameter vascular grafts for use in either transplantation or disease modeling[21-23].

Accordingly, here we report the development of a triple-layered coaxial extruder system for the fabrication of layered tubular structures that allow the simultaneous dispensing of three different materials using EBB systems. Our aim was to study how different design parameters and bioprinting conditions of this system affect the viability of embedded cells upon extrusion. Computational analyses were initially implemented to optimize design parameters of the coaxial extruder system based on predicted pressure distributions, and these findings were then validated experimentally on bioprinting experiments using human cells in alginate-based hydrogels. In addition, the triple-layered design allowed immediate bioink crosslinking upon extrusion by including a crosslinking solution as the outermost layer of the printed tubular structures, and the formation of hollow structures by posterior removal of sacrificial material contained in the innermost layer.

2 Materials and methods

2.1 Triple-layered coaxial nozzle design and *in silico* evaluation

A first prototype of a triple-layered coaxial nozzle was fabricated by assembling commercially available nozzle parts (Nordson EFD, Dunstable, Bedfordshire, UK). A mixture consisting of a cyanoacrylate solution and sodium bicarbonate was employed to adhere the different components into a single structure (**Figure 1A**). From a transverse view, the coaxial nozzle comprised three walls, two rings, and one cylinder, with Gauges (G) ranging from 13 to 25 G. This configuration led to three different flow channels, namely, channel *a*, *b,* and *c*, as shown in **Figure 1B**.

Based on this prototype, a computationally aided design model of the three flow channels was developed and studied using computational fluid dynamics simulations in COMSOL Multiphysics® software. A two-dimensional axisymmetric domain of flow channel *b* and a glass printing surface, with a 100 µm air interface in between, was modeled and simulated based on the overall design of the coaxial nozzle. This channel was of special interest as the nozzle is intended for the extrusion of single-layered tubular structures and the cell-laden hydrogel will be extruded through this channel. The hydrogel was conceived as a non-Newtonian fluid and its physical parameters, such as density and dynamic viscosity, were used as input for calibrating the models. Air was, however, conceived as a Newtonian fluid and its density and dynamic viscosity were also provided as input for the simulations. A parametric analysis was performed by varying the inlet pressure (P) of channel *b* between 10 and 70 kPa and the Gauge of this flow channel was fixed at 18 G. Outlet velocity and pressure were studied at the outlet of the flow channel and compared to previously reported literature to validate the design in terms of cell viability.

Three different coaxial nozzles were designed varying the area of the middle channel (namely, *b* in **Figure 1B**) and subsequently 3D printed using biocompatible photopolymer resins, namely, dental SG FLSGOR01 and dental LT clear (**Figure 1C**). The dimensions of each channel are reported in **Table 1**, along with the area of flow channel *b* (used

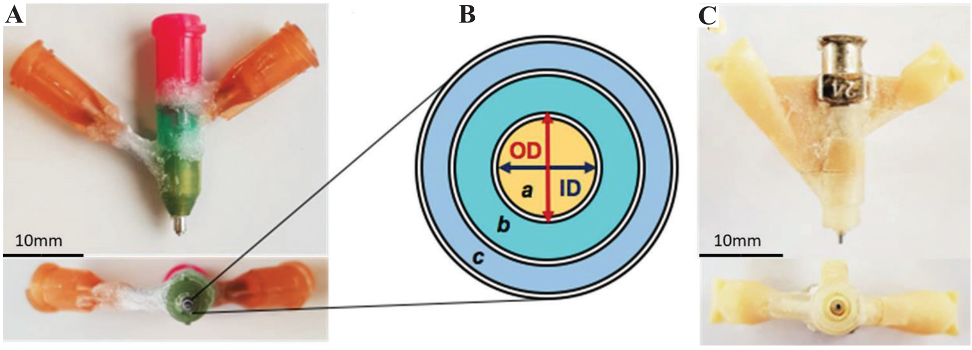

Figure 1. (A) Lateral and frontal view of the initial prototype of the triple-layered coaxial nozzle assembled with commercially available parts. (B) Schematic representation of the transverse view at the tip of the coaxial nozzle. The outer diameter and inner diameter of each channel were defined according to the results of the computational fluid dynamics simulations. (C) Three-dimensional printed coaxial nozzle.

Table 1. Geometric data of the designed coaxial nozzles. ID and OD stand for inner diameter and outer diameter, respectively. The three flow channels of each nozzle are labeled as *a*, *b*, and *c*, as shown in **Figure 1B**.

Parameter	**Nozzle 1**			**Nozzle 2**			**Nozzle 3**		
	a	***b***	***c***	***a***	***b***	***c***	***a***	***b***	***c***
Gauge (G)	23	18	14	25	18	14	20	15	13
ID (mm)	0.33	0.84	1.54	0.25	0.84	1.54	0.61	1.36	1.8
OD (mm)	0.64	1.27	1.83	0.52	1.27	1.83	0.91	1.65	2.41
OD – ID (mm)	0.32	0.43	0.29	0.27	0.43	0.29	0.30	0.29	0.61
Layer thickness (mm)		0.20			0.32			0.45	
Layer area (mm^2)		0.232			0.341			0.802	

for cell-laden hydrogel), which is continuously increasing from Nozzle 1 to Nozzle 3.

2.2 Preparation of hydrogels

For each of the channels (*a*, *b*, and *c*) described in section 2.1, different materials were used during the printing process. While channel *c* was perfused with $CaCl_2$ solution, the other channels were perfused with two different hydrogel compositions.

Channel *a* was used to print a support structure in the core, based on a methylcellulose-gelatin sacrificial ink, as described by Dranseikiene *et al*.[24] Briefly, the sacrificial biomaterial ink is composed of 9 % (w/v) Methylcellulose (Sigma, USA) and 5 % (w/v) gelatin (Sigma, USA) and was shown to exhibit good support characteristics after printing, while dissolving in culture conditions after 1 week.

The hydrogel used for printing with cells was an alginate-based bioink, prepared with a pre-crosslinking technique utilizing $CaCO_3$ and D-Glucono-δ-lactone (GDL). Concisely, a 2 % (w/v) alginate (VIVAPHARM® alginate PH176, JRS PHARMA GmbH & Co. KG, Rosenberg, Germany) solution was pre-crosslinked with 20 mmol/l $CaCO_3$ (Calcium carbonate precipitated for analysis EMSURE®, CAS 471-34-1, Merck KGaA, Darmstadt, Germany) and 40 mmol/l GDL (CAS 90-80-2, Merck KGaA, Darmstadt, Germany) at 4°C. After stirring continuously for 48 h, the hydrogel was allowed to warm up to room temperature and was subsequently mixed with cells (see section 2.4).

2.3 Setup for 3D bioprinting with coaxial nozzles

A commercially available fused deposition modeling 3D printer (Anycubic Prusa I3, ANYCUBIC 3D Printing, Shenzhen, China) was customized to allow the controlled deposition of hydrogels (**Figure 2**). For this purpose, three independent piston-driven extrusion systems were coupled to the machine and the feed rate (mm/s) was translated into pressure units (kPa) with the aid of an external system. Next, printheads suited for 12 mL Luer-lock syringes were adapted to the extrusion systems and their outlet tips were connected to the inlets of the 3D printed coaxial nozzles.

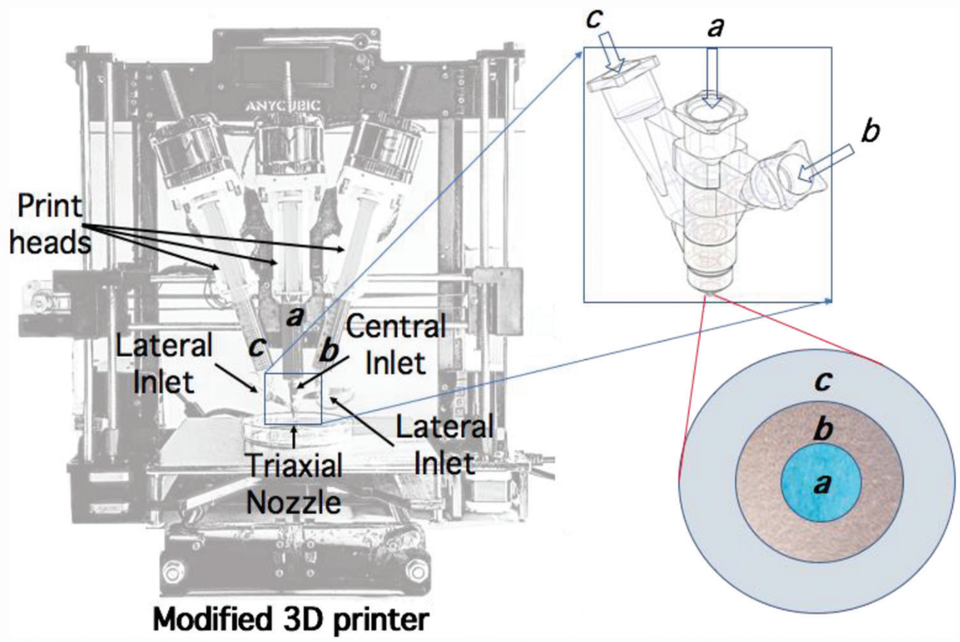

Figure 2. Three-dimensional (3D) bioprinter setup for bioprinting experiments. Three printheads were adjusted to a fused deposition modeling 3D printer with piston-driven extrusion systems and connected to the triple-channel coaxial nozzle. Each flow channel is labeled at the inlet and outlet of the coaxial nozzle for a better understanding of the reader.

2.4 Cell culture and embedding

Before bioprinting experiments, human bone osteosarcoma cells MG-63 (ATCC® CRL-1427™) were cultured in complete growth medium consisting of Dulbecco's Modified Eagle Medium supplemented with 10% (v/v) fetal bovine serum and 1% (v/v) Penicillin-Streptomycin (10,000 U/ml) and maintained in a CO_2 incubator at 37°C. Upon the culture reached a confluence of approximately 80–90%, cells were harvested with the aid of a 0.25 % (w/v) trypsin solution (Gibco™, Thermo Fisher Scientific, Waltham, MA, USA). The cell concentration of the obtained suspension was then estimated by staining with trypan blue and hemocytometer counting. Subsequently, cells were carefully embedded in the alginate-based hydrogel. To perform this, the hydrogel (without cells) was filled into a 12 ml Luer-lock syringe and connected to another syringe containing an 11×10^6 cells/ml cell suspension. To guarantee homogeneous mixing, the two components were extruded back and forth at least 10 times. The volume ratio was 10:1 (hydrogel:cell suspension), resulting in a final cell density of 1×10^6 cells/ml in the bioink.

2.5 Bioprinting of tubular structures

For bioprinting, the coaxial nozzles were submerged in 70% (v/v) ethanol for 1 h before experiments and subsequently washed with sterile 1 × PBS in a biosafety cabinet. The modified 3D printer was thoroughly wiped with 70% (v/v) ethanol and exposed to UV germicidal light for 1 h inside a biosafety cabinet.

Each nozzle comprised three flow channels at the tip, namely *a*, *b,* and *c* in **Figure 1B**. Two different hydrogels and a crosslinking solution were employed for bioprinting hollow, tube-like structures. A methyl cellulose-based hydrogel was used as a sacrificial material for the lumen (flow channel *a* in **Figure 3**) and an alginate-based bioink embedded with human bone osteosarcoma MG63 cells was used for the middle tubular channel (flow channel *b* in **Figure 3**). Calcium chloride ($CaCl_2$) 0.1 M solution was expelled through the outer channel of the coaxial nozzle (flow channel *c* in **Figure 3**) since it served as a crosslinking agent for the alginate bioink. All materials were dispensed coaxially by mechanical extrusion of the three separate printheads simultaneously. The resulting

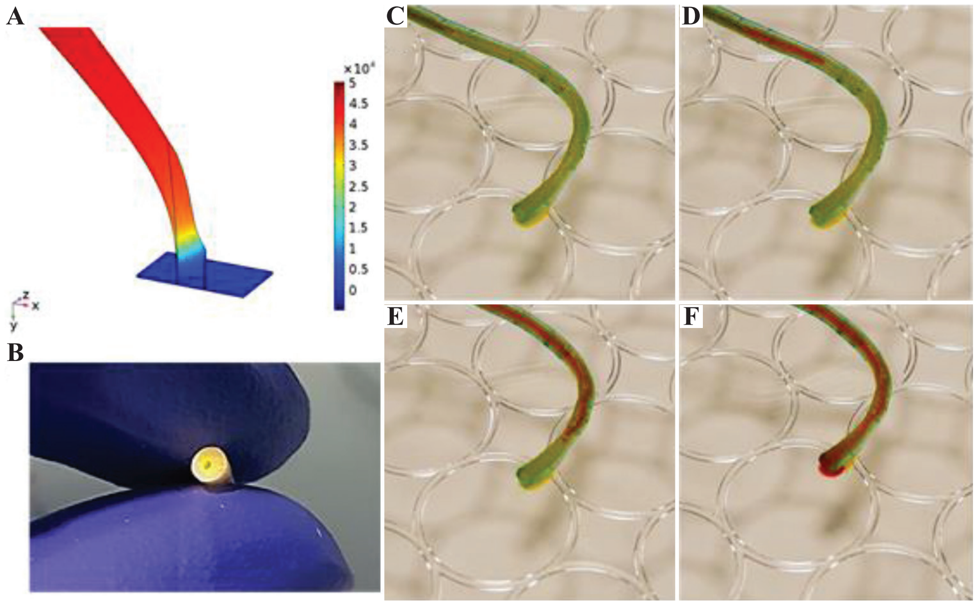

Figure 3. (A) Pressure distribution profiles along the geometry of one of the studied flow channels (flow channel *b*). Values on the color bar are displayed in Pa × 10^4. (B) Transverse view of one of the printed and perfused hollow cannular structures. (C), (D), (E) and (F) display one of the hollow cannular structures being perfused with 1 × PBS stained with red food coloring.

tubular structures were then perfused through the core channel with warm sterile 1 × PBS to wash away the sacrificial material.

This bioprinting procedure was performed with the three designed nozzles varying the extrusion pressure of the printhead connected to channel *b* since the cell-laden bioink was dispensed through this channel. The extrusion pressure of the other two channels was adjusted to achieve the same extrusion rate as that of channel *b*. Coaxial tubular structures were dispensed with three extrusion pressures: 26, 34, and 40 kPa, through each of the designed nozzles. Each combination of bioprinting parameters was performed in triplicates, resulting in a total of 27 extruded tubular structures.

2.6 Cell viability assessment

For studying the effect of the inlet extrusion pressure and the different coaxial nozzle geometries on cell survival, a Live/Dead (Sigma-Aldrich, St. Louis, MO, USA) assay was performed on the bioprinted tubular structures. Briefly, constructs were stained with calcein acetoxymethyl ester (calcein-AM) and propidium iodide (PI) immediately after bioprinting and fluid perfusion through the lumen, to visualize live and dead cells, respectively. The staining solution was prepared according to the manufacturer's instructions. Bioprinted constructs were subsequently submerged in it and incubated for 15 min at room temperature (~22ºC) protected from light. Samples were then washed with 1 × PBS and imaged using an epifluorescence microscope (ZEISS Axio Observer, Carl Zeiss AG, Oberkochen, Germany). One image from a random location on each sample was captured and later analyzed using the ImageJ software.

2.7 Statistical analysis

Data for cell viability was statistically analyzed with the aid of the GraphPad Prism software (GraphPad Software, La Jolla, CA, USA). The statistical distribution of the data was first studied with the Shapiro-Wilk normality test and a two-way ANOVA with Tukey's multiple comparisons tests was subsequently performed.

3 Results and discussion

In silico simulations, varying the extrusion, pressure was performed to investigate the impact that the overall design of the coaxial nozzle might have on cell viability. Since this nozzle is intended for the fabrication of single-layered tubular structures, cell-laden hydrogels will only be extruded through channel b; however, the simulations were performed for all channels. Fluid velocity and pressure distribution through the entire channel geometry were collected from the simulations. The minimum and maximum fluid velocities at the outlet were 13 and 43 mm/s, respectively. Moreover, velocity appeared to remain constant through the entire geometry for all extrusion pressures studied and, in each layer/area, into the nozzle geometry. However, that was not the case for pressure distribution since it seemed to decrease as the fluid approached the air interface between the nozzle and the collecting glass slide. According to the simulations, pressure distribution values at the tip of the flow channels fell to between 2 and 10 kPa, while pressures between 20 and 64 kPa could be experienced at the upper most regions of the *in-silico* flow channels. These values were then compared to those validated experimentally by previous studies for ordinary[25,26] and coaxial[27] nozzles. Nair *et al.* reported that cell viability decreases exponentially as a function of increasing shear stress, with cell viability above 60 % for pressures below 100 kPa and nozzle diameters between (150 and 400 μm)[26]. Yu and colleagues investigated this same relationship on coaxial nozzles and obtained very similar results[27]. Although these estimations depend widely on the rheological properties of the studied hydrogel and on the specific response of the cells utilized, we might be able to predict the high viability of cells bioprinted with the present coaxial nozzle. The predicted values collected for pressures experienced by cells on the bioprinting process fall within a safe range for cells according to these previous studies.

To confirm these notions and to investigate the effect of nozzle geometry, specifically the flow channel Gauge, on cell viability, bioprinting experiments were conducted with three different nozzles. As shown in **Table 1**, nozzles 1 and 2 allow the fabrication of single-layered hollow tubular structures of equal outer diameter (OD), but with different layer thicknesses. Likewise, nozzle 3 allows the fabrication of structures with a greater diameter and layer thickness than nozzles 1 and 2. These nozzles were subsequently 3D printed with biocompatible photopolymer resins (**Figure 1C**) and adapted to a commercially available and modified 3D printer for bioprinting experiments (**Figure 2**). These nozzles allow the fabrication of cannular structures of diameters in the range of 0.84–1.36 mm (OD) and 0.52–0.91 mm (ID), which fall within the average dimensions of human arteries[28]. As shown in **Figure 3**, single-layered cannular structures were successfully fabricated and perfused with a red-stained solution of 1 × PBS for demonstration purposes.

In addition to nozzle geometry, the effect of inlet pressure on cell viability was studied experimentally by varying the applied pressure of the mechanical extruder of flow channel *b* within 26–40 kPa. Three different values of extrusion pressures within this range were selected according to printing experiments with the alginate-based hydrogel. These values were 26, 34, and 40 kPa and the three of them fell within the material's printing window, as they allowed controlled and continuous deposition of a filament. An alginate-based bioink embedded with MG-63 cells was chosen for this evaluation since alginate is a widely used biocompatible material, easily extrudable and features rapid crosslinking upon exposition to divalent cations, which enables excellent shape fidelity in bioprinted constructs[29].

As shown in **Figure 4A and B**, most cells remain viable immediately upon deposition with all evaluated extrusion pressures and nozzles. The normal distribution of the data was first confirmed with the Shapiro-Wilk test ($P = 0.508$) before performing a two-way ANOVA on the data. Extrusion pressure ($P < 0.0001$) and nozzle geometry ($P < 0.0001$), as well as their interaction ($P < 0.001$), were found to have a significant effect on cell viability according to statistical analyses. Specifically, the viability of bioprinted structures through all nozzles seems to be significantly diminished with the rise of inlet extrusion pressure, as displayed in **Figure 4C**. In addition, all extrusion pressures evaluated through nozzle three yield significantly higher cell viability than nozzles 1 and 2, which suggests that a wider diameter in the tubular structures significantly reduces the stress to

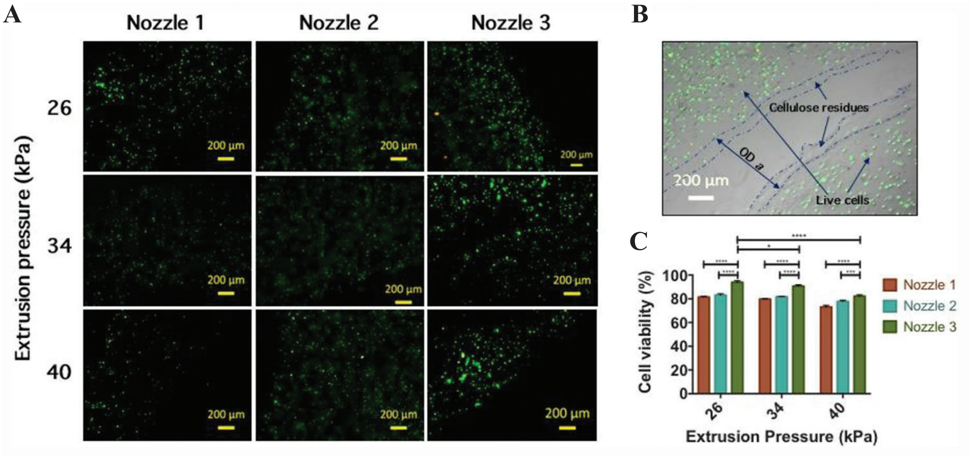

Figure 4. (A) Live/dead assay images of 3D printed cannular constructs with the three designed nozzles varying extrusion pressure of channel *b*. (B) Epifluorescent microscopy image of cannular structure after removal of the innermost sacrificial material. Cells embedded in the bioink extruded through channel *b* remain viable. (C) Cell viability of constructs immediately after bioprinting using the three designed nozzles and varying extrusion pressure between 26, 34, and 40 kPa. All configurations show high cell viability, but Nozzle 3 and low extrusion pressures yield the best results.

which cells are exposed during extrusion. Moreover, the viability of constructs extruded through nozzle 2 is only significantly different from those extruded through nozzle 1 when the inlet pressure is high (40 kPa), which indicates that layer thickness affects viability but to a lesser extent than the extrusion pressure. However, setting an 80 % cell viability threshold, these results suggest that all three coaxial nozzles could be used for the bioprinting of hollow tubular structures by applying an inlet extrusion pressure below 34 kPa.

The main goal of this research is to optimize the development of triple-layered coaxial nozzles for facilitating the fabrication of biomimetic tissues and organ-like constructs for tissue engineering and regenerative medicine applications. Furthermore, the enhanced development of triple-layered coaxial nozzles can help to solve the issues regarding vascularization, which remain as one of the key bottlenecks of the field[30]. The next step in our research is to apply these same concepts in the development of a four-layered coaxial nozzle, whose advantages compared to the coaxial nozzle presented here will be remarked. With one more layer, it will be easier to close mimic the complexity of the vascular network, taking into account that the current state of the art tissue conventional culture technique is limited to only triple co-culture (3 types of cells). Advancements in tissue culture techniques are necessary to address the bottleneck of maturing bioprinted multi-cellular 3D tissue constructs into functional tissues with a wide range of cells and biomaterials with differentiated layer co-culture within one single bioprinted construct.

The novelty of this work is adding value in the research field of bioprinting with a triple-layered coaxial nozzle development that has the potential to closely mimic the complexity of vascular networks found in the native human body in terms of histological and morphological of this vascular constructs, as well this development can replicate the wall thickness of a native blood vessel that generally comprised three layers with the innermost tunica intima layer made by continuous endothelium cells followed by the middle tunica layer made of elastic, smooth muscle cells and an outermost tunica adventitia layer made of surrounding fibroblast and collagen; an ideal tissue-engineered blood vessel should consist of those three layers, this coaxial nozzle can reduce the wall thickness of this kind of tissues obtained in other investigations[31] close mimicking the wall thickness of small arteries and veins in a real human body.

4 Conclusions

In silico simulations were performed for studying the pressure distribution exerted on cells during the bioprinting process, as well as the outlet velocity at the tip of three different flow channels. Our results confirmed those of previously reported studies and demonstrate the usefulness of *in silico* experiments in helping to optimize *in vitro* experiments. The results can be useful in guiding the future development of improved multi-layered coaxial nozzles.

Three triple-layered coaxial nozzles with different Gauges were first studied *in silico* regarding varying pressures and then successfully designed for the fabrication of single-layered hollow tubular structures of different dimensions. All nozzles displayed adequate bioprinting conditions to guarantee cell viability above 80 % in alginate-based hydrogels when extrusion pressure was kept below 34 kPa, meaning they are all suitable for bioprinting with bioinks with similar composition or rheological properties to the one studied in this project. Moreover, herein reported coaxial nozzles to allow the formation of perfusable cannular structures with dimensions that fall within the range of human arteries, which means they could be further exploited for the fabrication of multicellular vascular networks and vessel-like constructs with applications on tissue engineering. Our work paves the way for the rational development of coaxial nozzles useful for bioprinting multi-layered vascular channels or vessel-like constructs that truly resemble those found in native organs and organisms.

Acknowledgments

We would like to acknowledge the financial support received from the Colombian Administrative

Department of Science, Technology, and Innovation, COLCIENCIAS, and the National Doctorate Scholarship Program-647 and by the German Academic Exchange Service (Deutscher Akademischer Austauschdienst). DAAD, Research Grants-Short Term Grants, 2018. "No conflict of interest was reported by all authors."

Conflicts of interest

No conflicts of interest were declared by all authors.

References

1. Murphy SV, Atala A, 2014, 3D Bioprinting of Tissues and Organs. *Nat Biotechnol*, 32:773–85.
2. Pati F, Gantelius J, Svahn HA, 2016, 3D Bioprinting of Tissue/Organ Models. *Angew Chem*, 55:4650–65.
3. Heinrich MA, Liu W, Jimenez A, *et al*., 2019, 3D Bioprinting: From Benches to Translational Applications. *Small*, 15:1–47.
4. Jiang T, Munguia-Lopez JG, Flores-Torres S, *et al*., 2019, Extrusion Bioprinting of Soft Materials: An Emerging Technique for Biological Model Fabrication. *Appl Phys Rev*, 6:11310.
5. Paxton N, Smolan W, Böck T, *et al*., 2017, Proposal to Assess Printability of Bioinks for Extrusion-based Bioprinting and Evaluation of Rheological Properties Governing Bioprintability. *Biofabrication*, 9:4.
6. Ozbolat IT, Hospodiuk M, 2016, Current Advances and Future Perspectives in Extrusion-based Bioprinting. *Biomaterials*, 76:321–43.
7. Hölzl K, Lin S, Tytgat L, *et al*., 2016, Bioink Properties before, during and after 3D Bioprinting. *Biofabrication*, 8:32002.
8. Jungst T, Smolan W, Schacht K, *et al*., 2016, Strategies and Molecular Design Criteria for 3D Printable Hydrogels. *Chem Rev*, 116:1496–539.
9. Williams D, Thayer P, Martinez H, *et al*., 2018, A Perspective on the Physical, Mechanical and Biological Specifications of Bioinks and the Development of Functional Tissues in 3D Bioprinting. *Bioprinting*, 9:19–36.
10. Hospodiuk M, Dey M, Sosnoski D, *et al*., 2017, The Bioink: A Comprehensive Review on Bioprintable Materials. *Biotechnol Adv*, 35:217–39.
11. Hinton TJ, Jallerat Q, Palchesko RN, *et al*., 2015, Three-dimensional Printing of Complex Biological Structures by Freeform Reversible Embedding of Suspended Hydrogels. *Sci Adv*, 1:9.
12. Kelly BE, Bhattacharya I, Heidari H, *et al*., 2019, Volumetric Additive Manufacturing via Tomographic Reconstruction. *Science*, 363:1075–9.
13. Li J, Wu C, Chu PK, Gelinsky M, 2020, 3D Printing of Hydrogels: Rational Design Strategies and Emerging Biomedical Applications. *Mater Sci Eng R Rep*, 140:100543.
14. Lee A, Hudson AR, Shiwarski DJ, *et al*., 2019, 3D Bioprinting of Collagen to Rebuild Components of the Human Heart. *Science*, 365:482–7.
15. Bernal PN, Delrot P, Loterie D, *et al*., 2019, Volumetric Bioprinting of Complex Living-Tissue Constructs within Seconds. *Adv Mater*, 31:42.
16. Levato R, Jungst T, Scheuring RG, *et al*., 2020, From Shape to Function: The Next Step in Bioprinting. *Adv Mater*, 2020:1906423.
17. Moroni L, Burdick JA, Highley C, *et al*., 2018, Biofabrication Strategies for 3D *In Vitro* Models and Regenerative Medicine. *Nat Rev Mater*, 3:21–37.
18. Ravnic DJ, Leberfinger AN, Koduru SV, *et al*., 2017, Transplantation of Bioprinted Tissues and Organs: Technical and Clinical Challenges and Future Perspectives. *Ann Surg*, 266:48–58.
19. Ke D, Murphy SV, 2019, Current Challenges of Bioprinted Tissues Toward Clinical Translation. *Tissue Eng Part B Rev*, 25:1–13.
20. Kang HW, Lee SJ, Ko IK, *et al*., 2016, A 3D Bioprinting System to Produce Human-scale Tissue Constructs with Structural Integrity. *Nat Biotechnol*, 34:312–9.
21. Distler T, Ruther F, Boccaccini AR, *et al*., 2019, Development of 3D Biofabricated Cell Laden Hydrogel Vessels and a Low-Cost Desktop Printed Perfusion Chamber for *In Vitro* Vessel Maturation. *Macromol Biosci*, 19:9.
22. Jia W, Gungor-Ozkerim PS, Zhang YS, *et al*., 2016, Direct 3D Bioprinting of Perfusable Vascular Constructs Using a Blend Bioink. *Biomaterials*, 106:58–68.
23. Gao G, Park JY, Kim BS, *et al*., 2018, Coaxial Cell Printing of Freestanding, Perfusable, and Functional *In Vitro* Vascular Models for Recapitulation of Native Vascular Endothelium Pathophysiology. *Adv Healthc Mater*, 7:1–12.
24. Dranseikiene D, Schrüfer S, Schubert DW, *et al*., 2020, Cell-laden Alginate Dialdehyde Gelatin Hydrogels Formed in 3D Printed Sacrificial Gel. *J Mater Sci Mater Med*, 31:3–7.
25. Blaeser A, Campos DF, Puster U, *et al*., 2016, Controlling Shear Stress in 3D Bioprinting is a Key Factor to Balance Printing Resolution and Stem Cell Integrity. *Adv Healthc Mater*, 5:326–33.
26. Nair K, Gandhi M, Khalil S, *et al*., 2009, Characterization of Cell Viability during Bioprinting Processes. *Biotechnol J*, 4:1168–77.

27. Yu Y, Zhang Y, Martin JA, *et al*., 2013, Evaluation of Cell Viability and Functionality in Vessel-like Bioprintable Cell-laden Tubular Channels. *J Biomech Eng*, 135:1–9.
28. Widmaier EP, Raaff H, Strang KT, 2014, Vander's Human Physiology. 13th ed. McGraw Hill, New York.
29. Curley CJ, Dolan EB, Otten M, *et al*., 2019, An Injectable Alginate/Extra Cellular Matrix (ECM) Hydrogel Towards Acellular Treatment of Heart Failure. *Drug Deliv Transl Res*, 9:1–13.
30. Wei LN, Chee KC, Yu FS, 2019, Print Me An Organ! Why We Are Not There Yet. *Prog Polym Sci*, 97:1–45.
31. Schoneberg J, De Lorenzi F, Theek B, *et al*., 2018, Engineering Biofunctional *In Vitro* Vessel Models Using a Multilayer Bioprinting Technique. *Sci Rep*, 8:1–13.

ORIGINAL ARTICLE

3D Printing of Anisotropic Bone-Mimetic Structure with Controlled Fluid Flow Stimuli for Osteocytes: Flow Orientation Determines the Elongation of Dendrites

Aira Matsugaki[1], Tadaaki Matsuzaka[1], Ami Murakami[1], Pan Wang[2], Takayoshi Nakano[1]*

[1]Division of Materials and Manufacturing Science, Graduate School of Engineering, Osaka University, 2-1 Yamada-oka, Suita, Osaka 565-0871, Japan

[2]Singapore Institute of Manufacturing Technology, 73 Nanyang Drive, 637662, Singapore

Abstract: Although three-dimensional (3D) bioprinting techniques enable the construction of various living tissues and organs, the generation of bone-like oriented microstructures with anisotropic texture remains a challenge. Inside the mineralized bone matrix, osteocytes play mechanosensing roles in an ordered manner with a well-developed lacunar-canaliculi system. Therefore, control of cellular arrangement and dendritic processes is indispensable for construction of artificially controlled 3D bone-mimetic architecture. Herein, we propose an innovative methodology to induce controlled arrangement of osteocyte dendritic processes using the laminated layer method of oriented collagen sheets, combined with a custom-made fluid flow stimuli system. Osteocyte dendritic processes showed elongation depending on the competitive directional relationship between flow and substrate. To the best of our knowledge, this study is the first to report the successful construction of the anisotropic bone-mimetic microstructure and further demonstrate that the dendritic process formation in osteocytes can be controlled with selective fluid flow stimuli, specifically by regulating focal adhesion. Our results demonstrate how osteocytes adapt to mechanical stimuli by optimizing the anisotropic maturation of dendritic cell processes.

Keywords: Bioprinting, Collagen substrate, Mineralization, Osteocyte, 3D arrangement of bone matrix

***Corresponding Author:** Takayoshi Nakano, Graduate School of Engineering, Osaka University, Osaka, Japan; nakano@mat.eng.osaka-u.ac.jp

Received: June 03, 2020; ***Accepted:*** June 25, 2020; ***Published Online:*** July 27, 2020

Citation: Matsugaki A, Matsuzaka T, Murakami A, *et al*., 2020, 3D Printing of Anisotropic Bone-Mimetic Structure with Controlled Fluid Flow Stimuli for Osteocytes: Flow Orientation Determines the Elongation of Dendrites, *Int J Bioprint*, 6(4): 293. DOI: 10.18063/ijb.v6i4.293

1 Introduction

The highly ordered three-dimensional (3D) microstructured bone matrix determines the specialized anisotropic bone function[1]; for example, the collagen/apatite bone matrix shows anisotropic texture depending on the anatomical position, which realizes the mechanoadaptation of bone tissue[2-4]. Although several approaches have been made for the development of bone-mimetic structures *in vitro*[5-7], conventional monolayered two-dimensional (2D) cultures have limitations in approaching the crosstalk among multiple cell types in biomimetic niches. Development of an appropriate 3D platform is critical for the manufacturing of a functional bone tissue equivalent since a 3D environment is necessary for bone cell functionalization. In particular, osteocytes are embedded in the mineralized matrix with an ordered cell arrangement, surrounded by a networked lacunar-canaliculi system[8]. Increasing evidence shows that osteocytes play crucial roles in bone metabolism in response to the mechanical environment[9,10]. The cellular activities of osteocytes are regulated by the fluid flow inside canaliculi, which is primarily caused by compressive loading of the bone related to physical activity. Therefore, control of the anisotropic bone matrix microstructure and fluid flow stimuli must be established in 3D bone-mimetic constructs for understanding the relationship between osteocyte mechanosensation and bone tissue architecture.

3D bioprinting techniques represent an additive manufacturing technology for developing living tissues or organs[11]. Bioprinting procedures are mainly classified into three categories: extrusion[12], jetting[13,14], and vat polymerization techniques[15]. These procedures allow the positional control of cells throughout the cultivation period. Spatiotemporally controlled deposition of living cells and biomaterials is required for the establishment of the biomimetic construct; in this context, placement of each cell at the proper position under controlled cell maturation conditions is expected. Importantly, osteocytes are pivotal cells for the mechanical functionalization of bone tissue, and their function cannot be achieved without the 3D surrounding matrix environment[16]. We previously developed a 2D biofabrication method for controlling the ordered arrangement of osteoblasts using the extrusion method of collagen molecules[17]. While our work has revealed that monolayered control of osteoblast alignment is efficient for the development of oriented collagen/apatite matrix deposition[17-19], control of bone matrix-embedded osteocytes is hard to achieve in 2D culture; therefore, bone cell culture in a 3D niche is necessary for the spatiotemporal control of the bone-mimic structure.

In this study, an innovative method combining collagen extrusion and sheet lamination was developed. Furthermore, the functional responses of osteocytes to mechanical stimuli were addressed by providing directional fluid flow in parallel or perpendicular to the substrate 3D orientation.

2 Materials and methods

2.1 Fabrication of the 3D oriented collagen scaffold

3D oriented collagen substrates were produced by combining the sheet lamination (ASTM F2792) and hydrodynamic extraction methods[17]. Collagen solution (10 mg/mL in 0.02 N acetic acid, pepsin-solubilized collagen type-I derived from porcine skin (Nippi)) was deposited into phosphate buffer saline (PBS) solution under control with a three-axis robotic arm (Musashi Engineering), which could regulate the orientation and degree of orientation of collagen fibers (**Figure 1A**). Two types of 3D collagen scaffold ("random" and "oriented") were built using lamination method with control of a robotic arm in 3D directions. The collagen scaffold without preferred orientation was fabricated by controlled lamination of isotropic collagen sheets produced by deposition of type I collagen solution onto the flat field. The 3D scaffolds were soaked in PBS to obtain sufficient swelling.

2.2 Ethics statement

The Osaka University Committee for Animal Experimentation approved all the animal experiments (approval number: 27-2-1). The authors performed all experiments in accordance with the related guidelines for ethical and scientific animal experimentation.

2.3 Primary culture of mouse osteoblast

We isolated primary osteoblasts from the neonatal mice calvariae using sequential enzymatic protocol[20]. Calvariae were extracted from neonatal C57BL/6 mice in cold α-minimal essential medium (MEM) (Thermo Fisher Scientific), and the surrounding tissues and cells around the bone were cleanly eliminated. The extracted calvariae tissue was digested with collagenase (Wako)/trypsin (Nacalai Tesque). The digestion procedure was repeated five times at 37°C for 15 min each after the tissue was finely cut and washed with Hank's balanced salt solution (HBSS). After centrifugation of the first two

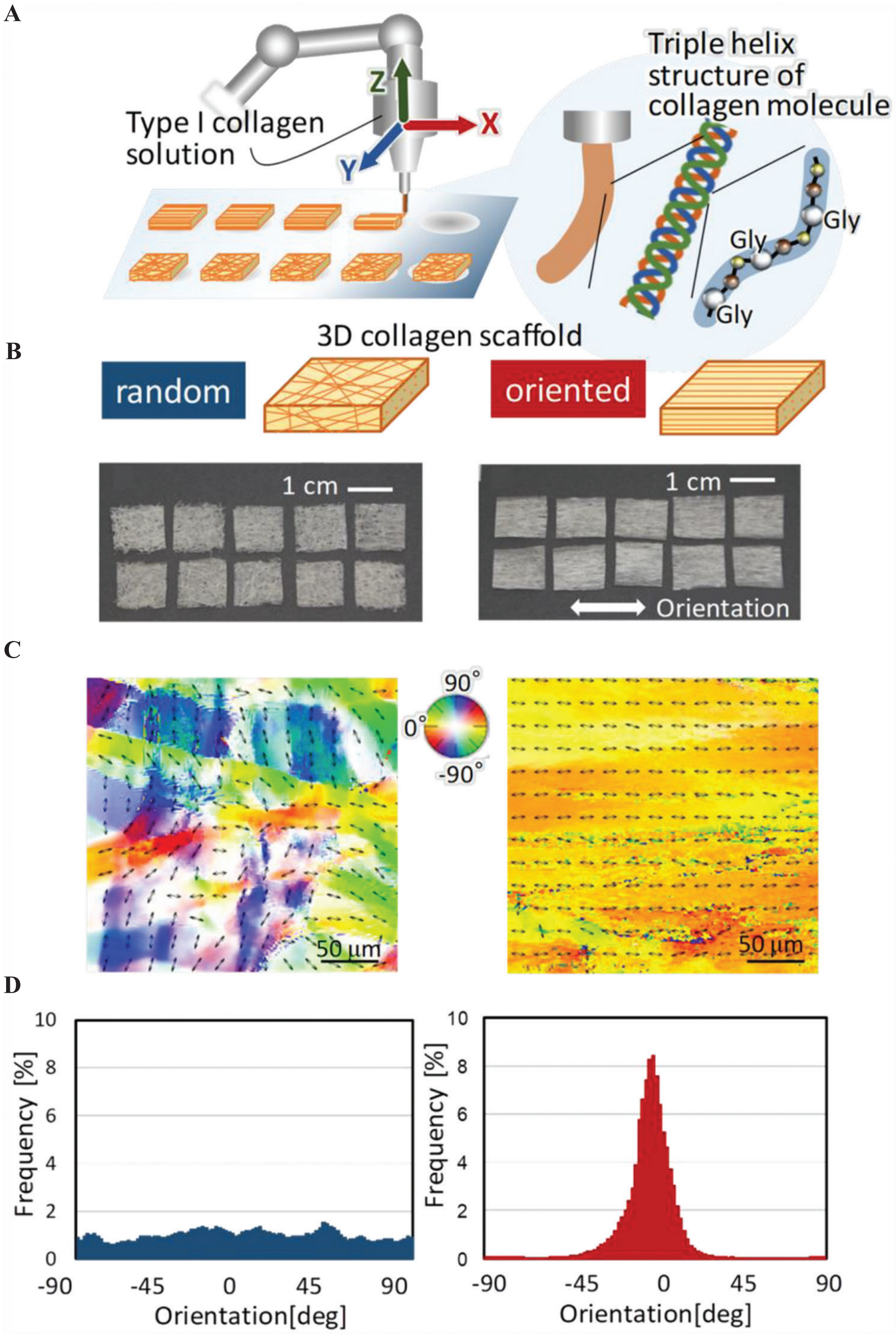

Figure 1. Fabrication of three-dimensional (3D) oriented collagen scaffolds with controlled molecular alignment. (A) Type I collagen solution was deposited with a controlled 3D robotic arm. Collagen solution was extruded from the nozzle, allowing fibril formation with aligned molecular arrangement of amino acid sequencing (Gly-X-Y). Each oriented collagen fiber sheet was laminated layer by layer for 3D construct. (B) Appearance of the fabricated 3D collagen substrates. Left; scaffold with random orientation. Right; one-directional oriented scaffold. (C) Birefringence analysis of the substrates. The bidirectional arrows and color maps show the orientation of collagen fiber in the obtained scaffold. (D) The angular distribution of the collagen fiber orientation in the scaffold determined from the corresponding birefringence images.

treatments, the supernatants were disposed. The obtained supernatants involving from the third to fifth treatments were collected in α-MEM. We filtrated the collections through a cell strainer (BD Biosciences), centrifuged, and the supernatant was removed. The extracted cells were resuspended in α-MEM containing 10% fetal bovine serum, penicillin/streptomycin (Thermo Fisher Scientific) for cell culture. The obtained cells were then plated into the fabricated specimens at a density of 2.0×10^4 cells per mL. The media were changed twice weekly, and after culturing for 1 week, the media were supplemented to reach final concentrations of 10 mM β-glycerophosphate (Tokyo Kasei), 50 μg/mL ascorbic acid (Sigma-Aldrich), and 50 nM dexamethasone (MP Bioscience).

2.4 Primary culture of osteocyte

We isolated primary osteocytes from mature murine femurs, humeri, and tibiae based on a sequential digestion method[21]. Long bones were excised from mature C57BL/6 mice in fresh α-MEM (Thermo Fisher Scientific) with penicillin/streptomycin. The surrounding tissues around the bone were eliminated. The obtained bone specimens were then cut into fraction of 1–2 mm in length and cleaned in HBSS. The pieces were exposed to total nine repeated cycles of enzymatic digestion procedure for 25 min at 37°C each step. During the first three digestions, we incubated the bone fragments with collagenase (Wako) solution followed by cleaning in HBSS thrice. From the fourth treatment, we incubated the bone fragments in collagenase and ethylenediaminetetraacetic acid in turns and cleaned in HBSS thrice. Following that, the treated bone fragments were cut and immersed in α-MEM with penicillin/streptomycin and 10% fetal bovine serum. Osteocyte-like cells were obtained from migrated cells from the cultured bone chips after 7–10 days. Isolated cells were plated into the fabricated 3D substrates at a diluted density of 1×10^5 cells/mL.

2.5 Fluid flow stimulation

The cell-seeded 3D scaffolds were inserted into custom-made flow chambers for fluid flow stimulation with a peak shear stress of 80 dyn/cm^2 for 4 h. Static control cells were also inserted into the flow chambers without flow stimulation. The applied shear stress was calculated based on the Hagen–Poiseuille equation:

$$\tau_w = {}^{4Q\mu}\!\big/\!{}_{\pi R^3} \tag{1}$$

Where, τ_w is the fluid shear stress, Q is the volumetric flow rate, R is the radius of tubing, approximating the flow channel as the same number of collagen fiber strings, and μ is the viscosity coefficient of the culture medium. To apply the Hagen–Poiseuille equation, the following conditions were satisfied: Steady-state laminar flow, inelastic tubing, and Newtonian fluid of culture medium.

2.6 Analysis of substrate collagen orientation

The collagen orientation in the fabricated scaffold was assessed using a birefringence measurement system (WPA-micro, Photonic Lattice). The integrated polarizer allowed to detect the polarization axis with the greater index of refraction (slow axis). The average direction of the slow axis in collagen molecule corresponding to each pixel was analyzed using the equipped software (WPA-VIEW, Photonic Lattice).

2.7 Immunostaining

The cells were fixed with paraformaldehyde and then washed with PBST (PBS-Triton X100) containing normal goat serum (Thermo Fisher Scientific) for 30 min to avoid non-specific binding of antibodies. We incubated the fixed cells with primary antibodies against Sclerostin (Abcam) or Src (Cell Signaling) at 4°C for half a day. After rinsing with PBST, we applied secondary antibodies (Alexa Fluor 546 Immunoglobulin G, Thermo Fisher Scientific) and DAPI (Thermo Fisher Scientific) at room temperature for 2 h. For visualization of F-actin, the cells were incubated with Alexa Fluor 488 phalloidin (Thermo Fisher Scientific). Finally, the stained cells were washed in PBST, followed by mounting using Antifade Reagent (Prolong Gold, Thermo Fisher Scientific). Fluorescent images were obtained under a confocal microscope (FV1000D-IX81, Olympus) and processed using the Adobe Photoshop 10.0 software. For quantitative analysis of dendritic cell processes, dendrites with length of more than 20 μm were counted[22]. The angle of cell processes was analyzed as a reference of substrate collagen orientation.

2.8 Gene expression analysis

We extracted total RNA from the cultured cells using column method (NucleoSpin RNA XS, Macherey-Nagel). The expression levels of Src gene were assessed with quantitative polymerase chain reaction (PCR) according to the manufacturer's guidelines (Applied Biosystems). The Ct value was set within the exponential stage in the PCR. The expression level for each target gene was determined by standardization of the expression value of *Gapdh*. We provide the obtained results as the gene expression (percentage) relative to *Gapdh* expression and then normalized to parallel group.

2.9 Crystallographic texture of the bone matrix

We analyzed the characterization of apatite crystals and their preferred *c*-axis orientation produced by osteoblasts using a microbeam X-ray diffraction system with Mo-Kα radiation (R-Axis BQ; Rigaku) at 50 kV and 90 mA[23]. The specimens were fixed in 10% formaldehyde for analysis. The preferred orientation of the apatite *c*-axis was evaluated. The relative integrated intensity ratio of the (002) diffraction peak to the (310) peak was calculated based on the measurement along the longitudinal axis and transverse direction of the specimens.

2.10 Statistical analysis

Statistical significance was assessed by one-way ANOVA, followed by Tukey's *post hoc* test. A significance of $P < 0.05$ was required for rejecting the null hypothesis.

3 Results

3.1 Fabrication of 3D oriented collagen scaffold with controlled molecular alignment

A 3D oriented microstructured collagen scaffold was successfully produced by an extrusion-based method combined with controlled lamination of each sheet (**Figure 1B**). Birefringence analysis of the fabricated substrates revealed that the control scaffolds showed no preferred alignment of collagen fibers, whereas unidirectional controlled extrusion allowed a uniformly aligned microstructure in one direction (**Figure 1C**). Quantitative analysis of the slow axis of collagen molecules (corresponding to the long axis of collagen fiber) exhibited random and unidirectional angular distribution of collagen fibers in the control and oriented substrates, respectively (**Figure 1D**).

3.2 Anisotropic bone matrix formation by 3D culture of primary osteoblasts

Primary osteoblast cells isolated from neonatal mice calvariae were cultured within the fabricated 3D oriented collagen substrates for 4 weeks in an osteoinductive environment (**Figure 2A**). Osteoblasts showed proliferative and differentiation activities inside the substrates with well-mineralized bone matrix formation. Cells embedded in the substrates showed Sclerostin-positive osteocyte-like morphology (**Figure 2B and C**). The mineralized bone matrix produced by the aligned osteoblasts presented a well-characterized X-ray diffractometer profile for apatite crystals. The integrated intensity ratio of (002)/(310) corresponding to the preferred orientation of the *c*-axis of apatite crystals, showed a significantly higher level along the longitudinal direction in the substrate collagen orientation rather than the transverse orientation of the substrates (**Figure 2D**).

3.3 Osteocyte responses for fluid flow stimulation inside 3D collagen substrates

Primary osteocytes were successfully obtained from the bone fragments derived from the mature bone tissue (**Figure 3A**). Cells inside the bone chips migrated and adhered onto the cell culture plate, presenting typical morphology with multiple cell processes (**Figure 3B**). Isolated osteocytes cultured inside the fabricated substrates were stimulated with controlled unidirectional

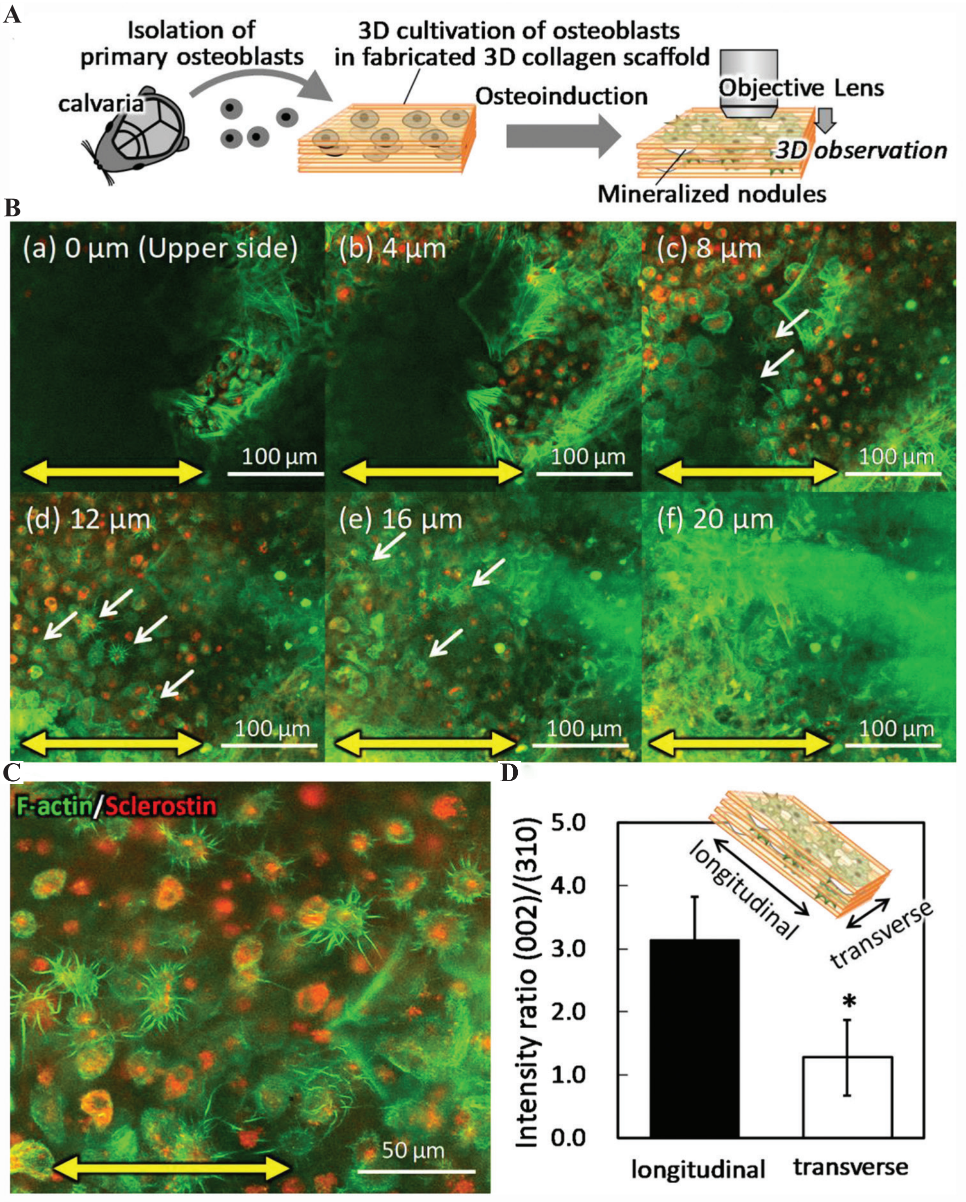

Figure 2. Anisotropic bone matrix formation in three-dimensional (3D) culture of primary osteoblasts. (A) Schematic illustration of the 3D culture procedure of primary osteoblasts. (B) Confocal microscopy analysis of immunofluorescent images of the cells inside the 3D mineralized matrix depending on the distance from the substrate surface. The substrate orientation is indicated by bidirectional yellow arrows. Arrows indicate the osteocyte-like cells with multiple dendritic processes. Green; F-actin, red; sclerostin. (C) Z-stacked immunocytochemical image of the cells inside the scaffold. Green; F-actin, red; sclerostin. (D) Microbeam X-ray diffraction analysis of the mineralized matrix. Bone matrix orientation was calculated with the intensity ratio of (002)/(310) in parallel and vertical direction to the substrate orientation. *: $P < 0.05$.

flow against the longitudinal direction of cell body, lacked cell processes along the substrate orientation, and generated the processes newly for the flow orientation (**Figure 3C**). Quantitative analysis of the cell process formation in the crossing direction against the substrate orientation showed significantly increased frequency in the vertical flow stimulated osteocytes (**Figure 3D**).

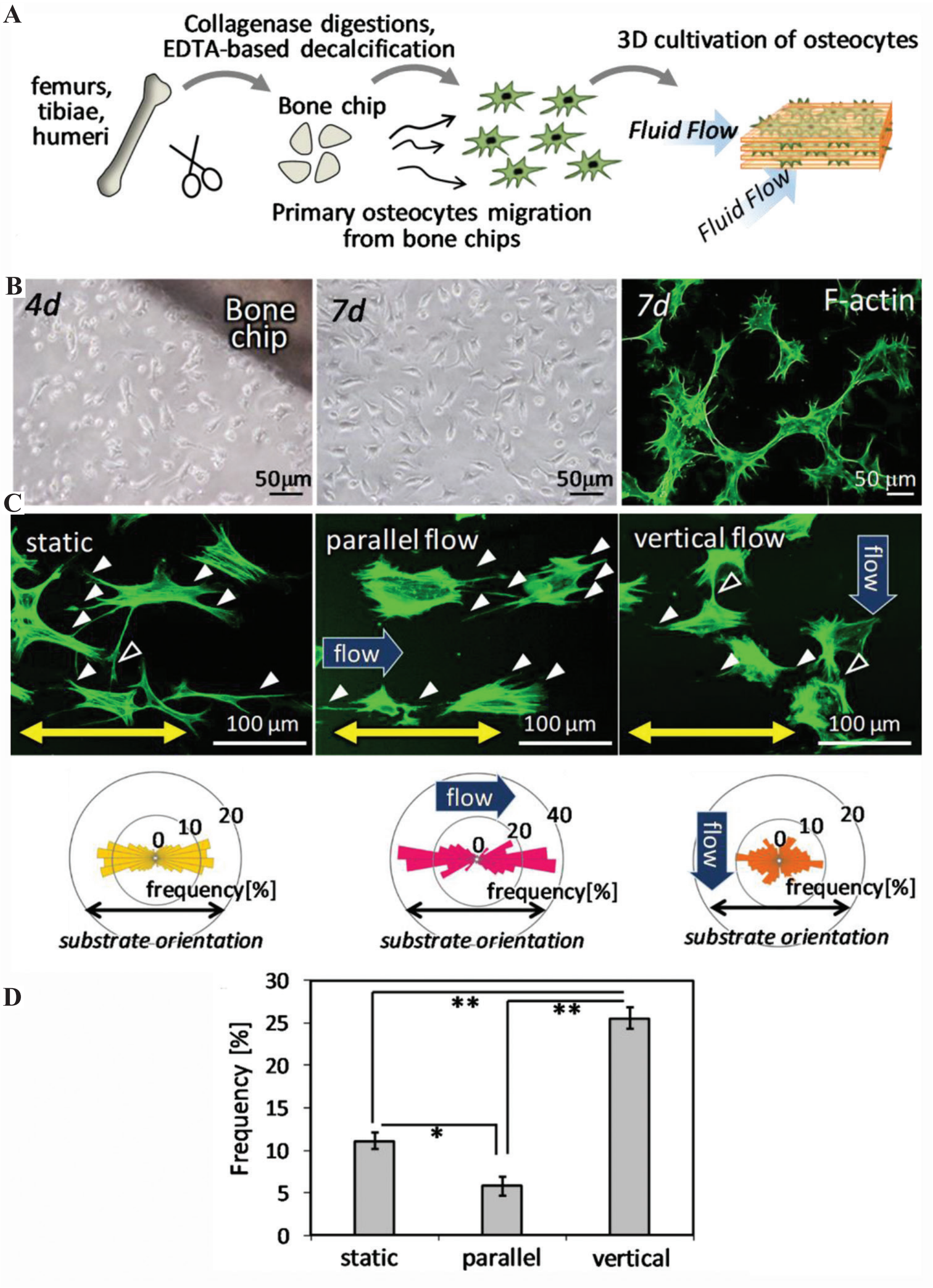

Figure 3. Osteocyte responses to the fluid flow stimulation inside three-dimensional (3D) collagen substrates. (A) Schematic illustration of 3D culture of primary osteocytes with controlled fluid flow stimuli. (B) Primary osteocyte-like cells migrated from the bone chips, with formation of mature dendritic cell processes. (C) Morphological change of osteocytes dendrites in response to the fluid flow direction. Green; F-actin. The directional distribution of the cell processes is shown below the corresponding images. (D) Appearance frequency of the cell process directing ± 30° from the vertical direction to substrate collagen orientation. *: $P < 0.05$, **: $P < 0.01$

3.4 Progressed expression of Src on stimulation with vertical fluid flow

Osteocytes exposed to the vertical flow had increased expression of the Src protein at the sites of elongated cell processes in the substrate orientation (**Figure 4A**). Gene expression analysis demonstrated significantly increased Src expression in the vertical flow-stimulated osteocytes (**Figure 4B**).

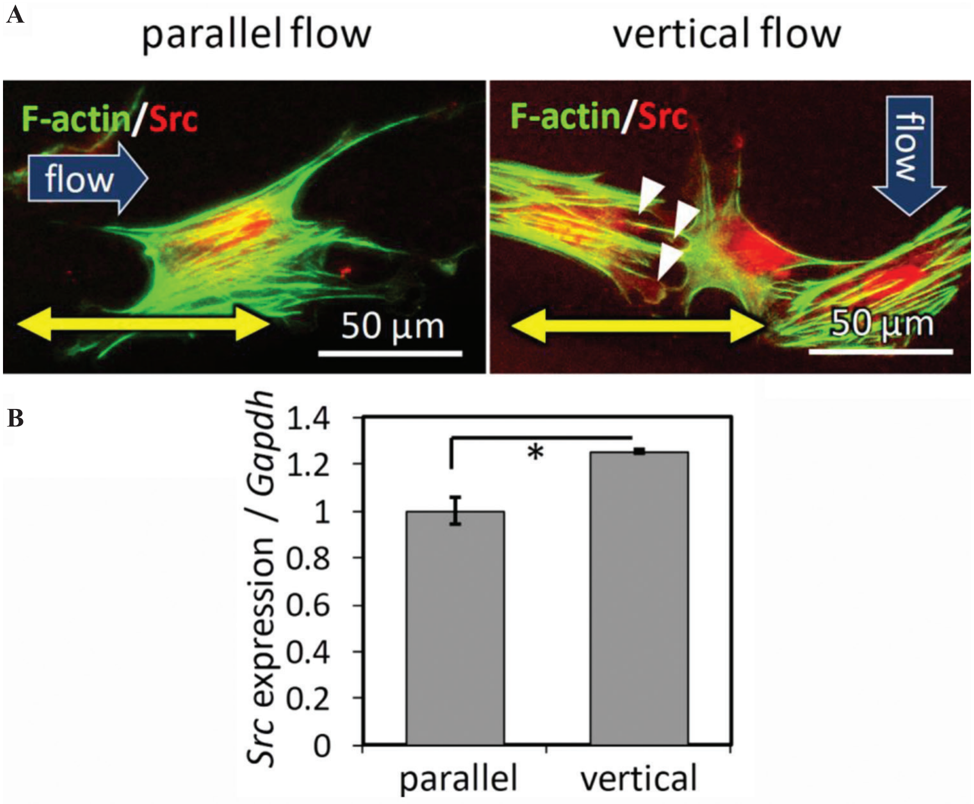

Figure 4. Src-mediated remodeling of osteocyte dendritic processes depending on the flow direction. (A) Immunocytochemical analysis of osteocytes under parallel and vertical flow. Arrowheads indicate the Src-positive focal adhesions. Green; F-actin, red; Src. Bidirectional arrows indicate the substrate collagen orientation. (B) Gene expression analysis of Src in osteocytes under parallel or vertical flow. *: $P < 0.05$.

These results indicate that the remodeling of cell processes is regulated by the reassembly of focal adhesion constructs mediated by Src expression.

4 Discussion

Engineering structurally organized 3D bone matrix constructs mimicking living bone tissue has great potential to accelerate the understanding of the cellular activities controlling various bone functions. In particular, the 3D arrangement of bone matrix and cellular components is essential for bone functionalization[24,25]. While traditional monolayer 2D cell culture systems provide a simple model of cell-cell interaction, 3D culture with biomimetic microstructure allows the artificial assembly of cellular networks and control of environmental factors[26]. In the present study, artificial 3D culture of osteocytes with preferred alignment of collagen scaffolds established the directional control of osteocyte orientation embedded inside the collagen substrates and revealed the mechano-induced remodeling of cell process generation by focal adhesion molecules.

Our novel 3D culture system provides freely controllable oriented collagen matrix scaffolds that show porosity enough for the migration and growth of cells inside the scaffold. It is noted that the cellular orientation mirrors the scaffold collagen orientation, leading to the construction of an anisotropic bone-like microstructured matrix (**Figure 2D**). The development of oriented bone matrix constructs is controlled by the interaction between aligned osteoblasts and scaffolds mediated by focal adhesion molecules[18,19]. The scaffold showed a diameter of approximately 50 µm for each collagen fiber, which is sufficient for cellular guidance through chemical interaction between collagen molecular orientation and cell receptors[27]. Our recent work revealed that the bone matrix orientation can be controlled by operating the cellular arrangement even using a 2D material surface[28,29]. While the cell alignment inside the mineralized nodules is not clearly detected because of the confluency in cells, confocal microscopy analysis demonstrated that the cell population varies depending on the cellular positioning inside the scaffold. The top layer of long-term culture products of osteoblasts presented fibroblast-like cell morphology, whereas cells inside the 3D collagen scaffold expressed the mature osteocyte marker protein Sclerostin and adopted dendritic cell morphology (**Figure 2C**). The results obtained from confocal microscopic images revealed that 3D culture of osteoblasts using oriented collagen scaffold established the spatial control of cells which mimics the living bone system; osteoblasts on the bone surface, osteocytes embedded in the bone matrix they produced. The cellular connections in the stacking direction should be clarified and it will be reported in our next study. The results indicate that the fabricated 3D oriented scaffold can provide a successful matrix environment for the differentiation and maturation of osteocytes. Furthermore, the fabricated structure involving osteoblasts and their differentiated osteocytes can help the creation of mini-organ for the development of next-generation regenerative medicine. In particular, the developed 3D culture model can provide effective platforms for understanding the responses of osteocytes to mechanical stimuli.

Primary osteocytes were seeded and cultured inside the 3D collagen scaffold to realize fluid flow stimuli to individual cells. Osteocyte-like cells were successfully isolated from the bone fragments of mature long bones, with the formation of actin-rich dendrite structures typical for the osteocyte morphology embedded within the mineralized matrix. Under static conditions, osteocyte-like cells inside the oriented substrates showed elongated cell bodies along the collagen substrate orientation with the preferred alignment of the dendritic cell processes which are mainly parallel to the collagen substrate, with a few dendrites across the substrate orientation. The flow rate was determined based on the previous report of direct evaluation of solute movement in canaliculi[30]. We previously reported that the bone tissue microstructure is determined by controlling artificial stress applied to bone[31]. To provide a simulated condition of artificially controlled mechanical stimuli, the fluid stimuli was set as a higher level (80 dyn/cm^2) compared to the static physiological level. Although the fluid flow stimuli were strictly determined by the calculation as mentioned above, the pores and fibers could work as a barrier to disturb the fluid flow stimuli. The computational fluid dynamics simulation is now in progress to clarify the relationship between flow dynamics and cell responses.

Mechanical stimuli with a parallel flow to the collagen substrate promoted the dendrogenesis in the direction of fluid flow. This means that the normal parallel relationship between the direction of dendrite process and fluid flow generated the shear stress on the process surface, resulting in stimulation of dendrite growth. On the other hand, the flow stimuli across collagen orientation induced the degeneration of the dendrites elongated to the collagen orientation, stimulating the generation of dendritic cell processes parallel to the flow direction (**Figure 3C and D**). In addition, the extended flow stimulation could alter the morphological change of osteocyte cell body, as well as dendritic remodeling. The preferred formation of dendritic cell processes along flow stimuli direction, as opposed to under static condition, significantly demonstrated the role of fluid flow on the orientation of osteocytes dendritic processes. That is, the fluid flow stimuli rather than the substrate matrix orientation determine the direction of dendrites elongation.

Osteocyte dendrogenesis is now recognized to be controlled by biological signals in response to mechanical strain, meaning that osteocytes can actively regulate the formation of dendritic processes[22,32,33]. In particular, Src has been studied as an essential regulator in mechanotransduction mediating integrin-cytoskeleton interaction[34]. Here, we demonstrate the directional dendritic process remodeling of osteocytes in response to fluid flow shear stress mediated by Src expression (**Figure 4**). The quantitative gene expression analysis revealed the upregulated expression of Src in vertical flow stimuli, whereas the expression in static condition will be investigated in our future study. Dendritic cell processes are anchored to the matrix wall through integrins, which experience fluid shear stress and transmit the mechanical stimuli into biochemical signals through multiple interactions with related proteins involving Src[35]. The upregulated expression of Src in vertical group means that the accelerated degradation of focal adhesion located in crossing direction to fluid flow was regulated accompanied with activated Src expression[36]. The obtained results indicate that osteocytes remodel dendritic cell processes to generate shear stress on their surface effectively under mechanical environmental stimuli. Our novel bioprinting technique allowed the establishment of bone-mimetic anisotropic 3D structure involving the desired arrangement of osteocytes inside the matrix, which are fully functionalized and surrounded with bone-like niche, compared to the traditional monolayer 2D culture system (**Figure 5**).

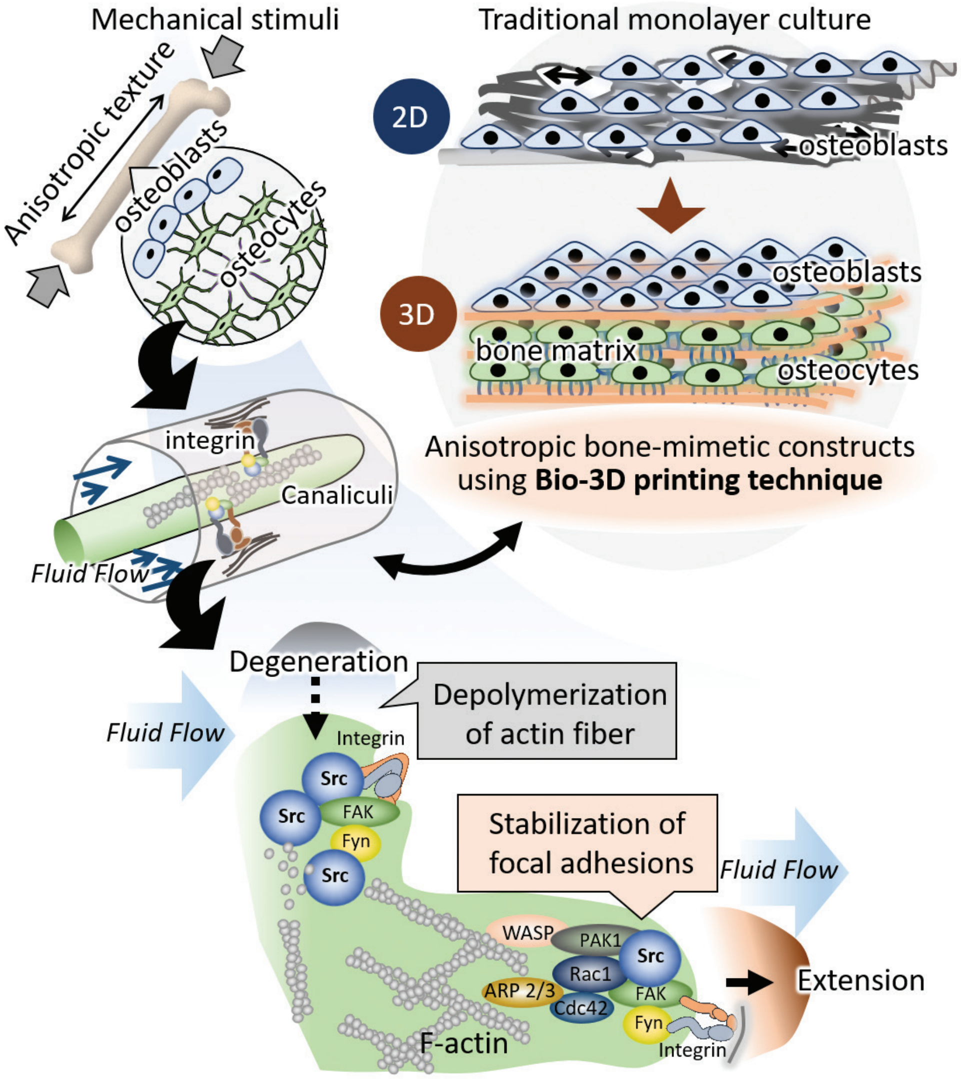

Figure 5. Novel bone-mimetic anisotropic three-dimensional (3D) construct fabricated with bio-3D printing technique. The obtained construct represents the 3D osteocytes networks which mimic the living bone tissue. Osteocytes remodel their dendritic processes to generate shear stress on their surface, resulting in the effective mechanosignaling.

5 Conclusion

A 3D bone-mimetic anisotropic microstructure was fabricated using the laminated layer method of oriented collagen sheets. Osteoblasts successfully constructed the aligned mineralized matrix with differentiation into mature osteocytes. The osteocytes embedded inside the scaffolds showed an ordered arrangement of the cell body as well as dendritic cell process, which remodeled their extrusion/degeneration depending on the flow direction. These findings indicate that functional adaptation of osteocytes in response to mechanical stimuli is regulated by the remodeling of cell processes mediated by Src expression in focal adhesions.

Acknowledgments

This research was funded by Grants-in-Aid for Scientific Research (S) (grant number 18H05254) and Grants-in-Aid for Scientific Research (A) (grant number 20H00308).

Conflicts of interest

The authors declare no conflicts of interest.

Authors' contributions

T. N. and A. MT. designed the study. T. M., A. MK., and A. MT. carried out the experiments. T. M., A. MT., P. W., and T. N. contributed to the interpretation of the results. A. MT. drafted the manuscript, P. W. and T. N. revised the manuscript content. All the authors contributed to the discussion of the results.

References

1. Ishimoto T, Nakano T, Umakoshi Y, *et al.*, 2013, Degree of Biological Apatite c -axis Orientation Rather than Bone Mineral Density Controls Mechanical Function in Bone Regenerated Using Recombinant Bone Morphogenetic Protein-2. *J Bone Miner Res*, 28:1170–9. DOI: 10.1002/jbmr.1825.
2. Schaff F, Bech M, Zaslansky P, *et al.*, 2015, Six-dimensional Real and Reciprocal Space Small-angle X-ray Scattering Tomography. *Nature*, 527:353–6. DOI: 10.1038/nature16060.
3. Nakano T, Kaibara K, Tabata Y, *et al.*, 2002, Unique Alignment and Texture of Biological Apatite Crystallites in Typical Calcified Tissues Analyzed by Microbeam x-ray Diffractometer System. *Bone*, 31:479–87. DOI: 10.1016/s8756-3282(02)00850-5.
4. Nakano T, Kaibara K, Ishimoto T, *et al.*, 2012, Biological Apatite (BAp) Crystallographic Orientation and Texture as a New Index for Assessing the Microstructure and Function of Bone Regenerated by Tissue Engineering. *Bone*, 51:741–7. DOI: 10.1016/j.bone.2012.07.003.
5. Hennessy KM, Pollot BE, Clem WC, *et al.*, 2009, The Effect of Collagen I Mimetic Peptides on Mesenchymal Stem Cell Adhesion and Differentiation, and on Bone Formation at Hydroxyapatite Surfaces. *Biomaterials*, 30:1898–909. DOI: 10.1016/j.biomaterials.2008.12.053.
6. Lee S, Obata A, Brauer DS, *et al.*, 2015, Dissolution Behavior and Cell Compatibility of Alkali-free MgO-CaO-SrO-TiO2-P2O5 Glasses for Biomedical Applications. *Biomed Glasses*, 1:151–8. DOI: 10.1515/bglass-2015-0015.
7. Prewitz MC, Seib FP, von Bonin M, *et al.*, 2013, Tightly Anchored Tissue-mimetic Matrices as Instructive Stem Cell Microenvironments. *Nat Methods*, 10:788–794. DOI: 10.1038/nmeth.2523.
8. Bonewald LF, 2011, The Amazing Osteocyte. *J Bone Miner Res*, 26:229–38. DOI: 10.1002/jbmr.320.
9. Odagaki N, Ishihara Y, Wang Z, *et al.*, 2018, Role of Osteocyte-PDL Crosstalk in Tooth Movement via SOST/Sclerostin. *J Dent Res*, 97:1374–82. DOI: 10.1177/0022034518771331.
10. Ganesh T, Laughrey LE, Niroobakhsh M, *et al.*, 2020, Multiscale Finite Element Modeling of Mechanical Strains and Fluid Flow in Osteocyte Lacunocanalicular System. *Bone*, 2020:115328. DOI: 10.1016/j.bone.2020.115328.
11. Ng WL, Chua CK, Shen YF, 2016, Print Me An Organ! Why We Are Not There Yet. *Prog Polym Sci*, 2016:101145.
12. Ozbolat IT, Hospodiuk M, 2016, Current Advances and Future Perspectives in Extrusion-based Bioprinting. *Biomaterials*, 76:321–43. DOI: 10.1016/j.biomaterials.2015.10.076.
13. Gudapati H, Dey M, Ozbolat I, 2016, A Comprehensive Review on Droplet-based Bioprinting: Past, Present and Future, *Biomaterials*, 102:20–42. DOI: 10.1016/j.biomaterials.2016.06.012.
14. Ng WL, Lee JM, Yeong WY, *et al.*, 2017, Microvalve-based Bioprinting Process, Bio-inks and Applications. *Biomater Sci*, 5:632–47. DOI: 10.1039/c6bm00861e.
15. Ng WL, Lee JM, Zhou M, *et al.*, 2020, Vat Polymerization-based Bioprinting Process, Materials, Applications and Regulatory Challenges. *Biofabrication*, 12:22001. DOI:

10.1088/1758-5090/ab6034.

16. Wang K, Le L, Chun BM, *et al*., 2019, A Novel Osteogenic Cell Line that Differentiates into GFP-Tagged Osteocytes and Forms Mineral with a Bone-Like Lacunocanalicular Structure. *J Bone Miner Res*, 34:979–95. DOI: 10.1002/jbmr.3720.
17. Matsugaki A, Isobe Y, Saku T, *et al*., 2015, Quantitative Regulation of Bone-mimetic, Oriented Collagen/Apatite Matrix Structure Depends on the Degree of Osteoblast Alignment on Oriented Collagen Substrates: Anisotropic Construction of Cell-Produced Mineralized Matrix. *J Biomed Mater Res A*, 103:489–99. DOI: 10.1002/jbm.a.35189.
18. Nakanishi Y, Matsugaki A, Kawahara K, *et al*., 2019, Unique Arrangement of Bone Matrix Orthogonal to Osteoblast Alignment Controlled by Tspan11-Mediated Focal Adhesion Assembly. *Biomaterials*, 209:103–10. DOI: 10.1016/j.biomaterials.2019.04.016.
19. Kimura Y, Matsugaki A, Sekita A, *et al*., 2017, Alteration of Osteoblast Arrangement Via Direct Attack by Cancer Cells: New Insights into Bone Metastasis. *Sci Rep*, 7:44824. DOI: 10.1038/srep44824.
20. Wong G, Cohn DV, 1974, Separation of Parathyroid Hormone and Calcitonin-sensitive Cells from Non-responsive Bone Cells. *Nature*, 252:713–5. DOI: 10.1038/252713a0.
21. Stern AR, Stern MM, Van Dyke ME, *et al*., 2012, Isolation and Culture of Primary Osteocytes from the Long Bones of Skeletally Mature and Aged Mice. *Biotechniques*, 52:361–73. DOI: 10.2144/0000113876.
22. Matsugaki A, Yamazaki D, Nakano T, 2020, Selective Patterning of Netrin-1 as a Novel Guiding Cue for Anisotropic Dendrogenesis in Osteocytes. *Mater Sci Eng C*, 108:110391. DOI: 10.1016/j.msec.2019.110391.
23. Noyama Y, Nakano T, Ishimoto T, *et al*., 2013, Design and Optimization of the Oriented Groove on the Hip Implant Surface to Promote Bone Microstructure Integrity. *Bone*, 52:659–67. DOI: 10.1016/j.bone.2012.11.005.
24. Ozasa R, Ishimoto T, Miyabe S, *et al*., 2019, Osteoporosis Changes Collagen/Apatite Orientation and Young's Modulus in Vertebral Cortical Bone of Rat. *Calcif Tissue Int*, 104:449–60. DOI: 10.1007/s00223-018-0508-z.
25. Matsugaki A, Harada T, Kimura Y, *et al*., 2018, Dynamic Collision Behavior between Osteoblasts and Tumor Cells Regulates the Disordered Arrangement of Collagen Fiber/Apatite Crystals in Metastasized Bone. *Int J Mol Sci*, 19:3474. DOI: 10.3390/ijms19113474.
26. Zeng J, Matsusaki M, 2019, Layer-by-Layer Assembly of Nanofilms to Control Cell Functions. *Polym Chem*, 10:2960–74. DOI: 10.1039/c9py00305c.
27. Lee S, Matsugaki A, Kasuga T, *et al*., 2019, Development of bifunctional oriented bioactive glass/poly(lactic acid) composite scaffolds to control osteoblast alignment and proliferation. *J Biomed Mater Res A*, 107:1031–41.
28. Ozasa R, Matsugaki A, Isobe Y, *et al*., 2018, Construction of Human Induced Pluripotent Stem Cell-derived Oriented Bone Matrix Microstructure by Using *In Vitro* Engineered Anisotropic Culture Model. *J Biomed Mater Res A*, 106:360–9. DOI: 10.1002/jbm.a.36238.
29. Matsugaki A, Fujiwara N, Nakano T, 2013, Continuous Cyclic Stretch Induces Osteoblast Alignment and Formation of Anisotropic Collagen Fiber Matrix. *Acta Biomater*, 9:7227–35. DOI: 10.1016/j.actbio.2013.03.015.
30. Wang L, Wang Y, Han Y, *et al*., 2005, *In Situ* Measurement of Solute Transport in the Bone Lacunar-canalicular System. *Proc Natl Acad Sci U S A*, 102:11911–6. DOI: 10.1073/pnas.0505193102.
31. Wang J, Ishimoto T, Nakano T, *et al*., 2017, Unloading-induced Degradation of the Anisotropic Arrangement of Collagen/Apatite in Rat Femurs. *Calcif Tissue Int*, 100:87–94. DOI: 10.1007/s00223-016-0200-0.
32. Zhang K, Barragan-Adjemian C, Ye L, *et al*., 2006, E11/gp38 Selective Expression in Osteocytes: Regulation by Mechanical Strain and Role in Dendrite Elongation. *Mol Cell Biol*, 26:4539–52. DOI: 10.1128/mcb.02120-05.
33. Thi MM, Suadicani SO, Schaffler MB, *et al*., 2013, Spray Mechanosensory Responses of Osteocytes to Physiological Forces Occur Along Processes and not Cell Body and Require $\alpha V\beta 3$ Integrin. *Proc Natl Acad Sci U S A*, 110:21012–7. DOI: 10.1073/pnas.1321210110.
34. Wang Y, Botvinick L, Zhao Y, *et al*., 2005, Visualizing the Mechanical Activation of SRC. *Nature*, 434:1040–5.
35. Schimmel L, Fukuhara D, Richards M, *et al*., 2020, c-SRC Controls Stability of Sprouting Blood Vessels in the Developing Retina Independently of Cell-cell Adhesion through Focal Adhesion Assembly. *Development*, 147:dev185405. DOI: 10.1242/dev.185405.
36. Skupien A, Konopka A, Trzaskoma P, *et al*., 2014, CD44 Regulates Dendrite Morphogenesis through SRC Tyrosine Kinase-dependent Positioning of the Golgi. *J Cell Biol*, 127:5038–51. DOI: 10.1242/jcs.154542.

ORIGINAL ARTICLE

Preheating of Gelatin Improves its Printability with Transglutaminase in Direct Ink Writing 3D Printing

Justin Jia Yao Tan[1,2†], **Cheng Pau Lee**[1,2†], **Michinao Hashimoto**[1,2*]

[1]Pillar of Engineering Product Development, Singapore University of Technology and Design, 8 Somapah Road, Singapore 487372, Singapore

[2]SUTD-MIT International Design Centre, Singapore University of Technology and Design, 8 Somapah Road, Singapore 487372, Singapore

†These authors contributed equally to this paper.

Abstract: Gelatin and transglutaminase (TG) ink is increasingly popular in direct ink writing three-dimensional (3D) printing of cellular scaffolds and edible materials. The use of enzymes to crosslink gelatin chains removes the needs for toxic crosslinkers and bypasses undesired side reactions due to the specificity of the enzymes. However, their application in 3D printing remains challenging primarily due to the rapid crosslinking that leads to the short duration of printable time. In this work, we propose the use of gelatin preheated for 7 days to extend the duration of the printing time of the gelatin ink. We first determined the stiffness of freshly prepared gelatin (FG) and preheated gelatin (PG) (5 – 20% w/w) containing 5% w/w TG. We selected gelatin hydrogels made from 7.5% w/w FG and 10% w/w PG that yielded similar stiffness for subsequent studies to determine the duration of the printable time. PG inks exhibited longer time required for gelation and a smaller increase in viscosity with time than FG inks of similar stiffness. Our study suggested the advantage to preheat gelatin to enhance the printability of the ink, which is essential for extrusion-based bioprinting and food printing.

Keywords: Gelatin, Transglutaminase, Direct ink writing, Extrusion-based 3D printing, Printability, Preheating

***Corresponding Author**: Michinao Hashimoto, Pillar of Engineering Product Development, Singapore University of Technology and Design, 8 Somapah Road, Singapore 487372, Singapore; hashimoto@sutd.edu.sg

Received: April 06, 2020; ***Accepted:*** June 07, 2020; ***Published Online***: September 08, 2020

Citation: Tan JJY, Lee CP, Hashimoto M, Preheating of Gelatin Improves its Printability with Transglutaminase in Direct Ink Writing 3D Printing, *Int J Bioprint*, 6(4): 296. DOI: 10.18063/ijb.v6i4.296.

1 Introduction

This paper discusses the effects of preheating gelatin on its printability through direct ink writing (DIW) three-dimensional (3D) printing. Recent developments in 3D printing and additive manufacturing have extended into the fields of tissue engineering[1,2], sensing[3], and food engineering[4,5]. In the field of tissue engineering, anatomical replicas of human organs such as skin, heart, lung, kidney, and liver have been printed. These 3D printed organs have been shown to express the characteristics of tissue markers and spatial orientations as native human organs[1]. Strategies have been developed to improve the resolution, shape fidelity, and complexity of these 3D printed organs. Examples include delaying cell sedimentation within the bioink through the addition of non-adhesive polymers or weakly crosslinked hydrogels[2]. In sensing, 3D printing has been used to fabricate multi-material, multifunctional stretchable electronic devices, ranging from wearable electronics, energy harvesting devices, to prosthetic bionic skins[3]. The adoption of 3D printing technology offers multiple advantages over traditional techniques to fabricate scaffolds, including uniformity and reproducibility in manufacturing, reduction of user error, and precise control over scaffold pore size, connectivity, and geometry[6]. Among the materials used in extrusion-based printing, natural biopolymers such as collagen, gelatin, and chitosan are promising candidates for bioprinting and food printing due to their excellent biocompatibility and abundance of cell recognition sites[7,8]. In addition, natural biopolymers such as gelatin are inexpensive to fabricate, and they can be synthesized with relative ease[9]. Essential physical properties (such as stiffness and water content) can be altered to obtain similar elastic modulus of native tissues such as skeletal muscle, which was previously reported to be within the range of 10 – 50 kPa[10]. Finally, gelatin is a generally edible material and can eventually be used for food printing as a ready-to-eat product without the need for post-processing. These properties make the gelatin as a desirable candidate for the application in 3D printing.

3D printing of gelatin would require adequate control over the physical properties of the gelatin inks. The melting point of gelatin is 30 – 37°C, depending on their bloom strength, pH, and concentration[11]; gelatin is unable to hold/retain its structure and would melt at physiological temperature. Permanent peptide bonds need to be formed between amino acids to ensure the integrity of the structure in a liquid medium and at physiological temperature. Among the most employed techniques to achieve permanent crosslinking are photocrosslinking and enzymatic crosslinking. Photocrosslinking between methacryloyl groups in Gelatin-Methacryloyl happens relatively fast (in the order of seconds), which rapidly confers structural stability to the printed scaffold[12]. Enzymatic crosslinking (i.e., using transglutaminase [TG]), on the other hand, takes place relatively slower (in the order of minutes) than photocrosslinking. Although slower, TG has been widely used as a meat glue to mediate the crosslinking of gelatin; the crosslinked product remains edible, which is the requirement for 3D food printing. In addition, enzymatic crosslinking does not produce free radicals and uncrosslinked monomers derived from photocrosslinking reactions that might adversely affect the cellular conditions. Both photocrosslinking and enzymatic crosslinking are permanent and confer mechanical strength to the crosslinked gelatin chains required for 3D printing. TG is often added to gelatin to facilitate the formation of the peptide bond between the γ-carbonyl group of glutamine residue and the ε-amino group of a lysine residue within the gelatin[9]. The formation of peptide bonds stabilizes the structure of the printed scaffold and improves its structural integrity. This enzymatic crosslinking is favored among other available methods of crosslinking (such as chemical crosslinking) due to the low occurrence of side reactions (due to substrate specificity) and no cellular toxicity of the enzymes. The use of enzymes also eliminates the need for specialized equipment and other photo-sensitive additives that may be toxic in nature[9].

DIW 3D printing has been widely demonstrated in 3D printing for polymers, foods, hydrogels[13, 14]. Polymers such as polyvinyl alcohol were 3D printed to serve as coating layers for controlling the drug release of active ingredients[15]. For the application in food printing, rheology-modified food inks have been printed using a DIW 3D printer to model complex 3D shapes without temperature control[5]. Potato starch-containing anthocyanin and lemon juice was 3D printed as a two-part gel system exhibited time-dependent color change in response to the diffusion of hydrogen ions from the lemon juice layer into the anthocyanin layer[16]. Such 3D-printable hydrogels included photo-curable polyethylene glycol acrylate, poly(2,6-dimethyl-1,4-phenylene oxide) acrylate, gelatin-methacrylate, and hyaluronan-methacrylate[17-19]. In addition, gelation can be triggered by printing a hydrogel-forming polymer solution into a bath of the reactive substance. It was reported that alginate printed into calcium solution using this method has yielded complex cell-laden 3D structures maintaining cell viability[20]. DIW of these hydrogel-forming polymers offers a rapid and relatively cell-friendly method for the making of cellular scaffolds[21]. In DIW 3D printing, a continuous ink filament is extruded through a nozzle onto a stationary substrate from a microscale syringe tip driven by either pneumatic pressure or mechanical force[22]. Although gelatin and TG ink is an ideal material for 3D printing, its application in 3D printing remains challenging because of the difficulty to control the physical and rheological properties of the ink.

In particular, 3D printing with gelatin and TG is limited by the rate of enzymatic crosslinking; the rapid crosslinking influenced the gelation time of the ink[9]. The fast crosslinking would result in the rapid gelation of the liquid gelatin ink. The gelation of the ink increases its viscosity and results in clumps in ink. These clumps diminish the quality of the printed structures and clog the nozzle during printing. It was reported that printing was only possible for approximately 3 min at 37°C before the crosslinking reaction prevents ink flow due to blockage[9]. Future optimization was therefore required to identify other approaches to extend the printing time.

To enhance the usability of the freshly prepared gelatin (which we term FG) inks crosslinked with TG in 3D printing, we propose to use preheated gelatin (which we term PG) inks to extend the printing time. We first evaluated the stiffness of hydrogels prepared from FG and PG crosslinked with TG. Envisaging applications in bioprinting, we identified the concentrations of gelatin and TG in ink. We then 3D printed grid patterns for FG and PG possessing similar stiffness and assessed their printability, gelation, and viscosity profiles. Finally, we incubated hydrogels in phosphate-buffered saline (PBS) to determine their swelling profiles. Our experiments suggested that hydrogels prepared from PG (10% w/w) offered approximately 4 to 10 times longer printing time. Finally, we found that PG inks exhibited greater shrinkage at low concentrations (i.e., 7.5% and 10% w/w) and greater swelling at high concentrations (i.e., 20% w/w) than FG inks of the same concentrations. The shrinkage of PG may allow reducing the size of the printed models by post-processing. Our study suggested the preheating of gelatin as a simple way to influence the printability and the volume change of the ink. The insights gained in this study shall be applicable for applications in 3D printing to extend the printing time of the gelatin and TG ink to fabricate large cellular scaffolds or intricate structures for bioprinting and food printing.

2 Results and discussion

2.1 Justification of approach

Several approaches are possible to extend the duration of the printable time for the gelatin inks crosslinked with TG, including (1) lowering the concentration of gelatin, (2) lowering the concentration of TG, and (3) altering printing temperature. In this paper, we excluded the alteration of the concentration of the materials from our possible approaches to achieve the goal. It was previously reported that changing gelatin concentration had a small effect on the gelation time of the gelatin and TG ink[9]. Lowering the TG concentration to increase the duration of printing was reported to lower the overall hydrogel stiffness greatly[9]; the resulting hydrogels possessed poor stability in aqueous environments due to the reduced degrees in crosslinking between gelatin chains. The uncrosslinked gelatin chains would be washed out in the surrounding aqueous environment, destabilizing the printed gelatin structure. Because of this reason, we fixed the concentration of TG as 5% w/w throughout the current study. Alteration of the printing temperature would influence the viscosity of the ink and the stability of TG, and we did not employ that approach to achieve extended printable time.

We selected to investigate the effect of preheating of gelatin. Gelatin absorbs water and swells in liquid media[23]. Preheating of gelatin has been reported to reduce its extent of swelling[24]. When the gelatin is preheated, the internal hydrogen bonds responsible for holding the triple helical structure of gelatin are broken. A previous study reported that the unfolding of the triple helical structure exposes more hydrophobic amino acids, increasing the surface hydrophobicity of the gelatin[25]. However, when gelatin undergoes chemical crosslinking, the formation of a rigid network reduces the extent of swelling in the resulting hydrogel[26]. In this study, we investigated the effect of swelling of FG and PG crosslinked with TG.

2.2 Evaluation of hydrogel stiffness

Initially, stiffness of hydrogels prepared from FG and PG crosslinked with TG (5% w/w) was investigated. Stiffness is an essential mechano-physical property that influences cell growth and function[27]. We intended to show that PG would be able to confer better printability than FG for the hydrogels yielding similar stiffness. We have chosen hydrogels yielding an estimated elastic modulus of 10 kPa, which is tissue-like stiffness deemed suitable for the culture of many cell types, including myoblasts, human primary keratinocytes, and human embryonic stem cells[28-30]. Amplitude sweep tests were conducted for FG and PG with the concentrations ranging from 5 to 20% w/w while keeping TG concentration at 5% w/w. We use the following nomenclature to describe the composition of FG and PG throughout the current study. For instance, FG10 indicates that the ink contained 10% w/w FG and 5% w/w TG, while PG10 indicates that the ink contained 10% w/w PG and 5% w/w TG. The hydrogel stiffness was determined by its elastic modulus, which was estimated from the storage modulus obtained from the viscoelastic region of the flow diagrams, as reported.[31] The estimated elastic modulus of both FG and PG hydrogels increased with gelatin concentrations. Exposure of gelatin to high temperatures for extended periods resulted in the thermal hydrolysis of the polypeptide chains. Thermal hydrolysis caused a decrease in the gel rigidity (i.e., gel strength)[32]. The stiffness of hydrogels of FG7.5 was similar to PG10, both of which yielded an estimated elastic modulus of approximately 10 kPa (**Figure 1**). We chose these two hydrogel compositions for our subsequent work because they yielded a tissue-like stiffness which deemed suitable for the culture of many cell types. Highly stiff substrates were not favored for cell cultures, as multiple studies have shown that cells preferentially grow and differentiate on soft, tissue-like substrates[33-35]. We also included FG10 for our later study as a control for preheating; FG10 and PG10 contained the same gelatin concentration, and the observed differences, if any, shall be attributed to the consequences of preheating. After identifying suitable inks (that is, FG7.5, FG10, and PG10), we proceeded to assess their printability.

2.3 3D printing of gelatin and TG inks and printability characterization

The printability of the inks was assessed at selected time points using the printability value (*Pr*)[36]. *Pr* indicated the degree of gelation of the extruded filament at the respective time points[36]. Three states of gelation were considered for the printed inks: Under-gelation, proper-gelation, and over-gelation. Under-gelation would yield obvious chamfers in the printed grids due to the fusion of the subsequent two layers of the interconnected filaments ($Pr < 1$). During proper-gelation, the interconnected filaments would demonstrate a perfect square shape or close to a square with regular edges ($Pr = 1$). Over-gelation, however, led to the formation of irregularly printed and interconnected filaments ($Pr > 1$). The larger values of *Pr* indicated the higher degree of gelation while the smaller *Pr* indicated the lower degree of gelation. We set the acceptable range of *Pr* to be 0.9 – 1.1, as reported previously with 3D printed hydrogel constructs[36].

FG7.5, FG10, and PG10 were printed in a grid pattern on a glass surface at 3 min, 5 min, 10 min, and every 5 min after that. The printing was stopped when the inks became clumpy or when the ink could not be extruded at the maximum pressure of the dispenser. The Hagen-Poiseuille equation suggested that the volumetric flow rate was inversely proportional to the viscosity of fluids[37]. Continuous increase in the viscosity required compensation by the increase in the applied pressure. We observed that extruding FG inks were more challenging than PG due to the rapid increase in the viscosity (**Figure 2A** and **2B**).

Under-gelation was observed for FG7.5 at 3 min but not for FG10 (**Figure 2A**). The duration

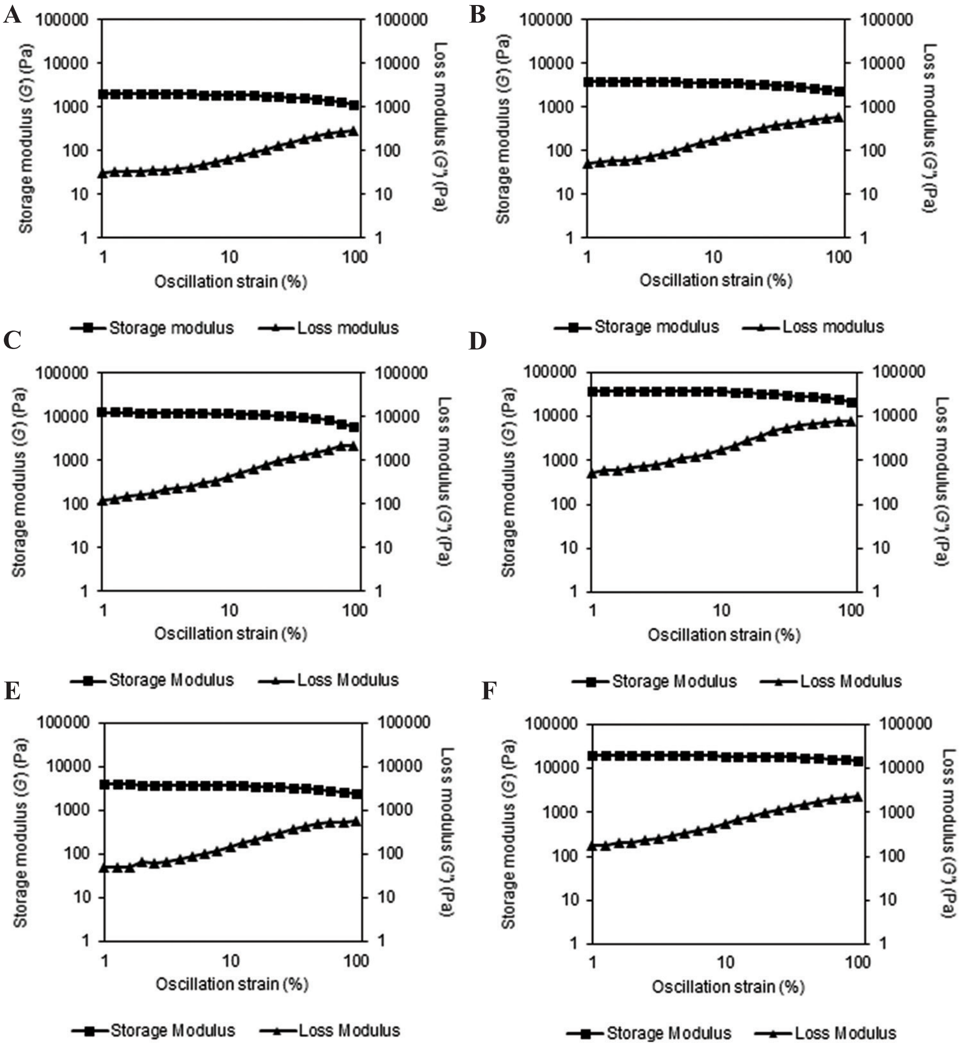

Figure 1. Flow diagrams of hydrogels made of different concentrations of FG and PG cross-linked with TG (5% w/w). (A) FG5. (B) FG7.5. (C) FG10. (D) FG20. (E) PG10. (F) PG20.

of under-gelation was the longest for PG10, which lasted at least 15 min (**Figure 2B**). The duration of proper-gelation was 5 min for FG7.5 and 20 min for PG10, respectively, while it was 2 min for FG10 (**Figure 2B**). Over-gelation was observed for FG7.5 and PG10 as the printed ink was clumpy and yielded the grids with irregular edges (**Figure 2A).** Over-gelation was also identified by a fractured grid morphology and disconnected filaments such as FG10 after 10 min. The gelation occurred most rapidly for FG10 among the three inks, where over-gelation manifested in a clogging nozzle and the filament barely extruded at the highest extrusion pressure (0.7 MPa). This clogging resulted in the inconsistent square grids with multiple broken interconnected filaments at 10 min, and the ink was hardly extruded at 15 min (**Figure 2A**). However, perfect squares may not be achieved even during proper gelation for every smaller square grid within the printed lattice. The discontinuity in the printed filament was due to a mismatch between the gelation state of the ink and the extrusion pressure. The ink became gradually gel-like in the nozzle with time due to crosslinking by TG. The increase in gelation required a corresponding increase in extrusion pressure to extrude the gel-like ink onto the substrate. However, as a single pressure was used to print the ink at every time point, small break

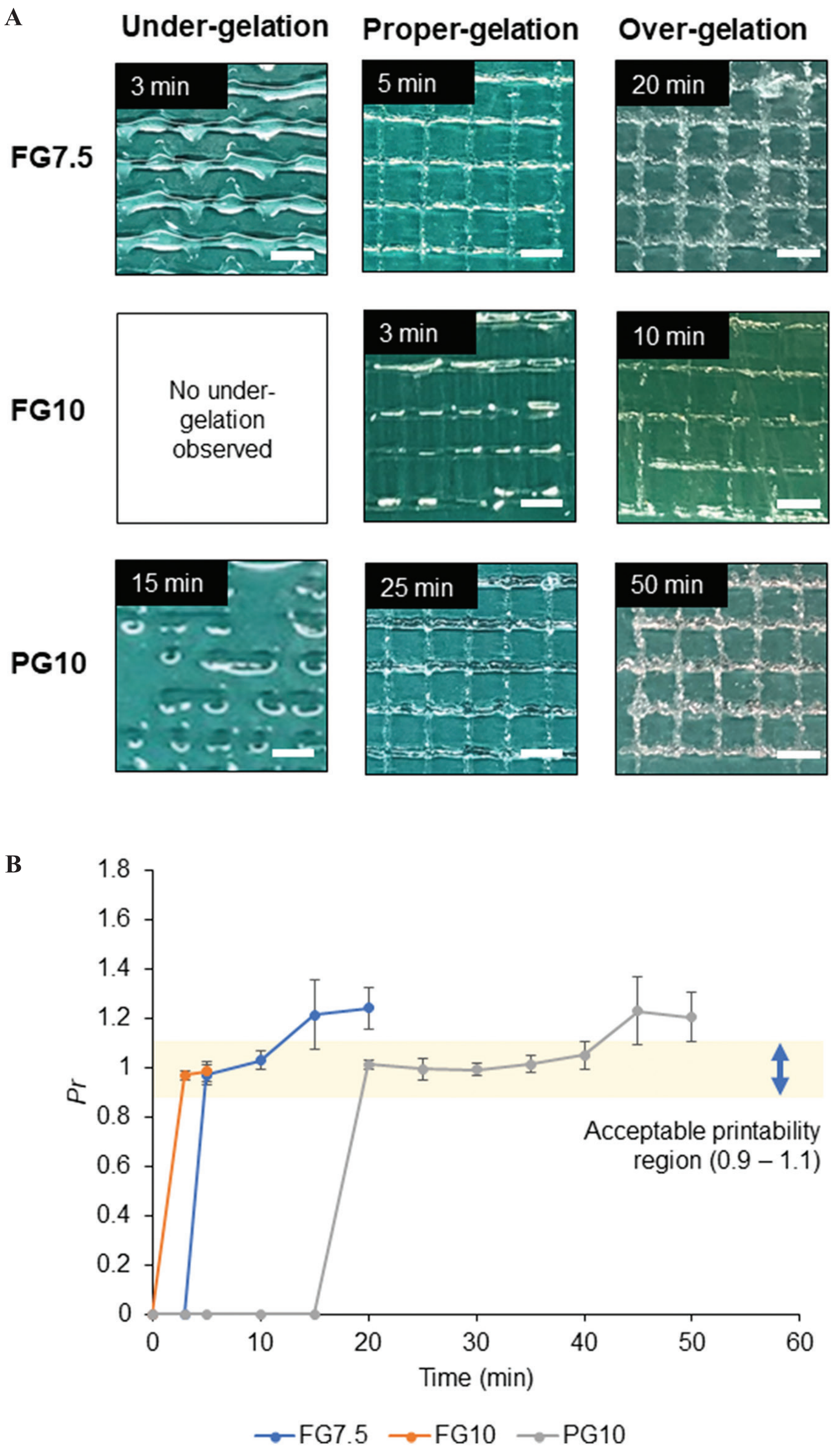

Figure 2. (A) Images of three-dimensional printed grid pattern using FG7.5, FG10, and PG10 each representing under-gelation, proper-gelation, and over-gelation, respectively. (Scale bar = 2.86 mm) (B) Evaluation of the duration of acceptable printability of the inks. The plot shows average *Pr* of the grid pattern at respective time points for FG7.5, FG10, and PG10.

(or discontinuity) could have occurred at specific points of the printed lattice. This error may not be critical due to the sufficiently large 3D printed lattice structure. We chose small square grids ($n = 5$) to calculate the average of Pr values at the respective time points. The values of Pr for FG7.5, FG10, and PG10 were plotted with respect to time to predict the duration for acceptable printability ($0.9 < Pr < 1.1$). Assuming linear changes in Pr between the data points, we estimated the duration of time that offered acceptable printability; the duration was the longest for PG10 (~20 min), which was higher than for FG7.5 (~5 min) and FG10 (~2 min) (**Figure 2B**).

2.4 Effect of PG ink on gelation time

The gelation of the ink triggered the phase change of the ink from liquid to gel due to enzymatic crosslinking. The viscosity of the ink became effectively infinite when the gelation completed[38]. The time point for the gelation allows us to approximate when the ink is printable with acceptable morphology and mechanical stability. We performed a time-sweep experiment to identify the gelation time of FG7.5, FG10, and PG10. The experiment was conducted at 40°C, which was consistent with the printing temperature of the inks. This temperature ensured that the gelation was solely due to enzymatic crosslinking but not due to the temperature at which the experiment was performed. The time point where the storage modulus matched with the loss modulus was recorded as the gelation time. Note that the reported values in this section include an extra 2.5 min (150 s) in addition to the time recorded by the rheometer (shown in the graphs in **Figure 3**). This extra time accounts for the time required to prepare the samples (i.e., mixing the gelatin with TG and loading it into the instrument). After the completion of the gelation, both storage and loss

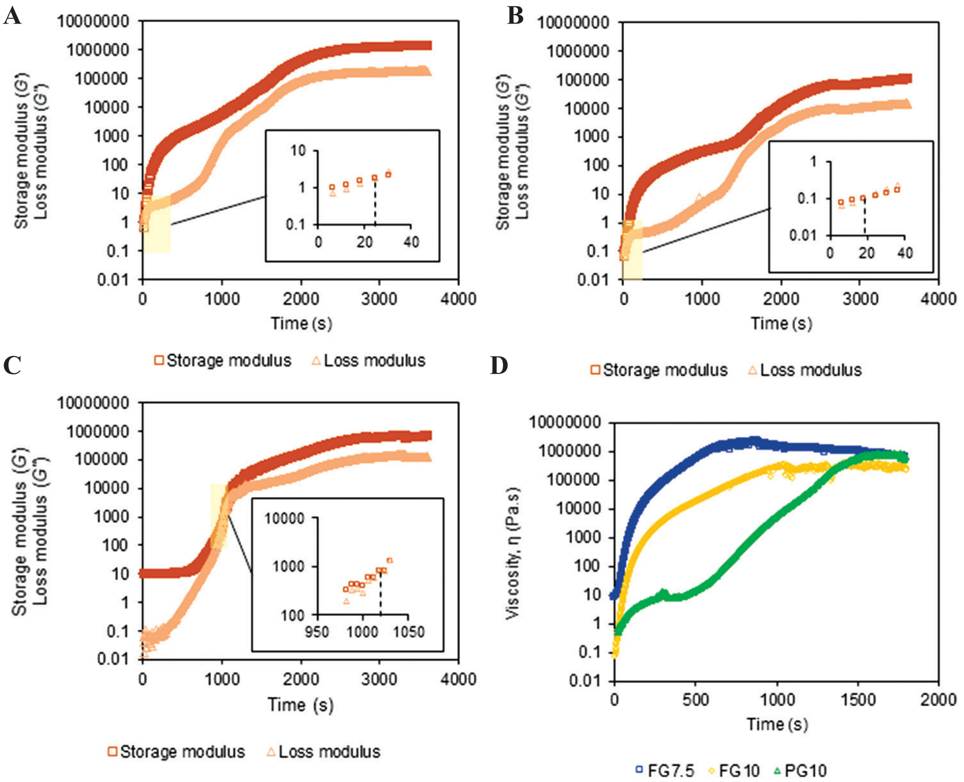

Figure 3. Rheological characterization of freshly prepared gelatin (FG7.5, FG10) and preheated gelatin (PG10). Time sweep tests indicating the storage modulus (G') and loss modulus (G'') of FG and PG at the respective concentrations: (A) FG7.5, (B), FG10, and (C) PG10. Regions of the curves were expanded to identify the gelation time point for each curve. (D) A plot showing the viscosity of FG7.5, FG10, and PG10 with time.

modulus reached a plateau. As observed with FG7.5 and FG10, the change in gelatin concentration had little effect on the gelation time for FG. However, the shorter gelation time in FG10 (~168 s) than FG7.5 (~174 s) may explain the mild spreading of FG7.5 ink at 3 min (**Figure 2A**), which was not apparent for FG10 (**Figure 2A**). PG10 exhibited the longest gelation time of 1169 s (19.4 min) (**Figure 3C**). This measurement was consistent with the spreading of PG10 ink at 20 min where proper-gelation was observed (**Figure 2B**).

2.5 Effect of preheating on ink viscosity

Viscosity is an essential parameter for extrusion-based printing as it determines the printability of the ink with a given pressure. A previous study has shown that the extrusion pressure is proportional to the zero-shear viscosity of the extruded filament[39]. The time-dependent change in the viscosity of the ink required us to control the extrusion pressure throughout the printing. We measured the viscosity of FG7.5, FG10, and PG10 over time (**Figure 3D**). The increase in the viscosity of FG and PG was due to the crosslinking of the gelatin by TG. The rate of increase in viscosity was evident by the gradient of the slope reflected in the viscosity-time curves, suggesting the required pressure to extrude the ink from the nozzle. The initial sharp increase in the viscosity of FG implied that the rapid increase in the extrusion pressure was required to ensure smooth printing. This rapid increase in the extrusion pressure resulted in somewhat unpredictable print quality with discontinuous or spread inks, which was observed for the FG inks (**Figure 3D**). The sharp increase in the viscosity for FG also explains the short duration of acceptable printability (**Figure 2B**) and rapid gelation (**Figure 3A, 3B**), both of which made the DIW 3D printing challenging for FG. In contrast, the increase in the viscosity occurred slower for PG10 than FG7.5 and FG10 (**Figure 3D**), allowing for relatively easy control over the printing pressure and smooth extrusion of the ink.

2.6 Swelling of hydrogels

The swelling test was performed on the hydrogels prepared from FG and PG. An isotonic environment was simulated with 1 × PBS, which would be an important consideration if the samples were used as cellular scaffolds. We studied the swelling of hydrogels by placing the hydrogel samples prepared from FG (FG7.5, FG10, and FG20) and PG (PG7.5, PG10, and PG20); all samples were crosslinked with TG (5% w/w) in 1 × PBS. The hydrogels were weighed at the beginning of the experiment and every 24 h post-soaking in 1 × PBS for 4 days. Their swelling ratios were plotted against the incubation time with 1 × PBS. (**Figure 4**)

For FG7.5, FG10, PG7.5, and PG10, a decrease in gel weights was observed post-soaking in 1 × PBS because 1 × PBS had a much higher ionic strength than the water contained in each gel. The gel placed in the hypertonic environment lost water due to the osmotic pressure. This effect surpassed the ability of hydrogels to absorb water, causing an overall decrease in the gel weights[26]. FG7.5 and FG10 showed a 20% reduction in gel weights after 24 h; the gel weights remained relatively constant up till 96 h subsequently. (**Figure 4**) In contrast, PG7.5 and PG10 exhibited up to 40% reduction in gel weights at 72 h, and remained relatively constant up till 96 h. At a high concentration of gelatin (i.e., FG20 and PG 20), we observed the swelling of the gel. FG20 showed 5% increase in gel weight after 24 h and remained relatively constant thereafter until 96 h. PG20 showed a 30%

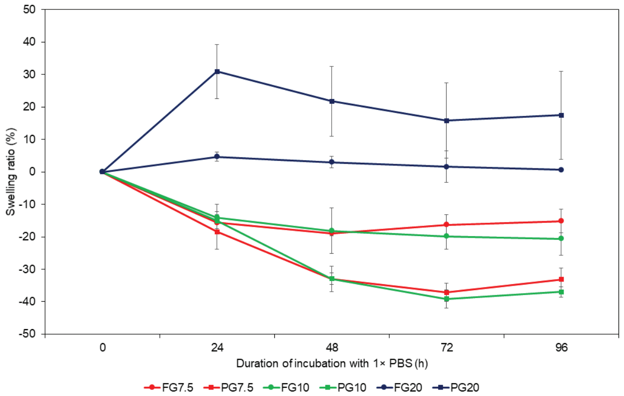

Figure 4. Swelling of the hydrogels. Changes in the swelling ratio for the respective FG and TG over 96 h incubation in 1× PBS. All samples of hydrogels contained 5% (w/w) of TG.

increase in gel weight after 24 h and equilibrated to a ~20% increase in gel weight until 96 h. The overall swelling could be attributed to a high concentration of gelatin (20%) in the hydrogel. Interestingly, FG exhibited smaller changes in gel weights than PG regardless of swelling or shrinking. This observation could be attributed to the rigidity of the gelatin network. Extended heating may cause the polypeptide chains of PG to be partially hydrolyzed. The resulting network in PG gel is more pliable than that in FG and may permit physical changes in the structure of the gel network. The flexibility of the gel network in PG allowed for an increased degree of shrinking or swelling in 1 × PBS, depending on the concentration of gelatin within the composition. Overall, the preheating of gelatin altered the properties to shrink or swell when placed in aqueous environments. The consideration of volume changes is essential when intending to create precise structures of gelatin by 3D printing. For the ink of PG10 that offered adequate printing duration, we shall account for the shrinkage if the printed model is used in aqueous environments.

3 Conclusions

In this paper, we explored the effect of preheating of gelatin to improve the duration of printable time in DIW 3D printing. Our study suggested that preheating gelatin for 7 days extended the duration of the acceptable printability 10 times longer than freshly prepared gelatin of the same concentration (10% w/w), and 4 times longer than freshly prepared gelatin with similar stiffness (10 kPa). The preheating of the gelatin altered the shrinking and swelling behaviors of the resulting hydrogels over 4 days in 1 × PBS, which provides an important consideration when the printed models are used in aqueous environments such as cell culture media. We believe the preheating of gelatin shall serve as a facile route to enhance the usability of gelatin in extrusion-based processes. Gelatin inks are increasingly used in DIW 3D printing to fabricate single-layered structures and multi-layered complex 3D structures that require a long duration of time for printing.

4 Materials and methods

4.1 Preparation of the inks and hydrogels

Freshly prepared gelatin (FG) was defined as gelatin (Porcine skin, Bloom 300, type A) (Sigma-Aldrich, USA) that had not undergone preheating. Briefly, FG stock was prepared by dissolving and mixing 12 g of gelatin powder with 18 g of distilled water in a water bath at 40 – 50°C with stirring until a clear yellow solution was obtained. Subsequently, the FG stock was kept at 4°C until further use. PG was prepared by placing an FG stock in a heat oven at 65°C for 7 days. Both gelatins were mixed with a 5% w/w TG (Moo Gloo TI TG) (Modernist Pantry, USA) to achieve their desired final concentrations before the experiments. To produce hydrogels, the final mixture was placed in the incubator at 37°C for 24 h to complete the crosslinking of gelatin by TG. The inks were prepared by mixing the gelatin stock solution that was pre-warmed to 40°C with TG. The mixture was subsequently stirred for 30 s before transferring into a metal syringe for printing. The addition of TG to gelatin initiated the gelation. The temperature of the ink was maintained in the syringe at 40°C throughout the printing.

4.2 DIW 3D printer and printability characterization

FG and PG inks were printed using a DIW 3D printer using a commercial 3D printing robot and a dispenser (SHOTmini 200 Sx and IMAGE MASTER 350 PC Smart, Musashi Engineering Inc., Japan). The dispenser was equipped with a single metal syringe (to maintain constant printing temperature) and a precise pressure controller (ML-5000XII and ML-808GX, Musashi Engineering Inc., Japan). MuCAD V software (Musashi Engineering Inc., Japan) was used to generate the design of the grid. Printing was performed with a metal nozzle head with a diameter of 200 μm under the dispending pressure ranging from 0.001 MPa to 0.7 MPa and the writing speed of 16 mm/s. The print speed was maintained at 16 mm/s to ensure the uniformity of the printing condition for all printing. The printing temperature was at 40°C.

4.3 Assessment of the printability

FG7.5, FG10, and PG10 were prepared at 0 min. The inks were printed in a grid pattern on a glass surface at 3 min, 5 min, 10 min, and every 5 min after that. The printing was stopped when the inks became clumpy or when the ink could not be extruded at the maximum pressure of the dispenser. The value of *Pr* was calculated from the printed grid pattern of the inks at respective time points. The entire printed grid pattern was a square measuring 2 cm by 2 cm, with a size of 4 cm^2. Briefly, *Pr* was calculated from the perimeter (*L*) and area (*A*) of each square shape ($n = 5$) within the printed grid pattern formed by the interconnected filaments using the formula: $Pr = L^2/16A$[36]. Optical images of the printed constructs were analyzed to determine the L and A of the interconnected filaments. All image processing was done using ImageJ software[40].

4.4 Rheological analysis of gelatin and TG ink

Rheometer (Discovery HR-2, TA Instruments, USA) with a 20 mm parallel plate was used to measure the gel storage modulus (*G'*), loss modulus (*G''*), gelation time, and viscosity for the various compositions of FG and PG samples at 40°C. *G'* and *G''* were determined by the oscillatory stress sweep test at a constant angular frequency of 10 rad s^{-1} with a logarithmic shear strain ramp from 1% to 100%. Gelation time was measured at 1% oscillation strain and 1 Hz frequency. Viscosity testing was performed at a constant shear rate of 0.01 s^{-1}.

4.5 Gel swelling

10 g of the gel solutions containing respective final concentrations of FG and PG were poured into a Petri dish (90 mm × 15 mm) and incubated at 37°C for 24 h to allow complete crosslinking of the gelatin chains. Subsequently, a square acrylic mold (20 mm × 20 mm × 2 mm) prepared from laser cutting was pressed into the hydrogel to create square pieces of the samples at 600 mg each. Each piece of hydrogel prepared from respective concentrations of FG or PG was placed into a Petri dish (30 mm × 15 mm) and incubated with 1 × PBS (Nacalai Tesque, Japan) for 4 days. The hydrogels were weighed before soaking in the media, and every 24 h up post-soaking until Day 4 ($n = 3$). The swelling ratio was calculated from the following equation:

$$Swelling\ ratio = \frac{W_t - W_o}{W_o} \times 100$$

where W_t was the weight of the swollen sample at the respective time point and W_o was the initial weight of the sample.

Acknowledgments

The authors would like to thank International Design Centre at Singapore University of Technology and Design (SUTD) (IDG11700103) and Agency for Science, Technology and Research (A*STAR) (A19B9b0067) for the project support. The authors thank the members of Hashimoto Group at SUTD for helpful feedback.

Conflicts of interest

The authors declare that they have no conflicts of interest.

Authors' contributions

J.J.Y.T., C.P.L., and M.H. planned the experiment. J.J.Y.T. and C.P.L. carried out the experiments. M.H. supervised the experiments. J.J.Y.T. and M.H. wrote the paper.

References

1. Ng WL, Chua CK, Shen YF, 2019, Print me an Organ! Why we are not there yet. *Prog. Polym. Sci*, 2019:101145. DOI: 10.1016/j.progpolymsci.2019.101145.
2. Lee JM, Ng WL, Yeong WY, 2019, Resolution and Shape in Bioprinting: Strategizing Towards Complex Tissue and Organ Printing. *Appl Phys Rev*, 6:011307. DOI: 10.1063/1.5053909.
3. Guo SZ, Qiu K, Meng F, *et al.*, 2017, 3D printed stretchable tactile sensors. *Adv Mater*, 29:1701218. DOI: 10.1002/adma.201701218.
4. Voon SL, An J, Wong G, *et al.*, 2019, 3D Food Printing: A

Categorised Review of Inks and their Development. *Virtual Phys Prototyp*, 14:203–18.

5. Karyappa R, Hashimoto M, 2019, Chocolate-based Ink Three-dimensional Printing (Ci3DP). *Sci Rep*, 9:1–11. DOI: 10.1038/s41598-019-50583-5.
6. Gariboldi MI, Best SM, 2015, Effect of Ceramic Scaffold Architectural Parameters on Biological Response. *Front Bioeng Biotech*, 3:151. DOI: 10.3389/fbioe.2015.00151.
7. Sun H, Zhu F, Hu Q, *et al.*, 2014, Controlling Stem Cell-mediated Bone Regeneration Through Tailored Mechanical Properties of Collagen Scaffolds. *Biomaterials*, 35:1176–84. DOI: 10.1016/j.biomaterials.2013.10.054.
8. Kuttappan S, Mathew D, Nair MB, 2016, Biomimetic Composite Scaffolds Containing Bioceramics and Collagen/Gelatin for Bone Tissue Engineering a Mini Review. *Int J Biol Macromol*, 93:1390–401. DOI: 10.1016/j.ijbiomac.2016.06.043.
9. Irvine SA, Agrawal A, Lee BH, *et al.*, 2015, Printing Cell-laden Gelatin Constructs by Free-form Fabrication and Enzymatic Protein Crosslinking. *Biomed Microdevices*, 17:16. DOI: 10.1007/s10544-014-9915-8.
10. Bettadapur A, Suh GC, Geisse NA, *et al.*, 2016, Prolonged Culture of Aligned Skeletal Myotubes on Micromolded Gelatin Hydrogels. *Sci Rep*, 6:28855. DOI: 10.1038/srep28855.
11. Osorio FA, Bilbao E, Bustos R, *et al.*, 2007, Effects of Concentration, Bloom Degree, and pH on Gelatin Melting and Gelling Temperatures Using Small Amplitude Oscillatory Rheology. *Int J Food Prop*, 10:841–51. DOI: 10.1080/10942910601128895.
12. Pepelanova I, Kruppa K, Scheper T, *et al.*, 2018, Gelatin-Methacryloyl (GelMA) Hydrogels with Defined Degree of Functionalization as a Versatile Toolkit for 3D Cell Culture and Extrusion Bioprinting. *Bioengineering* (*Basel*), 5:55. DOI: 10.3390/bioengineering5030055.
13. Karyappa R, Ching T, Hashimoto M, 2020, Embedded Ink Writing (EIW) of Polysiloxane Inks. *ACS Appl Mater Inter*, 12:23565–75. DOI: 10.1021/acsami.0c03011.
14. Karyappa R, Ohno A, Hashimoto M, 2019, Immersion Precipitation 3D Printing (ip 3DP). *Mater Horiz*, 6:1834–44. DOI: 10.1039/c9mh00730j.
15. Melocchi A, Parietti F, Maroni A, *et al.*, 2016, Hot-melt Extruded Filaments Based on Pharmaceutical Grade Polymers for 3D Printing by Fused Deposition Modeling. *Int J Pharm*, 509:255–63. DOI: 10.1016/j.ijpharm.2016.05.036.
16. Ghazal AF, Zhang M, Liu Z, 2019, Spontaneous Color Change of 3D Printed Healthy Food Product over Time after Printing as a Novel Application for 4D Food Printing. *Food Bioproc Tech.*, 12:1627–45. DOI: 10.1007/s11947-019-02327-6.
17. Dhariwala B, Hunt E, Boland T, 2004, Rapid Prototyping of Tissue-engineering Constructs, Using Photopolymerizable Hydrogels and Stereolithography. *Tissue Eng*, 10:1316–22. DOI: 10.1089/1076327042500256.
18. Skardal A, Zhang J, McCoard L, *et al.*, 2010, Photocrosslinkable Hyaluronan-gelatin Hydrogels for Two-step Bioprinting. *Tissue Eng Part A*, 16:2675–85. DOI: 10.1089/ten.tea.2009.0798.
19. Billiet T, Gevaert E, De Schryver T, *et al.*, 2014, The 3D Printing of Gelatin Methacrylamide Cell-laden Tissue-engineered Constructs with High Cell Viability. *Biomaterials*, 35: 49–62. DOI: 10.1016/j.biomaterials.2013.09.078.
20. Duan B, Hockaday LA, Kang KH, *et al.*, 2013, 3D Bioprinting of Heterogeneous Aortic Valve Conduits with Alginate/Gelatin Hydrogels. *J Biomed Mater ResA*, 101:1255–64. DOI: 10.1002/jbm.a.34420.
21. Kirchmajer DM, Iii RG, 2015, An Overview of the Suitability of Hydrogel-forming Polymers for Extrusion-based 3D-printing. *J Mater Chem B*, 3:4105–17. DOI: 10.1039/c5tb00393h.
22. Chang R, Nam J, Sun W, 2008, Effects of Dispensing Pressure and Nozzle Diameter on Cell Survival from Solid Freeform Fabrication Based Direct Cell Writing. *Tissue Eng Part A*, 14:41–8. DOI: 10.1089/ten.2007.0004.
23. Mondal MI, 2019, Cellulose-Based Superabsorbent Hydrogels. Springer, Berlin, Germany.
24. Tice L, Moore A, 1952, Heat Denatured Gelatin. *J Am Pharm Assoc*, 41:631–3.
25. Qi J, Zhang WW, Feng XC, *et al.*, 2018, Thermal Degradation of Gelatin Enhances its Ability to Bind Aroma Compounds: Investigation of Underlying Mechanisms. *Food Hydrocoll*, 83:497–510. DOI: 10.1016/j.foodhyd.2018.03.021.
26. Xing Q, Yates K, Vogt C, *et al.*, 2014, Increasing Mechanical Strength of Gelatin Hydrogels by Divalent Metal Ion Removal. *Sci Rep*, 4:4706. DOI: 10.1038/srep04706.
27. Janmey PA, Miller RT, 2011, Mechanisms of Mechanical Signaling in Development and Disease. *J Cell Sci*, 124:9–18.
28. Solon J, Levental I, Sengupta K, *et al.*, 2007, Fibroblast Adaptation and Stiffness Matching to Soft Elastic Substrates. *Biophys J*, 93:4453–61. DOI: 10.1529/biophysj.106.101386.
29. Mogha P, Srivastava A, Kumar S, *et al.*, 2019, Hydrogel Scaffold with Substrate Elasticity Mimicking Physiological-niche Promotes Proliferation of Functional Keratinocytes. *RSC Adv*, 9:10174–83. DOI: 10.1039/c9ra00781d.
30. Chan SW, Rizwan M, Yim EK, 2020, Emerging Methods for

Enhancing Pluripotent Stem Cell Expansion. *Front Cell Dev Biol*, 8:70. DOI: 10.3389/fcell.2020.00070.

31. Tan JJ, Tee JK, Chou KO, *et al.*, 2018, Impact of Substrate Stiffness on Dermal Papilla Aggregates in Microgels. *Biomater Sci*, 6:1347–57.
32. Croome R, 1959, The Rapid Formation and Breakdown of Gelatin Gels, and the Temperature-dependence of their Rigidity. *J Sci Food Agric*, 10:394–400. DOI: 10.1002/jsfa.2740100708.
33. Gerardo H, Lima A, Carvalho J, *et al.*, 2019, Soft Culture Substrates Favor Stem-like Cellular Phenotype and Facilitate Reprogramming of Human Mesenchymal Stem/Stromal Cells (hMSCs) through Mechanotransduction. *Sci Rep*, 9:1–18. DOI: 10.1038/s41598-019-45352-3.
34. Kureel SK, Mogha P, Khadpekar A, *et al.*, 2019, Soft Substrate Maintains Proliferative and Adipogenic Differentiation Potential of Human Mesenchymal Stem Cells on Long-term Expansion by Delaying Senescence. *Biol Open*, 8:bio039453. DOI: 10.1101/364059.
35. Gilbert PM, Havenstrite KL, Magnusson KE, *et al.*, 2010, Substrate Elasticity Regulates Skeletal Muscle Stem Cell Self-renewal in Culture. *Science*, 329:1078–81. DOI: 10.1126/science.1191035.
36. Ouyang L, Yao R, Zhao Y, *et al.*, 2016, Effect of Bioink Properties on Printability and Cell Viability for 3D Bioplotting of Embryonic Stem Cells. *Biofabrication*, 8:035020. DOI: 10.1088/1758-5090/8/3/035020.
37. Nauenberg M, 2014, A Paradox with the Hagen-Poiseuille Relation for Viscous Fluid Flow. *Am J Phys*, 82:82–5. DOI: 10.1119/1.4825138.
38. Mulder M, 2000, Membrane preparation. In: Encyclopedia of Separation Science: Phase Inversion Membranes. Elsevier, Amsterdam, Netherlands, pp. 3331–3346. DOI: 10.1016/b0-12-226770-2/05271-6.
39. Zhu S, Stieger MA, van der Goot AJ, *et al.*, 2019, Extrusion-based 3D Printing of Food Pastes: Correlating Rheological Properties with Printing Behaviour. *Innov Food Sci Emerg*, 58:102214. DOI: 10.1016/j.ifset.2019.102214.
40. Schneider CA, Rasband WS, Eliceiri KW, 2012, NIH Image to ImageJ: 25 Years of Image Analysis. *Nat Methods*, 9:671–5. DOI: 10.1038/nmeth.2089.

INTERNATIONAL JOURNAL OF BIOPRINTING

ISSN (print): 2424-7723

ABOUT THE JOURNAL

International Journal of Bioprinting is a biannual, double-blind peer-reviewed, open access journal. This journal focuses on the use of 3D printing technology with materials that incorporate viable living cells or biological elements to produce tissue or biotechnological products. Further discourses and technological advancements in bioprinting are the goals behind acceptance of high-quality basic and applied research: from concept creation to fabrication of the bioprinting process, associated clinical applications as well as social implications.

Whioce Publishing, official publisher for the journal welcomes researchers to submit their papers relevant to bioprinting for consideration via **http://ijb.whioce.com/** For general enquiries and order for prints and reprints, please write in to **IJB@whioce.com** for a fast response.

SUBMIT YOUR PAPERS HERE

ABOUT THE PUBLISHER

WHIOCE
PUBLISHING PTE. LTD.

Whioce Publishing in Singapore is a registered publisher of excellent quality academic journals for an international readership. We deliver exceptional editorial support for the advancement and dissemination of scientific research by linking readers and researchers with networks and industries. We have ambitions to get our journals indexed in prominent databases such as EI, SCI, SSCI and AHCI, thereby aiming to be a first-class knowledge platform for researchers worldwide.

Whioce Publishing also engages in publishing e-books, organizing academic conferences and educational trainings, and providing translational services.

International Journal of Bioprinting is an
independent open access journal published
by Whioce Publishing Pte.Ltd.

WHIOCE PUBLISHING PTE. LTD.
PROVIDING
FIRST-CLASS SCIENTIFIC INFORMATION
FOR TOP SCHOLARS

Whioce Publishing Pte.Ltd.
7030 Ang Mo Kio Avenue 5
#04-15 Northstar@AMK
Singapore 569880
Tel: +65 65702707/65702718
Fax: +65 65702803

See www.whioce.com/contact for a full list of offices and contact information.

Whioce Publishing Pte.Ltd. is a company registered in Singapore (No. 201427293E), whose registered office
is at 7030 Ang Mo Kio Avenue 5 #04-15 Northstar@AMK Singapore 569880